Functionalized gold nanorods for sensing thyroid stimulating hormone and bioimaging application

By

Sanjana Varma

10BB19J26012

A thesis submitted to the
Academy of Scientific & Innovative Research
for the award of the degree of
DOCTOR OF PHILOSOPHY
in

SCIENCE

Under the supervision of

Dr. Bhushan P. Chaudhari

CSIR- National Chemical Laboratory, Pune

Academy of Scientific and Innovative Research
AcSIR Headquarters, CSIR-HRDC campus
Sector 19, Kamla Nehru Nagar,
Ghaziabad, U.P. – 201 002, India

February 2025

Certificate

This is to certify that the work incorporated in this Ph.D. thesis entitled, ***"Functionalized gold nanorods for sensing thyroid stimulating hormone and bioimaging application"***, submitted by ***Sanjana Varma*** to the Academy of Scientific and Innovative Research (AcSIR), in fulfillment of the requirements for the award of the Degree of ***Doctor of philosophy in science***, embodies original research work carried-out by the student. We, further certify that this work has not been submitted to any other University or Institution in part or full for the award of any degree or diploma. Research material(s) obtained from other source(s) and used in this research work has/have been duly acknowledged in the thesis. Image(s), illustration(s), figure(s), table(s) etc., used in the thesis from other source(s), have also been duly cited and acknowledged.

Sanjana Varma

Date: 24-02-2025

(Student)

Dr. Bhushan P. Chaudhari

Date: 24-02-2025

(Supervisor)

STATEMENTS OF ACADEMIC INTEGRITY

I, ***Sanjana Varma***, a Ph.D. student of the Academy of Scientific and Innovative Research (AcSIR) with Registration No. ***10BB19J26012*** hereby undertake that, the thesis entitled ***"Functionalized gold nanorods for sensing thyroid stimulating hormone and bioimaging application"*** has been prepared by me and that the document reports original work carried out by me and is free of any plagiarism in compliance with the UGC Regulations on *"Promotion of Academic Integrity and Prevention of Plagiarism in Higher Educational Institutions (2018)"* and the CSIR Guidelines for *"Ethics in Research and in Governance (2020)"*.

Signature of the Student

Date: 24-02-2025

Place: Pune

It is hereby certified that the work done by the student, under my supervision, is plagiarism-free in accordance with the UGC Regulations on *"Promotion of Academic Integrity and Prevention of Plagiarism in Higher Educational Institutions (2018)"* and the CSIR Guidelines for "*Ethics in Research and in Governance (2020)*".

Signature of the Supervisor

Name: Dr. Bhushan P. Chaudhari

Date: 24-02-2025

Place: Pune

I dedicate this thesis to my grandparents, my parents, my brother, Tanishq Varma and my supervisor, Dr. Bhushan P. Chaudhari.

For their blessings, love, and unwavering support

Acknowledgement

The successful completion of this PhD thesis was contingent upon the steadfast assistance and direction of several individuals. All of the people who have helped me improve both academically and personally throughout this time have my deepest thanks and debt. Thanks to the Almighty, I consider myself fortunate and privileged to have received the wonderful chance to enter the esteemed institute CSIR-National Chemical Laboratory (CSIR-NCL). NCL is highly known across the world for its meticulous work, serene setting, and well-equipped laboratories.

I am blessed and extremely pleased to be mentored by my supervisor, Dr. Bhushan P. Chaudhari, who is kind, wise, and compassionate. Working under Sir's guidance improved my personality and gave me access to the newest methods, which definitely made my PhD work easier. I was able to go through challenging moments because of Bhushan Sir's inspiring and guiding demeanour, constant support, and advice. I am forever grateful for his ingenious mentorship, which has shaped me into a confident and independent researcher ready to embrace the future. I extend my sincere gratitude to Sir for his unwavering faith in my abilities and for affording me multiple opportunities to achieve academic excellence.

I am deeply grateful to my Doctoral Advisory Committee (DAC) members, Dr. Manjusha Shelke, Dr. Mahesh Dharne, and Dr. Mahesh Kulkarni, for their invaluable guidance and support throughout my PhD journey. Their timely feedback, constructive criticism, and unwavering encouragement were instrumental in my academic growth. I am indebted to my DAC members for creating a conducive academic environment that fostered my intellectual development. I would also like to express my sincere gratitude to the Director of CSIR-NCL and the current and former Head of the Biochemical Sciences Division for providing state-of-the-art facilities and opportunities to conduct my research at NCL. Furthermore, I extend my thanks to the Council of Scientific and Industrial Research (CSIR) for the fellowship and the Academy of Scientific and Innovative Research (AcSIR) for my PhD registration.

I want to express my gratitude to the NCL’s Central Analytical Facility (CAF) for its efficient and timely characterization services. I am thankful to the Student Academic Office (SAO), AcSIR office, Digital Information Resource Centre (DIRC), Biochemical Science Division staff, and Library of NCL for their prompt assistance throughout my tenure. I am grateful to the late Dr.

Mohan Wani, Former Director of the National Centre for Cell Science (NCCS), Pune, for allowing me to carry out *in vitro* studies at NCCS. I would also like to thank Dr. Manas Santra for his warm welcome and collaborative spirit for the *in vitro* analysis. I am indebted to Dr. Pradeep Chaudhari for his invaluable contribution to CT imaging studies and for allowing me to work at the Advanced Centre for Treatment Research and Education in Cancer (ACTREC), Navi Mumbai. I would like to express my sincere gratitude to Mr. Bhabani S. Mahanty for his guidance and support during the CT imaging analysis. I am grateful to Dr. Mohana Krishna Reddy Mudium, Director of the Institute of Pesticide Formulation Technology (IPFT), Gurgaon, and Dr. Samsul Alam for the ICP-MS analysis. I am also extremely thankful to Dr. Virendra Gajbhiye for providing the necessary facilities for LFA studies at Agarkar Research Institute (ARI), Pune. Further, I would like to extend my gratitude to the SATHI-BHU facility and Mr. Shailendra Kumar for the photoacoustic study.

The conducive and collegial atmosphere of the laboratory, coupled with the steadfast support of my former labmates, Mrs. Aliesha Moudgil, Mrs. Neha Jaiswal, Ms. Rajnigandha Shende, Mrs. Ujwala Mulik, Mr. Deepak Shelke, Mr. Aditya Kadam, Mrs. Shweta Kokade, Mr. Rahul Shah, Ms. Sayali Tambe and Mr. Aagam Bamb, created a positive and productive research environment. I am especially thankful to Aliesha Moudgil for her invaluable assistance, encouragement, and technical expertise, which made my journey smoother. Further, I would like to thank my current labmates, Ms. Dimpal Burade, Mr. Lakshit Kumar Pandit, Ms. Kajal Bari and Mr. Tejas Gade, for continuing the same supportive, learning and friendly lab environment. The support of all my current labmates is also invaluable to me. I'll cherish the memories I made with my labmates. They made my PhD journey truly special.

Thanks won’t be enough for the unwavering trust, patience, and support of my mother, Mrs. Namita Varma and my father, Mr. Sudhir Varma. Despite the distance, I always felt their love and encouragement. Their constant belief in me has been instrumental in my success. My parents always had my back, irrespective of the situation. I owe them for their love, blessings, and unwavering support. My brother, Mr. Tanishq Varma, has been a constant source of support and friendship. I'm grateful for our shared experiences and his unwavering belief in me. Thank you for always being there to listen, laugh, and back me. I have a great deal of gratitude for my beloved family because they have always kept faith in me. They have prepared a foothold for me, and I am

grateful for their favors. I am also deeply indebted to my grandparents, whose wisdom and values have been a constant source of inspiration. Their dream of higher education has motivated me to pursue my PhD. I am forever grateful for their love, support, and blessings. A special thanks to my amazing friends, who have been a source of laughter, motivation, and much-needed sanity during my PhD journey. Last but not least, I would like to extend my heartfelt thanks to my teachers from school and college whose guidance and mentorship have shaped my character and aspirations.

Abbreviations

Abbreviations	Full Form
GNR	Gold Nanorod
NIR	Near-Infrared
LSPR	Localized Surface Plasmon Resonance
SPR	Surface Plasmon Resonance
DDA	Discrete Dipole Approximation
SERS	Surface-Enhanced Raman Scattering
MBA	Mercaptobenzoic Acid
4-ATP	4-Amino Thiophenol
PL	Photoluminescence
TPL	Two-Photon Luminescence
1D	One-Dimensional
PA	Photoacoustic
PAI	Photoacoustic Imaging
EBL	Electron-Beam Lithography
FIB	Focused Ion Beam
CTAB	Cetyltrimethylammonium Bromide
TOAB	Tetradodecylammonium Bromide
BDAC	Benzyl (Dimethylhexadecyl) Ammonium Chloride
UPD	Under Potential Deposition
UV	Ultraviolet
PEG	Polyethylene Glycol
GD2	Disiloganglioside
MUA	11-mercaptoundecanoic acids
OSCC	Oral Squamous Cell Carcinoma

PAA	Polyacrylic Acid
PSS	Polystyrenesulfonate
PAH	Poly(allylamine hydrochloride)
PDDAC	Poly(diallyldimethylammonium chloride)
PEI	Polyetherimide
EDC	1-Ethyl-3-(3-dimethylaminopropyl) carbodiimide
NHS	N-Hydroxysuccinimide
TEOS	Tetraethyl Orthosilicate
MOF	Metal-Organic Framework
HA	Hyaluronic Acid
EPR	Enhanced Permeability and Retention
RES	Reticuloendothelial System
IUPAC	International Union of Pure and Applied Chemistry
WHO	World Health Organization
PoC	Point-of-Care
LFA	Lateral Flow Assay
PDMS	Polydimethylsiloxane
LFIA	Lateral Flow Immunochromatographic Assay
SELEX	Systematic Evolution of Ligands by Exponential Enrichment
AuNP	Gold Nanoparticle
QD	Quantum dot
UCNP	Upconverting Nanoparticle
MNP	Magnetic Nanoparticle
MAR	Magnetic Assay Reader
CNS	Central Nervous System
PNS	Peripheral Nervous System
TSH	Thyroid-Stimulating Hormone

TRH	Thyroid-Releasing Hormone
FSH	Follicle-Stimulating Hormone
hCG	Human Chorionic Gonadotropin
LH	Luteinizing Hormone
NHANES	National Health and Nutrition Examination Survey
FDA	Food and Drug Administration
MRI	Magnetic Resonance Imaging
PET	Positron Emission Tomography
CT	Computed Tomography
US	Ultrasound
SPECT	Single-Photon Emission Computed Tomography
OI	Optical Imaging
3D	Three-Dimensional
FDA	Food and Drug Administration
DTPA	Diethylenetriamine Pentaacetic Acid
DOTA	Tetraazacyclododecanetetraacetic Acid
SPIO	Superparamagnetic Iron Oxide
ESION	Ultrasmall-Sized Iron Oxide Nanoparticle
2D	Two-Dimensional
OCT	Optical Coherence Tomography
ER	Estrogen Receptors
PR	Progesterone Receptors
HER 2	Human Epidermal Growth Factor Receptor 2
γPGA	Poly-γ-Glutamic Acid
TNBC	Triple Negative Breast Cancer
PBS	Phosphate Buffered Saline
BSA	Bovine Serum Albumin

SDS	Sodium Dodecyl Sulfate
NCIM	National Collection of Industrial Microorganisms
NCCS	National Centre for Cell Science
RPMI	Rosewell Park Memorial Institute
DMEM	Dulbecco's Modified Eagle Medium
FBS	Fetal Bovine Serum
MTT	3-(4,5-Dimethylthiazol-2-yl)-2,5-Diphenyltetrazolium Bromide
DMSO	Dimethyl sulfoxide
RT	Room Temperature
DI	Deionized
TEM	Transmission Electron Microscopy
HETEM	High-Resolution Transmission Electron Microscopy
FESEM	Field Emission Scanning Electron Microscopy
SAED	Selected Area Electron Diffraction
XRD	X-Ray Diffraction
EDX	Energy Dispersive X-Ray
STEM	Scanning Transmission Electron Microscopy
XPS	X-Ray Photoelectron Spectroscopy
FTIR	Fourier Transform Infrared
ICP-MS	Inductively Coupled Plasma Mass Spectrometry
OD	Optical Density
BE	Binding Efficiency
RBC	Red Blood Cell
HU	Hounsfield Unit
ANOVA	Analysis of Variance
LPW	Longitudinal Plasmon Wavelength
TPW	Transverse Plasmon Wavelength

Table of Contents

List of Tables

List of Figures

ABSTRACT

Chapter 1: Introduction and Review of Literature

Gold nanorods (GNRs) are ideal agents for probing diseases through imaging and sensing due to their favorable optical properties, ease of surface functionalization and biocompatibility. (Cheng et al., 2011) GNRs have two surface plasmon resonance (SPR) bands, corresponding to a transverse (short axis) and a longitudinal (long axis) band (J. Cao et al., 2012; H. Huang et al., 2012; H. Zhang et al., 2016). The longitudinal band can be tuned from visible to near-infrared (NIR) region depending on the size and aspect ratio of GNRs (Rizwan Younis et al., 2021; J. Zhou et al., 2017). GNR's localized surface plasmon resonance (LSPR) spectrum is sensitive to changes in the refractive index of the surroundings. This property makes them an efficient molecular probe for various applications. Also, it is one of the major properties that enable GNRs to sense specific target-binding actions (J. Cao et al., 2012; H. Huang et al., 2012; H. Zhang et al., 2016). GNRs also show a diverse color range with various aspect ratios when in a colloidal suspension (Cao et al., 2014). Additionally, GNRs exhibit strong NIR absorption and scattering, which are very attractive for *in vivo* biomedical imaging due to minimal NIR (700–1300 nm) light absorption by most human tissues and water (Kim et al., 2023; Thu Haine & Niidome, 2017). Owing to all these properties, GNRs are very appropriate nanomaterials for bioimaging and biosensing studies.

Biosensing and bioimaging are the two important aspects of diagnosing or detecting, and monitoring any biomedical conditions. According to the World Health Organization (WHO), the diagnostics for developing countries should be defined as REASSURED: real-time connectivity, ease of specimen collection and environmental friendliness, affordable, sensitive, specific, user-friendly, rapid and robust, equipment free and deliverable to end-users (Parolo & Merkoçi, 2013; Sena-Torralba et al., 2022). Interestingly, nanomaterials play a crucial part in improving existing biosensors, and they are delivering more advantages in the development of novel biosensors (Parolo & Merkoçi, 2013). The nanomaterials-based sensors can be electrochemical, colorimetric, thermal, magnetic, optical, etc.(P. Malik et al., 2013). However, paper-based nano biosensors, mainly lateral flow assay (LFA), have gained more popularity due to their ergonomic attribute. Nanoparticles are majorly used as labels for LFAs like gold nanoparticles (AuNPs), latex beads, quantum dots, upconversion nanoparticles, liposomes, magnetic nanoparticles, etc. (Bahadır &

Sezgintürk, 2016; Parolo et al., 2020; Posthuma-trumpie & Korf, 2009; Sajid et al., 2015). However, these labels, apart from AuNPs, carry disadvantages: low sensitivity, photobleaching, instability, and batch-to-batch variations (Bahadır & Sezgintürk, 2016; Sajid et al., 2015), generating the need for more efficacious labels for LFA.

Bioimaging is a non-invasive method of scrutinizing biological activity over a certain time period. It facilitates the visualization of subcellular features as well as every single tissue in higher-order organisms (N. Malik et al., 2019). It is used for disease diagnosis and therapy. Some examples of bioimaging techniques are fluorescence imaging, magnetic resonance imaging (MRI), positron emission tomography (PET) imaging, computed tomography (CT), photoacoustic imaging (PAI) etc (Erathodiyil & Ying, 2011). Although, these imaging modalities have inadequacies which can be surpassed by combining two or more imaging modalities together. This combining of imaging is termed as multimodal imaging (Y. Huang et al., 2012; Morato et al., 2021; Rieffel et al., 2015; H. Wang et al., 2024). The clinically used traditional contrast agents or imaging probes come up with multiple drawbacks like rapid metabolization, poor resolution, lack of multimodality, etc. However, nanoparticles, especially GNRs interventions, could overcome all these drawbacks of conventional imaging agents (H. Wang et al., 2024).

Statement of the problem

Thyroid-stimulating hormone (TSH) levels in the serum are determined to assess thyroid-related diseases. The normal TSH level in a healthy person ranges from 0.5 µIU/mL to 5 µIU/mL. Conventionally, several immunoassays are used to determine the TSH levels in the body. However, the lack of sensitivity and difficult operational conditions lead to the development of the point-of-care (POC) LFA for analyzing TSH (Bikkarolla et al., 2022; Jeong et al., 2013; H. Wang et al., 2014). The commercially available TSH testing kits are qualitative and only used for the detection of hypothyroidism; however, due to low TSH levels in hyperthyroidism, there are no LFAs for the detection of hyperthyroidism based on TSH (Choi et al., 2017). Many studies have prepared LFA for the estimation of TSH using a fluorescent dye (Jeong et al., 2013), magnetic nanoparticles (Znoyko et al., 2020), gold nanoshells (Bikkarolla et al., 2022) and AuNPs (Choi et al., 2017; You et al., 2013) as labels. However, LFAs prepared using a fluorescent dye, and AuNPs could not determine hyperthyroidism without the reader's involvement (Choi et al., 2017; Jeong et al., 2013; You et al., 2013). Further, the magnetic nanoparticles LFAs require prolonged detection

time, and the problem of excessive magnetic enrichment is also associated with them (Ghosh et al., 2023) and it is difficult to achieve the reproducibility and maintain the stability of gold nanoshells (Y. C. Wang et al., 2018), which could affect their sensitivity. Therefore, GNRs have the ability to assess both hypothyroidism and hyperthyroidism through LFA without employing the reader.

Furthermore, breast cancer is the second most common cancer around the world, with more than 2.3 million cases in the year 2022 (International Agency for Research on Cancer, 2024). Due to these intricate characteristics, the early diagnosis of breast cancer is highly required for effective treatment and cure, as well as to avoid relapses. The commonly used imaging techniques are not sensitive enough to detect small lesions in case of metastasis (Mu et al., 2017). These limitations of conventional ways to detect and monitor breast cancer can be addressed by using GNRs as a multimodal contrast agent or imaging nanoprobes, owing to their unique properties. Many articles prove that the GNRs are the efficient multimodal contrast agent for imaging and studying breast cancer (H. Guo et al., 2021; L. Luo et al., 2020; F. Xia et al., 2022; Yao et al., 2021; Yue et al., 2019). However, there is still a need to develop more biocompatible GNRs-based multimodal imaging probes for their successful clinical translation.

We proposed MUA-modified GNRs (MUA-GNRs), which were further functionalized with TSH antibodies and biosynthesized poly-γ-glutamic acid (γPGA) for nanobiosensing and multimodal bioimaging investigations, respectively

We hypothesized that the TSH antibody functionalized GNRs could act as a sensitive and selective label for LFA, which could help to diagnose both hypothyroidism and hyperthyroidism without employing any analytical technique. Further, γPGA-MUA-GNRs could function as an efficient and biocompatible CT imaging and PAI dual-modal imaging/contrast agent. Thus, we proposed the following objectives for the study:

1. Optimization, synthesis and characterization of gold nanorods
2. Surface functionalization of gold nanorods
3. Preparation and demonstration of proof of concept of lateral flow assay test strip
4. Sensitivity and selectivity testing of lateral flow assay test strip

5. Bioimaging studies of gold nanorods

Chapter 2: Materials and Methods

We followed the following protocols for the synthesis and characterization of GNRs.

2.1. Synthesis and Functionalization of GNRs

We synthesized GNRs by seed-mediated growth method by using cetyltriammonium bromide (CTAB) as a surfactant (Nikoobakht & El-Sayed, 2003). The CTAB from the GNR surface was replaced by 11-mercaptoundecanoic acid (11-MUA) by using the pH-mediated method (J. Cao et al., 2012). Mouse monoclonal TSH antibody (10-2427) was covalently attached to the surface of MUA-GNRs by the EDC/NHS method. GNRs and MUA-GNRs were further functionalized with γPGA by stirring the mixture for 2 hr at room temperature (RT).

2.2. Characterization of Various GNRs

The LSPR spectra of plain and various functionalized GNRs were recorded in a UV-visible spectrophotometer. Malvern Zetasizer Pro (Malvern Panalytical, UK) was used for zeta potential measurements. The morphology of the GNRs was determined using transmission electron microscopy (TEM), high-resolution transmission electron microscopy (HRTEM) and field emission scanning electron microscopy (FESEM). X-ray diffraction (XRD) and selected area electron diffraction (SAED) analysis were used to validate the crystallinity of the GNRs. Further, the elemental composition of GNRs was determined through energy dispersive X-ray (EDX), scanning transmission electron microscopy (STEM) mapping and X-ray photoelectron spectroscopy (XPS) analysis. Fourier transform infrared **(**FTIR) spectra were recorded to determine the presence of functional groups in different types of GNRs after synthesis and functionalization. Inductively coupled plasma mass spectrometry (ICP-MS) was employed to quantify the gold content in different GNRs. The Bradford assay quantified TSH antibodies functionalized with GNRs. The colloidal stability of the various GNRs was tested by storing them at 4°C and recording the zeta potential values and LSPR spectra at determined time intervals.

2.3. Preparation and Testing of LFA

The sample pad, conjugate pad and test pad were prepared and assembled and then cut to form LFA strips of 4 mm width. The sensitivity of the LFA was determined by using different

concentrations of TSH (0.01µIU/ml to 20µIU/ml), and the intensity of the test line was observed through the naked eye. Similarly, the selectivity of the LFA was tested by using hormones such as follicle-stimulating hormone (FSH), luteinizing hormone (LH) and human chorionic gonadotropin (hCG).

2.4. *In-vitro* and Bioimaging Studies

The MTT assay tested the cell viability in MCF-7, MDA-MB-231 and MCF-10A cell lines when treated with different groups of GNRs. The uptake of the various GNRs was tested on the MCF-7, MDA-MB-231 and MCF-10A cell lines and quantified by ICP-MS. Hemolysis assay analyzed the hemocompatibility of different groups of GNRs. Further, the phantom CT and PAI studies tested the CT and photoacoustic signal generation potential of various GNRs.

Chapter 3: Optimization, Synthesis, and Characterization of GNRs

We optimized the process parameters of the seed-mediated growth method to synthesize GNRs for biosensing and bioimaging applications. We noticed that 1 mM gold precursor concentration, 0.2 M CTAB, 250 µl silver nitrate ($AgNO_3$) (4 mM), 75 µl ascorbic acid, and 12 µl seed aged for 30 min, pH 3 and reaction time 2 h were appropriate to synthesize monodisperse and stable GNRs of aspect ratio around 3.8. Major factors that affect the synthesis of GNRs were found to be gold precursor concentration, CTAB concentration, silver nitrate concentration and its volume as well, ascorbic acid volume, seed volume, and pH.

The synthesized GNRs capped with CTAB had a longitudinal SPR band around 751 nm, which was in NIR area and a transverse SPR band around 511 nm. The zeta potential of GNRs was found to be +49.98 ± 6.29 mV. The positive charge was due to the CTAB capping on their surface. The size of GNRs based on HRTEM analysis was found to be 41.72 ± 5 nm x 11 ± 2 nm. This size was also in line with the FESEM data. The EDX spectrum of GNRs recorded by HRTEM confirms the presence of elements gold (Au), carbon (C), oxygen (O) and bromine (Br) which was also supported by STEM mapping and XPS spectrum. The SAED pattern and XRD spectra with peaks at 2Ɵ values 38.24º, 44.46º, 64.69º and 77.66º correspond to planes (111), (200), (220) and (311), respectively, confirmed the crystalline nature of the GNRs. The FTIR spectrum corroborated the synthesis of CTAB-capped GNRs.

Chapter 4: Optimization, Synthesis, and Characterization of MUA-modified GNRs (MUA-GNRs)

We optimized the process parameters of surface modification of GNRs with 11-MUA to replace toxic CTAB and to decorate GNRs with a carboxyl group (-COOH). We varied the solvents used to dissolve 11-MUA and studied how those solvents affected the surface modification of GNRs. The parameters like 11-MUA volume (1, 2 and 3 ml), time (6, 8, 10, and 12 hr) and stirring speed (600, 700, 800 and 900 rpm) were further varied to modify the surface of GNRs. Based on the red shift in the longitudinal plasmon wavelength (LPW) of GNRs and zeta potential studies, we optimized an alkaline aqueous solvent, 2 ml 11-MUA to modify 5 ml GNRs, 800 rpm stirring speed and 8 hr as the time required to modify GNRs.

We detected a red shift of around 20 ± 4 nm in the LPW of GNRs after its surface modification with 11-MUA. The LPW of CTAB-GNRs was 751 nm, which was shifted to 773 nm. The zeta of MUA-GNRs was -36.53 ± 2.96 mV. The negative was due to the -COOH group. The size of MUA-GNRs was 42.97 ± 3.23 nm x 11.9 ± 1.76 nm, which was corroborated by FESEM analysis. The SAED patterns suggested the crystalline nature of MUA-GNRs. Further, the presence of Au, C, O and sulfur (S) instead of Br in EDX, STEM mapping and XPS studies confirmed the replacement of CTAB with 11-MUA. FTIR studies also proved that the CTAB on the surface of GNRs was replaced by 11-MUA. Also, the MUA-GNRs were highly stable in a borate buffer (pH 9), although deionized water can also be used as a medium to disperse them.

Chapter 5: Functionalization of GNRs and Development of LFA

Chapter 5A: Optimization, Synthesis and Characterization of TSH Antibody Functionalized GNRs

We have functionalized MUA-GNRs with TSH antibody (Ab-GNRs) through covalent peptide linkage, which was used as a conjugate for LFA preparation. We optimized the buffer for the reaction as well as the concentration of antibody required for functionalization (5, 25 and 50 µg/ml) and the concentration of sucrose (2, 5 and 10%) should be added in the resuspension buffer to store Ab-GNRs based on UV-visible and zeta potential studies. It was observed that the stability and structural integrity of GNRs were maintained when the functionalization process was performed in the borate buffer. Further, the antibody concentration for functionalization was

fixed at 50 µg/ml. Lastly, to keep Ab-GNRs stable, the percentage of sucrose that should be added to the resuspension buffer of Ab-GNRs was optimized to 5%.

The LPW of Ab-GNRs was around 814 nm, which was red-shifted by around 41 ± 3 nm compared to the LPW of MUA-GNRs. The zeta potential of Ab-GNRs was -15.14 ± 0.78 mV. The decrease in the zeta potential of the Ab-GNRs compared to MUA-GNRs confirms the functionalization of GNRs with TSH antibodies. The size of Ab-GNRs was found to be 43.56 ± 5.16 nm x 11.59 ± 1.93 nm through HRTEM, which was supported by the FESEM results too. The presence of nitrogen (N) signal along with Au, S, O and C in the EDX, STEM mapping and XPS spectrum of Ab-GNRs confirmed that the TSH antibodies were conjugated with the MUA-GNRs. The FTIR analysis also corroborated this. The % binding efficiency of the TSH antibody was 83.38 ± 0.34 %. Also, it was found that the MUA-GNRs and Ab-GNRs were stable in colloidal suspension for 3 months and 15 days, respectively, when stored at 4 ^{o}C.

Chapter 5B: Preparation and Optimization of LFA

We used Ab-GNRs as a label to detect TSH through LFA. To enhance the sensitivity of the LFA to detect TSH, we optimized certain conditions like the optical density (OD) of the label (5, 10 and 20), the concentration of the capture antibody (1, 2 and 3 mg/ml) and the volume of sample (30, 40 and 50 µl) needed for the LFA. However, before this the performance of the Ab-GNRs to detect TSH was tested via UV-visible-NIR spectroscopy studies. The limit of detection (LOD) of the conjugate (Ab-GNRs) determined via a red shift in the LPW of Ab-GNRs after binding of TSH was found to be 0.05 µIU/ml. Also, the conjugate was selective for TSH. Further, based on the color development on the test line and control line of the LFA, we finalized 20 OD of the conjugate, 3 mg/ml concentration of the capture antibody and 50 µl sample volume for the LFA. The LOD of the LFA was found to be 0.3 µIU/ml, and the LFA was specific towards TSH; it did not show any cross-reactivity with the hormones FSH, LH and hCG. Additionally, this LFA can provide reproducible results for 3 months when stored in a desiccated environment.

The LFA was capable of semi-quantitatively elucidating hypothyroidism and hypothyroidism based on the TSH without using any quantification method. As, the normal range of TSH in adult humans is 0.5-5 µIU/ml. Therefore, when the concentration of TSH in the sample is below 0.3 µIU/ml, there will be no appearance of the test line, or a very faint test line will appear, signifying hyperthyroidism. While, when the concentration of TSH is above 5 µIU/ml, a darker test line will

appear, leading to the determination of hypothyroidism. We have successfully prepared fast, user-friendly and robust LFA by using GNRs as a reporter or label or conjugate to detect TSH. Thus, GNRs acted as a potent and sensitive label for LFA.

Chapter 6: Functionalized GNRs for Bioimaging Studies

Chapter 6A: Optimization, Synthesis and Characterization of γ-PGA Functionalized GNRs

We have surface-coated GNRs and MUA-GNRs with a biologically synthesized anionic polymer, i.e. γPGA, to enhance the biocompatibility of the GNRs. Initially, we have simultaneously screened three different types of γPGA biosynthesized by using different substrates as well as the commercially available one and optimized the concentration of γPGA appropriate for functionalizing GNRs. Then, we also optimized the volume of γPGA required to functionalize 5 ml suspension of GNRs and MUA-GNRs, based on the red shift in the LPW and zeta potential measurements. The γPGA of 1 mg/ml concentration, which was synthesized using tomato waste as a substrate, was finalized. The volume of γPGA was optimized to 1 ml.

The red shift of 24 ± 2.64 nm and 38 ± 4.58 nm was observed in the LPW of GNRs and MUA-GNRs, respectively, after functionalization with γPGA, and the zeta potential of GNRs changed to negative after coating with γPGA i.e. -28.06 ± 1.58 mV as well as the zeta potential of γPGA-MUA-GNRs (-27.59 ± 0.44 mV) was decreased compared to the zeta potential of MUA-GNRs. Based on HRTEM analysis, the size of γPGA-GNRs and γPGA-MUA-GNRs were 43.22 ± 3.8 nm x 12.2 ± 1.58 nm and 45.71 ± 3.29 nm x 12.9 ± 1.84 nm, respectively, which were also supported by FESEM analysis. The SAED pattern confirmed the crystalline nature of both γPGA-GNRs and γPGA-MUA-GNRs. The EDX, STEM mapping and XPS spectrum revealed the presence of Au, C, N, O and Br in γPGA-GNRs, whereas there was the presence of Au, C, N, O and S in γPGA-MUA-GNRs. Further, the FTIR findings suggested that the surface of GNRs and MUA-GNRs were successfully coated with the γPGA. The GNRs, MUA-GNRs, γPGA-GNRs and γPGA-MUA-GNRs were found to be highly stable and structural integrity was maintained for 3 months when stored at 4 ^{o}C.

Chapter 6B: *In vitro* Efficacy and Bioimaging Studies

The GNRs, γPGA-GNRs, MUA-GNRs, and γPGA-MUA-GNRs were found to be stable in the cell culture media. The cell viability assay established the great biocompatibility of the γPGA-

MUA-GNRs in both cancerous (MCF-7 and MDA-MB-231) and normal breast cell lines (MCF-10A). Also, the MUA-GNRs and γPGA-MUA-GNRs do not have inherent cytotoxic potential due to the absence of CTAB on them, making them biocompatible multimodal imaging probes. The cell viability of γPGA-MUA-GNRs in MCF-7, MDA-MB-231 and MCF-10A was found to be above 91% at its maximal concentration. The hemolytic assay further established the biocompatibility. The γPGA-GNRs, MUA-GNRs, and γPGA-MUA-GNRs showed great hemocompatibility with less than 6% hemolysis at their highest concentration. The cellular uptake studies revealed higher uptake of γPGA-MUA-GNRs compared to other groups of GNRs in all three cell lines. However, the uptake was slow in MCF-10A cells compared to the cancerous MCF-7 and MDA-MB-231 cell lines.

The phantom CT imaging and PAI studies confirmed the great dual-modal cancer imaging potential of biocompatible γPGA-MUA-GNRs. A good linear relationship was recorded between the CT and photoacoustic intensity and the concentrations of all the groups of GNRs based on Au content. Notably, the CT and photoacoustic contrast ability of all the groups of GNRs were slightly better than the conventional contrast agents. Thus, γPGA-MUA-GNRs could serve as an effective dual-modal CT imaging and PAI contrast agent.

Chapter 7: Conclusions & Future Prospects

We performed a robust optimization of the seed-mediated growth method for synthesizing GNRs. This study enables the synthesis of GNRs for biosensing, bioimaging and other applications by altering the identified parameters to achieve the desired specifications. We also optimized various factors for surface modification of GNRs with 11-MUA and subsequently with TSH antibody and γPGA to make them sensitive and selective to detect TSH and endow them with biocompatibility. The high-end analytical techniques supported the synthesis of stable, monodisperse and appropriately surface-modified GNRs.

The LOD of the LFA prepared using Ab-GNRs as a label was 0.3 μIU/ml. Also, the LFA was specific towards TSH; it did not show any cross-reactivity with the hormones FSH, LH and hCG. The LFA was capable of semi-quantitatively elucidating hypothyroidism and hyperthyroidism based on the TSH without employing any quantification technique. As the normal range of TSH in adult humans is 0.5-5 μIU/ml, therefore when the concentration in the sample is below 0.3 μIU/ml, there will be no appearance of the test line and if it is between 0.5-0.3 μIU/ml, a very faint

test line will form, as from 0.5 µIU/ml the clear test line appeared on the device. Thus, by this hyperthyroidism could be estimated. However, when the concentration of TSH is above 5 µIU/ml, the darker test line will appear, leading to the detection of hypothyroidism.

In bioimaging studies, the γPGA-MUA-GNRs showed cell viability above 91% in all three cell lines (MCF-7, MDA-MB-231 and MCF-10A) at their maximum concentration, thus, revealing the biocompatibility of γPGA-MUA-GNRs. Also, the γPGA-MUA-GNRs were also found to be hemocompatible with <3% hemolysis at its maximal concentration. The cellular uptake studies showed higher uptake of γPGA functionalized GNRs compared to other groups of GNRs in all three cell lines. Thus, γPGA coating enhanced the cellular uptake efficiency of the GNRs. The γPGA-MUA-GNRs also showed excellent CT and photoacoustic signals, which were slightly better than the conventional CT and PAI contrast agents. A good linear relationship was noted between the CT and photoacoustic intensity and the concentrations (based on Au content) of γPGA-MUA-GNRs. Therefore, γPGA-MUA-GNRs can effectively applied as a dual-modal CT imaging and PAI contrast agent that have the combined advantages of high spatial/ density resolution and high sensitivity.

This proof-of-concept study highlights the proficient TSH sensing potential of stable Ab-GNRs as a label in LFA. Also, it demonstrates the multimodal imaging capability of biocompatible γPGA-MUA-GNRs. The LFA can be further tested with real samples for its subsequent clinical use. Also, the multiplexed LFA can be prepared to estimate all thyroid-related hormones (TSH, T4 and T3) together. The MUA-GNRs can also be employed as a label for other LFAs after functionalizing them with desired biomolecules to detect various biomedical and environmental analytes. Thereafter, the γPGA-MUA-GNRs need to be tested in animal models. It can also be functionalized with ligands to achieve the precise targeted dual-modal imaging of cancers and other biomedical conditions. Furthermore, the GNR-based imaging probes could also be utilized for personalized treatment and diagnosis of any diseases or disorders.

CHAPTER 1

Introduction and Review of Literature

1.1. Gold nanorods (GNRs)

Gold nanorods (GNRs) have pulled wide attention for biomedical applications due to their unique properties (X. Huang et al., 2009; Rizwan Younis et al., 2021). It has a pseudo-one-dimensional structure which resembles a capsule shape (Kesharwani et al., 2023). The research on GNRs was initiated in 1990; however, in 1997, Yu et al. efficaciously synthesised GNRs by employing the electrochemical approach. Later, El Sayed's and Murphy's groups made significant contributions to the synthesis history of GNRs. They used a seed-mediated approach to synthesize GNRs. The seed-assisted growth method is commonly employed to prepare GNRs (J. Zhou et al., 2017).

The attractive feature of GNRs, which is responsible for their popularity in various biomedical applications, is their two surface plasmon resonance (SPR) bands. The transverse band results from electron oscillations along the short axis, while the longitudinal one occurs due to the oscillations along the long axis. A change in the aspect ratio (length/width) of GNRs causes the longitudinal SPR band to shift from the visible portion of the electromagnetic spectrum into the near-infrared (NIR) (700-1300 nm) area (Kim et al., 2023). Additionally, GNRs also comprise of features like ease of surface functionalization, biocompatibility (Cheng et al., 2011; Gui & Cui, 2012), strong scattering ability, long-term photostability, less plasmon damping, more significant extinction coefficient and localized surface plasmon resonance (LSPR) (Truong et al., 2012; J. Zhou et al., 2017; J. Cao et al., 2012). Further, the NIR light does not get absorbed much by water, and most of the human tissues, and GNR's characteristic of having absorption and scattering in the NIR region makes them a potent *in vivo* biomedical imaging (Kim et al., 2023; Thu et al., 2017). Also, the LSPR spectrum of GNRs is subtle to the variation in the medium's refractive index; thus, this feature makes them an ideal sensing agent. Also, it is a significant property that enables GNRs to sense the specific target binding actions (J. Cao et al., 2012; H. Huang et al., 2012; H. Zhang et al., 2016). GNRs also show diverse colour ranges in colloidal suspension depending on their aspect ratio. Thus, it can also serve as a potent colorimetric label for biosensing (J. Cao et al., 2014). Furthermore, it has been reported in some studies that GNRs have more blood circulation time than spherical gold nanoparticles (AuNPs), which makes them ideal drug delivery and biomedical imaging agents (Kim et al., 2023). Therefore, the multifunctional attributes of GNRs make them an efficient agent for both biosensing and bioimaging applications.

1.2. Properties of GNRs

1.2.1. LSPR

The attractive optical properties of metallic nanoparticles are ascribed to the way they interact with the incident light, which is also imitated by their intense color (X. Huang et al., 2009). Upon light illumination, the conduction band's free electrons suffer collective coherent oscillation resonating with light's frequency. Consequently, this matching of oscillating frequency of the conduction band electrons and incident light leads to strong resonance recognized as SPR and localized SPR for bulk metal and its nano counterpart, respectively. This oscillation led to the restoration of coulomb force by inducing the separation of charge between the conduction band electron and the ionic core of the metal, causing surface electrons to oscillate in response to the incident electromagnetic field (Rizwan Younis et al., 2021; J. Zhou et al., 2017; Varma et al., 2025; X. Huang et al., 2009). This SPR oscillation is the reason for strong light absorption, which can be noticed by the UV-vis spectrum (X. Huang et al., 2009; Varma et al., 2025).

The transverse and longitudinal SPR bands of GNRs result from the oscillation of electrons along the short and long axis, respectively, in response to the incident light. However, LSPR along the short axis appear in the visible region, while along the long axis appears from the visible to NIR region (Fig. 1.1) (X. Huang et al., 2009; J. Wang et al., 2016; J. Zhou et al., 2017; Varma et al., 2025; Rizwan Younis et al., 2021; Khan et al., 2021). The longitudinal SPR band of GNRs is susceptible to variation in the particle size, surrounding medium and dielectric properties. These factors influence the electron charge density on the nanoparticle's surface (X. Huang et al., 2009; J. Zhou et al., 2017; Varma et al., 2025). However, the transverse band is resistant to changes in the aspect ratio, surrounding medium and dielectric properties of the GNRs. This attribute of GNRs can be well understood by Gans theory of dipole approximation which was deduced to describe the optical behaviour of the ellipsoidal nanoparticles (X. Huang et al., 2009; Varma et al., 2025; Khan et al., 2021). Thus, the optical traits of GNRs could be tweaked by varying their aspect ratio. The SPR excitation of gold nanomaterials enhances their light absorption by 5-6 orders of magnitude concerning the dye molecules (X. Huang et al., 2009; J. Zhou et al., 2017). This feature makes GNRs an ideal imaging and sensing agent.

The application of discrete dipole approximation (DDA) and successful study of the relative contribution of scattering and abortion on the total extinction at different sizes of GNRs, as well as at various aspect ratios, was done by Lee and El-Sayed. DDA is a commanding tool for

calculating the optical properties of nanoparticles. They have reported that the quantum yield is augmented just by elongating the shape from 0.326 for a sphere to 0.603 for a rod. This may be due to the reduction in plasmon dephasing of nanorods in comparison with spherical nanoparticles. So, at a particular aspect ratio for larger rod scattering efficiency dominates and for smaller one's absorption efficiency dominates (X. Huang et al., 2009; Lee & El-Sayed, 2005; Khan et al., 2021). From these studies, it was found out that for the imaging application, larger nanoparticles are favoured owing to their greater light scattering efficacy as compared to smaller nanoparticles, which are preferred for photothermal therapy due to their more excellent light absorbing efficiency (X. Huang et al., 2009; Khan et al., 2021). GNR scattering wavelength can also be tuned till the NIR range by varying their aspect ratios; due to this property under white light illumination, they could function as multicolour (orange to ruby red) -coded probes for biosensing studies. Additionally, GNRs have the unique capacity to concentrate the free-space optical field at subwavelength areas next to their surfaces. This leads to the electric field's augmentation mainly around the high curvature area of GNRs, resulting in a variety of light-driven mechanisms which can be used for imaging purposes (J. Zhou et al., 2017). Thus, it is evident that the LSPR properties of GNRs define their uniqueness, which makes them distinctive and superior to other gold nanoparticles. This property has a significant role in applying GNRs for various biomedical studies.

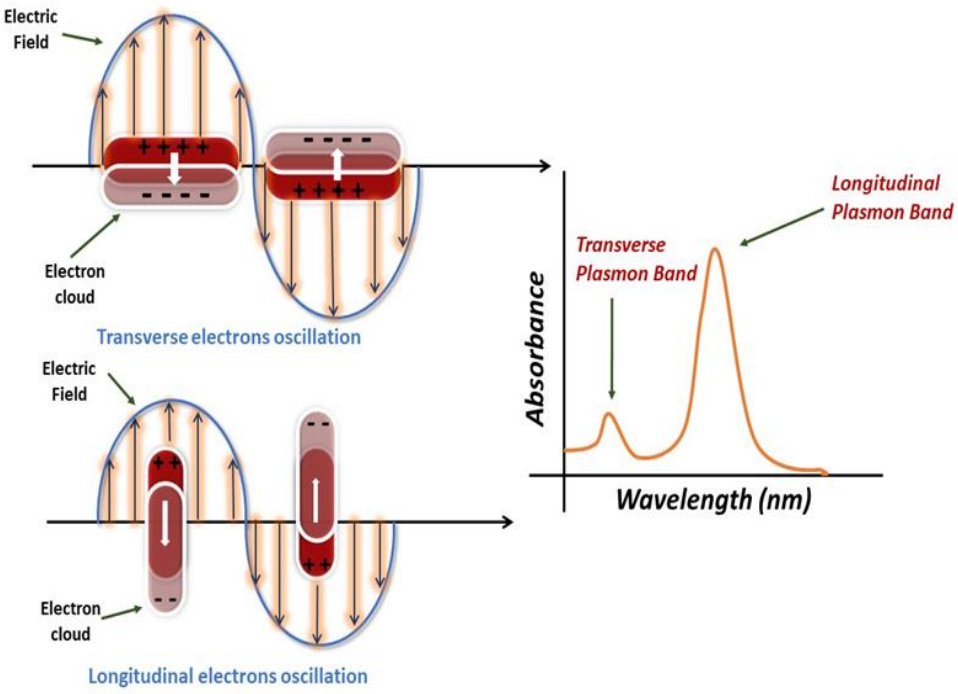

Figure 1.1 LSPR property of GNRs (Modified from Varma et al., 2025)

1.2.2. Surface-enhanced Raman scattering (SERS) properties

The inelastic scattering of the photons when the molecules are excited to advance rotational and vibrational energy levels is defined as Raman scattering. After adsorbing on the metallic nanoparticles surface, some special substrate's Raman signal gets augmented by multiple orders, resulting in the phenomenon of SERS. This enhancement can either be chemical or electromagnetic, and it can also be amplified by 10^{14} folds at the hotspots, which helps detect small molecules. Although, electromagnetic enhancement holds a crucial function in SERS (Kesharwani et al., 2023; J. Zhou et al., 2017; Varma et al., 2025).

The localized electromagnetic fields are enhanced owing to their LSPR property, mainly at the high curvature areas of GNRs. Hence, to enhance the electromagnetic surface enhancement effect, the incident laser wavelength should match the LSPR peak's wavelength of metallic nanoparticles (Kesharwani et al., 2023; J. Zhou et al., 2017; Varma et al., 2025). One study investigated the size and shape-related SERS behaviour of GNRs along with Mercaptobenzoic acid (MBA) and noticed the augmentation in the SERS signal when the excitation source's wavelength coincided with the longitudinal SPR band of GNRs (H. Guo et al., 2009).

The LSPR properties make GNR a competent substrate for SERS (J. Zhou et al., 2017; Kesharwani et al., 2023). Many investigators have examined the efficacy of GNRs in enhancing the SERS of Raman molecules. Hu et al. studied SERS signal amplification of 4-amino thiophenol (4-ATP) by conjugating it to the surface of different shapes of gold nanoparticles. They noticed a significant SERS signal improvement with 3.3 rod-shaped gold nanoparticles of aspect ratio 3.3 and with dog bone-shaped particles. Interestingly, it was found that due to the lighting rod effect, the enhancement was 8 times more in 3.3 aspect ratio GNRs when compared with 2.4 aspect ratio GNRs (Hu et al., 2007). Also, one study infers that GNR aggregates and assemblies can boost electromagnetic fields more due to its plasmon coupling property. The study assessed that the SERS signal of film prepared with aggregated GNRs was greater than the film prepared directly by depositing GNRs on glass. This was due to the sturdy electromagnetic coupling among the tightly put GNRs (Y. Wang et al., 2008). Thus, the SERS property of GNRs is useful for both sensing and imaging of small biomolecules.

1.2.3. Photoluminescence (PL) properties

Mooradian reported and explained the photoluminescence property of noble metals first time in 1969 (J. Wang et al., 2016; J. Zhou et al., 2017). The major principle behind photoluminescence or single photon luminescence is, primarily, the generation of electron-hole

pairs by excitation of electrons to the sp band from d-band. Then, by scattering process, excited electrons come back to a lower energy level, which is above the Fermi level, by losing energy to the photon lattice, finally resulting in radiative (photon emission) recombination of sp band electrons with the holes in the d band (Khan et al., 2021; J. Zhou et al., 2017; Varma et al., 2025; X. Huang et al., 2009). LSPR of GNRs has an imperative function in the quantum efficiency of GNRs. After properly establishing an electrochemical method for synthesising GNRs, El-Sayed and coworkers widely scrutinized the photoluminescence property of GNRs (J. Zhou et al., 2017; Varma et al., 2025).

Nanomaterials of metals have many magnitudes higher quantum efficiency than their bulk counterparts (J. Wang et al., 2016). Moreover, there is a direct relationship between the rise in PL wavelength and the aspect ratio of nanorods. Remarkably, GNRs or nanorods under the 3 aspect ratio have 6 orders more quantum efficiency than their bulk. Concurrently, it was also observed that up to the 3-aspect ratio, the augmentation is quadratic in quantum efficiency, although above it, the quantum efficiency of nanorods is reduced. Furthermore, Eustis and El-Sayed also noticed a reduction in the intensity of the augmented emission as the aspect ratio of nanorods was taken above 3.5 (Eustis & El-Sayed, 2005; Khan et al., 2021; Varma et al., 2025; X. Huang et al., 2009). Using simulations, the authors explained the dependence of this emission on the longitudinal band's plasmonic field potency. Further, the augmentation of the light's interband absorption by the plasmonic field clings to the degree of overlay among the SPR and interband absorption bands. Lastly, the plasmon field's intensification of emitted fluorescence light relies on the SPR absorption band and the fluorescence spectrum. The dynamic nature of the intersection between the SPR band and the interband is a direct consequence of the LSPR wavelength's dependence on the GNR aspect ratio (X. Huang et al., 2009; Khan et al., 2021). PL of GNRs is majorly dependent on their polarization of incident light, LSPR of GNRs and the dielectric constant of the surrounding medium (Varma et al., 2025; J. Wang et al., 2016).

Alternatively, the two-photon luminescence (TPL) phenomenon is more sensitive than single-photon luminescence. The aspect ratio of GNRs directly affects the TPL wavelength (X. Huang et al., 2009; J. Wang et al., 2016; J. Zhou et al., 2017; Varma et al., 2025). The main principle behind TPL is similar to single photon luminescence (J. Wang et al., 2016). Herein, this process involves a two-step excitation. First, an intraband transition occurs just below the Fermi level. Subsequently, a d-band excitation fills the void created in the first step. Finally, radiative recombination of the outstanding electrons and holes produces PL (X. Huang et al., 2009;

Varma et al., 2025). Interestingly, it was determined that the TPL of a single GNR is almost 58 times greater than a single rhodamine molecule. Also, it is possible to find out the area of GNR generating strong PL response by locally exciting the region of interest on nanorod and concurrently noticing the PL of the whole rod (J. Wang et al., 2016). GNRs also have the property of three-photon luminescence or multi-photon luminescence at a longer wavelength. However, the three PL of longer GNRs is more beneficial than the TPL of shorter GNRs. It was due to its deeper penetration, minimal photobleaching, no photodamage and very less background autofluorescence (J. Wang et al., 2016).

GNRs are able to circumvent photoblinking and photobleaching very effectively, which makes them an ideal probe for imaging studies (J. Wang et al., 2016). The above-discussed unique optical properties of GNRs glorify them among other nanoparticles, leading to a boom in their use for various biomedical applications.

1.2.4. Photothermal properties

By phonon-incorporated process, GNRs are capable of converting light into heat in just the time of picoseconds (ps). The process takes place by the transfer of absorbed energy of incident light in the form of oscillations to the free electrons, which is further conveyed to the phonon bath. Ultimately, this leads to a rise in the temperature of the surrounding medium (X. Huang et al., 2009; Rizwan Younis et al., 2021; J. Zhou et al., 2017; Varma et al., 2025; Kesharwani et al., 2023). It should be marked that this whole process is independent of its shape, size and longitudinal and transverse SPR of GNRs (X. Huang et al., 2009; Kesharwani et al., 2023; J. Zhou et al., 2017). Also, the high absorption cross-section of GNRs helps to achieve more conversion of light into heat. He et. al. studied this and determined that GNRs converted 80% of light energy into heat. This property makes GNRs the beneficial agent for drug or gene release and cancer therapeutic applications (G. S. He et al., 2010; Rizwan Younis et al., 2021; J. Zhou et al., 2017; Varma et al., 2025; Kesharwani et al., 2023).

However, the change in assembly state, geometries, the longitudinal SPR band and the concentration of GNRs would affect the photothermal conversion efficiency of GNRs (Kesharwani et al., 2023; J. Zhou et al., 2017; Varma et al., 2025). The overlapping of incident light wavelength with the longitudinal SPR wavelength of GNRs causes maximum photothermal conversion by GNRs. Also, it was studied that with the increase in size of GNRs, the conversion efficiency decreases, owing to the more light scattering by the larger GNRs (H. Chen et al., 2010). Jang et al. noted that GNR concentration is a more important factor than the

irradiation power for the heat distribution in the tissues (Jang et al., 2011). Furthermore, some studies demonstrated the effect of the assembly of GNRs on their photothermal efficiency. In one study, one-dimensional (1D) assembled GNRs were prepared using thiol (-SH), which had an absorption band in the NIR region. They observed that assembled GNRs had more outstanding photothermal efficiency than unassembled ones (Sheng et al., 2014). It is necessary to determine the effect of assemblies on GNRs because, after cellular uptake, GNRs tend to clump or aggregate, which may affect the final results of the studies (Kesharwani et al., 2023; J. Zhou et al., 2017; Rizwan Younis et al., 2021).

Besides, by absorbing strong pulsed laser due to rapid heating as well as thermoplastic expansion, the gold nanoparticles are capable to engender ultrasound. This feature is termed the photoacoustic (PA) effect or derivative of photothermal conversion. The signals emitted by this effect are termed photoacoustic signals, which can be easily converted into images by employing ultrasound detectors. Photoacoustic imaging (PAI) executed by using GNRs could enhance the sensitivity and specificity of the diagnostic (Kesharwani et al., 2023; J. Zhou et al., 2017; Varma et al., 2025). Many researchers have explored GNRs for simultaneous photothermal therapy and photoacoustic imaging applications.

1.3. Synthesis of GNRs

Many approaches could be employed for the preparation of monodisperse, high quality and uniform GNRs (X. Huang et al., 2009; Varma et al., 2025). The synthesis methods are divided into top-down and bottom-up approaches (Fig. 1.2). The bottom-up approach is nothing but assembling the atoms or molecules to form the particles; contrarily, a top-down approach is cutting down the bulk material into the nano size. Although bottom-up approaches are more beneficial than top-down ones in many factors, they can be easily translated into a large scale (J. Zhou et al., 2017; Varma et al., 2025; Rizwan Younis et al., 2021).

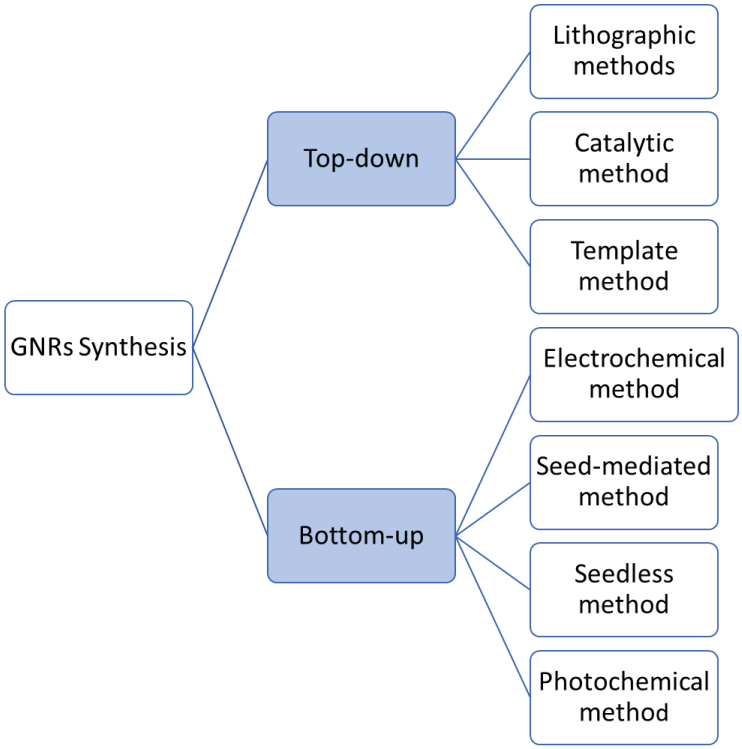

Figure 1.2 Different synthesis methods of GNRs

1.3.1. Top-down approaches

The top-down approaches involve the usage of techniques such as laser ablation, etching, etc. The merits associated with this approach are the formation of uniform GNRs, its assembly and control over the shape could also be achieved. However, the demerits of this approach are more empowering than its merits. This includes the expensive translation to large scale and imperfection in the surface structure of GNRs due to the crystallographic damage which happens during the fabrication process (J. Zhou et al., 2017; Varma et al., 2025; Rizwan Younis et al., 2021). The various top-down methods are explained below.

1.3.1.1. Lithographic methods

This method is by far the most experimentally tedious method for the synthesis of gold nanostructures. There are two commonly used Lithographic techniques for the synthesis of GNRs: electron-beam lithography (EBL) and focused ion beam (FIB) lithography. EBL initially involves the coating of a substrate with an electron-sensitive resist. Upon exposure to an electron beam, patterns of nanometer-scale openings in the resist are formed, through which gold can be deposited. By the lift-off process, which includes the use of acetone, the unexposed resist and the gold deposited on it are easily removed, leading to the formation of complex gold nanostructures. Meanwhile, FIB lithography produces desired nanostructures by sputtering

away unwanted film material with a rastered gallium ion beam. However, there are limitations associated with these methods, like not having proper control over the dimensions, polycrystalline particles, etc (X. Huang et al., 2009). Billiot et al. synthesized GNRs by this method (Billot et al., 2006).

1.3.1.2. Catalytic method

This method uses catalytic spherical nanoseeds for the direct growth of 1D nanorods on the substrate (X. Huang et al., 2009). Taub et al. used this method for GNR synthesis. In this, nanoparticles were attached to the substrate with the help of a linker. Subsequently, when this substrate was placed in an aqueous solution, 15% of the nanorods formed along with other different shapes (Taub et al., 2003). This method has been modified in terms of substitute ways of linking the nanoparticles as well as to avert the formation of other shapes (X. Huang et al., 2009).

1.3.1.3. Template method

As the name suggests, this method consists of a template which is made up of nanoporous tracked etched anodized ammonia or polycarbonate membrane(Vigderman et al., 2012; Alshangiti et al., 2023; X. Huang et al., 2009; Pérez-Juste et al., 2005). Further, to form the conductive base on the template, a thin layer of silver (Ag) or copper is sputtered(Alshangiti et al., 2023; Pérez-Juste et al., 2005). Utilizing electrochemical reduction, gold ions precursor is converted into gold atoms, which are then deposited within the pores of the template. After that, by chemically etching the template membrane, an ordered array of GNRs can be obtained (Alshangiti et al., 2023; X. Huang et al., 2009; Pérez-Juste et al., 2005; Vigderman et al., 2012). These GNRs are then redispersed in water or other solvent by agitation or sonication (Pérez-Juste et al., 2005). Also, polymeric material like poly (vinyl pyrrolidone) is utilized, to provide stability to GNRs and avert their aggregation (Alshangiti et al., 2023; Pérez-Juste et al., 2005; Vigderman et al., 2012). The length of the GNRs is normal to the substrate, while the width depends on the diameter of the pore on the template. However, by aluminium metal anodization in the acidic medium, pores of diameters from 5-200nm can be concocted. Although, the GNR's length could be tuned by altering the gold deposited during the process on the template. By this method, excellent control over the aspect ratio of GNRs can be achieved (Alshangiti et al., 2023; X. Huang et al., 2009; Pérez-Juste et al., 2005; Vigderman et al., 2012). There are also some limitations with this method, like a lower yield of GNRs, the removal of the templates being tedious and expensive, etc. Despite these drawbacks, this method is used for the synthesis

of GNRs for bio-related and other purposes (Alshangiti et al., 2023; Vigderman et al., 2012). There are some reports which have used templates like pores of mesoporous silica SBA 15 and silica nanotubes instead of nanoporous templates for the synthesis of GNRs by template method (Vigderman et al., 2012).

1.3.2. Bottom-up approaches

1.3.2.1. Electrochemical method

Wang and co-workers had firstly innovated this method for GNRs synthesis (Alshangiti et al., 2023; S. S. Chang et al., 1999; Khan et al., 2021; Pérez-Juste et al., 2005; Vigderman et al., 2012; J. Zhou et al., 2017; Varma et al., 2025; X. Huang et al., 2009). Also, before the development of the seed-based method, it was the utmost preferred method for GNR formation (Khan et al., 2021; J. Zhou et al., 2017; Varma et al., 2025; X. Huang et al., 2009). Briefly, this method uses a gold (Au) plate as an anode and, as a cathode, a platinum plate. These plates are dipped in an electrolytic solution, which comprises cetyltrimethylammonium bromide (CTAB) as a surfactant and tetradodecylammonium bromide (TOAB) as a co-surfactant. As the electrolysis process begins, Au ions in $AuBr_4^-$ form is produced from the anode; subsequently, they are reduced to Au atoms at the cathode plate by forming a complex with the CTAB micelle. Additionally, the silver (Ag) plate is also used to manage the size of GNRs by releasing the Ag ions due to the redox reaction among the Au ions and the Ag plate. Also, to augment the mixing of surfactants and for the formation of elongated (rod-shaped) CTAB micelles, acetone and cyclohexane are employed, respectively. Thereafter, with the help of ultrasonication the GNRs can be dispelled from the cathode (Alshangiti et al., 2023; S. S. Chang et al., 1999; Khan et al., 2021; Pérez-Juste et al., 2005; Vigderman et al., 2012; J. Zhou et al., 2017; Varma et al., 2025). By this method, GNRs of aspect ratio 1-7 can be synthesized with longitudinal SPR band at 1050 nm. Also, the precise mechanism of silver in the method is unclear (Vigderman et al., 2012; J. Zhou et al., 2017; Varma et al., 2025). The majority of GNRs prepared using this method are single crystalline in nature and grew along the (001) direction (X. Huang et al., 2009; Khan et al., 2021; Vigderman et al., 2012). Controlled synthesis of GNRs for various applications can be achieved by this method only by controlling the various factors like surfactant/template molecules, applied potential, and electrolyte composition. However, this method is time-consuming and not easily scalable (Alshangiti et al., 2023). A more intricate understanding of the factors involved in this method is required to synthesize GNRs of particular aspect ratios for various applications.

1.3.2.2. Seed-mediated growth method

This method is commonly utilized to synthesize GNRs. It is owing to its merits like facile nature and high yield of monodisperse GNRs, can be straightforwardly attained by this method (J. Zhou et al., 2017; Alshangiti et al., 2023; X. Huang et al., 2009; Rizwan Younis et al., 2021; Varma et al., 2025; Khan et al., 2021). Moreover, this method offers flexibility in surface modification of GNRs, and control over the size of GNRs can be achieved without difficulties (X. Huang et al., 2009). In 1989, Wiesner and Wokaun prepared anisometric gold colloids. For which they added gold nuclei to a gold precursor solution ($HAuCl_4$). The nuclei were formed by the reduction of gold precursor solution with phosphorous. Further, the GNR's growth was started by adding hydrogen peroxide solution (X. Huang et al., 2009; Wiesner & Wokaun', 1989).

Jana et al. ascertained the present concept of this method; they used the citrate-capped small gold nanoparticles as a seed to form gold nanorods. This seed reduced the $HAuCl_2$ in the growth solution. This $HAuCl_2$ was previously formed by ascorbic acid-based reduction of $HAuCl_4$. This solution also contained CTAB and Ag ions (X. Huang et al., 2009; Jana et al., 2001). The same group also modified this method into 3 steps, but there were some drawbacks associated with it (X. Huang et al., 2009; Khan et al., 2021). Further, in 2003, Nikoobakht and El-Sayed used CTAB as a surfactant for seed development and to regulate the size of GNRs, silver ions were used (Nikoobakht & El-Sayed, 2003). By their method, high-yield of the GNRs of aspect ratio in the range of 1.5 to 4.5 were obtained. Also, this method does not require repetitive centrifugation to separate out spherical particles. Moreover, while using this method, it is simpler to stop the overgrowth of GNRs just by centrifugation or by adding sodium sulfide (X. Huang et al., 2009; Khan et al., 2021).

This method involves two solutions: the seed and the growth solution. The spherical gold nanoparticles of size around 4 nm is the seed solution. It is formed by the strong reducing agent, i.e., sodium borohydride (NaBH4), which assists in the reduction of Au^{3+} ions in the presence of a surfactant. Although the growth solution contains CTAB (surfactant) and gold precursor, later, to reduce Au^{3+} to Au^{+}, ascorbic acid was incorporated in it as a weak reducing agent. Silver nitrate ($AgNO_3$) is also used in growth solutions to control the aspect ratio of GNRs (Khan et al., 2021; Alshangiti et al., 2023; X. Huang et al., 2009; Vigderman et al., 2012; J. Zhou et al., 2017; Varma et al., 2025; Rizwan Younis et al., 2021). The growth solution is usually maintained at 30 ^{o}C, to circumvent the crystallization of CTAB. Thereafter, the freshly

prepared seed solution was incorporated into the growth solution; to begin the GNR formation, the initiation can be simply assessed by the color change of the mixture (J. Zhou et al., 2017; Varma et al., 2025; Rizwan Younis et al., 2021). Seed solution induces the reduction of Au^{+} to Au^{0} by catalysing the ascorbic acid present on their surface, which subsequently results in the formation of GNRs (X. Huang et al., 2009; Khan et al., 2021; Varma et al., 2025; Alshangiti et al., 2023). The total taken by this method is 2-4 hr. Besides, the method can be altered in multiple ways to accomplish the synthesis of GNRs of varied aspect ratios. The aspect ratio of GNRs could be tweaked from 2-5 just by altering the concentration of Ag ions. Moreover, by using citrate capped seed and three-step method synthesis of high aspect ratio GNRs could be attained; however, employing CTAB capped seeds contributes to the formation of lower aspect ratio GNRs (J. Zhou et al., 2017; Varma et al., 2025; Rizwan Younis et al., 2021). Nikoobakht and El-Sayed explained that by using benzyl (dimethylhexadecyl) ammonium chloride (BDAC) as a co-surfactant with CTAB, synthesis of GNRs aspect ratio up to 10 can be achieved. Additionally, the concentration of silver ions is also required to be controlled in a binary surfactant system to obtain higher aspect ratio GNRs (Nikoobakht & El-Sayed, 2003; X. Huang et al., 2009). Similarly, by employing the Pluronic F-127 co-surfactant system, monodisperse GNRs of aspect ratio 20 could be synthesized (Khan et al., 2021; X. Huang et al., 2009). Although, to get GNRs of the needed aspect ratio with 1 ml/20 minutes rate, growth solution can be progressively added to the already prepared GNRs solution after 1^{st} stage (X. Huang et al., 2009; Nikoobakht & El-Sayed, 2003). There are many factors that control the aspect ratio, monodispersity, yield, and shape of GNRs in the seed-mediated growth method. These factors are seed concentration, seed size, seed structure, temperature, pH, ascorbic acid concentration, gold precursor concentration, surfactants, additives, surface active agent concentration, solvents, and also the ageing time of GNRs. Surprisingly, along with this, the CTAB source is also the deciding factor for GNR's morphology. The variation in the manufacturer or catalogue number of CTAB can affect the morphology of GNRs as well as existence of impurities in CTAB affects the yield and monodispersity of GNRs (X. Huang et al., 2009; J. Zhou et al., 2017; Rizwan Younis et al., 2021). It has been found that the small GNRs could be synthesized by altering the molar ratio of seed to Au^{3+} because as the concentration of seeds increases, the size of GNRs decreases. In addition to all these, $[HAuCl_4]$:$[AgNO_3]$ ratio is also one of the noteworthy parameters to control the aspect ratio of GNRs. The width of GNRs increases at a lower $[HAuCl_4]$:$[AgNO_3]$ ratio (Rizwan Younis et al., 2021). Moreover, the addition of additives like Hofmeister salts (i.e., NaSCN, $NaClO_4$, $NaNO_3$, NaBr, NaCl, and $NaHSO_4$) in the growth solution also controls the size of GNRs. In

one study, it was shown that the regulated preparation of GNRs was dependent on the interaction between salts and both Au and CTAB (Pallares et al., 2015; Rizwan Younis et al., 2021). By varying the concerned factors appropriately, GNRs of the desired size can be synthesized. Also, the GNRs are of two types: monocrystalline, which is synthesized using CTAB-coated seeds with silver ions, while the other one, i.e. pentatwinned, is synthesized employing citrate-coated seeds without Ag ions (Rizwan Younis et al., 2021; Vigderman et al., 2012).

Numerous mechanisms have been suggested for the preparation of GNRs using the seed-based method. According to some theories, CTAB functions as a template for rod formation. It was thought that CTAB preferably gets attached to (110) or (100) gold faces, and due to this, gold atoms are deposited on the (111) face, resulting in the formation of GNRs along the (100) face. Another mechanism proposes that after the ascorbic acid-based reduction of gold precursor in the growth solution, the $AuCl_2$-CTAB complex was formed by binding of gold dichloride ($AuCl_2$) with CTAB. This complex has the capability of binding at the tip of gold nanoparticles at a higher rate, resulting in the growth of rods (Khan et al., 2021; X. Huang et al., 2009). Further, it was proposed that under potential deposition (UPD) of silver ions also holds an essential part in the formation of rods (J. Zhou et al., 2017). After the incorporation of silver nitrate ($AgNO_3$) in the CTAB solution, there is the quick development of silver bromide (AgBr). These Ag^+ ions adsorb on gold nanoparticle surfaces and immediately reduce to silver atoms on the (110) face, which is the side surface of nanorods. This averts the deposition of gold atoms on side faces, so the gold atoms are deposited on (111) faces, leading to nanorods formation (X. Huang et al., 2009; J. Zhou et al., 2017; Rizwan Younis et al., 2021). Also, it is necessary to mention that slow UPD terminated the growth of GNRs (Fig. 1.3) (Rizwan Younis et al., 2021; J. Zhou et al., 2017). Silver is required to break the symmetry of the gold nanoparticles; contrarily, no anisotropic growth was observed in the absence of silver (Rizwan Younis et al., 2021). Overall, based on several studies, many mechanisms have been proposed for the seed-mediated synthesis of GNRs. But, it is intricate to comprehend the growth mechanism of GNRs due to the various ways involved in synthesizing GNRs by seed-mediated method (Rizwan Younis et al., 2021; J. Zhou et al., 2017).

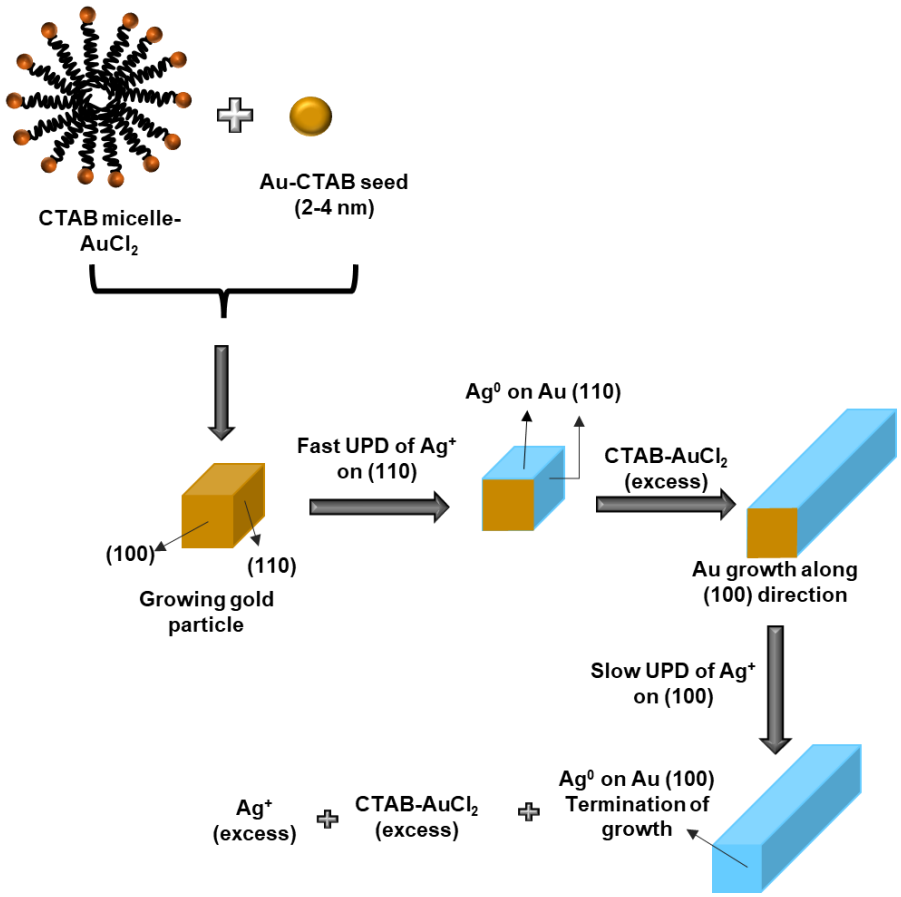

Figure 1.3 Mechanism of seed-mediated synthesis of GNRs (Adapted from Orendorff & Murphy, 2006)

1.3.2.3. Seedless method

The seedless method is the one-pot synthesis of GNRs. As the name suggests, it does not involve the seed formation step like the seed-mediated method. In this method, sodium borohydride ($NaBH_4$) is incorporated into the medium, which contains gold precursor, silver nitrite, CTAB, and ascorbic acid. Herein, the nucleation and the growth occur in the same system (Khan et al., 2021; Rizwan Younis et al., 2021; Vigderman et al., 2012; Varma et al., 2025; X. Huang et al., 2009). By varying the reaction temperature, the concentration of $NaBH_4$ (Khan et al., 2021; Rizwan Younis et al., 2021; Varma et al., 2025; X. Huang et al., 2009), pH, CTAB concentration and silver ions concentration, the size of GNRs could be modified (Varma et al., 2025; Rizwan Younis et al., 2021). In this method, CTAB forms an elongated micelle that acts as a template for synthesising GNRs. However, in this method, more spherical particles are formed compared to rods because it is tough to regulate the nucleation kinetics of the procedure (Rizwan Younis et al., 2021; Varma et al., 2025). Ali et al. found that by decreasing pH, the reduction potential of ascorbic acid and $NaBH_4$ was reduced, which leads

to the production of monodisperse small GNRs. Therefore, pH has an imperative part in synthesising GNRs by this method (Ali et al., 2012). However, the major drawback associated with this method is its low reproducibility (Vigderman et al., 2012), which commonly restricts its use. This method mainly prepares small GNRs (Rizwan Younis et al., 2021). Xu et al. controlled the growth kinetics of the synthesis by adding a specific amount of hydrochloric acid (HCl) and sodium hydroxide (NaOH) and prepared GNRs of aspect ratio 6-20. They had prepared small GNRs with tuneable longitudinal SPR in the NIR region (X. Xu et al., 2014). Researchers have also used this method with various modifications to synthesise uniform GNRs continuously (Vigderman et al., 2012).

1.3.2.4. Photochemical method

In the photochemical method, ultraviolet (UV) light is used for the photo reduction of gold to form GNRs (Alshangiti et al., 2023; Khan et al., 2021; Vigderman et al., 2012; Varma et al., 2025; Pérez-Juste et al., 2005; X. Huang et al., 2009). As per one approach, it was suggested that ion pairs are formed by the biding of auric acid with the elongated surfactant micelles, which are rod-shaped. Thereafter, electrons get transferred from metal ions to ligands upon UV excitation, which reduces metal ions to metal. However, the two-step aggregation process leads to rod formation. In the first step, the preliminary particles are formed due to the aggregation of metal nuclei. Further, due to particular surface stabilization by surfactant, the second aggregation occurs, which is a primary crystal aggregation, finally resulting in rod formation (Khan et al., 2021; Varma et al., 2025; X. Huang et al., 2009). In another approach, it was suggested that chemical and photochemical methods can be combined together to form GNRs. Here, first, Au^{+} is formed by the reduction of Au^{3+} due to ascorbic acid, which is subsequently reduced to Au by UV light (Alshangiti et al., 2023; Varma et al., 2025; Vigderman et al., 2012). The photochemical method also involves the use of silver ions and additives like hexane and acetone. Acetone generates ketyl radicals under UV irradiation, which is an active reducing agent (Vigderman et al., 2012; Varma et al., 2025). This method consists of numerous variations, which include variations of components such as silver ions, irradiation time, surfactants, UV light intensity, etc. The accurate control of these factors leads to the formation of GNRs of the desired size (Alshangiti et al., 2023; Varma et al., 2025). For example, UV light of 300 nm results in the formation of longer GNRs with narrow size distribution as compared to UV light of 254 nm (Khan et al., 2021; X. Huang et al., 2009). Silver ions help to improve the yield of GNRs with a similar growth mechanism to the seed-mediated growth method (Khan et al., 2021; Pérez-Juste et al., 2005; Vigderman et al., 2012, X. Huang et al., 2009).

Although this is a single-step process for GNR synthesis, which lessens the use of toxic chemicals but the scalability of this is difficult (Alshangiti et al., 2023).

In addition to the above-discussed methods for synthesizing GNRs, there are many other less popular methods due to their limitations. Although, these methods are capable of producing high-quality GNRs when subjected to certain modifications. These methods are proton beam irradiation, solvothermal reduction, bioreduction, microwave reduction, X-ray irradiation and ultrasonic method. Table 1.1 summarizes the merits and demerits of various methods of synthesis of GNRs (Table 1.1)

Table 1.1 Merits and demerits of several methods utilized to synthesize GNRs

Sr. No.	Synthesis Methods	Merits	Demerits
		Top-down approaches	
1.	Lithographic methods	Hazardous chemicals are not needed	Improper control over the dimensions Polycrystalline particles Tedious
2.	Catalytic method	Hazardous chemicals are not needed	Multiple shaped populations
3.	Template method	Excellent control over the aspect ratio of GNRs can be achieved Reproducible	Removal of the template is tedious and expensive Limited flexibility for varying the aspect ratio of GNRs
		Bottom-up approaches	
4.	Electrochemical method	Simple Minimize the use of harmful chemicals	Scalability is difficult Limited control over the aspect ratio of GNRs Generation of spherical particles
5.	Seed-mediated method	Excellent control over the aspect ratio of GNRs can be achieved Monodisperse nanorods	Involve the use of toxic chemicals like CTAB Multi-step method

		Scalable Simple Reproducible Ease of surface functionalization	
6.	Seedless method	One-step method The size of GNRs can be regulated	Challenging to control the nucleation kinetics of the method Mixed nanospheres and nanorods formation Low reproducibility Involve the use of toxic chemicals like CTAB
7.	Photochemical method	Single step process Lessen the use of harmful chemicals	Scalability is difficult Limited control over the aspect ratio of GNRs Generation of different shape particles

1.4. Functionalization of GNRs

CTAB is the most commonly used surfactant for synthesising GNRs; it imparts a positive surface charge to GNRs. However, due to the toxic nature of CTAB, it is necessary to replace or mask it from the biocompatible GNRs for numerous biomedical applications. The majority of CTAB is removed after synthesis by the washing step, although to ensure the biocompatibility of GNRs, it is necessary to functionalize them with different biocompatible molecules (J. Zhou et al., 2017; Varma et al., 2025). Currently, there are 3 major strategies for surface modification of GNRs with various biomolecules. The strategies are direct ligand exchange, surface coating and layer-by-layer self-assembly (Fig. 1.4) (X. Huang et al., 2009; J. Zhou et al., 2017; Varma et al., 2025; Vigderman et al., 2012).

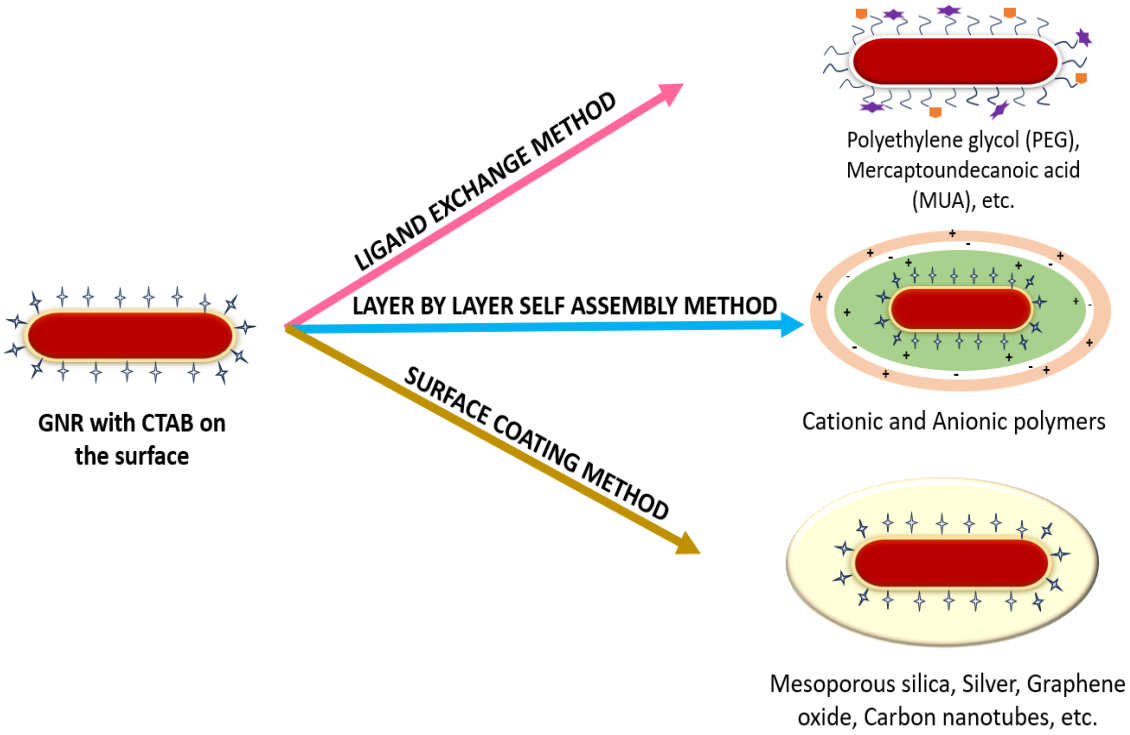

Figure 1.4 Functionalization strategies for GNRs (Image source: Varma et al., 2025)

1.4.1. Direct ligand exchange

This method is the most commonly used method for functionalizing GNRs with various biomolecules and also to covalently attach other biofunctional materials to them. This method involves the use of a mass-driven process to replace the CTAB on the surface of GNRs with various organic or biomolecules. The thiol group containing molecules are majorly used for this approach owing to the strong nature of the Au-S bond (Vigderman et al., 2012; J. Zhou et al., 2017; Varma et al., 2025; X. Huang et al., 2009). The metal-sulfur bond is stronger than the bond of different types of functional groups like amines ($-NH_2$), phosphors, alcohols and carboxylic (-COOH) groups with the metal (X. Huang et al., 2009; Varma et al., 2025). The thiolated molecules such as chitosan (C. H. Wang et al., 2011), DNA (Gaiduk et al., 2010) and polyethylene glycol (PEG) (L. Xie et al., 2023) form the organic layer around the GNRs by binding to its surface. These molecules not only enhance the biocompatibility and stability of GNRs but also help to reduce their cytotoxicity (J. Zhou et al., 2017; Varma et al., 2025). The complete ligand exchange is generally undertaken by employing heating and sonication to avoid the aggregation of GNRs (X. Huang et al., 2009; Varma et al., 2025).

In one study, thiolated chitosan functionalized GNRs were subsequently functionalized with disiloganglioside (GD2) monoclonal antibodies to use them for photothermal therapy (C.-W.

Chang et al., 2009). PEG-SH modification of GNRs is more advantageous than the modification with other molecules. Because the PEGylated GNRs are stable in media as well as other aqueous or organic solvents, it has long circulation time and great biocompatibility (Gui & Cui, 2012; J. Zhou et al., 2017; Varma et al., 2025; Khan et al., 2021). In one study, GNRs were modified with mPEG and imaging tags to employ them for simultaneous therapy and diagnosis of tumor cells (L. Xie et al., 2023). Similarly, wang et al. used PEGylated GNRs for multimodal imaging (MRI and fluorescence imaging) of breast cancer (C. Wang et al., 2009).

Besides, GNRs can also be secondarily functionalized with other molecules by employing thiolated ligands with supplementary functional groups like carboxyl, amine, hydroxyl, etc. (J. Zhou et al., 2017). Thus, this approach could easily attach ligands whose thiolation is challenging, such as proteins, folic acid, antibodies, aptamers, peptides, etc., to the surface of GNRs. The widely used biofunctional materials are 3-mercaptopropionic acid (MPA), cysteamine, 11-mercaptoundecanoic acids (MUA) (X. Huang et al., 2009) and thiolated PEG with -NH_2 or -COOH functional groups at one end (Boyer et al., 2010). In one study, PEGylated GNRs were covalently functionalized with anti-EGFR antibodies to bioimage oral squamous cell carcinoma (OSCC) cells (Gong et al., 2013). Similarly, PEG-GNRs were covalently functionalized with transferrin by Li et al. for two-photon microscopic imaging in Hela cells (J. L. Li & Gu, 2010).

11-MUA is a linker with the carboxylic group at one end and sulfur at another. Thus, it can easily bind to GNRs by forming Au-S bonds and through its carboxylic group, other non-thiolated biomolecules could be covalently functionalized on GNRs (Vigderman et al., 2012; Varma et al., 2025; Khan et al., 2021). Thus, in one study, Cao et al. replaced CTAB from the surface of GNRs with 11-MUA to further covalently functionalize them with human IgG antibodies for biosensing purposes (J. Cao et al., 2012). Inversely, Wang et al. used cystamine dihydrochloride to decorate GNRs with the -NH_2 group, to which the goat anti-*E. coli* and *S. typhimurium* antibodies were covalently bonded for detection of pathogens (C. Wang & Irudayaraj, 2008).

1.4.2. Layer-by-layer self-assembly method

Herein, there is electrostatic layer-by-layer consecutive adsorption of anionic and cation polyelectrolytes straightly on the CTAB-coated GNRs. As, CTAB imparts the positive charge to the GNRs, therefore the first layer of anionic polymers like polyacrylic acid (PAA) or

polystyrenesulfonate (PSS) is deposited on GNRs (X. Huang et al., 2009; Vigderman et al., 2012; J. Zhou et al., 2017; Varma et al., 2025). Thereafter, the negatively charged GNRs could be altered with cationic polyelectrolytes like poly(diallyldimethylammonium chloride) (PDDAC) or poly(allylamine hydrochloride) (PAH) (J. Zhou et al., 2017; Varma et al., 2025; Vigderman et al., 2012) or polyetherimide (PEI) (Varma et al., 2025; J. Zhou et al., 2017). This process could be repeated several times to improve the GNR's biocompatibility (Vigderman et al., 2012; J. Zhou et al., 2017). Besides, various biological polyelectrolytes like glycosaminoglycan or chitosan could also be employed for this approach (Vigderman et al., 2012).

Along with improving the stability and biocompatibility of GNRs, this approach paves the way to electrostatically or hydrophobically conjugate charged molecules, such as a gene, proteins, drugs, etc., on the GNRs (J. Zhou et al., 2017; Varma et al., 2025). Furthermore, this approach of functionalization of GNRs is easy, fast, and effective, but the long-term conjugation of the electrostatically functionalized molecules on GNRs is uncertain (X. Huang et al., 2009). However, by this method also, -COOH or -NH_2 groups can be outlined on GNRs, which could be used to covalently attach the biomolecules to GNR's surface (X. Huang et al., 2009; Vigderman et al., 2012; Varma et al., 2025). For example, the electrostatic adsorption of PSS decorates GNRs with the -COOH group, which can be used to covalently attach any biomolecules through their amine group via EDC/NHS coupling (X. Huang et al., 2009; Varma et al., 2025) for biomedical applications. Many studies employed PSS-modified GNRs for attaching cationic anti-cancer drug, doxorubicin, for cancer therapy (F. Yin et al., 2015; J. Zhou et al., 2017; Venkatesan et al., 2013). Further, GNRs modified with cationic polyelectrolytes like PEI (Shen et al., 2014) and PAH (F. Yin et al., 2015) were subsequently modified with anionic small interfering RNA (siRNA) for gene therapy.

1.4.3. Surface coating method

This method involves the use of inorganic materials to coat GNRs in their thin shell. This method also leads to the formation of biocompatible GNRs with the effective removal of CTAB. The most widely utilized inorganic material to surface coat GNRs is mesoporous silica, owing to its simpler synthesis process and biologically safe nature. The GNRs are coated with silica by using the common Stober method. Briefly, it involves the use of NaOH or ammonium hydroxide solution to adjust the pH of GNRs suspension to 10. Subsequently, by tetraethyl orthosilicate's (TEOS) hydrolysis and condensation, silica is deposited on GNRs under mild

stirring. However, the thickness of the silica shell can be tuned by varying the TEOS concentration and the reaction time (J. Zhou et al., 2017; Varma et al., 2025). The silica-modified GNRs were employed for an extensive range of biomedical purposes. Awad et al. utilized silica-covered GNRs for photoacoustic imaging in breast cancer cell line MD-MBA-231. They found that silica-modified PEG-GNRs showed better contrast than only PEG-modified GNRs (Awad et al., 2020). Moreover, coating GNRs with silane agents opens up the chance for more supplementary surface functionalization (J. Zhou et al., 2017). In one study, dendritic mesoporous silica was coated on GNRs (GNRs-MSNs) further, on which iron-based metal-organic framework (MOF) was formed, were used for therapy and trimodal imaging of breast cancer by attaching hyaluronic acid (HA) on their surface (H. Guo et al., 2021).

Apart from silica, many various types of inorganic materials, such as silver, carbon nanotubes, metal oxides, and graphene can also be used to surface coat GNRs (J. Zhou et al., 2017). Wang et al. used silica-modified GNRs which were further covalently functionalized with carbon nanotubes for *in vivo* photoacoustic imaging studies of gastric cancer (C. Wang et al., 2014). Silver-coated GNRs loaded with doxorubicin were explored for therapy of triple-negative breast cancer (Jenkins et al., 2017). Xu et al. tested graphene-modified GNRs loaded with doxorubicin for chemophotothermal therapy of hepatoma (C. Xu et al., 2013). Further, one study used iron oxide and GNRs nanocomposite formed by a seed-mediated method for sensing goat IgM antibodies (H. Zhang et al., 2012).

1.5. Accumulation, uptake, and clearance

GNRs or any other nanoparticles passively accumulate in the tumor area as a result of the enhanced permeability and retention (EPR) effect. This effect relies on the size of the nanoparticles. Malignant cells need large amounts of nutrients due to their uncontrolled growth and division. To fulfil this, the solid tumor develops new vasculature through which more blood can be supplied; this is known as angiogenesis. These angiogenic vasculatures have disordered arrangements of endothelial cells, resulting in gaps between them from which nanoparticles can passively accumulate at the tumor site (Dreaden et al., 2011; Gao & Chen, 2023; Yuan et al., 2021). Also, the characteristic impaired lymphatic recovery from tumor sites leads to the accumulation and retention of nanoparticles in the tumor interstitium. The EPR effect is also related to the heterogeneity of tumors, the location of the same tumor, the type of tumor as well as the size of nanoparticles (Dreaden et al., 2011; Gao & Chen, 2023). While studying the gold nanoparticle's size- and morphology-dependent intake in the cervical cancer cells (HeLa),

Chan and co-workers found that internalization was more at a 50 nm diameter of bare nanoparticles and that the uptake of colloidal GNRs was decreased with the increasing aspect ratio (Chithrani et al., 2006). However, for active accumulation of nanoparticles at the tumor site, they are functionalized with antibodies, peptides, nucleic acid and ligands, which enhance tumor targeting of nanoparticles (Gao & Chen, 2023; Yuan et al., 2021).

Nanoparticles are internalized via endocytic pathways. Particles below 200 nm are taken up by micropinocytosis, while the phagocytic pathway takes up the larger particles. Micropinocytosis occurs either by a caveolae-dependent, clathrin-dependent, or clathrin/caveolae-independent route. In the caveolae pathway, caveosomes carry the nanomaterials, which are further passed either to the endoplasmic reticulum/Golgi body or enter the endosomal pathway. While, in the clathrin-dependent pathway, the transfer of nanoparticles occurs via lysosomes, although some portions of nanoparticles are also transferred back into the extracellular space (Mohd-Zahid et al., 2019; Moudgil et al., 2023). The uptake via these pathways is size-dependent (Fig. 1.5). Further, the surface charge of nanoparticles also influences their cells' uptake. Cationic particles are easily taken up by cells owing to their electrostatic interaction with the negatively charged cell membrane (Dreaden et al., 2011; Mohd-Zahid et al., 2019). Neutral nanoparticles may network with the cell via hydrogen bonds or hydrophobic interactions, while negatively charged nanoparticles might interact with the positively charged membrane proteins, which results in a repulsive interaction with the anionic cell surface, subsequently heading to endocytosis. Additionally, the surface hydrophobicity of nanoparticles is also responsible for their uptake; hydrophobic nanoparticles can easily interact with cell membranes, while hydrophilic nanoparticles cannot (Mohd-Zahid et al., 2019). Xie et al. noticed that the accumulation of GNRs was more than the spherical nanoparticles in RAW264.7 cells, while the uptake of GNRs was through a clathrin-mediated pathway (X. Xie et al., 2017)

The pharmacokinetics of nanoparticles consist of their adsorption, distribution, metabolism and excretion. This is essential to find out the toxicity, therapeutic efficacy and dosage of nanoparticles. When nanoparticles enter the body, they can be cleared by the reticuloendothelial system (RES). It is a mononuclear phagocytic system that eliminates nanoparticles via phagocytic, metabolic and degradative processes by immune cells (Gao & Chen, 2023). To avoid the clearance of nanoparticles through RES, they are surface functionalized with polymers to neutralize their surface charge so that their circulation time can be increased and nonspecific RES uptake can also be circumvented, resulting in their enhanced efficacy (Dreaden et al., 2011; Gao & Chen, 2023). It has been found that PEG-modified GNRs had a

17 h circulatory half-life in nude mice. Also, hydrophobic molecules are readily taken up by RES, so these polymers also elevate the hydrophilicity of GNRs, which circumvents their removal by RES due to minimal protein absorption on their surface. Proteins or molecules like opsonin, when absorbed on the surface of the nanoparticle, initiate their phagocytic uptake (Dreaden et al., 2011). However, by functionalizing nanoparticles or increasing their hydrophilicity, there is a chance of less uptake of nanoparticles by the tumor cells or the target cells. So, it is challenging to achieve long circulation time along with improved cellular uptake by tumor cells. By maintaining these factors, enhanced therapeutic efficacy of nanoparticles can be achieved (S. Liao et al., 2021).

The clearance of nanomaterials from the body is vastly reliant on their size and surface properties. Typically, larger particles are cleared by RES, although smaller particles undergo renal clearance. Gold nanoparticles of hydrodynamic diameter below 6-8nm can be cleared by renal clearance because they can pass through glomerular capillary walls (Dreaden et al., 2011; Gao & Chen, 2023; Xu et al., 2023). Although the particles that cannot be filtered via the kidney or renal pathway are taken up by kuffer cells and metabolized by hepatocytes, they are subsequently excreted in bile. The fenestrations of the hepatic sinusoid, located between Kupffer cells and hepatocytes, have pores of 100–200 nm. This size allows particles smaller than this upper limit to pass through the fenestrations and gain access to the lymphatic circulation or the hepatocytes (Dreaden et al., 2011; Gao & Chen, 2023; Xu et al., 2023; Bose et al., 2014). But, the particles between 20-200 nm accumulate in the RES organs, where they undergo slow degradation and excretion. However, this accumulation can cause harmful effects on the body (Bose et al., 2014; Gao & Chen, 2023). All these accumulation, uptake and clearance of GNRs or any nanoparticles are dependent on the size, shape, surface properties and route of administration of nanoparticles. When applied to biomedical applications, these factors are crucial to determining the destiny of nanoparticle biological systems.

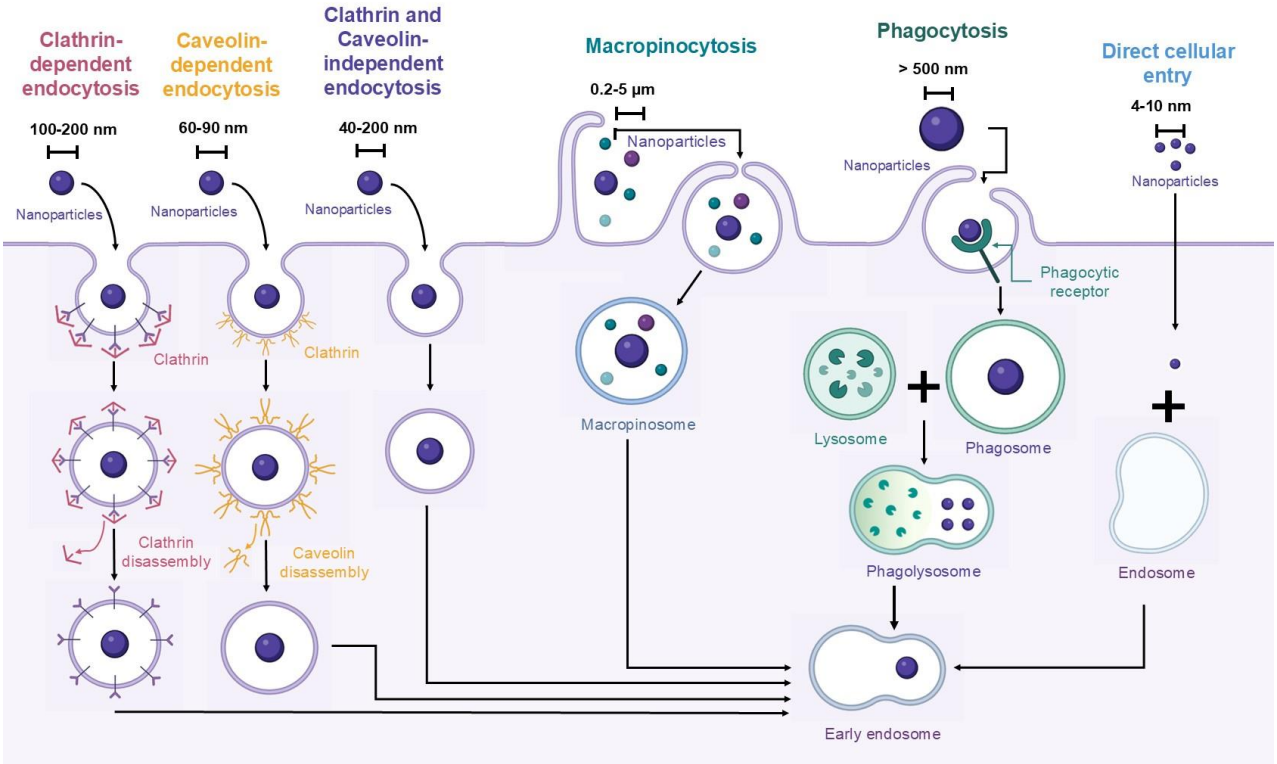

Figure 1.5 General uptake pathways of nanoparticles

1.6. Applications of GNRs

1.6.1. Biosensing

A biosensor is an analytical tool that helps to detect biological substances by combining the biological recognition element with the transducer (Chamorro-Garcia & Merkoçi, 2016; Rizwan et al., 2018; Salahvarzi et al., 2017). A biosensor is "a device that uses biochemical reactions mediated by isolated enzymes, organelles or whole cells to detect the effects of chemical compounds by electrical, thermal or optical signals", according to the International Union of Pure and Applied Chemistry (IUPAC). The first biosensor was invented by Clark and Lyons in 1962. It was an electrochemical biosensor designed to determine the glucose content in biological samples. Nowadays, biosensors have swapped various conventional analytical methods to detect biological agents. This is due to conventional techniques' tedious, complex and expensive operation. Also, biosensors are interdisciplinary devices involving the fields of physics, material sciences, electronics, chemistry, biology and optics (Rizwan et al., 2018). Thus, the biosensors are becoming more and more popular day by day.

1.6.1.1. Biosensor components

The two ultimate components of a biosensor are a transducer and a bioreceptor. A bioreceptor is generally a recognizing molecule, which can be DNA, RNA, enzymes, antibodies, aptamers, synthetic receptors, cell receptors, microorganisms, etc (Chamorro-Garcia & Merkoçi, 2016; Rizwan et al., 2018). The attachment of the biomolecules with the transducer is the initial step of any biosensor, which is termed as immobilization. The immobilization of biomolecules can be done by covalent bonding or cross-linking, which is the chemical approach, or it can also be achieved by encapsulation or adsorption, which is the physical approach (Rizwan et al., 2018).

The transducer is the other vital component of the biosensor. The function of the transducer is to measure the physical change (temperature, mass, light, etc) that takes place upon the interaction of the bioreceptor with the analyte of interest; this change was further transformed into a measurable electrical signal comparable with the analyte. The transducer transfers the signals to the detector for further amplification, analysis and conversion into readable units (Chamorro-Garcia & Merkoçi, 2016; Rizwan et al., 2018). According to the transducers or signal types, the biosensors are mainly optical, electrochemical, thermal, colorimetric and piezoelectric. For example, an optical biosensor detects changes in the electromagnetic wave when the analyte interacts with the bioreceptor. However, electrochemical biosensors sense the chemical change on the electrode upon the interaction of the analyte with the biomolecule and produce electrical signals. Further, the thermal biosensor detects temperature change and the piezoelectric detects mass change in the communication of the analyte with the biomolecules (Rizwan et al., 2018). The biosensor components are mentioned in Figure 1.6 (Fig. 1.6).

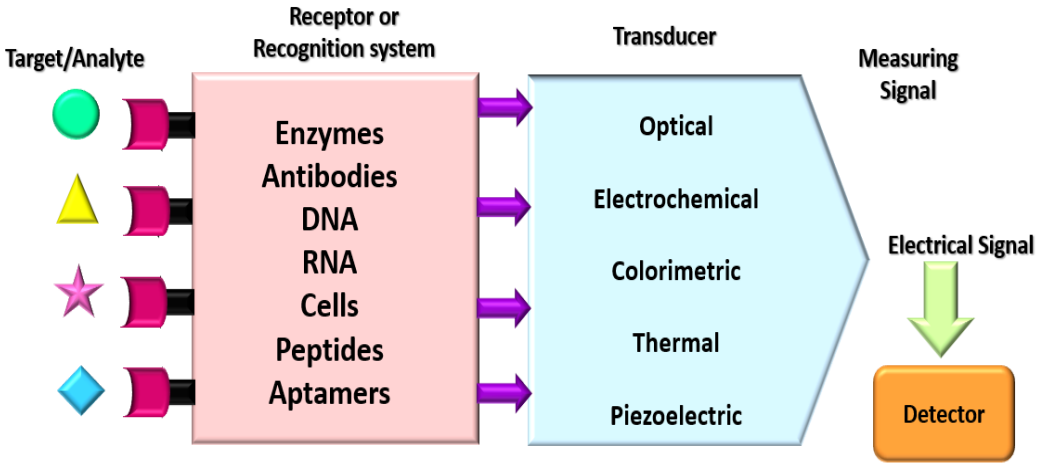

Figure 1.6 Components of a biosensor

1.6.1.2. Paper-based nanobiosensors

According to the World Health Organization (WHO), the term ASSURED should be applied to define the developing countries' diagnostics. Each letter of the term is explained as affordable, sensitive, specific, user-friendly, rapid and robust, equipment and deliverable to end-users (Parolo & Merkoçi, 2013; Sena-Torralba et al., 2022). Two additional criteria, R and E, which signify real-time connectivity and ease of specimen collection and environmental friendliness, respectively, were added then to the original ASSURED, forming the new abbreviation of REASSURED (Sena-Torralba et al., 2022). Interestingly, nanomaterials are playing a crucial part in improving the existing biosensors, and they are delivering more advantages in the development of novel biosensors. The incorporation of nanomaterials in biosensing systems significantly increased their sensitivity and stability and made the devices more cost-effective (Parolo & Merkoçi, 2013). Biosensors involving nanomaterials as one of the components are termed as nanobiosensors. Multiple types of nanomaterials-based biosensors are available depending upon the inherent properties of the particular nanomaterials used. The nanomaterials-based sensors can be electrochemical, colorimetric, thermal, magnetic, optical, etc.(P. Malik et al., 2013).

However, paper-based nano biosensors have gained more popularity due to their ergonomic attribute. It is a brilliant example of the ASSURED diagnostic device, which involves the intersection of nanotechnology and sensing. The merits of paper-based nanobiosensors are their user-friendly nature, cost-effectiveness, sensitivity and specificity, work on immunoreactions, rapid, not require high-end analytical techniques, stability, and results can be easily predicted by the end users. The pregnancy test kit is the best example of a paper-based point-of-care (PoC) biosensor. Paper-based nanobiosensors are easy to fabricate; they can be easily produced in limited resource areas without hampering their performance. It can be developed using inkjet, screen, or wax printing technologies. The first paper-based sensor was developed by Martin and Synge, which can be called as paper chromatography’s discovery. They were also the recipient of the Nobel Prize in chemistry in 1952. Further, one more breakthrough in paper-based nano biosensors was noticed after the introduction of the PoC biosensors and the pregnancy test kit, which is the first lateral flow assay (LFA) in the market. After this, there was a boon in the preparation of various PoC paper-based nanobiosensors to evaluate of various biomarkers, infectious diseases, diabetes, pathogens, etc. (Parolo & Merkoçi, 2013), resulting in the enhancement of the market of paper-based devices, mainly LFAs. Paper-based nanobiosensors have played a crucial role in tackling the COVID-19 pandemic.

1.6.1.3. Different types of paper-based nanobiosensors

Dipstick

The dipstick device is prepared by pre-storing the reagents on the paper. It is the most straightforward paper-based sensor, in which analysis is done just by blotting the sample on the dipstick. A versatile example of this is the pH strip. However, the major demerit of the dipstick is the unfeasibility of designing more advanced assays, which are often required for diagnostics applications (Parolo & Merkoçi, 2013).

µPADs

The µPADs are the combination of microfluidics with the paper. The advantages of µPADs include low sample requirement, which can easily flow through the channel without employing any external energy source; these are cost-effective and multiplexed, and quantitative estimation is highly possible with them. They are designed by generating hydrophilic channels in the hydrophobic paper. The methods generally used to develop µPAD are polydimethylsiloxane (PDMS) plotting, wax printing, photolithography, inkjet etching, cutting and plasma etching. Although, a long optimization time is needed to develop the device (Parolo & Merkoçi, 2013).

LFAs

The immense popularity of the LFAs is mainly due to their advantages like ergonomic nature, specificity, rapidity, sensitivity, portability, cost effectivity and no tedious sample preparation or quantification method is needed (Fig. 1.7) (Ghosh et al., 2023; S. B. Park & Shin, 2022; Sajid et al., 2015). The paper provides porous matrices, which help in instrument-less microfluidics and support a variety of biological interactions, which could help design numerous nanobiosensing strategies (Sena-Torralba et al., 2022). Lateral flow test strips enable the detection and quantification of specific substances within intricate mixtures. The process involves placing a sample on the device, with results typically generated in 10-20 minutes. (Posthuma-trumpie & Korf, 2009). The LFA bio-sensing platform has four key parts: sample pad, conjugate pad, test pad, and absorbent pad. (Parolo & Merkoçi, 2013). Like dipstick, all the reagents are pre-stored in the LFA. However, they also incorporate the merit of the sample flow, which is beneficial for enhancing the sensitivity of the LFA as the sample flows through the multiple zones, which have their particular function (Parolo et al., 2020; Parolo & Merkoçi, 2013). Further, various components of the LFAs are discussed.

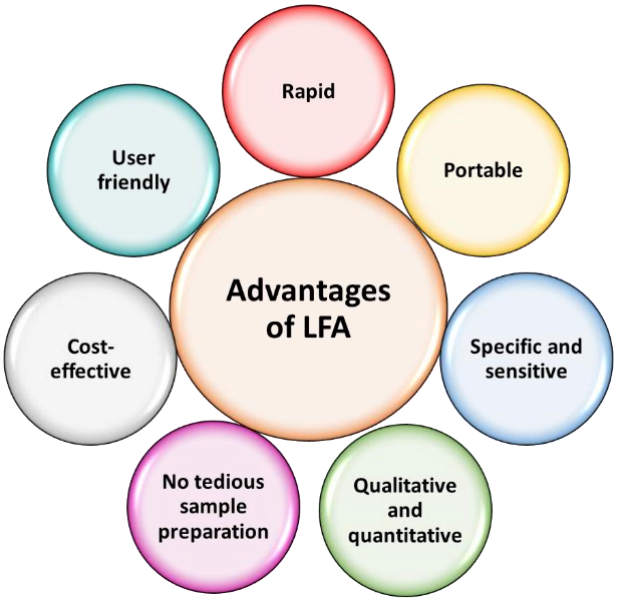

Figure 1.7 Advantages of LFAs

1.6.1.4. Components of the LFAs

1.6.1.4.1. Pads of LFAs

1. The sample pad is generally composed of cellulose. It purifies the sample by removing the dirt and stores the assay buffer in dry form to guarantee ideal assay conditions during the analysis. Also, the role of the pad is to guarantee the even movement of the sample.
2. The next LFA pad is the conjugation pad. It is generally made up of glass fibres. Its principal function is to store the bioreactor conjugated labels, which are mainly nanomaterials in the dried form as well as to release them upon wetting. This pad is the area where the initial interaction between the analyte of interest and the bioreceptor occurs. The conjugate pad should contain features like low non-specific binding to circumvent the retention of label or analyte, good mechanical strength, and constant flow and bed volume.
3. The third pad is the detection pad, which is generally made up of nitrocellulose. In this pad, the signal is developed in the area where capture reagents are fixed. This pad contains the control as well as the test line. The characteristics of this pad are to enable the homogenous flow, circumvent nonspecific binding and to capture the bioreceptors with solid functionalization without degrading them
4. The last pad is the adsorbent pad, whose role is to adsorb the extra fluid. Therefore, due to this pad, the volume of the sample can be increased, which subsequently leads to the enhancement of the sensitivity of the LFA. In the absence of this pad, the liquid evaporates consistently along the strip as the flow halts on reaching the end of the membrane. Thus,

due to the labels' failure to migrate till the end of the test pad leads to their accumulation on the test pad and a subsequent intensification in background noise. However, its presence allows labels to reach till the end of the strip, thus enhancing the performance of the LFA. Notably, adsorbent pads can be handled and fabricated using standard procedures without any special steps (Parolo et al., 2020; Parolo & Merkoçi, 2013; Sajid et al., 2015). Figure 1.8 shows the different pad and their assembly (Fig. 1.8).

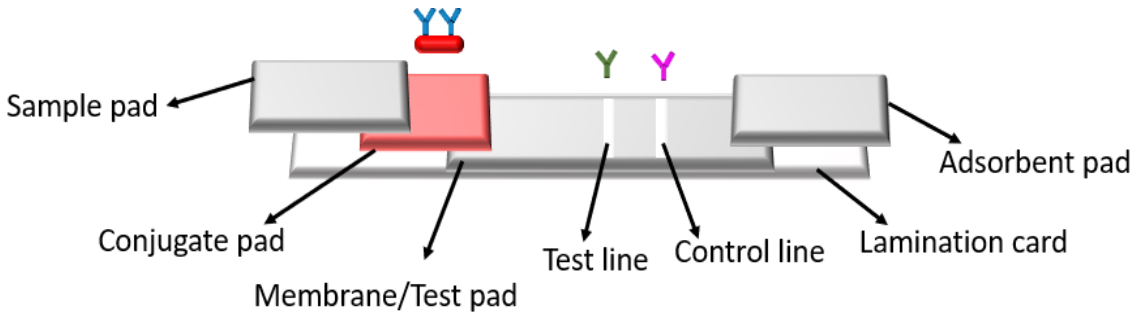

Figure 1.8 Assembly and components of the LFA

1.6.1.4.2. Formats of LFAs

Sandwich format

It is the most common format of LFA for molecules of >1 kDa. In this format, labels, which can be nanoparticles or enzymes or dyes, are conjugated with the aptamer or the antibody against the target is coated on a conjugate pad. Further, the other aptamer or primary antibody for the analyte is coated on the test line area of the detection pad. However, the control lines comprise the secondary antibody or probe specific to the aptamer or antibody conjugated on the label (Ghosh et al., 2023; Sajid et al., 2015). The antibodies can be monoclonal or polyclonal, depending on the target of interest (Parolo et al., 2020). Upon introducing the sample into the LFA, it migrates through the conjugate pad, facilitating the binding of the analyte to the labelled antibody designed to capture it. This results in the generation of analyte-antibody-label conjugate. This complex further migrates to the detection pad through the capillary force. Thus, on the detection pad, the analyte-antibody-label complex is captured by the antibody immobilized on the test line, forming a sandwich of the analyte between the detection and the capture antibody. This forms the complex of detection antibody on the label-analyte-capture antibody. This results in the appearance of color at the test line, whose intensity proportionally increases with the amount of analyte in the sample. Further, the excess label-antibody conjugate will combine with the secondary antibody on the control line. Therefore,

the development of colour at the control line confirms the appropriate functioning of the LFA. The adsorbent pad adsorbs the excess buffer and sample (Parolo et al., 2020; Sajid et al., 2015; Ghosh et al., 2023). This format can be used for both qualitative and quantitative detection. Also, there is no direct competition of the detection antibody with the analyte so the potent interfering substances would not hamper the assay performance. This format is simpler to develop and interpret and highly sensitive (Dey et al., 2023). Figure 1.9 displays a schematic of the general sandwich format of LFA (Fig. 1.9).

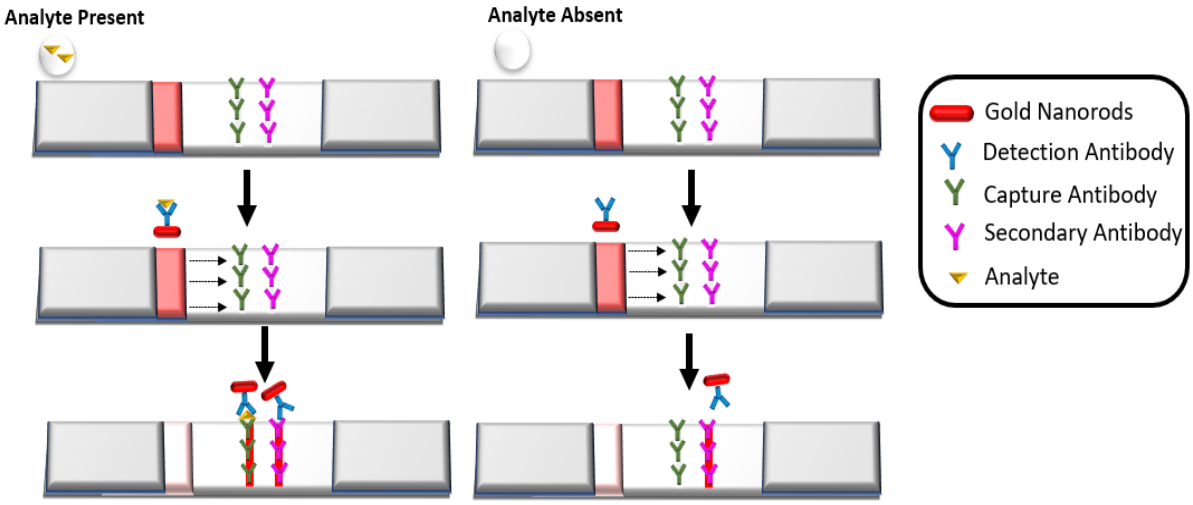

Figure 1.9 Schematic representation of the sandwich format of LFA

Competitive format

This format of LFA is preferential for the low molecular weight targets, which is inefficient in binding with the two antibodies simultaneously. Competitive formats show no test line color when the analyte is present, but color develops at both lines when it's absent. There are two layouts of competitive format. The first layout consists of labelled biomolecules on the conjugate pad. At the test line, the same antigen/analyte that is to be detected is immobilized, while the test line consists of a secondary antibody, which is specific for the primary detection antibody present on the label. Thus, when the sample containing the desired analyte is introduced in the LFA, it moves through the capillary action to bind with the labelled biomolecule on the conjugate pad. So, the binding site of the labelled biomolecule will be occupied with the analyte, so it will not bind with the analyte/antigen on the test line, resulting in no appearance of the color there. However, when the target is absent in the sample or it is present in a very low concentration, the binding site of the labelled biomolecule will be

available to combine with the analyte fixed at the test line, leading to color development there. Therefore, there will be competition among the desired analyte and the antigen fixed on the test line to bind with the labelled biomolecule (Fig. 1.10). Further, the primary antibody is coated on the test line in another layout while the labelled analyte is dispensed on the conjugate pad. So, when the sample containing the target is added to the device, the target in the sample and the labelled analyte will compete to combine with the primary antibody (Parolo et al., 2020; Sajid et al., 2015; Ghosh et al., 2023). A competitive format is more suitable for qualitative and semi-qualitative analysis. Also, it is more difficult to interpret and develop compared to the sandwich format (Dey et al., 2023).

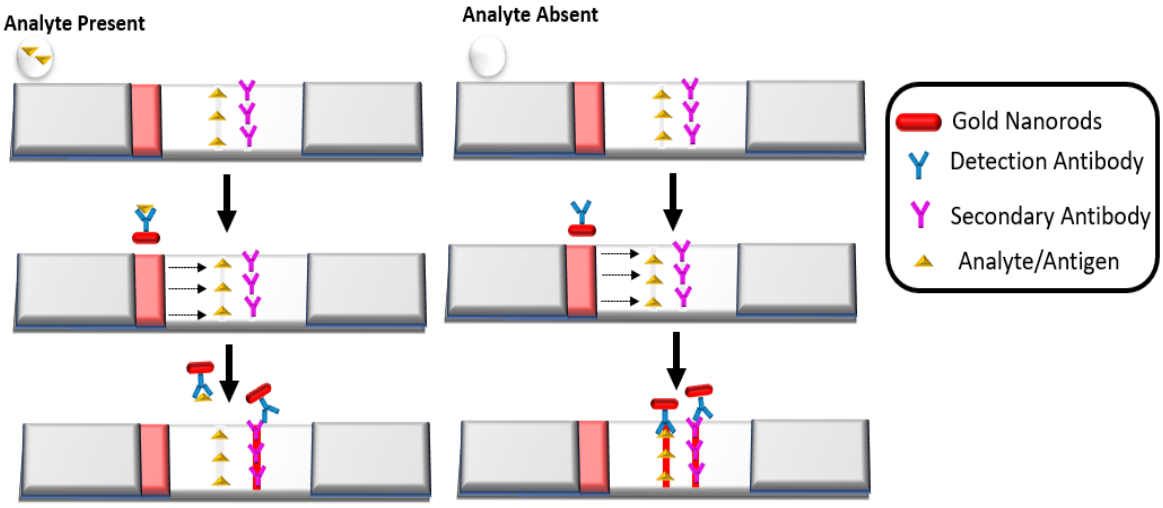

Figure 1.10 Schematic representation of the competitive format of LFA

Multiplex detection format

Multiplex format helps to determine more than one target simultaneously. Thus, in this format, the number of test lines is equivalent to the number of targets needed to be determined. This format is beneficial when the interrelated targets, which conclude the clinical condition in combination, must be measured simultaneously. Multiplex LFA can be designed in various ways depending on the number of targets to be detected. Strips with test lines in a T-shape or star shape can be prepared. LFAs can be miniaturized, for example, the microarray-based multiplex estimation of DNA sequences, which enhances the sensitivity and decreases the use of reagents as well as reduces the sample volume needed for the assay (Ghosh et al., 2023; Sajid et al., 2015).

1.6.1.4.3. Bioreceptors for LFAs

There are many types of bioreceptors which can be employed for LFA such as antibodies, nucleic acid, aptamers, etc. Table 1.2 summarizes the commonly used bioreactors along with their merits and demerits (Table 1.2).

Antibodies

Antibodies are commonly used as a bioreceptors for LFA. Antibodies are immobilized on the test and the control lines, as well as they are conjugated on the labels. Thus, the immunochemical interactions of the antibodies and the analyte occur. The LFA involving antibodies is called lateral flow immunochromatographic assay (LFIA) (Ghosh et al., 2023; Sajid et al., 2015). The antibody that particularly binds with a certain specific antigen is termed a primary antibody. In contrast, an antibody that binds with another antibody or other antibody is an antigen, termed a secondary antibody. In LFA, the test line contains the primary antibody, while the secondary antibody is fixed on the control line (Bahadır & Sezgintürk, 2016; Ghosh et al., 2023; Sajid et al., 2015). The process of generating antibodies involves immunizing an animal with the target of interest. The antibodies produced are subsequently subcloned and purified, depending on the specific purpose of use. However, producing antibodies against toxic analytes is problematic because animals may not sustain their toxicity (Sajid et al., 2015). Both monoclonal and polyclonal antibodies can be used in LFAs (Parolo et al., 2020).

Aptamers

Aptamers are synthetic nucleic acids discovered in 1990. These are generated by the *in vitro* SELEX process. Aptamers can selectively bind with a variety of target molecules due to their high association constant. Organic molecules with molecular weight from 100-10000 Da are suitable targets for the aptamers. Aptamers can efficiently differentiate between the closely associated targets owing to their unique affinity towards them. The merits of aptamers are their simple production process, supreme stability, easy labelling process, simpler structure alteration, reproducibility, amplification after selection, and application flexibility (Ghosh et al., 2023; Sajid et al., 2015). However, its performance is exceptionally reliant on the composition and the buffer's ionic attribute (Parolo et al., 2020).

Molecular beacons

Molecular beacons are DNA hairpin structures which comprise of fluorophore and quencher at their opposite ends, respectively. Thus, the quencher restricts the fluorophore from producing fluorescence in the absence of the analyte; however, in the presence of complementary DNA, which is the target, the hairpin structure opens up forcefully, resulting in the generation of fluorescence signals. The targets for molecular beacons can be toxins, nucleic acid sequences, proteins, etc. These are very specific and selective biorecognition molecules. Molecular beacons are characterized by a loop region of 15-30 base pairs that is complementary to the target and a stem region of 4-6 base pairs. DNA probes can also be used in LFAs to determine DNA sequences associated with various genetic illnesses. Although, DNA hybridized complexes are intricate compared to antigen-antibody complexes (Ghosh et al., 2023; Sajid et al., 2015). Thus, antibodies are preferred over DNA as a bioreceptor for LFA (Ghosh et al., 2023).

Table 1.2 Merits and demerits of commonly used bioreceptors for LFAs

Sr. No.	Bioreceptors	Merits	Demerits	References
1.	Monoclonal antibodies	Low batch-to-batch variations Highly specific	Costly Lengthy production process	(Parolo et al., 2020; Sequeira-Antunes & Ferreira, 2023; Tetyana et al., 2021)
2.	Polyclonal antibodies	Easy production Cost-effective Contains multiple binding sites	Batch-to-batch variations Less specific Cross-reactive	
3.	Aptamers	Cost-effective Stable Great batch reproducibility Can recognize a wide range of target molecules	Performance depends upon the ionic strength of the buffer as well as the other molecules present in the buffer	
4.	Fragments	Cheaper and easy to reproduce	Less stable than the whole antibody mainly	

		Very less variations batch-to-batch Avoid non-specific binding Able to enhance the number of bioreactors per probe	due to the absence of the F_c region in them
5.	Nucleic acid	Good specificity Bind with a wide range of targets Cost-effective Easy production	Chances of non-specific binding Unstable Complex designing
6.	Enzymes	High specificity Rapid response Catalytic activity Mild operating conditions	Immobilization issues Costly Stability issues Chances of non-specific binding

1.6.1.4.4. Labels for LFAs

Many types of nanomaterials can be employed as labels for LFA, such as gold nanoparticles, liposomes, carbon-based nanomaterials, quantum dots, magnetic nanoparticles, etc. Table 1.3 summarizes the commonly used labels in LFAs, along with their merits and demerits (Table 1.3).

Gold nanoparticles (AuNPs)

Colloidal AuNPs are the widely employed detector labels for the LFAs. Their strong red color, owing to their SPR, is a significant reason for using them as labels for LFAs. Due to the colour, naked-eye detection can be easily achieved by employing them in LFAs. They are also stable, easy to functionalize, have low toxicity and are simple to prepare via numerous methods (Ghosh et al., 2023; Parolo et al., 2020; Sajid et al., 2015). Further, the optical traits of AuNPs rely on their shape and size. The color of colloidal gold nanoparticles changes with their size.

The size of AuNPs could be tuned by altering the concentration of chemical reagents. Thus, these properties reduce the analysis time and help in reliable on-site analysis (Bahadır & Sezgintürk, 2016; Ghosh et al., 2023; Sajid et al., 2015).

Carbon-based nanomaterials

The carbon nanotubes or nanoparticles have emerged as an efficient alternative to the AuNPs. However, they do not have an SPR property, but their intense black color makes them a potent label for LFAs. Carbon nanomaterials are cost-effective, can be easily conjugated with biomolecules, and are less likely to aggregate (Bahadır & Sezgintürk, 2016; Ghosh et al., 2023; Sajid et al., 2015; Parolo et al., 2020). Also, they have good electrical and optical features (Bahadır & Sezgintürk, 2016). However, the nonspecific adsorption of biomolecules on the surface of carbon nanomaterials and their irregular structure are the major issues associated with them (Sajid et al., 2015).

Dye-loaded latex beads

Dye-loaded latex beads are another cheaper substitute to the AuNPs. These can be obtained in multiple colors and are resistant to physical and chemical damage. Although, due to their less sensitivity compared to AuNPs, they are preferred for qualitative assessment (Parolo et al., 2020).

Quantum dots (QDs)

QDs are semiconductor nanomaterials with great physiochemical properties (Sajid et al., 2015). QDs are the labels which are capable of photoluminescence on excitation under UV light. Their optical feature could be tuned by varying the elemental composition and size. QDs are resistant to photobleaching compared to organic dyes, can be easily functionalized with bioreceptors and are stable (Bahadır & Sezgintürk, 2016; Parolo et al., 2020; Sajid et al., 2015). Also, the QDs are resistant to metabolic degradation and maintain their fluorescent properties in cells or organisms (Sajid et al., 2015). However, the QDs are toxic, require a UV lamp for excitation and are more expensive than the AuNPs (Parolo et al., 2020).

Upconverting nanoparticles (UCNPs)

UCNPs also received good attention as the label for LFAs. They have excitation in the NIR region. Thus, the auto-florescence can be circumvented. Further, their emission occurs in the visible area. UCNPs are more precise labels compared to QDs (Parolo et al., 2020; Sajid et al.,

2015). UCNPs can be synthesized easily and do not photo-degrade the bioreceptors, due to their excitation in the infrared region (Sajid et al., 2015). Although, UCNPs require bulky and expensive NIR lasers, that is intricate for the PoC estimation, therefore limiting their use as labels in LFAs (Parolo et al., 2020). Further, they show batch-to-batch variations in the preparation of the reporters, which could affect the performance of the LFA(Sajid et al., 2015)

Liposomes

Liposomes are the spherical vesicles which comprise of one or two phospholipid bilayers. They carry both hydrophobic and hydrophilic features. Their properties vary with the size, surface charge, lipid composition and the synthesis method. Liposomes are widely used for drug delivery approaches (Bahadır & Sezgintürk, 2016). Thus, it can also be used as a label by loading the fluorescent dyes in them. Also, it is easy to functionalize them with the bioreceptors (Parolo et al., 2020). However, it comes with the disadvantage of less structural stability, which is affected by factors like pH, detergents, osmotic pressure, etc (Bahadır & Sezgintürk, 2016). Also, their synthesis techniques are intricate (Parolo et al., 2020), which limits their use in LFAs.

Magnetic nanoparticles (MNPs)

These are multipurpose labels for the LFAs because they can generate magnetic and optical signals. They have intense color, which can be measured with optical readers (Parolo et al., 2020; Sajid et al., 2015). Apart from this, the MNPs are stable, sensitive, and biocompatible, and they can be easily functionalized with biomolecules(Bahadır & Sezgintürk, 2016; Ghosh et al., 2023; Sajid et al., 2015). They can also be easily used for quantitative detection using the MAR (magnetic assay reader). There are two types of MNPs: paramagnetic and superparamagnetic. The paramagnetic particles have disadvantages like increased detection time, affecting the liquid flow in LFAs and interfering with the immune reaction of antigens and antibodies. However, superparamagnetic MNPs do not comprise these drawbacks. But, both paramagnetic and superparamagnetic MNPs carry the disadvantage of excessive magnetic enrichment (Ghosh et al., 2023).

Table 1.3 Merits and demerits of commonly used labels in LFAs

Sr. No.	Labels	Merits	Demerits	References
1.	Gold nanoparticles (AuNPs)	Easy functionalization Intense color Stable Ease of synthesis and scalability Sensitive	Requires analytical technique for quantitative assay	(Bahadır & Sezgintürk, 2016; Ghosh et al., 2023; Parolo et al., 2020; Sajid et al., 2015)
2.	Carbon-based nanomaterials	Inexpensive than gold nanoparticles Ease of synthesis and scalability Intense black color Easy functionalization Stable	Irregularity in the shape of particles Non-specific binding of biomolecules Requires analytical technique for quantitative assay Weaker signal than AuNPs	
3.	Latex beads	Inexpensive than gold nanoparticles Multiple colors are available Resistant to physiochemical damage	Less sensitive Requires analytical technique for quantitative assay Weaker signal than AuNPs	
4.	Liposomes	Easy conjugation Multiple labels can be loaded	Sensitive to pH, detergents and ionic strength Requires analytical technique for quantitative assay	

5.	Quantum dots	Strong fluorescent signal Multiple colors are available Stable	Requires analytical technique for quantitative assay Higher toxicity Photobleaching reduces sensitivity
6.	UCNPs	Excitation in IR range Multiple colors are available Strong fluorescent signal Sensitive than QDs Low matrix interference	Low batch-to-batch reproducibility Expensive than QDs Requires analytical technique for quantitative assay
7.	MNPs	Lower background interference High signal-to-noise ratio Magnetic and colorimetric signal Highly sensitive	Optical signal is weak Require reader for magnetic measurements Constrict liquid flow Prolong detection time Excessive magnetic enrichment

1.6.1.4.5. Detection of LFAs

Qualitative detection

The qualitative analysis is done by visual detection of the presence or absence of the color at the test line. This is a very quick generation of the results in YES or NO, which is a major reason for the LFAs' popularity. Qualitative detection is very rapid and helps clinicians to diagnose the condition quickly (Fig. 1.11) (Parolo et al., 2020; Sajid et al., 2015).

Semi-quantitative detection

This is also visual detection, but it is based on the barcode-style LFAs. The intensity as well as quantity of test lines provide a basis for semi-quantitative analysis. This type of detection is helpful when the concentration of two or more types of analytes needs to be evaluated. Thus,

by assessing the test line's color intensity, the end user can conclude which analyte is in higher and which is in lower concentrations. Further, this detection is also used to estimate the threshold of the target i.e. the test line will appear only if the analyte is above the threshold level in the sample. Also, it can be used to group analyte concentrations into various categories depending on the concentration ranges (Fig. 1.11) (Parolo et al., 2020).

Quantitative detection

Recently, many methods have been developed to enable quantitative assessment through LFAs. This mainly involves the use of smartphone cameras or devoted readers (Parolo et al., 2020; Sajid et al., 2015). LFAs generally require optical detectors or readers; however, this can also be integrated with electrochemical detectors. The optical strip readers measure the color intensity of the test and control lines, but it must be highly sensitive to the various intensities of the colors (Fig. 1.11) (Sajid et al., 2015). However, to accurately achieve the quantification through LFAs, the strips should be highly reproducible to avoid batch-to-batch variation in the analysis, and the calibration curve should be plotted meticulously. Also, to avoid the interference of the light with the quantification of the analyte, the quantification should always be done using the same light conditions(Parolo et al., 2020; Sajid et al., 2015). Similarly, the conditions should be maintained while using smartphones, coupled with the image processing software (Fig. 1.11) (Parolo et al., 2020; Sajid et al., 2015). Moreover, multiplexed evaluation can also be achieved through multiplex LFAs by using dedicated readers (Parolo et al., 2020).

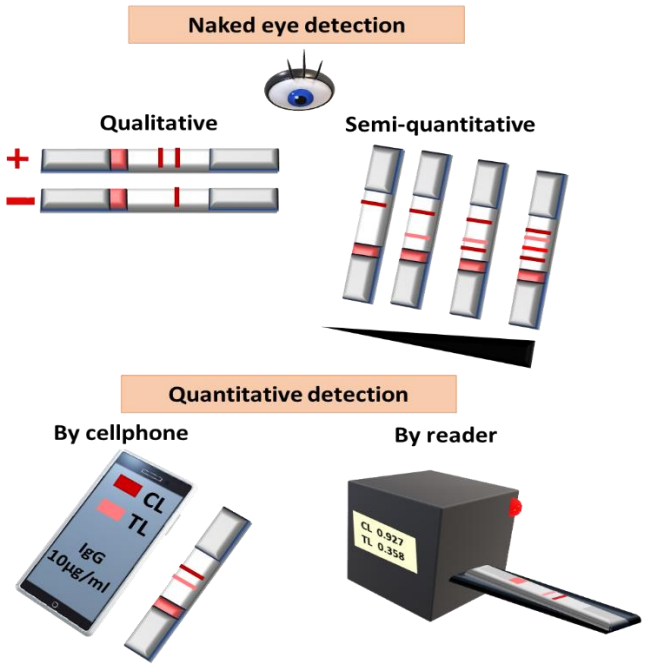

Figure 1.11 Readouts for LFAs (Adapted from Parolo et al., 2020)

1.6.1.5. LFA for sensing of TSH

The thyroid gland is a butterfly-shaped gland (Maurya H., 2018) that lies below the Adam's apple, along the front of the neck (Singh, 2020). It has two side lobes connected by a bridge (isthmus) in the middle (Singh, 2020). The thyroid gland secretes three hormones i.e. Triiodothyronine (T3), Tetraiodothyronine (thyroxine or T4) and Calcitonin. These hormones are responsible for regulating the metabolic rate in the body (Nilsson & Fagman, 2017). They regulate the heart rate, body temperature, menstrual cycle, growth, central nervous system (CNS), peripheral nervous system (PNS), cholesterol level, calcium level, etc (Nilsson & Fagman, 2017; Walls & Mihai, 2017).

Thyroid-stimulating hormone (TSH) or thyrotropic hormone or thyrotropin, which is released by the anterior pituitary gland and, in turn, controlled by thyrotropin-releasing hormone (TRH), which is generated by the hypothalamus, controls the thyroid's hormonal production. TSH helps in the production of thyroxine (T4), which is further converted to triiodothyronine (T3) by stimulating the thyroid gland. These T3 and T4 regulate the release of TSH by negative feedback inhibition. It is a glycoprotein hormone produced by thyrotroph cells in the anterior pituitary gland, which regulates the endocrine function of the thyroid (Fig. 1.12) (Rossi et al., 2024). It consists of two subunits, namely the alpha and the beta subunit (approximately 28 kDa)(Choi et al., 2017; Wani et al., 2016). The α-subunit is common in TSH, human chorionic gonadotropin (hCG) hormone, luteinizing hormone (LH) and follicle-stimulating hormone (FSH). However, the specific biological activity of each hormone is provided by the β-subunit of these hormones (Wani et al., 2016).

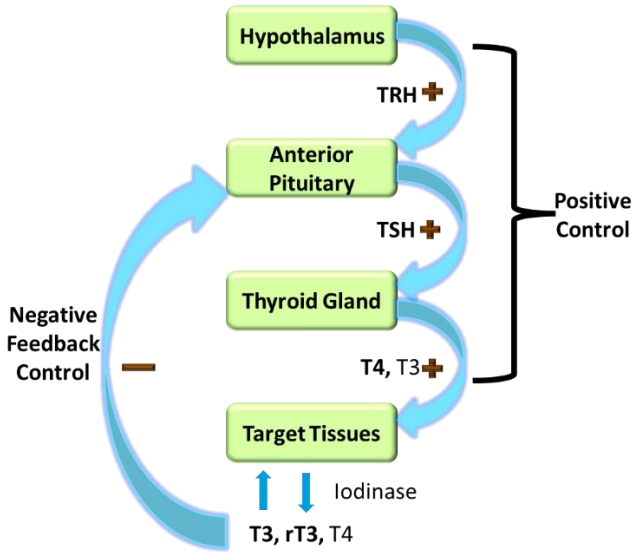

Figure 1.12 Regulation of thyroid hormones

In 2002, the United States National Health and Nutrition Examination Survey (NHANES III) investigated that 0.5% of the general population had overt hyperthyroidism, and 0.7% had subclinical hyperthyroidism, with a complete frequency of 1.3%. The general frequency of hypothyroidism in the NHANES III study was 4.6% (Taylor et al., 2018). The clinical survey indicates that over one-third of Indians have thyroid problems, meaning that over 32% of Indians have had thyroid abnormalities in one form or another (Maurya H., 2018). The inland Indian cities like Bangalore, Ahmedabad, Hyderabad, Kolkata and Delhi reported a notably greater incidence of hypothyroidism and hyperthyroidism than the coastal ones such as Chennai, Mumbai and Goa, according to a survey study conducted in eight Indian cities (Unnikrishnan et al., 2013).

Hyperthyroidism and hypothyroidism are thyroid conditions due to excessive and less production of thyroid hormones, respectively (Choi et al., 2017). TSH levels in blood/serum are one of the prime indicators of hyperthyroidism and hypothyroidism, as well as any thyroid diseases. In normal adults, it ranges from 0.5 μIU/ml to 5 μIU/ml. Thus, the TSH levels above 5 μIU/ml indicate subclinical hypothyroidism or hypothyroidism, while below 0.5 μIU/ml specify hyperthyroidism (Bikkarolla et al., 2022; Choi et al., 2017). The increasing global prevalence of thyroid diseases might take the TSH estimation to 2.56 billion USD by 2028 (Zheng et al., 2024). Conventional blood tests or immunoassays for detecting TSH are not rapid, lack sensitivity, are not user-friendly, require sample preparation, require laboratory techniques and are not simple to operate. Therefore, these drawbacks generated the need for the PoC testing method for the estimation of TSH (Bikkarolla et al., 2022; H. Wang et al., 2014; Jeong et al., 2013). Majorly, PoC electrochemical biosensors were developed to assess TSH. However, these sensors have certain drawbacks, like passivation and instability, and they are easily influenced by environmental elements (Rossi et al., 2024). Therefore, the paper-based sensors are an efficient alternative to the PoC electrochemical sensors. Although these are majorly qualitative but quantitative estimation is highly possible by employing dedicated readers. Notably, the commercially available TSH testing LFAs are qualitative, which can only determine hypothyroidism since the TSH levels drop below 0.5 μIU/ml in hyperthyroidism, which is a very low concentration to detect (Choi et al., 2017). Thus, there is a crucial need to design more sensitive and ergonomic paper-based sensors for simultaneously evaluating both hypothyroidism and hyperthyroidism, depending on TSH levels. This paper-based biosensor can also be easily tamed to assess other biological markers. Table 1.4 summarizes studies that use paper-based sensing methods to estimate TSH using gold nanoparticles (Table 1.4).

Table 1.4 LFA for TSH detection using gold nanoparticles

Sr. No.	Nanoparticle	Readout System Used	LOD	Reference
1	Spherical AuNPs	Cell phone camera	0.31 µIU/ml	(You et al., 2013)
2	Spherical AuNPs	- SERS	1.5 µIU/ml 0.025 µIU/ml	(Choi et al., 2017)
3.	Gold nanoshells	-	0.16 µIU/mL	(Bikkarolla et al., 2022)

In view of the substantial superiority of GNRs over the other gold nanoparticles, we did a proof-of-concept study to prove GNRs as a proficient label for LFAs. The study also intended to develop an ergonomic LFA that could potentially evaluate hypothyroidism and hyperthyroidism without appointing any quantification techniques. To the best of our knowledge, GNRs (rod-shaped) have not been implemented as labels for LFA to detect TSH. However, numerous other types of biosensors have engaged GNRs for TSH determination.

1.6.2. Bioimaging

A comparatively newer application of digital technology in the medical area is bioimaging. It is a non-invasive method of scrutinizing biological activity over a certain time period. Aside from physically deducing, it aids in revealing the 3D configuration of specimens and does not impede any of the many life activities, like respiration, movement, etc. It facilitates the visualization of subcellular features as well as every single tissue in higher-order organisms (N. Malik et al., 2019). It is used for disease diagnosis and therapy. Some examples of bioimaging are fluorescence imaging, magnetic resonance imaging (MRI), positron emission tomography (PET) imaging, etc (Erathodiyil & Ying, 2011).

Medical imaging techniques like MRI, ultrasound (US) imaging, positron emission tomography and single-photon emission computed tomography (PET and SPECT), optical imaging (OI) and computed tomography (CT) help to determine structural and biological features in living organisms (Morato et al., 2021; Varma et al., 2025; H. Wang et al., 2024; Y. Huang et al., 2012). Although, these imaging modalities have inadequacies which can be surpassed by combining two or more imaging modalities together. This combining of imaging is termed as multimodal imaging (Morato et al., 2021; Rieffel et al., 2015; H. Wang et al., 2024; Varma et al., 2025; Y. Huang et al., 2012). Multimodal imaging is immensely valuable for

detailed diagnosis of disease from the molecular to the cellular level, and this will subsequently lead to an accurate line of treatment (therapy or surgery) for a complete cure of clinical conditions (Morato et al., 2021; Rieffel et al., 2015; Varma et al., 2025).

The clinically used traditional contrast agents or imaging probes are prone to limitation of poor spatial resolution. Further, these agents are quickly mobilized due to their small structure, and they have the potency to cause toxicity, resulting in damage to the kidneys. Additionally, these agents cannot be incorporated into multimodal imaging techniques. Figure 1.13 summarizes the drawbacks of conventional imaging contrast agents (Fig. 1.13). However, all these drawbacks of conventional imaging agents can be overcome by employing nanomaterials as multimodal imaging agents (H. Wang et al., 2024). The features such as low toxicity, high sensitivity, exceptional physiochemical properties, small size and long circulation time make nanomaterials a potent multimodal bioimaging agent (Mu et al., 2017; Varma et al., 2025; H. Wang et al., 2024).

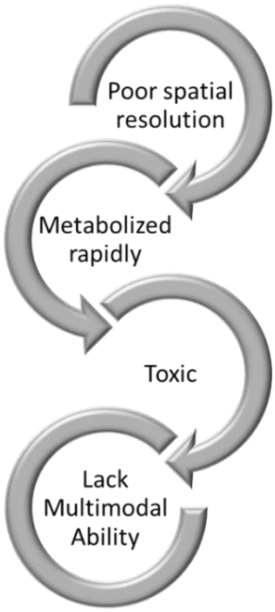

Figure 1.13 Drawbacks of conventional imaging contrast agents

The use of nanomaterials for detecting clinical illnesses by employing the multimodal bioimaging strategy is a fascinating area of study. However, GNRs are very potent nanoparticles in multimodal bioimaging due to their extraordinary properties. The typical property of GNRs, which aids in imaging applications, is their LSPR property longitudinal (Kesharwani et al., 2023; J. Zhou et al., 2017; Varma et al., 2025; Rizwan Younis et al., 2021; Kim et al., 2023). The longitudinal SPR band of GNRs can appear from visible to NIR region

depending upon the size and aspect ratio of GNRs. Thus, the excitation in the NIR region is beneficial for imaging applications with GNRs because most human tissues and water show minimal NIR light absorption (Kim et al., 2023; Thu et al., 2017; Varma et al., 2025). Moreover, GNRs are endowed with multiple unique properties, which makes them perfect imaging contrast agents to diagnose various clinical issues. Briefly, these properties are its biocompatibility, chemical inertness, ease of surface functionalization, great capacity to attenuate X-ray and photothermal effect, large extinction coefficient, enhanced light scattering, etc. (Rizwan Younis et al., 2021; J. Zhou et al., 2017; Varma et al., 2025). Figure 1.14 summarizes the advantages of GNRs as imaging contrast agents (Fig. 1.14).

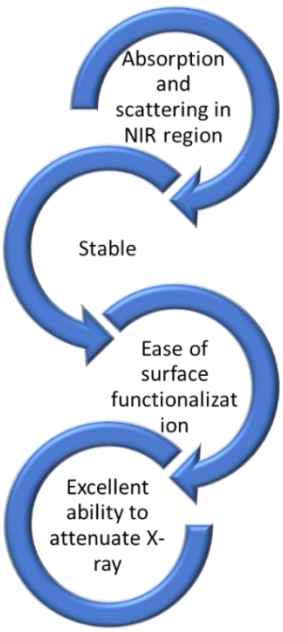

Figure 1.14 Advantages of GNRs as an imaging contrast agent

1.6.2.1. Different types of imaging methods and contrast agents used in them

Molecular imaging has been considered an effective tool for diagnosing and monitoring various diseases and disorders (D. Chen et al., 2016; X. Li et al., 2020; Varma et al., 2025). Molecular imaging techniques help to keep track of the biological processes at tissues, cells as well as at subcellular levels, leading to successful treatment of the diseases (Calatayud et al., 2023; M. Liu et al., 2020; D. Shahbazi-Gahrouei et al., 2019a; Varma et al., 2025). MRI, PET, CT and PAI are the most prevailing imaging modalities that can distinguish between the affected and the surrounding normal tissues (X. Li et al., 2020) and also aid in assessing the structural and functional details of the body (Rieffel et al., 2015). Integration of contrast agents with these imaging modalities augments their sensitivity and specificity to

identify clinical issues (Key & Leary, 2014; X. Li et al., 2020; Varma et al., 2025). In a further section, different types of commonly used imaging methods for detecting clinical issues and how contrast agents are helpful in these techniques are highlighted in detail. Figure 1.15 summarizes the contrast agents used in various imaging techniques (Fig. 1.15).

1.6.2.1.1. MRI

The properties like high spatial and temporal resolution and deep tissue penetration make MRI a popular and widely used imaging technique (X. Li et al., 2020; Y. Liu et al., 2022; D. Shahbazi-Gahrouei et al., 2019a; Z. Zhang et al., 2019; Varma et al., 2025; Y. Huang et al., 2012). It involves the use of non-ionizing radiations, and it is non-invasive (Y. Liu et al., 2022; Morato et al., 2021; D. Shahbazi-Gahrouei et al., 2019a; Z. Zhang et al., 2019; Varma et al., 2025; L. Li et al., 2023). Thus, it aids in acquiring both structural and functional features in living beings (Y. Huang et al., 2012; Morato et al., 2021; D. Shahbazi-Gahrouei et al., 2019a; Z. Zhang et al., 2019; Varma et al., 2025). However, the key problem linked with MRI is its low sensitivity. Yet, this can be subjugated by applying MRI contrast agents (D. Shahbazi-Gahrouei et al., 2019a; Z. Zhang et al., 2019; Varma et al., 2025). This low sensitivity is due to the limit over the magnetic field's power to achieve the spatial resolution of 1mm. The US FDA had permitted a magnetic field of 3-Tesla strength (Key & Leary, 2014). This technique is mainly used to distinguishingly diagnose tumors from normal cells (Z. Zhang et al., 2019).

The basic principle of MRI is that under the influence of electromagnetic fields, the protons orient themselves in the direction of the magnetic field. Thus, when the specific resonance frequency is applied, it causes excitation of the nuclei, which return to their initial state by transferring energy and generating signals. These signals are converted into images (Calatayud et al., 2023; Key & Leary, 2014; D. Shahbazi-Gahrouei et al., 2019a). The relaxation of protons on turning off the radio frequencies is of two types: longitudinal relaxation time (T1) and transverse relaxation time (T2) (Y. Huang et al., 2012; Key & Leary, 2014; Zeng et al., 2022).

Therefore, the contrast agents used in MRI are of two types: Positive contrast agents (T1), which decrease the longitudinal relaxation time and negative contrast agents (T2), which reduce the transverse relaxation time (Z. Zhang et al., 2019; Varma et al., 2025; Morato et al., 2021). The commonly used T1 contrast agents are Gadolinium (Gd^{3+}) chelates, for example, Gd-tetraazacyclododecanetetraacetic acid (Gd-DOTA), Gd-diethylenetriamine pentaacetic acid (Gd-DTPA), etc. Although, these contrast agents are required in high dosages because of their nonspecific distribution and mediocre longitudinal relaxation rate (Y. Huang et al., 2012;

X. Li et al., 2020). Another contrast agent is superparamagnetic iron oxide (SPIO) nanoparticles. It is a T2 contrast agent and is also FDA-approved. Another iron oxide-based contrast agent is ultrasmall-sized iron oxide nanoparticles (ESIONs) which are less than 4 nm in size but is a good T1 contrast agent (Y. Huang et al., 2012; Zeng et al., 2022; Varma et al., 2025; D. Shahbazi-Gahrouei et al., 2019b) Many nanoparticles such as $MnFeO_4$, $CoFe_2O_4$ and $NiFe_2O_4$ are competent T2 contrast agents. Also, Gd-based nanoparticle contrast agents like $GdPO_4$, GdF_3, and Gd_2O_3 can augment the signal of T1-weighted MRI. Notably, these MRI contrast agents are in the initial stage of studies, which needs proper pharmacokinetics and biocompatibility studies for their use in humans (Y. Huang et al., 2012; Zeng et al., 2022; Varma et al., 2025). Considering this, there is a need for more effectivity and novel nanomaterials-based T1 and T2 contrast agents to enhance MRI efficiency. Moreover, there are no intrinsic magnetic characteristics in GNRs. Therefore, they cannot function directly as an MRI contrast agent. However, functionalizing the traditional MRI contrast agents with the GNRs can improve their contrast potential (Varma et al., 2025).

1.6.2.1.2. CT imaging

CT imaging engages the use of X-rays. It can generate both two-dimensional **(**2D) (Key & Leary, 2014; D. Shahbazi-Gahrouei et al., 2019a; Z. Zhang et al., 2019; Varma et al., 2025) and 3D (Key & Leary, 2014; X. Li et al., 2020; Z. Zhang et al., 2019; Varma et al., 2025) cross-sectional images of several organs. Thus, it is an effective technique for diagnosing and keeping track of cancer (D. Shahbazi-Gahrouei et al., 2019a; Varma et al., 2025). CT imaging carries the advantage of deeper penetration and high spatial resolution, also, it is non-invasive. The technique also provides information about the structural and functional facts of humans (Y. Huang et al., 2012; Z. Y. Ma et al., 2013; D. Shahbazi-Gahrouei et al., 2019b; Varma et al., 2025). Although, the key curb of this method is the inability to distinguish between the target and neighbouring tissues because of its low signal-to-noise ratio. Nevertheless, the limitation can be overcome by employing contrast agents (Key & Leary, 2014; D. Shahbazi-Gahrouei et al., 2019a; Varma et al., 2025).

CT imaging works on the difference in attenuation of photons by the materials. Mass energy-absorption coefficients and X-ray energy mass-attenuation coefficients are the two major factors in studying the attenuation, energy absorption and penetration instigated by the material. Mass attenuation coefficients measure the X-ray opacity of the substance. In contrast, the ionization caused by the incident X-ray in the material is measured by the mass energy-

absorption coefficient. These two coefficients evaluate the performance of contrast agents (Key & Leary, 2014). Further, the image is generated based on the density of X-rays absorbed in different tissues (Y. Huang et al., 2012).

The clinically accepted contrast agents for CT imaging are iodinated small aromatic compounds and barium sulfate (X. Li et al., 2020; Varma et al., 2025). Moreover, bismuth and gadolinium can also be applied in CT imaging (Z. Zhang et al., 2019; Varma et al., 2025). However, some limitations are associated with these molecules, such as their toxic nature, rapid metabolism, vague distribution and less circulation time. Thus, these limitations can be subjugated by applying nanomaterials as a CT contrast agent (Y. Huang et al., 2012; Key & Leary, 2014; L. Li et al., 2023; X. Li et al., 2020; Z. Zhang et al., 2019; Varma et al., 2025). Metallic nanoparticles, chiefly gold, are potent CT contrast agents because of their photoelectric, energy conversion, and catalytic properties. Furthermore, gold's X-ray absorption coefficient is higher than iodine's (L. Li et al., 2023; Varma et al., 2025). Gold's higher atomic number (79) and greater mass density (19.32 g/cm^3) compared to iodine explain this (Z. Y. Ma et al., 2013; Varma et al., 2025). When Von Maltzahn et al. employed PEG-GNRs as a CT contrast agent, they reported that GNRs showed two-fold more X-ray attenuation than iodine and a circulation time of 17 hr (Von Maltzahn et al., 2009). Till now, many such studies have proven that gold nanoparticles are more competent contrast agents for CT imaging.

1.6.2.1.3. PET and SPECT imaging

PET and SPECT are nuclear magnetic imaging modalities that have the potential to generate *in vivo* 3D images of the body. These modalities function on the estimation of radionuclides capable of emitting positrons or one or two gamma rays. These imaging modalities are also efficient in providing both structural and functional details of the body owing to their sensitivity, specificity, and more profound penetration power (Key & Leary, 2014; Varma et al., 2025; X. Li et al., 2020). These techniques are usually utilized to detect and monitor malignancies (Z. Zhang et al., 2019; Varma et al., 2025). PET uses isotopes such as ^{68}Ga, ^{11}C, ^{13}N, ^{76}Br, ^{124}I, ^{15}O, ^{18}F, ^{89}Zr and ^{64}Cu. Meanwhile, SPECT uses gamma-emitting heavy radioisotopes such as ^{111}In, ^{99m}Tc (Calatayud et al., 2023; Y. Huang et al., 2012; Key & Leary, 2014; Varma et al., 2025), and ^{123}I (Calatayud et al., 2023; Key & Leary, 2014; Varma et al., 2025). These radioisotopes are labelled on biomolecules also used as tracers, for example, ^{11}C-raclopride, 2-[^{18}F] fluoro-2-deoxy-D-glucose (^{18}F-FDG), ^{111}In-monoclonal endoglin, ^{64}Cu-DOPA (Dopamine), ^{99m}Tc-sestamibi, etc and are used as tracers for PET and SPECT imaging

(Y. Huang et al., 2012; Varma et al., 2025). In PET, the positrons emitted by the radioisotopes from the nucleus collide with the electrons. This generates two gamma rays, and the positron and electron are annihilated. The detector generates a PET image by detecting the gamma rays. Similarly, in SPECT, one or two gamma rays are emitted (Calatayud et al., 2023; Key & Leary, 2014). However, SPECT is less sensitive than PET (Calatayud et al., 2023; Y. Huang et al., 2012; Key & Leary, 2014). PET is the robust nuclear magnetic imaging modality (Calatayud et al., 2023). ^{18}F-FDG is the widely utilized small-molecular radiotracer for PET imaging, which helps in assessing high glucose-utilizing cells (cancer cells) (Calatayud et al., 2023; X. Li et al., 2020; D. Shahbazi-Gahrouei et al., 2019b; Z. Zhang et al., 2019; Varma et al., 2025). The key inadequacy of these imaging techniques is that the analyst gets less time to acquire the images because of the short half-life of radioisotopes. Also, these are radiative modalities (Key & Leary, 2014). However, the ability to readily incorporate radiolabeled isotopes into GNRs makes them valuable tools for PET imaging, enhancing the quality of the resulting images (Varma et al., 2025).

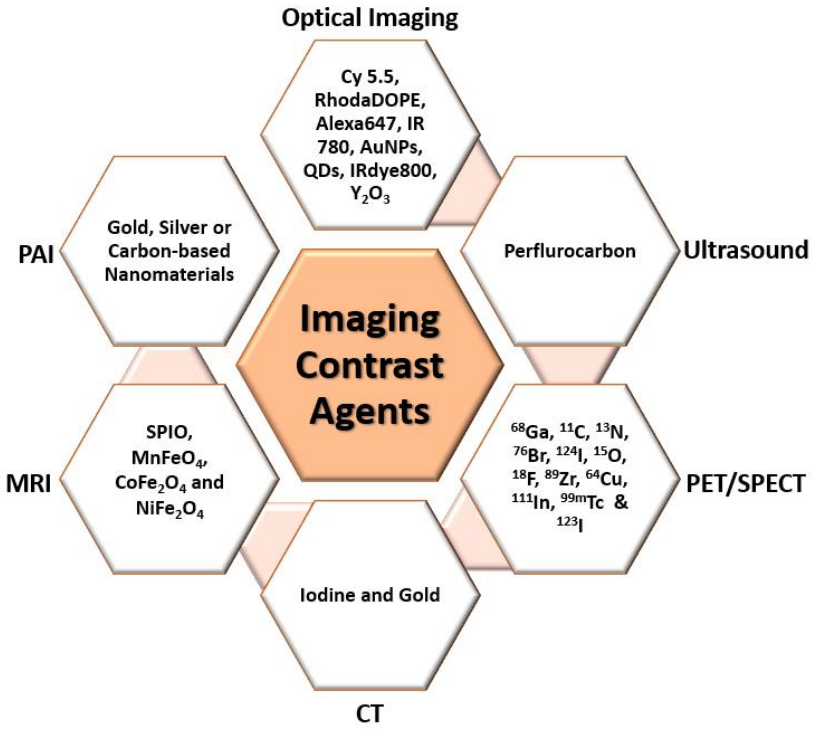

Figure 1.15 Different types of imaging contrast agents

1.6.2.1.4. Photoacoustic imaging (PAI)

The photoacoustic effect is the driving factor for photoacoustic imaging (Z. Y. Ma et al., 2013; Varma et al., 2025; X. Li et al., 2020). Briefly, this technique involves a specific power density

non-ionizing pulsed laser beam; upon exposure to this beam, the tissues produce heat, initializing thermoelastic expansion of biomolecules, which further leads to the generation of ultrasonic waves. These ultrasonic waves are used for image generation (L. Li et al., 2023; Z. Y. Ma et al., 2013; Zeng et al., 2022; Varma et al., 2025; X. Li et al., 2020). PAI uses both acoustic and optical effects, due to which this imaging method can effectively assess tissues from depth with high contrast as well as good spatial resolution (C. Wang et al., 2019; Zeng et al., 2022; Varma et al., 2025; X. Li et al., 2020) PAI can generate a 3D ultrasonic image (Varma et al., 2025; C. Wang et al., 2019). Incorporating contrast agents improves this imaging technique's performance (X. Li et al., 2020). Moreover, due to the optical, thermal and acoustic properties, nanomaterials are counted as an efficient photoacoustic contrast agent (Varma et al., 2025; L. Li et al., 2023). Gold, silver or carbon-based nanomaterials can be used for PAI. Among gold nanoparticles, GNRs are the promising contrast agents for PAI. GNRs show an excellent PA effect (X. Li et al., 2020; Zeng et al., 2022; Varma et al., 2025; Z. Y. Ma et al., 2013). Nanomaterials' PA effect helps diagnose and monitor malignancies efficaciously (L. Li et al., 2023; Varma et al., 2025). This imaging technique can also be used for organ and organelles imaging, so it is unsurprising to note that it establishes a clinical niche in mapping sentinel lymph nodes, breast cancer imaging, and brain imaging. This is a very versatile technique. Owing to this, its integration with the endoscopic systems by its miniaturization has been studied (Rieffel et al., 2015). This is one of the emerging imaging modalities for cancer diagnosis and imaging-based cancer therapy.

1.6.2.1.5. Optical imaging (OI)

Optical imaging involves the use of nonionizing radiation like infrared light, ultraviolet or visible light to assess biological processes (Y. Huang et al., 2012; D. Shahbazi-Gahrouei et al., 2019a; Varma et al., 2025). It is a non-invasive, cheaper and sensitive imaging modality (Calatayud et al., 2023; Y. Huang et al., 2012; Key & Leary, 2014; Varma et al., 2025). However, optical imaging is a broad term; in the true sense, it includes numerous imaging modalities (Calatayud et al., 2023; Varma et al., 2025). Basically, optical imaging functions upon the excitation of electrons under the influence of electromagnetic radiation. This excitation and responses are further translated into images (D. Shahbazi-Gahrouei et al., 2019a; Varma et al., 2025). This is a brilliant tool for real-time imaging studies (Key & Leary, 2014; X. Li et al., 2020; Varma et al., 2025). Besides, optical imaging is constrained to pre-clinical examination only. Although, incorporating efficacious imaging agents could help in its clinical translation (Calatayud et al., 2023).

Optical imaging includes techniques like fluorescence imaging, which involves the use of fluorophores (organic or quantum dots) as a contrast agent. This is a very cheap and highly sensitive technique that helps to monitor cancer. Although, these fluorophores have the limitation of photobleaching, which can be knocked out by using GNRs for imaging. The unique optical properties of GNRs, like enhanced absorption and scattering, tunable SPR, biocompatibility, photostability, etc, make them ideal for fluorescence imaging (Z. Y. Ma et al., 2013). Nanomaterials show an EPR effect so that tumor targeting can be achieved. Some nanomaterials show the NIR region fluorescence spectrum, which helps in better contrast and more profound tissue imaging (Y. Huang et al., 2012; L. Li et al., 2023).

Another optical modality where GNRs act as a great imaging agent is two-photon luminescence imaging; as already discussed earlier, GNRs have TPL properties. It is a potent technique for *in vivo* and *in vitro* cancer imaging. TPL imaging provides 3D spatial resolution and it also diminishes the background autofluorescence by tissues. Studies have shown that the TPL signal of GNRs is far better than that of conventional TPL probes. GNRs are also a good probe for dark-field scattering imaging owing to their light-scattering properties in the NIR region. GNRs functionalized with ligands were widely explored for dark-field cancer imaging. GNRs can be imaged in their actual color with great contrast in dark field imaging (Z. Y. Ma et al., 2013).

Optical imaging also includes optical coherence tomography (OCT), which uses short coherence light sources to deliver 3D images of the subject. OCT uses an optical scattering medium for cross-sectional imaging. The OCT image is formed based on various absorption-scattering profiles of the medium. As NIR penetrates maximum in tissues, thus, OCT imaging provides a high spatial resolution of the tissues. It is also employed in cancer diagnosis and imaging. GNRs are also a great probe for OCT imaging of tumors due to their exceptional optical properties (Z. Y. Ma et al., 2013).

Further, GNRs are also employed in SERS imaging due to their SERS signal enhancement property. SERS imaging is a very sensitive and specific imaging technique. The use of nanoparticles as a SERS probe along with reporter molecules augments the quality of SERS imaging. This imaging can also be used for monitoring, treating and imaging cancer (C. Wang et al., 2019). To conclude, optical imaging modalities have enormous ability for clinical image-guided therapy and diagnosis of malignancies. This ability can be further enhanced by incorporating nanomaterials instead of conventional imaging probes for optical imaging.

Table 1.5 highlights the merits and demerits of different imaging modalities (Table 1.5). These limitations can be knocked off by designing multimodal imaging probes, which can be simultaneously used for various imaging modalities. This results in more accurate diagnosis and treatment of diseases by escaping the chances of false positive or false negative estimations.

Table 1.5 Merits and demerits associated with different imaging modalities

Sr. No.	Imaging Modalities	Merits	Demerits	References
1.	MRI	• No contact with damaging radiation • High spatial resolution • Non-invasive • High penetration depth	• Extended processing time • Costly • Less sensitive	(Y. Huang et al., 2012; J. Liao et al., 2014; Varma et al., 2025; Das et al., 2019; X. Li et al., 2020)
2.	CT imaging	• High spatial resolution • Great penetration depth • Non-invasive	• Less sensitivity • Involves ionizing radiation • Non-quantitative • Restricted imaging in soft tissue • Limitation in biocompatible contrast agent	
3.	PET imaging	• Whole-body scanning possible • Good penetration depth • Heightened sensitivity	• Expensive • Radiation risk • Small imaging time	

4.	Ultrasound (US) imaging	• Real-time imaging • Cheaper • Clinician friendly	• Operator-dependent examination • Low resolution • Limitation in imaging of bones and lungs
5.	Optical imaging	• Non-invasive • Sensitive • High temporal resolution • Cost-effective	• Non-quantifiable • Low penetration depth
6.	SERS imaging	• Sensitive • Rapid signal procurement • Multiplex imaging	• Interference by fluorescence • Laser-induced photodamage of tissues
7.	Photoacoustic imaging (PAI)	• 3D image reconstruction • Highly sensitive • Rapid • High spatial resolution	• Low tissue penetration • Can cause phototoxicity in the adjacent tissues
8.	Fluorescence (FL) imaging	• Non-invasive • Sensitive • Multifarious imaging	• Poor tissue diffusion depth • Excessive photobleaching • Cause phototoxicity • Low spatial resolution

1.6.2.2. Multimodal imaging

Accurate diagnosis of any disease plays a crucial role in meticulous treatment. Although there are many single imaging modalities for the diagnosis but this often has less sensitivity and gives only particular information at a time (Varma et al., 2025; X. Li et al., 2020). Interestingly, there is no single, self-reliant imaging modality which gives comprehensive information on the anatomical and functional processes in the body (Khan et al., 2021; Z. Y. Ma et al., 2013; Varma et al., 2025; Burke et al., 2017). Each of these modalities has certain limitations. Although, uniting the complementary imaging method would help to overcome the limitations, resulting in the accurate assessment and subsequent treatment of the medical condition (Y. Huang et al., 2012; X. Li et al., 2020; Z. Y. Ma et al., 2013; Varma et al., 2025). This compounding of two or more imaging methods is stated as multimodal imaging (D. Chen et al., 2016; Rieffel et al., 2015; R. Thomas et al., 2013; Varma et al., 2025; Y. Huang et al., 2012).

The multimodality can be achieved by two approaches: one by uniting the scanners or imaging machine, while the second approach involves the preparation of multimodal imaging contrast agents (Burke et al., 2017; Rieffel et al., 2015; Varma et al., 2025). Multimodal imaging is the more precise way to monitor and treat medical conditions, especially cancer (R. Thomas et al., 2013; Varma et al., 2025; Khan et al., 2021) as well as to strategize surgeries (Rieffel et al., 2015; Varma et al., 2025). By employing a multimodal imaging approach, it is possible to determine cellular and molecular details by bypassing invasive methods to do so (Shahbazi-Gahrouei et al., 2019b; Varma et al., 2025). Multimodal imaging also contributes to drug development by helping to study the pharmacokinetics and ADME (absorption, distribution, metabolism and excretion) profile of the innovative formulations (Burke et al., 2017; Varma et al., 2025). Nanoparticles are potent multimodal imaging agents subjected to their large surface area, small size and ease of surface functionalization (Khan et al., 2021; Rieffel et al., 2015; Burke et al., 2017). Moreover, nanoprobes can be distributed in large payloads in a single dose, which consequently helps to attain profound specificity towards the target (D. Shahbazi-Gahrouei et al., 2019b; Varma et al., 2025). The development of multimodal imaging methods could result in a change from a technology-driven approach to a more disease-oriented approach that is beneficial for the clinical and preclinical fields.

The clinically executed PET-CT scanner is the most apt example of the multimodal imaging system. The systems combine the advantages of both CT and PET imaging, enhancing sensitivity to detect anatomical and physiological features in the organism (Rieffel et al., 2015;

Varma et al., 2025). Similarly, PET-MRI was also unified for clinical use to enhance the sensitivity and resolution of the imaging (Rieffel et al., 2015; Varma et al., 2025; D. Chen et al., 2016). These multimodal systems are also incorporated for preclinical *in vivo* studies. However, the key shortcomings related to multimodal systems are the requirement of highly trained and qualified operators and the exclusive process needed to establish combinatorial functioning in the clinical setup. Also, some technological problems are tricky to overcome. Nevertheless, multimodal imaging systems are progressing. Also, there are many multimodal scanners that are already in use or in the process of development in preclinical areas (Rieffel et al., 2015; Varma et al., 2025).

Another aspect of multimodal imaging is the multimodal contrast agents. The most common representative example of this is the optical-MR imaging combination. MRI can achieve high spatial resolution and deep tissue penetration, although it is less sensitive (Burke et al., 2017; Khan et al., 2021; Z. Y. Ma et al., 2013; Varma et al., 2025; X. Li et al., 2020). On the other hand, optical imaging is sensitive, but it cannot achieve high spatial resolution and deeper tissue penetration. Thus, MRI and optical methods complement each other, leading to accurately diagnosing medical conditions (Burke et al., 2017; Khan et al., 2021; Z. Y. Ma et al., 2013; Varma et al., 2025). Similarly, CT and optical imaging can also be combined.

GNRs are extensively investigated as multimodal contrast agents or imaging probes (Z. Y. Ma et al., 2013; Varma et al., 2025; Khan et al., 2021). GNRs were modified with indocyanine green-loaded mesoporous silica by Luo et al., which functioned as dual-modal NIR fluorescence and CT imaging agents (T. Luo et al., 2011). Similarly, Yang and coworkers synthesized magnetic gold-nanorod/ PNIPAAmMA nanoparticles as a dual-modal imaging probe for MRI and PAI (Yang et al., 2013). A combination of more than two imaging modalities has also been explored with GNRs. Xie et al. developed PEG functionalized and AIE fluorescent dye NPAPF loaded GNRs (NPAPF-GNRs@PEG) for *in vitro* and *in vivo* fluorescence, CT and PAI as well as for various therapies for tumour (L. Xie et al., 2023).

1.6.2.3. Multimodal imaging of breast cancer using GNRs

With around 2.3 million incidences in 2022, breast cancer attained the place of second most common cancer worldwide. Also, as per the Globocan 2022 report, it is the 4th most common cancer in mortality, with around 0.67 million deaths (International Agency for Research on Cancer, 2024). However, it is estimated that by 2030, the statistics of breast cancer will increase further, with around 3.2 million cases per year (Moudgil et al., 2023; Varma et al., 2025). This

cancer is more prevalent in females, although it can also happen in males, but the rate is very low. Figure 1.16 shows the stats of incidences and mortality of breast cancer worldwide, and sex-wise data in females is also given in Figure 1.17 (International Agency for Research on Cancer, 2024). Notably, a 40% enhancement was observed in an advanced form of male breast cancer from year 1975 to 2015. This is due to the lack of awareness in males (Moudgil et al., 2023; Varma et al., 2025). WHO has assessed that 192,020 females in India are connected with breast cancer, which is around 14% of the country's total cancer incidences. Also, in India, as per the Globocan 2022 report, breast cancer is the most common cancer in mortality among both sexes (Fig. 1.18) (International Agency for Research on Cancer, 2024).

The unrestrained proliferation of breast cells/tissues is the key feature of breast cancer (Nag et al., 2024). Breast cancer is very heterogeneous. The heterogeneity results from numerous morphologies of neoplastic cells, discrepancies at the molecular level in the related biomarkers, and genetic irregularities. Furthermore, the heterogeneity could be inter or intra-tumor, i.e., the difference between the tumors among individuals and the difference within a tumor, respectively (Moudgil et al., 2023; Polyak, 2011; Varma et al., 2025). Also, heterogeneity could be temporal or spatial; in temporal, the discrepancies develop because of tumor progression, whereas in spatial, there are irregularities in tumors at different sites (Moudgil et al., 2023; Turashvili & Brogi, 2017; Varma et al., 2025). Moreover, the tumor microenvironment is also responsible for the heterogeneous nature of breast cancer. Therefore, due to the heterogeneity, the clinical diagnosis and the responses to therapy are diverse among individuals with breast cancer. There are numerous plausible risk factors like genetic predisposition, breast-related aspects, reproductive factors, demographic elements, hormonal factors, nexus of breast cancer, lack of physical activities, alcohol intake and obesity (Moudgil et al., 2023; Varma et al., 2025).

According to histology, breast cancer can be invasive and non-invasive. However, the molecular classification is related to the hormone receptors like the estrogen receptors (ER) and progesterone receptors (PR), as well as the human epidermal growth factor receptor 2 (HER 2). Luminal A type involves both hormone receptors (ER and/or PR), but there is the absence of HER 2. Besides, luminal B includes ER and/or HER 2, but the PR may be present or absent. Another is there i.e. HER 2 enriched, which involves overexpression of HER 2 receptors (Feng et al., 2018; Moudgil et al., 2023; Varma et al., 2025). Next is triple-negative breast cancer (TNBC), where no receptors are present (Moudgil et al., 2023; Núñez et al., 2018; Varma et al., 2025).

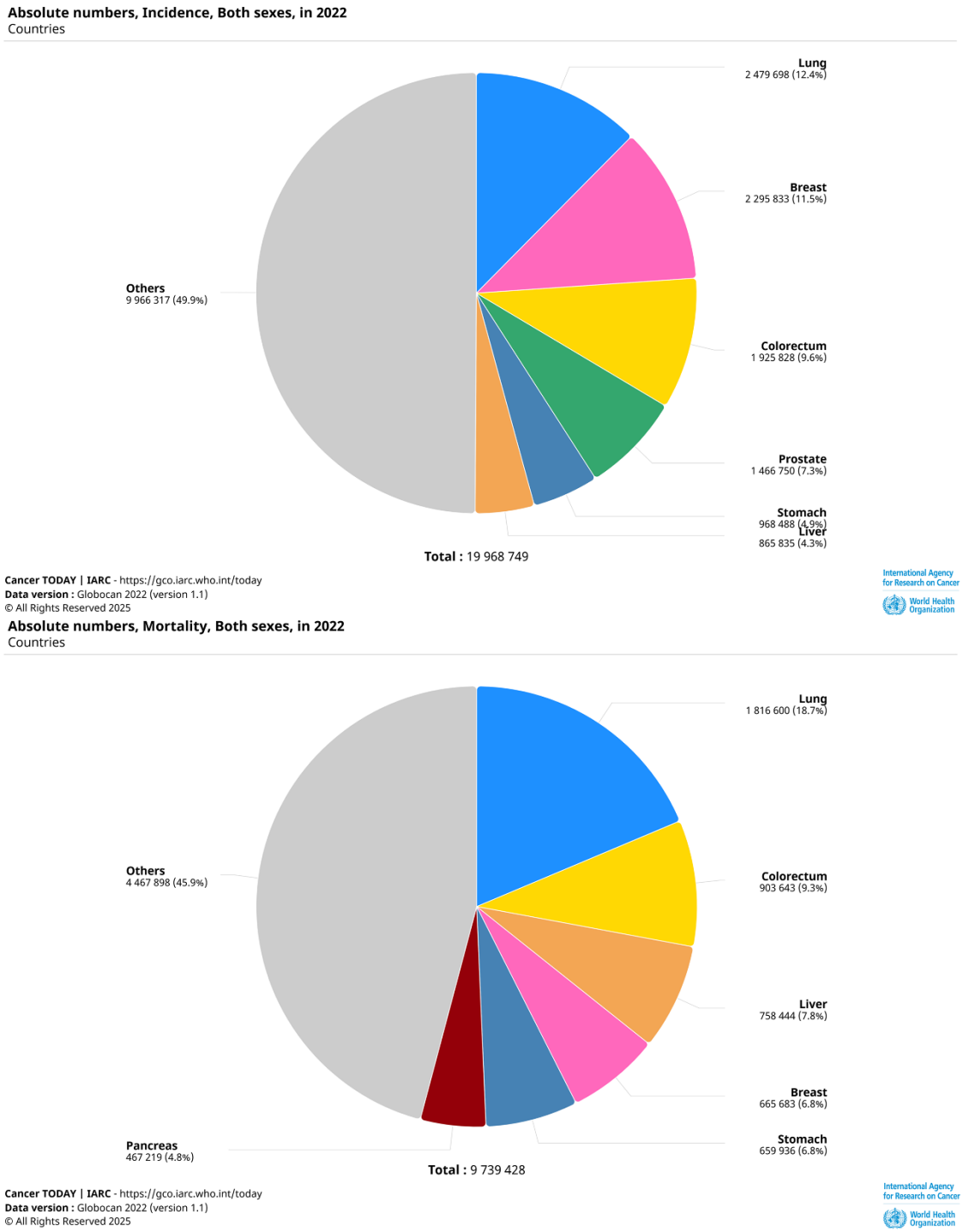

Figure 1.16 Breast cancer incidences and mortality worldwide (IARC-Globocan, 2022)

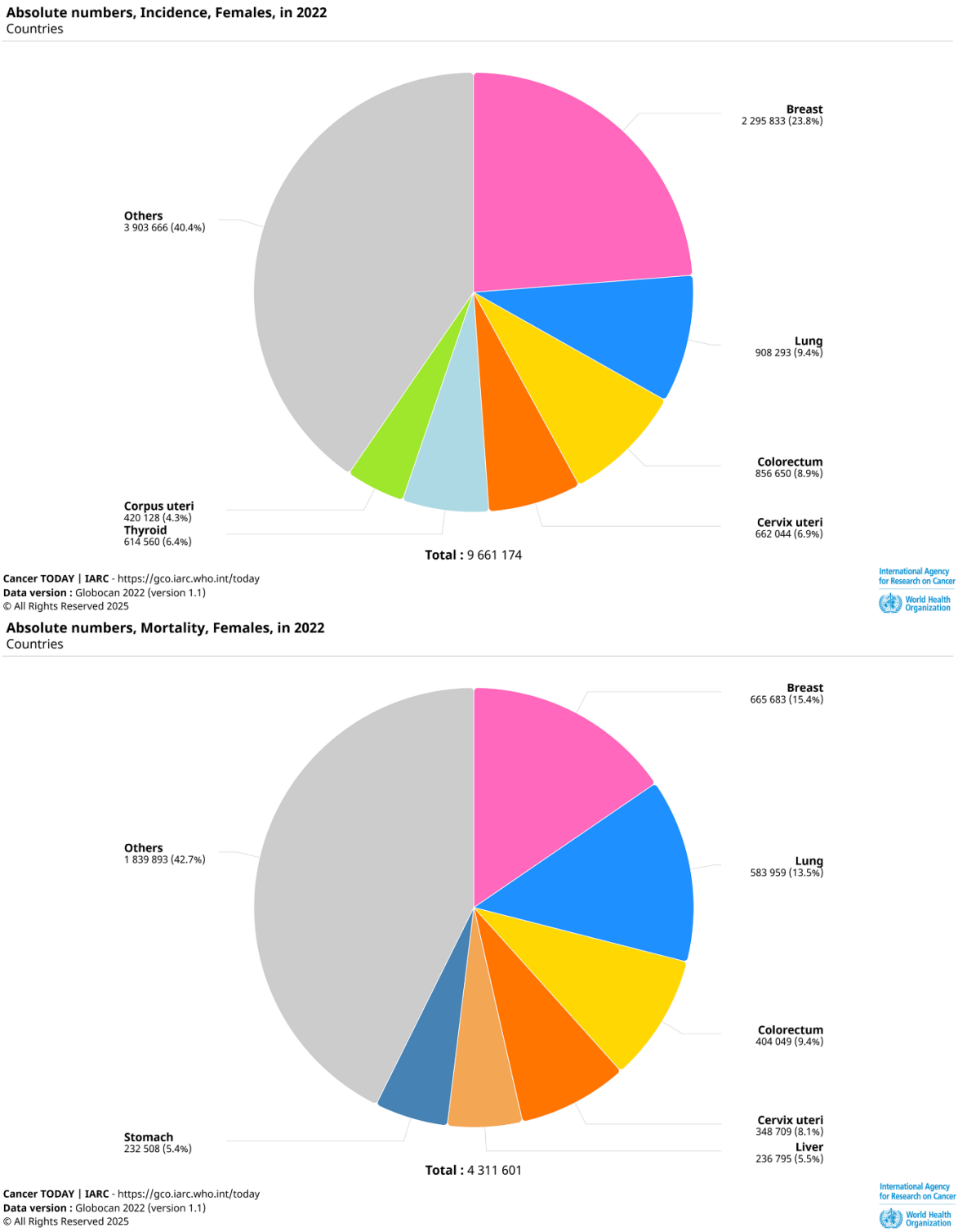

Figure 1.17 Breast cancer incidences and mortality in females worldwide (IARC-Globocan, 2022)

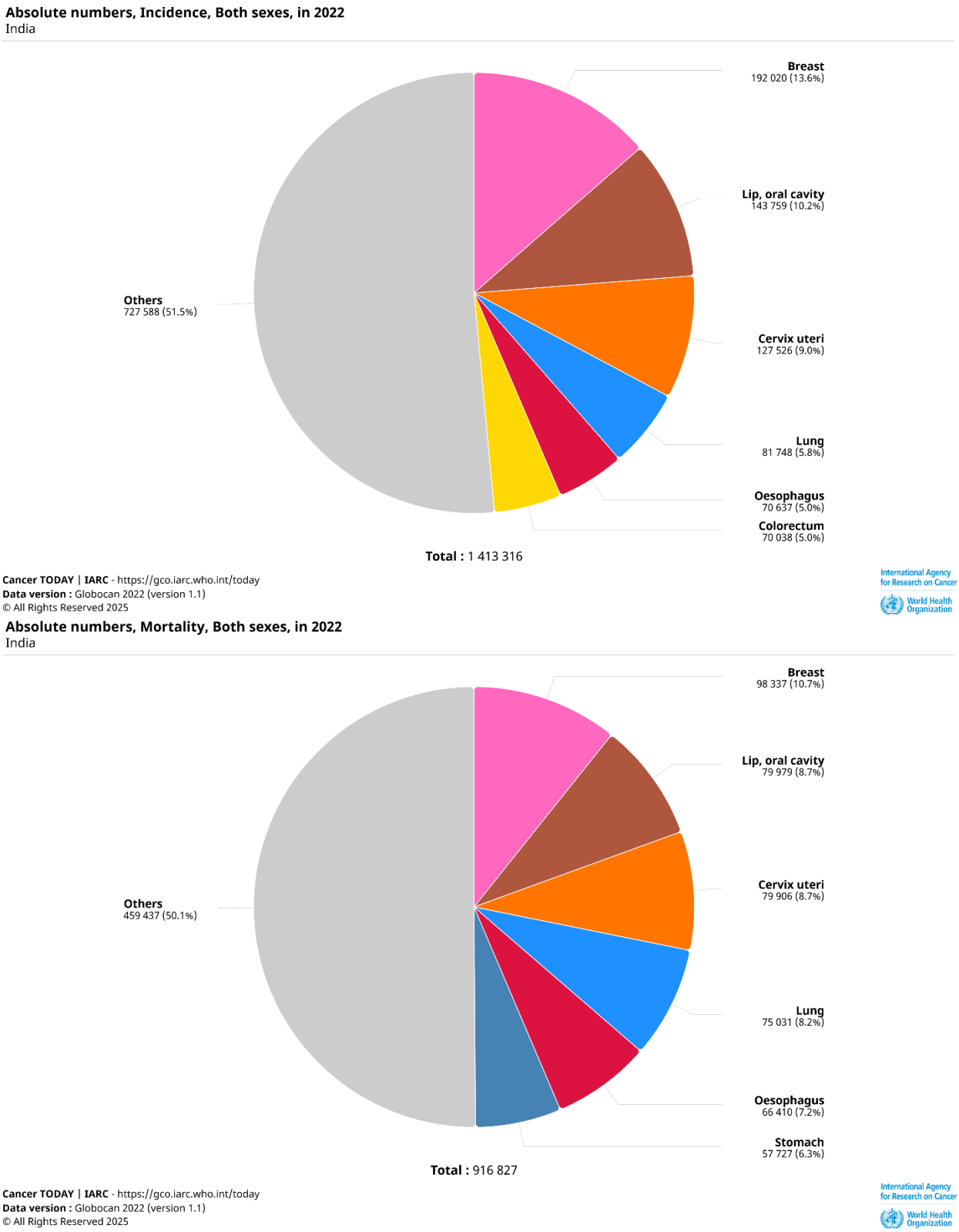

Figure 1.18 Breast cancer incidences and mortality in India (IARC-Globocan, 2022)

Considering the intricate features of breast cancer, its early detection is highly required for precise treatment and to prevent relapses. Mammography is the commonly employed traditional method to diagnose breast cancer (Núñez et al., 2018; Varma et al., 2025; Avitabile

et al., 2018). Although, it can fail to detect 20% of newly developed cancer (Núñez et al., 2018). This can be overcome by employing the imaging methods such as CT, MRI, US imaging, etc. The imaging techniques that are generally used to diagnose breast cancer are highlighted in Figure 1.19 (Fig. 1.19). Further, the findings of the imaging studies are supported by invasive and painful biopsy and blood test studies (Moudgil et al., 2023; Mu et al., 2017; Varma et al., 2025; Avitabile et al., 2018). Moreover, the imaging methods are not sensitive enough to diagnose metastasis (Mu et al., 2017). Notably, mammography is also ineffective in detecting ER-negative tumors (Núñez et al., 2018). Thus, to achieve a complete cure for breast cancer, its diagnosis should be sturdy, providing comprehensive information about the size, type, status of malignancy and metastasis, stage, receptors, etc., of the tumor (Moudgil et al., 2023; Varma et al., 2025). Therefore, detailed diagnosis can be attained by incorporating contrast agents with the imaging methods and by integrating the imaging modalities. Nanomaterials can serve as potential imaging agents which are capable of surpassing the inadequacies related to the imaging methods for breast cancer estimation. Additionally, by also involving a multimodal imaging approach along with nanoparticles, sensitive detection and therapy could be achieved.

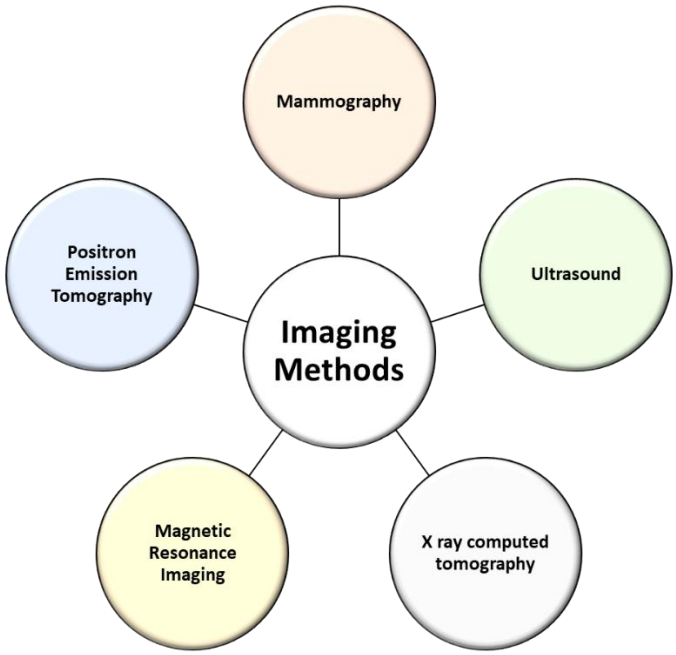

Figure 1.19 Imaging methods used for breast cancer diagnosis

Here, GNRs have been enlightened as a multimodal contrast agent or imaging probe for breast cancer estimation, tracking and image-guided therapy due to their extraordinary properties. Adding up the multimodal imaging attribute on GNRs will also subjugate the drawbacks related to single-modal imaging and will enhance the chance of accurate diagnosis by multiple folds.

Many articles prove that the GNRs are the efficient multimodal contrast agent for imaging and studying breast cancer. The effectiveness of functionalized GNRs in multimodal imaging studies of breast cancer can be explained by *in vitro* phantom studies/ phantom imaging, *in vitro* cell imaging and *in vivo* imaging. Our work employed the functionalized GNRs for dual-modal CT and photoacoustic imaging due to their remarkable ability to achieve X-ray attenuation and photoacoustic effects. Thus, Table 1.6 has a comprehensive list of the researchers who have used GNRs for multimodal CT and PAI of breast tumors (Table 1.6).

Table 1.6 Studies undertaken by using GNRs as a multimodal contrast agent/imaging probe for PAI and/or CT imaging of breast cancer

Nanoparticles	**Size (Length x Width/ Diameter)**	**Imaging modalities**	***In vitro* models**	***In vivo* models**	**References**
PEG-GNR conjugated Bombesin (GNR-PEG-BBN)	37 ± 5 nm x 10 ± 5 nm	PAI and Bright-field imaging	T47D cells	Breast cancer cells injected in female BALB/c mice	(Heidari et al., 2014)
Pegylated Gold nanorods (PEG-GNRs)	-	PAI and X-ray imaging		Tumor-bearing mouse	(G. Huang et al., 2011)
Plasmonic–magnetic hybrid nanoparticle	40 ± 5 nm x 8 ± 3 nm	Confocal imaging and PAI	-	MDA-MB-231 cells injected in female BALB/c athymic nude mice	(C. Xu, Feng, et al., 2018)
PLGA-PEG polymer nanoparticle	285 ± 29 nm	PAI and FL imaging	BT474 cells and MDA-	-	(Y. Wang et al., 2021)

containing gold nanorods (PLGA-PEG-GNRs)			MB-231 cells		
GNRs-based peptide nanoassemblies (GPNAs)	24 nm x 11 nm	PAI, NIR FL imaging and CT imaging	MDA-MB-231 cells and MCF-7 cells	MDA-MB-231 or MCF-7 cells injected female BALB/c nude mice	(Yao et al., 2021)
Pillar[5]arene-modified GNRs	62.98nm x 14.17 nm	FL imaging, Confocal imaging and PAI	4T1 cells	4T1 tumor-bearing mice.	(Song et al., 2021)
GNRs and InP/ZnS quantum dots covered in a silica medium (Au@QD@SiO_2/ PEG-c(RGDfC))	61.23 ± 1.69 nm x 17.62 ± 2.15 nm	CT imaging, FL imaging and Confocal imaging	HeLa and MCF-7 cells and phantom	HeLa tumor-bearing nude mice	(L. Zhang et al., 2018)
Gold nanorods	45 nm x 10 nm	Diffuse optical tomography, CT imaging and SPR-enhanced optical imaging (SPROI) technique	Phantom	4T1 tumor-bearing female nude mice	(K. Xu et al., 2018)

Bacteria like mesoporous silica-covered GNRs (^{89}Zr-bGNR@MSN-PEG)	104.6 ± 5.6 nm x 68.6 ± 5.2 nm	PET imaging and PAI	-	4T1 tumor-bearing mice	(C. Xu, Chen, et al., 2018)
AuNR@PAA/ CaP Yolk–Shell NPs	60 nm x 15 nm	PAI and CT imaging	Phantom	-	(G. Li et al., 2018)
Peptosomes hybridized with gold nanorods	25nm	FL imaging and CT imaging	-	4T1 tumor model in Balb/c mice	(Hasannia et al., 2022)
DOX loaded PEG-FA_ GNR-Lipos nanohybrid	27nm x 9nm	CT imaging and FL imaging	Phantom and MDA-MB-231 cells	-	(Chauhan et al., 2018)
SiO_2-coated AuNRs and PEG-GNRs	35.93 ±5.2 nm x 8.94 ±1.08 nm	PAI and US imaging	Phantom	-	(Awad et al., 2020)
Multifunctional nanodrug coating a drug self-framework delivery system on gold nanorod (Au NRs@DSFDSs NPs)	140 nm x 42 nm	PAI and FL imaging	Phantom	MCF-7 cells injected in mice	(Hou et al., 2022)

Macrophage-loaded Anionic-AuNRs	25 ± 2 nm x 5 ± 1 nm	PAI, Confocal imaging and BIO TEM	Phantom	4T1 tumor-bearing mice	(An et al., 2019)
Cucurbit[7]uril modified GNRs (OX/FA/CB[7]-Au NRs)	77nm x 19 nm	FL imaging, CT imaging, OCT imaging and PAI	4T1 cells and L02 cells	4T1 tumor-bearing BALB/c mice	(Yue et al., 2019)
Folic acid functionalized gold nanorod with mesoporous silica (GNR-MS-FA)	90 ± 10 nm	CT imaging and FL imaging	4T1 Cells and NIH-3T3 cells	4T1 tumor-bearing female BALB/c mice	(Prasad et al., 2018)
Magneto-Plasmonic Nanocapsules (GNR@IOs-DOX nanocapsules)	-	MRI, PAI and Confocal imaging	4T1 cells	4T1 tumor-bearing mice	(L. Huang et al., 2016)
Gold nanorods with scintillator complex (GSE-HP)	57.1 ± 2.9 nm x 15.7 ± 1.4 nm	CT imaging and PAI	-	4T1 tumor-bearing BALB/c mice	(L. Luo et al., 2020)
Gold nanorods/mesoporous silica with metal organic	56 nm x 13 nm	MRI, CT imaging and PAI	-	4T1 tumor-bearing female BALB/c mice	(H. Guo et al., 2021)

framework and hyaluronic acid (GNRs-MSNs-MA)					
Nitroxide-radicals–altered GNRs	39.2 nm x 10.18 nm	CT imaging and MRI	Phantom	4T1 tumor-bearing female BALB/c mice	(L. Xia et al., 2018)
Gold nanorods with europium-based coordination polymer (GNRs@EuCP)	50 nm x 15 nm	FL imaging, PAI and CT imaging	Phantom	-	(F. Xia et al., 2022)
Ammonium bicarbonate and GNRs into folic acid-coupled liposomes (FA-GNR-ABC-DOX/Lips)	47.35 ± 2.31 nm	CT imaging and US imaging	Phantom	S180 tumor-bearing mice	(N. Zhang et al., 2017)
Silver-covered GNRs loaded with doxorubicin (AuNR/Ag/Dox-EpCAM)	36 nm x 12 nm	SERS imaging and PAI	4T1 cells	-	(Jenkins et al., 2017)
PEG gold nanorods (PEG-GNR)	46.2± 4.2 nm X 16.5± 1.4 nm	US imaging, PAI and OCT imaging	-	4T1 tumor-bearing mice	(J. Park et al., 2021)

Gold nanorods vesicles (AuNR@PEG/PolyRu Vesicle)	35 nm x 7 nm	FL imaging and PAI	MCF-7 cells, 4T1 cells and phantom	MCF-7 cells injected in BALB/c nude mice	(Ge et al., 2020)
Radiolabeled GNRs	-	PAI, and SPECT/CT imaging	Phantom	-	(Agarwal et al., 2011)

1.6.2.4. Patents

Approved patents on the GNRs-based nanoprobes utilized for multimodal breast cancer bioimaging are listed in Table 1.7.

Table 1.7 Patents related to multimodal imaging of breast cancer using GNR-based imaging agents

Title	Patent no.	References
Gold / Lanthanide nanoparticle conjugates and uses thereof	US10406111B2	(Boyes et al., 2019)
Nanocomposites and methods of making same	US11119099B2	(Biris et al., 2021)
Multifunctional metal Nanoparticles having a polydopamine-based surface and methods of making and using the same	US8784895B2	(Messersmith et al., 2014)
Nanocomposites, methods of making same, and applications of same for multicolor surface enhanced raman spectroscopy (SERS) detections	US10830767B2	(Biris et al., 2020)

1.7. Hypothesis and objectives

To acknowledge the biosensing and bioimaging potential of GNRs, we aimed to synthesize GNRs and modify them with 11-MUA (MUA-GNRs), which could be subsequently functionalized with TSH antibody (Ab-GNRs) and biosynthesized poly-γ-glutamic acid (γPGA) (γPGA-MUA-GNRs) for biosensing and bioimaging investigations, respectively (Fig. 1.20). To synthesize robust, stable, and biocompatible Ab-GNRs and γPGA-MUA-GNRs, we intended to optimize the process parameters for GNR synthesis by the seed-mediated method and various functionalization process factors to achieve great specificity of particles for TSH detection and biocompatibility for bioimaging purpose. We then planned to optimize the factors to enhance the sensitivity of the LFA for estimating both hypothyroidism and hyperthyroidism based on TSH. Further, we intended to investigate the biocompatibility of γPGA functionalized GNRs and MUA-GNRs on MCF-7, a hormone receptor-positive cell line, MDA-MB-231, a TNBC cell line and MCF-10A, a normal breast epithelial cell line. We also aimed to assess the hemocompatibility of γPGA functionalized GNRs and MUA-GNRs. Subsequently, we envisioned examining the CT imaging and PAI contrast agent potential of γPGA functionalized GNRs and MUA-GNRs by phantom imaging studies.

We hypothesized the following:

- TSH antibody functionalized GNRs could act as a sensitive and selective label for LFA, which could help to diagnose both hypothyroidism and hyperthyroidism without employing any analytical technique.

- γPGA-MUA-GNRs could function as an efficient and biocompatible CT imaging and PAI dual-modal contrast agent.

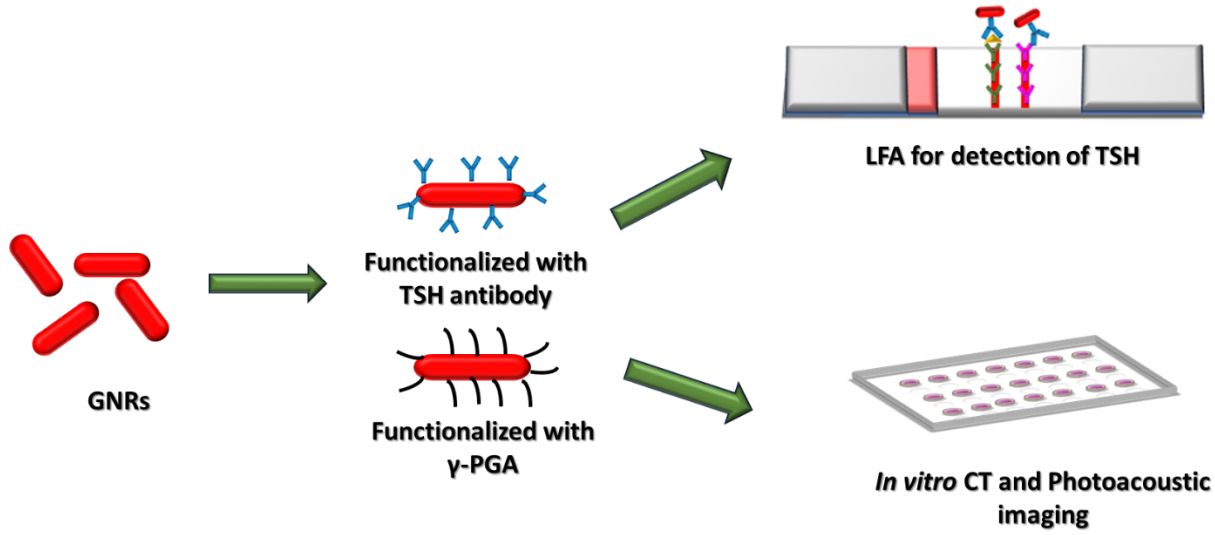

Figure 1.20 Schematics of biosensing and multimodal bioimaging using GNRs

Based on the hypothesis, we followed the following objectives to carry out the study:

1. Optimization, synthesis and characterization of gold nanorods
2. Surface functionalization of gold nanorods
3. Preparation and demonstration of proof of concept of lateral flow assay test strip
4. Sensitivity and selectivity testing of lateral flow assay test strip
5. Bioimaging studies of gold nanorods

CHAPTER 2

Materials and Methods

2. Materials and Methods

2.1. Materials

Table 2.1 List of chemicals/materials used in the study and their sources

Chemicals/ Materials	Source
Gold (III) chloride trihydrate ($HAuCl_4.3H_2O$)	Sigma-Aldrich
CTAB	Sigma-Aldrich
L-Ascorbic acid	Sigma-Aldrich
Silver nitrate ($AgNO_3$)	Sigma-Aldrich
Hydrochloric acid (HCl)	Sigma-Aldrich
NaOH	HiMedia
Sodium borohydride ($NaBH_4$)	HiMedia
Sodium chloride (NaCl)	HiMedia
11-Mercaptoundecanoic acid (11-MUA)	Sigma-Aldrich
1-ethyl-3-(3-dimethylaminopropyl) carbodiimide (EDC)	Sigma-Aldrich
N-hydroxysuccinimide (NHS)	Sigma-Aldrich
Boric acid	Sigma-Aldrich
Phosphate Buffered Saline pH 7.4 Sterile (PBS)	Sigma-Aldrich
Bovine serum albumin (BSA)	Sigma-Aldrich
Sucrose	Sigma-Aldrich
Tween 20	Sigma-Aldrich
Sodium azide (NaN_3)	Sigma-Aldrich
Sodium dodecyl sulfate (SDS)	Sigma-Aldrich
Methanol	Sigma-Aldrich
TSH from human pituitary	Sigma-Aldrich
FSH from human pituitary	Sigma-Aldrich
LH from human pituitary	Sigma-Aldrich
hCG	Sigma-Aldrich
Anti-Mouse IgG (whole molecule) antibody produced in goat	Sigma-Aldrich
Mouse Monoclonal TSH antibody (10-2429)	Fitzgerald
Mouse Monoclonal TSH antibody (10-2427)	Fitzgerald
Sample pad (Whatman MF1)	Cytiva

Test pad (Nitrocellulose membrane, Whatman FF120HP)	Cytiva
Absorbent pad (Whatman CF4)	Cytiva
Conjugate pad (Whatman standard 14)	Cytiva
γPGA	NCIM
γPGA	Sigma-Aldrich
MCF-7 cell line	NCCS repository
MDA-MB-231 cell line	NCCS repository
MCF-10A cell line	NCCS repository
Rosewell Park Memorial Institute- 1640 (RPMI-1640)	HiMedia
Dulbecco's Modified Eagle Medium (DMEM)	HiMedia
Fetal Bovine Serum (FBS)	Gibco
Cholera Toxin	Sigma-Aldrich
Hydrocortisone	Sigma-Aldrich
DMEM/F12	Gibco
EGF	Peprotech
Horse Serum	Gibco
Penicillin-Streptomycin	Gibco
Insulin	Sigma-Aldrich
3-(4,5-Dimethylthiazol-2-yl)-2,5-Diphenyltetrazolium Bromide (MTT)	Sigma-Aldrich
Dimethyl sulfoxide (DMSO)	Sigma-Aldrich
Triton X 100	HiMedia
Bradford reagent	HiMedia
Nitric acid (HNO_3)	HiMedia

2.2. Methods

2.2.1. Synthesis of GNRs

GNRs were synthesized using a seed-based growth method (Nikoobakht & El-Sayed, 2003). It was a two-step protocol, in the first step 3-5 nm Au nanoseeds were synthesized by using $HAuCl_4.3H_2O$ (0.5 mM) and CTAB (0.2 M) in 1:1 volume ratio and the mixture was reduced by dropwise adding the 600 µl freshly made and ice-cold $NaBH_4$ (10 mM) to the mixture kept under stirring. Further, stirring was continued for 2 min and thereafter, the

prepared seeds were left at room temperature (RT) for some time. This is known as seed aging.

Subsequently, in the second step, the mixture of 5 ml $HAuCl_4.3H_2O$ (0.5 mM), 5 ml CTAB (0.2 M) and $AgNO_3$ (4 mM) was prepared. 70 µl ascorbic acid (78.8 mM) was further incorporated into the mix, resulting in the formation of a colorless solution. Lastly, 12 µl Au seeds were added to the mixture and color change was noticed in 10-20 min. Further, the GNRs were purified by centrifuge at 12000 rpm for 15 min (twice) and resuspended in deionized (DI) water.

2.2.2. Synthesis of MUA-GNRs

The CTAB from the GNR surface was replaced by 11-MUA by using the pH-mediated method (J. Cao et al., 2012). For this, 11-MUA was dispersed in DI water, then 0.2 M NaOH was added dropwise, followed by periodic sonication until the MUA was dissolved. To replace CTAB from the GNRs surface, 2 ml 11-MUA (20 mM) was added to the 5 ml GNRs suspension, and the mixture was vigorously stirred for 24 hr. The excess MUA was removed by centrifugation at 8000 rpm for 20 min (twice) and the MUA-GNRs were redispersed in pH 9 borate buffer (0.01 M).

2.2.3. Synthesis of Ab-GNRs

Mouse Monoclonal TSH antibody (10-2427) was covalently attached to the surface of MUA-GNRs by the EDC/NHS method (J. Cao et al., 2012). Herein, freshly prepared 0.05 M EDC (20 µl)) and 0.1 M NHS (20 µl) were added to 1 ml MUA-GNRs and vortexed for 25 min to stimulate the -COOH group of 11-MUA. Thereafter, 50 µl of 1mg/ml TSH antibody was added to the mixture and vortexed gently. After incubation of 1 hr, the mix was centrifuged to separate Ab-GNRs at 8000 rpm for 20 min; after this step, the supernatant was stored for the analysis of % binding efficiency of the antibody. Moreover, Ab-GNRs were washed twice with washing buffer (1% BSA in 0.01 M borate buffer at pH 9). The washing buffer also blocks the surface of GNRs so that the nonspecific binding can be prevented. Finally, the Ab-GNRs were stored at 4^{o}C after resuspension in the washing buffer before use.

2.2.4. Synthesis of γPGA-GNRs and γPGA-MUA-GNRs

The γPGA functionalized GNRs were prepared with certain modifications to the reported protocol (Guan et al., 2014; J. Y. Liu et al., 2019). Briefly, 1 mg/ml γPGA (250 µl) was added in 1 ml GNRs or MUA-GNRs. The mixture was stirred for 2 hr at RT and finally, the γPGA

functionalized GNRs were collected after centrifugation at 12000 rpm for 15 min (twice) and resuspended in 1 ml DI water.

2.2.5. Characterization of various GNRs

2.2.5.1. UV-visible-NIR spectroscopy

The LSPR spectra of plain and various functionalized GNRs were recorded in a UV-visible spectrophotometer (Lambda 750, PerkinElmer). This gives information regarding the size, shape, functionalization, stability and structural integrity of the GNRs. Herein, the suspension medium was taken as the reference. All the samples were assessed in triplicate.

2.2.5.2. Zeta potential analysis

The zeta potential measurements were undertaken by Malvern Zetasizer Pro (Malvern Panalytical, UK) at 25 °C (173 ° non-invasive backscattering angle). All the samples were assessed in triplicate, and three independent measurements were recorded for each sample.

2.2.5.3. Morphology of GNRs

The morphology of the GNRs was determined using transmission electron microscopy (TEM) (Tecnai G2 20 S-Twin), high-resolution transmission electron microscopy (HRTEM) (JEOL JEM-F200) and field emission scanning electron microscopy (FESEM) (FEI NOVA NANOSEM 450) techniques. For TEM and HRTEM analysis, plain and various functionalized GNRs were diluted in DI water or suspension medium, and 4-5 µl GNRs were drop cast on the 200-mesh carbon-coated copper grid followed by air drying before the analysis. Similarly, the diluted GNR samples were drop-cast on the silicon wafer and air-dried before FESEM analysis. Also, the selected area electron diffraction (SAED) pattern and the fringes were recorded using HRTEM.

2.2.5.4. X-ray diffraction (XRD) analysis

XRD study was undertaken to authenticate the crystallinity of GNR using an 'X' Pert Pro powder XRD (PANalytical) by using the freeze-dried powder of GNRs, which was mounted on the XRD plate. The analysis was performed for 30 minutes from a 5-80^{o} angle.

2.2.5.5. Elemental analysis of GNRs

Primarily, the elemental analysis was performed using the energy dispersive X-ray (EDX) accessory of HRTEM, which was further confirmed by the scanning transmission electron

microscopy (STEM) accessory of HRTEM. At the same time, no special sample preparation was required for these; it can be done by using the same morphology determination sample of HRTEM discussed earlier. Similarly, EDX spectra were also recorded using FESEM. However, for FESEM's EDX analysis, the concentrated samples were drop-cast on carbon tape and air-dried before analysis.

Further, all the types of GNRs were also analysed with X-ray photoelectron spectroscopy (XPS) (XPS - K ALPHA, Thermo Fisher Scientific Instruments) for their elemental composition. The samples were prepared by forming a thin film of various types of GNRs on the silicon wafer, which was air-dried before the analysis.

2.2.5.6. Fourier transform infrared spectroscopy (FTIR)

FTIR spectra were recorded to determine the presence of functional groups in different types of GNRs after synthesis and functionalization. The infrared spectral profiles were recorded on Tensor 27 (Bruker) in the wavenumber range of 4000–600 cm^{-1}. Each sample was subjected to 40 runs.

2.2.5.7. Quantification of Au content in various GNRs

The Au content in all the types of GNRs was quantified by using inductively coupled plasma mass spectrometry (ICP-MS). The GNRs were dissolved in aqua regia and Au concentration was determined (C. Xu, Feng, et al., 2018; Yue et al., 2019). All the types of GNRs had an optical density (OD) 1 for this study.

2.2.5.8. Quantification of TSH antibody on Ab-GNRs

After tagging TSH antibody on MUA-GNRs, the particles were centrifuged at 8000 rpm for 30 min, and the supernatant was collected to quantify the untagged antibody. The percentage binding efficiency (% BE) of TSH antibody on the MUA-GNRs surface was calculated by the following formula:

$$BE\ (\%) = \frac{Intial\ weight\ of\ TSH\ Ab - Untagged\ TSH\ Ab}{Initial\ weight\ of\ TSH\ Ab} \times 100$$

The untagged antibody was calculated using the straight-line equation attained by plotting a standard curve of bovine serum albumin (BSA) and determining the protein concentration using the Bradford assay (Bradford, 1976) (Fig. 2.1). Varied dilutions of BSA were made from the stock of 1 mg/ ml of BSA, i.e., 1,5,10,15, 20 and 25 µg/ml. 500 µl Bradford reagent was

added to 250 µl BSA dilutions, and the reaction mixture was incubated for 5 min. The absorbance was read after 5 min by a UV-visible spectrophotometer at 590 nm. The concentration of TSH antibody was calculated using the straight-line equation.

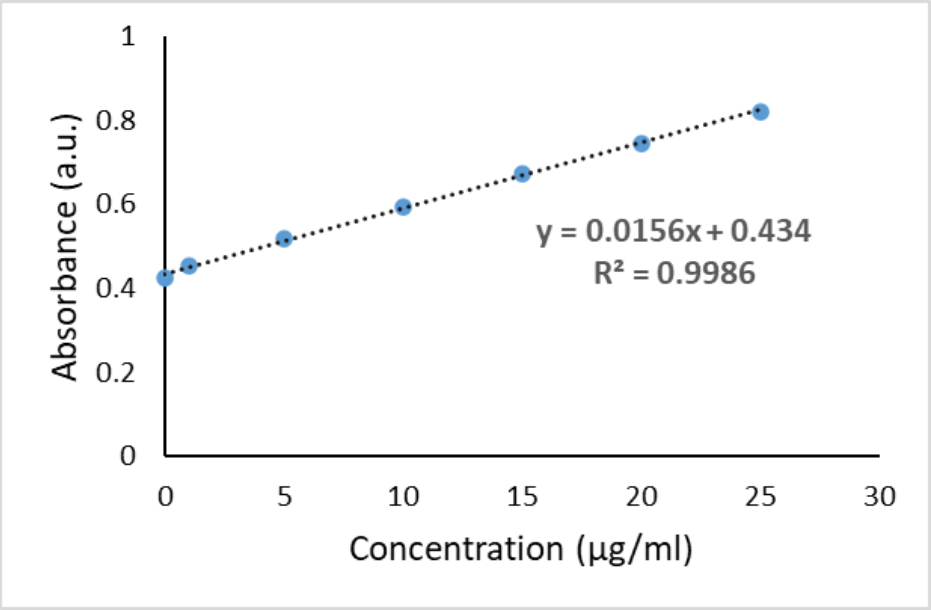

Figure 2.1 Standard curve of BSA

2.2.6. Stability studies

The stability of the various GNRs was tested at 4°C. The LSPR spectrum and zeta potential values were determined over time. These values were recorded periodically by withdrawing aliquots from the stock to detect changes happening during storage. The stability studies were performed at various steps to proceed further with the experiments. Briefly, we assessed the stability of MUA-GNRs before the functionalization of the TSH antibody for 7 days to finalize the suspension medium. Further, the stability of MUA-GNRs and Ab-GNRs was investigated in borate buffer for biosensing studies. For bioimaging application, the stability of GNRs, MUA-GNRs, γPGA-GNRs and γPGA-MUA-GNRs were assessed in DI water for 3 months, and thereafter, before commencing the *in vitro* efficacy studies, the stability of all types of GNRs was evaluated in the DMEM for 48 hr.

2.2.7. Preparation of LFA

2.2.7.1. Preparation of sample pad

The sample pad was pretreated with a borate buffer of pH 8 (50 mM), which contained 1% BSA, 0.5% Tween-20, 0.01 % SDS and 0.02% NaN_3, and then dried at 37°C for 2 hr (Parolo et al., 2020; Pham et al., 2022; Tao et al., 2018).

2.2.7.2. Preparation of conjugate pad

The conjugate, Ab-GNRs, dispersed in pH 9 borate buffer (0.01M) containing 1%BSA and 5% sucrose, was sprayed on the conjugate pad and vacuum dried (Parolo et al., 2020).

2.2.7.3. Preparation of test pad

The test pad was pretreated with PBS (pH 7.4), containing 5% methanol and 2% sucrose (stabilizer) for 15 min and dried under a vacuum at 37ºC for 2 hr (Parolo et al., 2020; Shukla et al., 2011). Further, the capture antibody, i.e. mouse monoclonal TSH antibody (10-2429), was dispensed on the test line, and the anti-Mouse IgG (whole molecule) antibody produced in goat (2 mg/ml) was dispensed on the control line by using the dispenser (SS Easy Printer, LPM-02). Thereafter, the test pad was dried in a dehumidified environment at 37ºC for 2 hr (Parolo et al., 2020).

2.2.7.4. Assembly of LFA

The LFA was assembled according to the protocol reported (Mills et al., 2022; Parolo et al., 2020). Firstly, the test pad was mounted on the backing card, then an absorbent pad was placed near the control line side of the test pad and was 1mm overlapped on the test pad. Then, the conjugate pad was positioned on the test line side of the test pad and was 1mm overlapped on the test pad. Lastly, the sample pad was mounted by overlapping it on the conjugate pad. Further, the 4 mm strips were cut by using a cutter (SS Programmable Strip Cutter Model M-70) and stored with desiccants.

2.2.7.5. Assay procedure

The TSH dilutions were prepared in an assay buffer and 50 µl was added to the sample pad. Further, after 10 min, the intensity of color formed at the test line was observed through the naked eye.

2.2.7.6. Sensitivity and selectivity testing

The sensitivity of the LFA was tested by using different concentrations of TSH (0.01 µIU/ml to 20 µIU/ml), and the intensity of the test line was observed through the naked eye. The selectivity of the prepared LFA was tested by adding 50 µl of FSH (15 mIU/ml), LH (25 mIU/ml) and hCG (100 mIU/ml) hormones, dispersed in assay buffer to the sample pad and observing the colour change at the test line.

2.2.8. *In vitro* efficacy studies

2.2.8.1. Cell viability assay

MCF-7, MDA-MB-231 and MCF-10A cells were seeded in a 96-well plate (4000 cells per well) and incubated for 24 hr at 37°C, in 5% CO_2 atmosphere (L. Xia et al., 2018). The media was also supplemented with 10% fetal bovine serum and penicillin/streptomycin solution. After that, the cells were treated with GNRs, MUA-GNRs, γPGA-GNRs and γPGA-MUA-GNRs at varied Au concentrations (5, 25, and 50 µM) and incubated at 37°C for 48 hr. After the incubation, 20 µl MTT (5 mg/ml) was added to each well and further incubated for 4 hr at 37°C. The formazan crystals formed were then dissolved by adding 100 µl DMSO (F. Xia et al., 2022; L. Zhang et al., 2018), and the reading was taken at 570 nm on a Multiscan Go Thermo Scientific plate reader. The following formula then calculated the % cell viability (Chauhan et al., 2018):

$$Cell\ viability\ (\%) = \frac{A\ of\ treated\ cells}{A\ of\ control\ cells} \times 100, \qquad (where, A = Absorbance)$$

We plotted a graph for % cell viability against Au concentrations in GNRs, MUA-GNRs, γPGA-GNRs and γPGA-MUA-GNRs and calculated the IC_{50} values using the KyPlot software.

2.2.8.2. Cellular uptake analysis

MCF-7, MDA-MB-231 and MCF-10A cells (2×10^5 cells per well) were seeded in 6-well plates and incubated 24 hr at 37 ºC in a humidified 5% CO_2 atmosphere. The cells were treated with different GNRs at 5 µM of Au concentration and incubated at 37ºC for 30 min, 3 hr, 6 hr, 12 hr and 24 hr. Thereafter, the media was removed, and the plates were washed with PBS twice. The cells were harvested in PBS by mechanically scrapping from the plates and centrifuged at 3000 rpm for 3 min. The supernatant was removed, and the pellet was washed with DI water and centrifuged at 3000 rpm for 3 min. Further, the pellet was dissolved by aqua-

regia and the amount of Au element was quantified by ICP-MS (P. Huang et al., 2011; C. Wang et al., 2018; C. Xu, Feng, et al., 2018; W. Xu et al., 2017).

2.2.8.3. Hemolysis assay

The hemolysis assay was performed according to the reported procedure (J. Chen et al., 2020; M. Li et al., 2023; Saravanakumar et al., 2022; C. Wang et al., 2018). Briefly, 1 ml of sheep blood was resuspended in 10 ml PBS (pH 7.4). The suspension was centrifuged at 2000 rpm for 10 minutes at 4°C. Further, the red blood cell (RBC) pellet was collected and washed three times with PBS (pH 7.4). 4% v/v RBC suspension was prepared for the assay in PBS. Thereafter, 300 µl of the RBC suspension was mixed with 300 µl of plain and functionalized GNRs at different Au concentrations (5, 25, 50, 75 and 100 µM) and incubated at 37°C for 2 hr. The PBS was used as a negative control, and 1% Triton-X-100 was used as a positive control for the assay. After incubation, the suspensions were centrifuged at 2000 rpm for 10 min at 4°C. Further, 100 µl of supernatant was transferred to a 96-well plate, and the absorbance of the supernatant was recorded at 545 nm by a plate reader (EPOCH, Bio-Tek Instruments, USA). The % hemolysis was calculated using the following equation.

$$\%\ Hemolysis = \left(\frac{Absorbance_{sample} - Absrbance_{negative}}{Absorbance_{positive} - Absorbance_{negative}}\right) \times 100$$

2.2.9. Bioimaging studies

2.2.9.1. Phantom CT imaging

The phantom study was done to study the relationship between the imaging probe concentrations and the CT signal strength as well as to validate the CT contrast property of the probes. For this, 200 µl of GNRs and γPGA-GNRs with Au concentrations 2, 4, 8, 12 and 24 µM and MUA-GNRs and γPGA-MUA-GNRs with Au concentrations 100, 200, 300, 400 and 500 µM were added in the Eppendorf tube. The CT images were acquired by using a micro-CT scanner (Quantum GX2, PerkinElmer, USA). The parameters for the analysis were 50 kV tube voltage and 88 µA tube current. The Hounsfield unit (HU) values were obtained, and a curve was plotted for the HU value versus concentrations of different groups of GNRs based on Au content. Iohexol at the same concentrations was used as a standard (L. Luo et al., 2020; L. Xie et al., 2023; L. Zhang et al., 2018). The concentrations selected were below the IC_{50} of different groups of GNRs.

2.2.9.2. Phantom PAI

The phantom study was performed to establish the relationship between the imaging probe concentrations and the PAI signal strength as well as to authenticate the PAI contrast property of the probes. The photoacoustic phantom images were generated by acquiring the PA intensity of GNRs and γPGA-GNRs at 2, 4, 8, 12 and 24 μM Au concentrations and MUA-GNRs and γPGA-MUA-GNRs at 100, 200, 300, 400 and 500 μM Au concentrations. The concentrations selected were below the IC_{50} of different groups of GNRs. For this study, the Vevo LAZR-X imaging system (FUJIFILM Visual Sonics, Canada) was used at 780 nm excitation wavelength (Hou et al., 2022; L. Luo et al., 2020; L. Xie et al., 2023). Further, a curve was plotted for the PA intensity versus concentrations of different groups of GNRs based on Au content. We have used methylene blue as a standard which is a clinically applied PAI contrast agent, at the same concentrations (Attia et al., 2019; Han et al., 2022).

2.2.10. Statistical analysis

Data are presented as mean ± standard deviation calculated using Microsoft Office Excel. One-way analysis of variance (ANOVA) and the t-test were performed using GraphPad Prism, and the p-values ≤ 0.05 were considered statistically significant. UV-Vis-NIR spectra, XPS spectra, FTIR spectra, XRD spectrum and zeta potential graphs were plotted using Origin Pro 8 software. The IC_{50} values were calculated using KyPlot software.

CHAPTER 3

Optimization, Synthesis, and Characterization of GNRs

3.1. Introduction

Gold nanorods (GNRs) are ideal agents for probing diseases through imaging and sensing due to their favorable optical properties, ease of surface functionalization and biocompatibility. (Cheng et al., 2011) GNRs have two SPR bands, transverse (short axis) and a longitudinal (long axis) band (J. Cao et al., 2012; H. Huang et al., 2012; H. Zhang et al., 2016). The longitudinal band can be tuned from visible to NIR depending on the size and aspect ratio of GNRs (Rizwan Younis et al., 2021; J. Zhou et al., 2017). GNR's LSPR spectrum is sensitive to changes in the refractive index of the surroundings. This property makes them an efficient molecular probe for various applications. Also, it is one of the major properties that enable GNRs to sense specific target-binding actions (J. Cao et al., 2012; H. Huang et al., 2012; H. Zhang et al., 2016). GNRs also show a diverse color range with various aspect ratios when in a colloidal suspension (J. Cao et al., 2014). Additionally, GNRs exhibit strong NIR absorption and scattering, which are very attractive for *in vivo* biomedical imaging due to minimal near-infrared light absorption by most human tissues and water in the NIR (700–1300 nm) area (Kim et al., 2023; Haine & Niidome, 2017). Owing to all these properties, GNRs are very appropriate nanomaterials for bioimaging and biosensing studies.

There are various methods for the synthesis of gold nanorods: the template method, photochemical method, electrochemical method, seed-mediated growth method and seedless method. Among them, the seed-mediated growth method is more commonly used, and it is already the main method of wet chemical synthesis of gold nanorods (Cheng et al., 2011; H. Huang et al., 2012; John et al., 2013; J. Zhou et al., 2017). In other methods, precise control of different parameters is difficult, which may cause the quality of the gold nanorods to fluctuate, the operation is very complex and the output is relatively low (Li & Cao, 2012).

Seed mediated method is a two-step method for GNR synthesis. In the first step, Au seed particles are prepared, which are subsequently added to a growth solution. The growth solution usually contains a gold precursor ($HAuCl_4.3H_2O$), surfactant (CTAB), growth directional agents (CTAB and $AgNO_3$) and a reducing agent (ascorbic acid) (Alshangiti et al., 2023; X. Huang et al., 2009; Khan et al., 2021; Rizwan Younis et al., 2021; Vigderman et al., 2012; J. Zhou et al., 2017). This method is preferred because the nucleation and growth steps are separate, which gives better control over growth kinetics and yields highly monodispersed GNRs (Scarabelli et al., 2015). The ascorbic acid is too weak to reduce Au^{3+} to Au^0. Thus, it reduces Au^{3+} to Au^{1+}. Further, the reduction of Au^{1+} to Au^0 was carried out with the seed

solution. Seeds act as nucleation centers, catalyzing the reduction of Au^{1+} to Au^{0} on their surface (Alshangiti et al., 2023; X. Huang et al., 2009; Khan et al., 2021; Smitha et al., 2013).

In this study, we optimized the process parameters of the seed-mediated growth method to synthesize GNRs for biosensing and bioimaging applications. We evaluated gold precursor concentration, CTAB concentration, silver nitrate concentration, its volume as well, ascorbic acid volume, seed volume, seed aging time, pH and time of synthesis. We characterized these GNRs by various analytical techniques. This comprehensive study provides a thorough insight into GNR synthesis, specifies the role of every process factor, and helps control particular parameters to synthesize GNRs of desired specifications for a wide range of applications.

3.2. Method

We synthesized GNRs by using the chemical method of synthesis, which is the seed-mediated growth method (Fig. 3.1), elaborated in Chapter 2, section 2.2.1, and optimized various factors responsible for controlling the size, shape and stability of GNRs based on the LSPR spectrum and zeta potential. The experiments were done by varying one factor at a time, keeping other factors constant.

3.2.1. Effect of gold precursor concentration

We first varied the concentration of gold precursor ($HAuCl_4.3H_2O$) and saw its effect on the LSPR spectrum and zeta potential of the GNRs. Specifically, we assessed six different concentrations, i.e. 0.25 mM, 0.5 mM, 1 mM, 2 mM, 4 mM and 8 mM.

3.2.2. Effect of CTAB concentration

Next, we varied the concentration of CTAB and saw its effect on the LSPR spectrum and zeta potential of the GNRs. Specifically, we assessed two different concentrations i.e. 0.1 M and 0.2 M. We have also recorded TEM images of GNRs at these two concentrations.

3.2.3. Effect of $AgNO_3$ concentration and volume

Silver nitrate plays a crucial in the synthesis of GNRs. We varied $AgNO_3$ concentration from 2 mM to 10 mM with a difference of 2 mM and analyzed its effect on the LSPR spectrum and zeta potential of the GNRs. Further, at 4 mM $AgNO_3$ concentration, we varied its volume. The volumes were 100, 150, 200, 250 and 300 µl. This was assessed on the basis of the LSPR spectrum and zeta potential analysis.

3.2.4. Effect of ascorbic acid

The effect of ascorbic acid on the synthesis of GNRs was studied by varying its volume. The volumes were 65, 70, 75, 80 and 85 µl. At all these volumes, the LSPR spectrum and zeta potential of GNRs were recorded.

3.2.5. Effect of seed

Firstly, we evaluated the effect of seed aging time on the synthesis of GNRs by varying it at five different time points, i.e. 5 min, 15 min, 30 min, 45 min and 1 hr. We recorded the LSPR spectrum and zeta potential data at all the time points. Finally, we have assessed the effect of seed volume (6, 12, 18, 24 and 30 µl) on GNR synthesis on the basis of LSPR spectrum and zeta potential analysis.

3.2.6. Effect of pH

The pH was varied from 2 to 11 to study its effect on GNR synthesis. Its effect was also assessed on the basis of LSPR spectrum and zeta potential analysis.

3.2.7. Effect of time

Lastly, the effect of time was evaluated on the synthesis of GNRs. The time points were 30 min, 1, 2, 4, 6, 8, 10, 12, 14, 16, 18, 20, 22 and 24 hr. At all the time points, LSPR spectrum and zeta potential data were recorded.

3.2.8. Characterization of GNRs

GNRs synthesized with the final optimized values of the synthesis process were characterized for their LSPR spectrum by UV-visible spectroscopy, zeta potential by particle size analyzer, the morphology by HRTEM, elemental analysis by EDX using HRTEM and by XPS, elemental mapping by STEM, crystalline nature by SAED using HRTEM and by XRD and the functional groups by FTIR. The technical details of the analytical techniques are provided in Chapter 2, section 2.2.5.

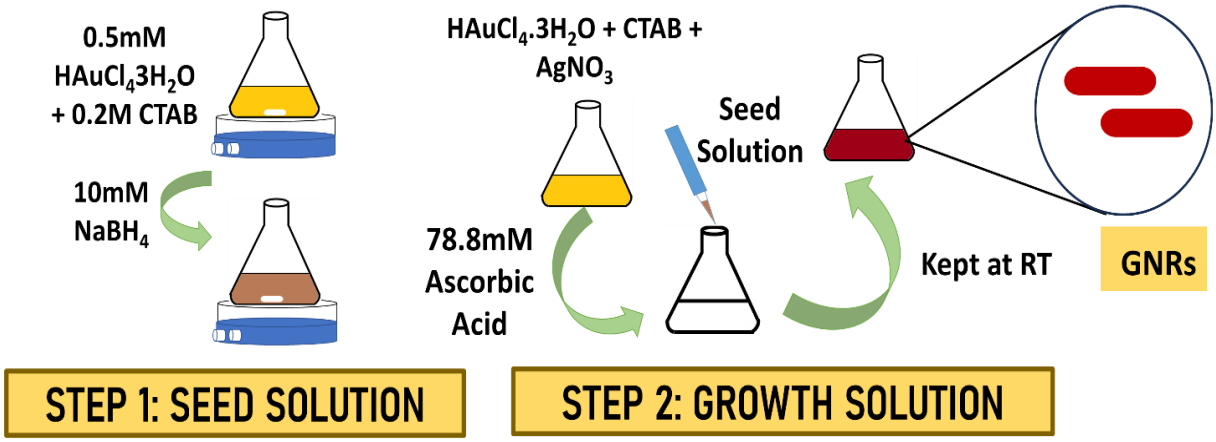

Figure 3.1 Schematics of synthesis of GNRs by seed-mediated growth method

3.3. Results and discussion

The process parameters of GNRs were studied so that control over the size and shape of GNRs could be achieved. This helped us in further surface functionalization of GNRs for bioimaging and biosensing purposes.

3.3.1. Seed solution analysis

We have synthesized small-sized gold nanoseeds (3-5 nm) (Cheng et al., 2011) for the synthesis of gold nanorods. This was confirmed by its brown color and a slight bump around 477 nm was observed in the UV-visible spectrum of gold nanoseeds (Fig. 3.2). The absence of a sharp peak in the UV-visible spectrum itself signifies that the size of gold nanoseeds was very small. Our results corroborated with the other studies (Hue et al., 2021; Nikoobakht & El-Sayed, 2003; N. Thomas & Mani, 2016; Watt et al., 2015). However, the expansion of the plasmon band of the nanoseeds were due to their size being smaller than the mean free path of 'free' electrons (Hue et al., 2021).

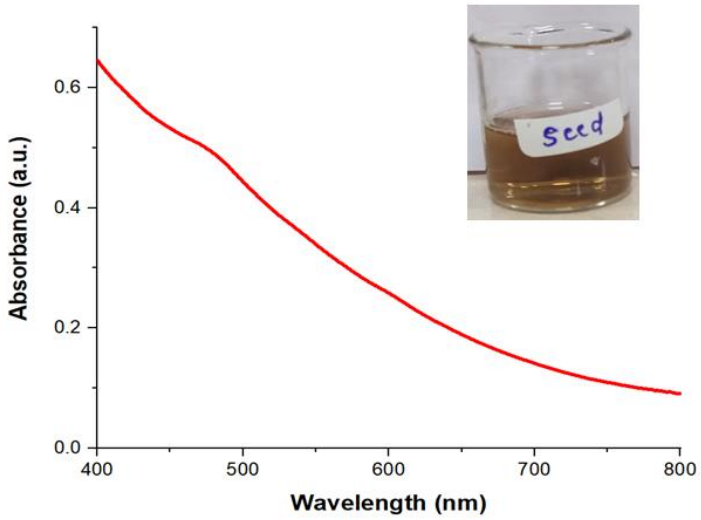

Figure 3.2 UV-visible spectrum of gold nanoseeds

3.3.2. Effect of gold precursor concentration

Gold precursor concentration is the major factor in controlling the size and morphology of GNRs. It was found that at 0.25 and 0.5 mM, the particles were formed, but it was not of proper rod shape because there was no appearance of well-differentiated transverse and longitudinal SPR bands. However, at 1 mM, a well-defined LSPR spectrum of the rod was obtained with the longitudinal plasmon wavelength (LPW) around 750 nm. Interestingly, as the concentration increased, the longitudinal SPR band blue shifted, and finally, at 8 mM, we found only one SPR band, which signifies the formation of spherical gold nanoparticles (Fig. 3.3) (Table 3.1). Boyne et al. also observed that with the increase in the concentration of $HAuCl_4.3H_2O$, the plasmonic band was blue-shifted. Similar trends were found in our analysis after 1 mM concentration (Boyne et al., 2016). Further, the zeta potential (ANOVA p-value = 0.035) exhibited significant change on varying the gold precursor concentration. However, it was noted that zeta potential was above +40 mV for GNRs synthesized at all the concentrations of $HAuCl_4.3H_2O$ (Fig. 3.4) (Table 3.1). This confirms that GNRs had good electrostatic stability (Bhattacharjee, 2016; Honary & Zahir, 2013). Finally, we have finalized 1 mM $HAuCl_4.3H_2O$ concentration for the synthesis of GNRs.

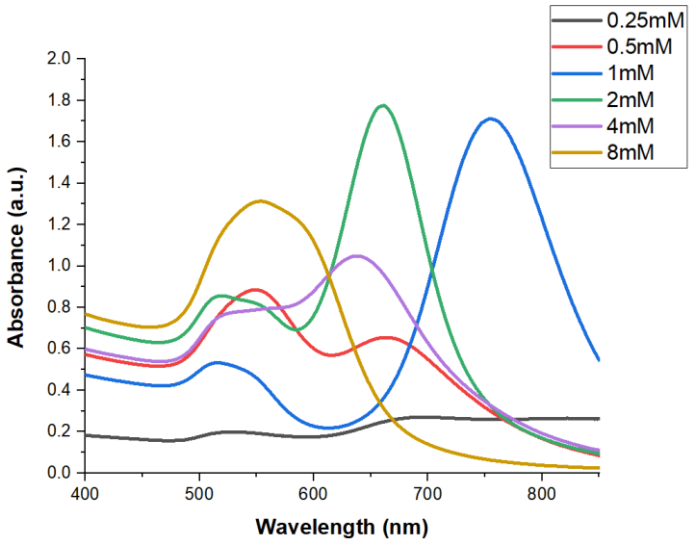

Figure 3.3 UV-visible spectra of GNRs at different concentrations of gold precursor ($HAuCl_4.3H_2O$)

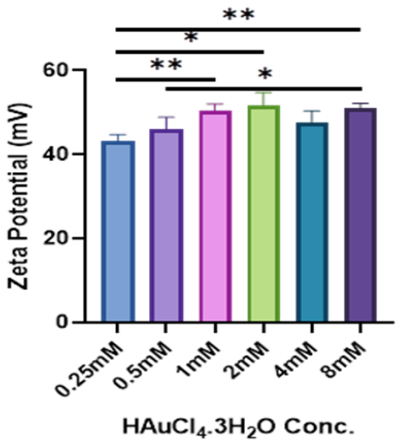

Figure 3.4 Effect of gold precursor ($HAuCl_4.3H_2O$) concentrations on zeta potential of GNRs

Table 3.1 LPW and zeta potential of GNRs at different concentrations of gold precursor ($HAuCl_4.3H_2O$)

Gold Precursor Concentration (mM)	LPW (nm)	Zeta Potential (mV)
0.25	Absorbance very less	43.08 ± 1.64
0.5	664 (absorbance very less) ± 4	46.09 ± 2.75
1	754.33 ± 5.03	50.35 ± 1.74

2	660.33 ± 3.78	51.76 ± 3
4	639.66 ± 4.16	47.72 ± 2.66
8	No Peak	51.11 ± 1.11

3.3.3. Effect of CTAB concentration

On varying CTAB concentrations, well-defined longitudinal and transverse SPR bands were found in the UV-visible spectra. But the transverse band was found around 527 nm at 0.1 M CTAB concentration, which proves the presence of spherical gold nanoparticles along with rods (Fig. 3.5). However, the longitudinal band of GNRs at 0.1 M concentration of CTAB was at a significantly lower wavelength compared to the longitudinal SPR band of GNRs at 0.2 M concentration (Table 3.2). The p-value on performing an unpaired t-test was found to be <0.0001 (Fig. 3.6a). Further, on TEM analysis it was confirmed that GNRs synthesized at 0.1 M CTAB concentration contain more spherical gold nanoparticles as compared to GNRs synthesized at 0.2 M CTAB concentration (Fig. 3.7). The zeta potential analysis confers the stability of GNRs at both concentrations of CTAB (Table 3.2). Based on an unpaired t-test, there was a non-significant difference (p-value = 0.5165) between the zeta potential of GNRs synthesized at 0.1 M and 0.2 M CTAB concentrations (Fig. 3.6b). Thus, 0.2 M CTAB concentration was finalized for GNR synthesis.

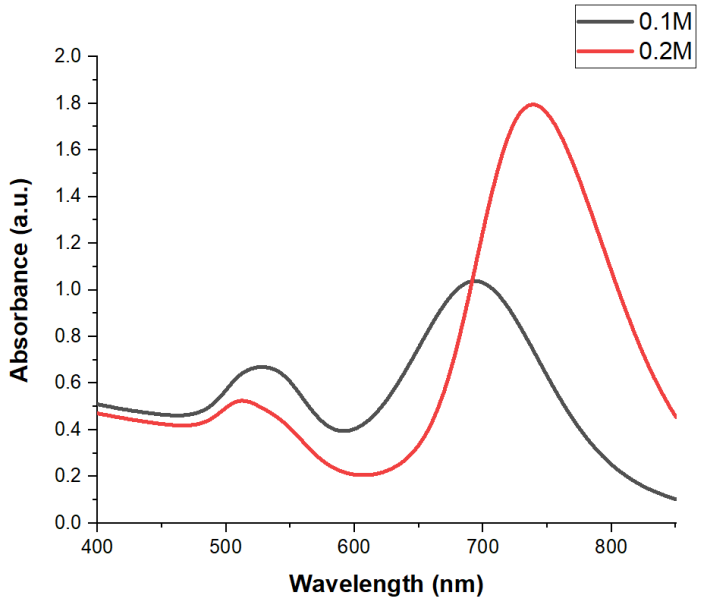

Figure 3.5 UV-visible spectra of GNRs at different concentrations of CTAB

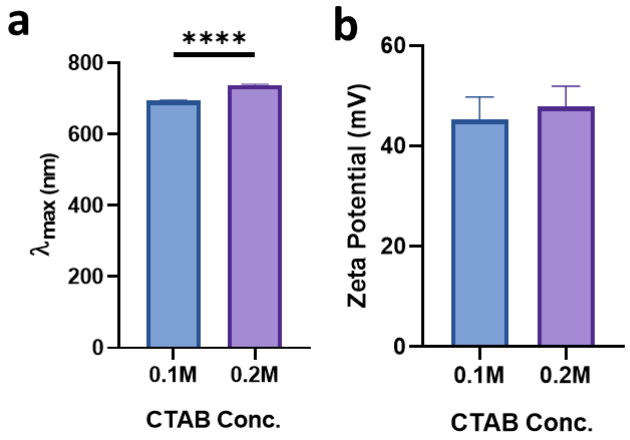

Figure 3.6 Effect of CTAB concentrations on a) LPW and b) zeta potential of GNRs

Table 3.2 LPW and zeta potential of GNRs at different concentrations of CTAB

CTAB Concentration (M)	LPW (nm)	Zeta Potential (mV)
0.1	694.66 ± 1.52	45.29 ± 4.48
0.2	739 ± 2	47.8 ± 4.14

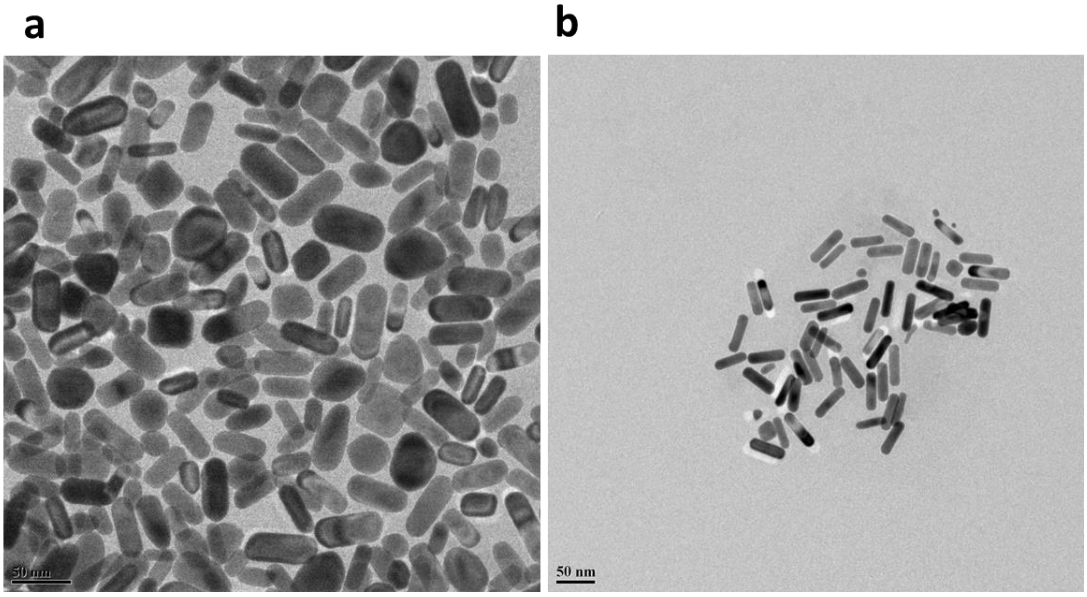

Figure 3.7 TEM image of GNRs at a) 0.1 M CTAB and b) 0.2 M CTAB

3.3.4. Effect of $AgNO_3$ concentration and volume

Silver ions hold a very crucial role in the formation and controlling growth of GNRs. Silver ions combine with the bromine of CTAB to form AgBr, which favorably deposits on lateral faces (110) of GNRs and prevents the deposition of gold there, so the gold deposits on another face (100), resulting in the formation of rod morphology (X. Huang et al., 2009; Khan et al., 2021; Rizwan Younis et al., 2021; Scarabelli et al., 2015; Zhou et al., 2017). Here, when $AgNO_3$ concentration was varied, the maximum LPW was observed at 4 mM concentration. However, there was an increase in the size of GNRs as the concentration of silver increased, but up to a certain limit after that, the size decreased, which was confirmed by the blue shift in LPW from 6 mM concentration (Fig. 3.8a) (Table 3.3). This finding was corroborated by the results of another study, where it was observed that as the concentration of silver ions increases, the size of GNRs also increases, but up to a certain limit after that, the trend reverses (Nikoobakht & El-Sayed, 2003). Based on statistical analysis, it was found that $AgNO_3$ concentration significantly affected the LPW (ANOVA p-value = <0.0001) of GNRs (Fig. 3.9a), but it had a non-significant effect on zeta potential (ANOVA p-value = 0.3707) of GNRs. Also, the zeta potential of GNRs at every concentration of $AgNO_3$ was above +40 mV (Fig. 3.9b) (Table 3.3). Finally, 4 mM $AgNO_3$ concentration was optimized for GNR synthesis.

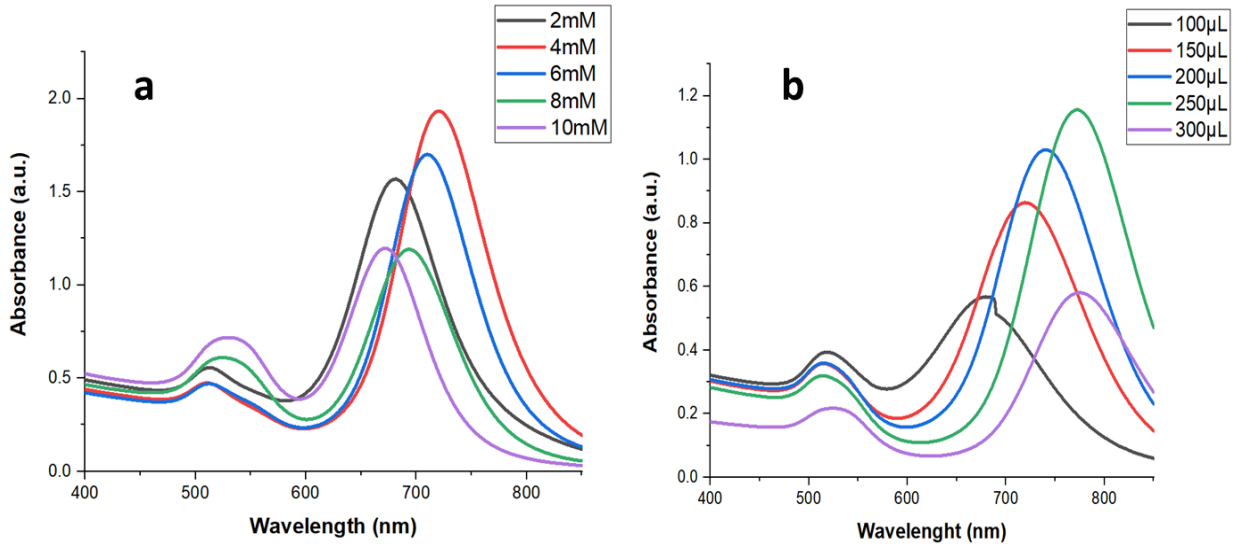

Figure 3.8 UV-visible spectra of GNRs at different a) concentrations of $AgNO_3$ and b) volumes of 4 mM $AgNO_3$

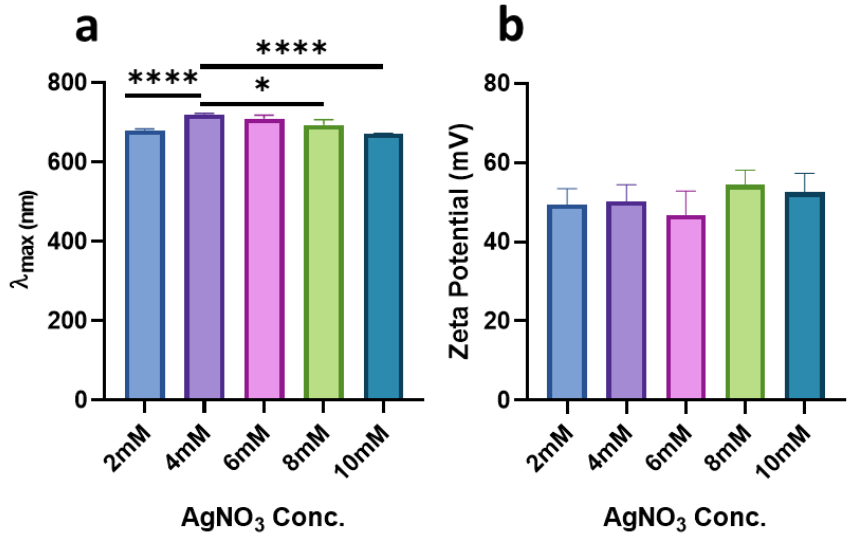

Figure 3.9 Effect of $AgNO_3$ concentrations on a) LPW and b) zeta potential of GNRs

Table 3.3 LPW and zeta potential of GNRs at different concentrations of $AgNO_3$

$AgNO_3$ Concentration (mM)	LPW (nm)	Zeta Potential (mV)
2	680.33 ± 3.78	49.45 ± 3.97
4	720.33 ± 2.30	50.25 ± 4.15
6	710 ± 8.88	46.81 ± 6.02
8	694 ± 13.07	54.34 ± 3.77
10	671.33 ± 0.57	52.59 ± 4.69

Further, at 4 mM $AgNO_3$, when its volume was varied, it was found that the LPW red-shifted with the increase in the volume of $AgNO_3$ up to 250 µl. However, after that, there was a non-significant change in the LPW of GNRs at 300 µl $AgNO_3$. This increase in LPW means the size of GNRs was increased as the volume of $AgNO_3$ was increased (Fig. 3.8b) (Table 3.4). Also, based on the statistical analysis, it was found that $AgNO_3$ volume significantly affects the LPW (ANOVA p-value = <0.0001) of GNRs (Fig. 3.10a), but it had a non-significant effect on zeta potential (ANOVA p-value = 0.6345) of GNRs. Also, the zeta potential of GNRs at every

volume of $AgNO_3$ was above +35 mV (Fig. 3.10b) (Table 3.4). Finally, 250 µl $AgNO_3$ was finalized for GNR synthesis.

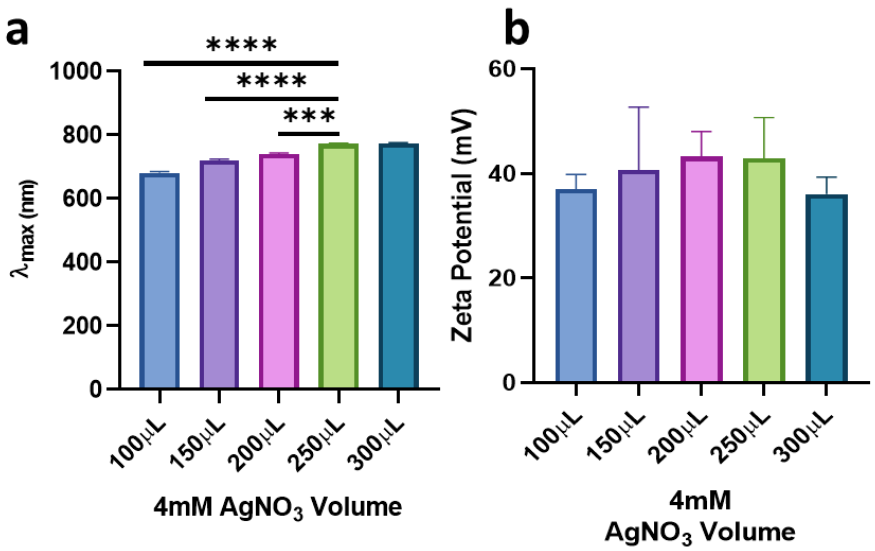

Figure 3.10 Effect of $AgNO_3$ volumes on a) LPW and b) zeta potential of GNRs

Table 3.4 LPW and zeta potential of GNRs at different volumes of $AgNO_3$

$AgNO_3$ Volume (µL)	LPW (nm)	Zeta Potential (mV)
100	681.33 ± 4.16	37.08 ± 2.74
150	720.33 ± 5.03	40.66 ± 12.07
200	740.66 ± 2.51	43.26 ± 4.81
250	772.33 ± 2.51	42.91 ± 7.79
300	774.33 ± 1.52	36.06 ± 3.25

3.3.5. Effect of ascorbic acid volume

On varying the ascorbic acid volume, maximum LPW was observed at 75 µl. Although, there was no particular trend of change in LPW on changing the volume of ascorbic acid (Table 3.5). Interestingly, it was observed that as the volume of ascorbic acid increased, the absorbance of the longitudinal SPR band of GNRs also increased (Fig. 3.11). This was also observed by John et. al. in their study (John et al., 2013). This parameter significantly (ANOVA p-value =

<0.0001) affects the LPW of GNRs (Fig. 3.12a). The zeta potential study at different volumes of ascorbic acid showed that GNRs synthesized at all the volumes possess zeta potential above +40 mV (Table 3.5). Thus, this parameter had a non-significant (ANOVA p-value = 0.1218) effect on the zeta potential of GNRs (Fig. 3.12b). Finally, 75 µl ascorbic acid was selected for the synthesis of GNRs.

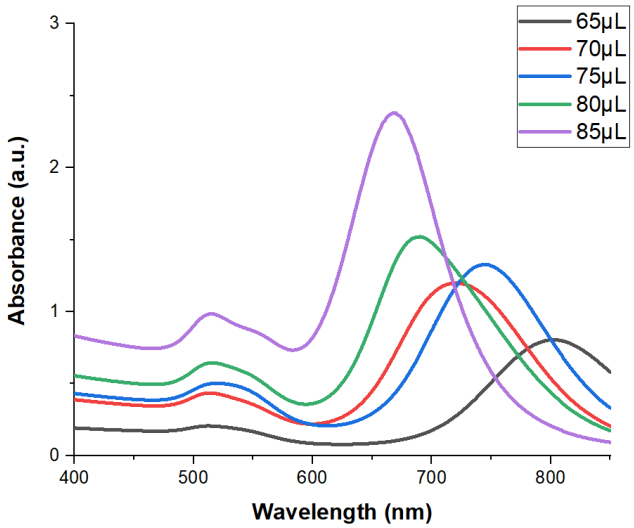

Figure 3.11 UV-visible spectra of GNRs at different volumes of ascorbic acid

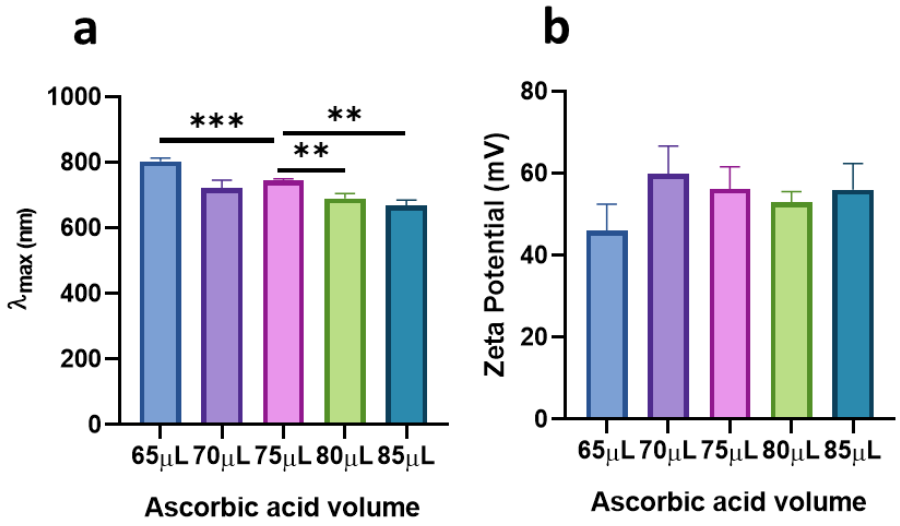

Figure 3.12 Effect of ascorbic acid volumes on a) LPW and b) zeta potential of GNRs

Table 3.5 LPW and zeta potential of GNRs at different volumes of ascorbic acid

Ascorbic Acid Volume (µL)	LPW (nm)	Zeta Potential (mV)
65	802.66 ± 10.26	46.05 ± 6.44
70	720.33 ± 24.58	59.74 ± 6.86
75	744.66 ± 4.93	56.14 ± 5.42
80	690 ± 14.79	52.86 ± 2.60
85	668 ± 16.52	55.93 ± 6.46

3.3.6. Effect of seed

The amount of seed is the major factor in controlling the size of GNRs. In many studies, it was found that as the concentration of seed increases, the aspect ratio of GNRs decreases, leading to shorter GNRs (Sau & Murphy, 2004; Smitha et al., 2013). Herein, contrarily, on varying the seed volume, it was observed that there was an increase in LPW after 6 µl seed volume. However, from 12-30 µl the LPW did not have too much difference (Fig. 3.13) (Table 3.6). It was confirmed by statistical unpaired t-test also, a non-significant difference was observed between the LPW of GNRs synthesized at 12-30 µl seed volume. Also, based on ANOVA (p-value = 0.0004), this parameter significantly affects the LPW of GNRs (Fig. 3.14a) while it had a non-significant (p-value = 0.1110) effect on the zeta potential of GNRs (Fig. 3.14b). However, at all the seed volumes, the zeta potential confirms the good stability of GNRs (Table 3.6). Additionally, it was also observed that with the increase in seed volume, there was a decrease in the absorbance of the longitudinal plasmon band of GNRs (Fig 3.13), which signifies a decrease in the yield of GNRs with the increasing volume of seed. The 12 µl seed volume was optimized for the synthesis of GNRs.

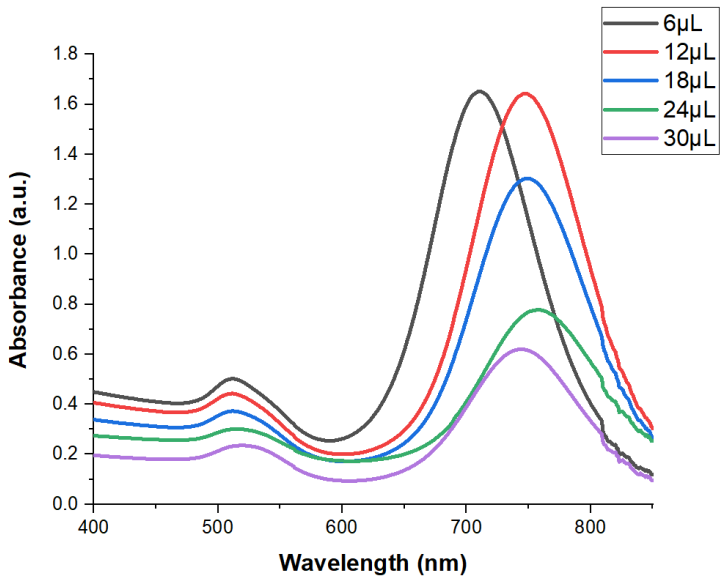

Figure 3.13 UV-visible spectra of GNRs at different volumes of seed

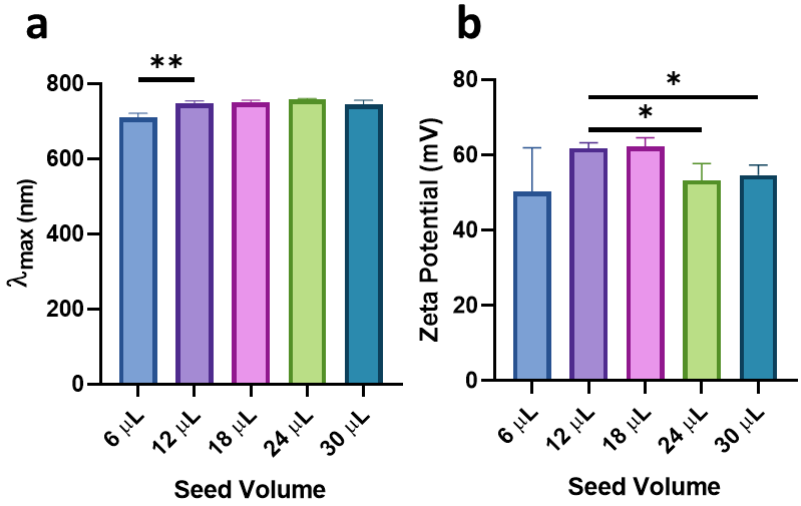

Figure 3.14 Effect of seed volumes on a) LPW and b) zeta potential of GNRs

Table 3.6 LPW and zeta potential of GNRs at different volumes of seed

Seed Volume (µL)	LPW (nm)	Zeta Potential (mV)
6	710 ± 11.26	50.2 ± 11.68
12	747 ± 6.55	61.76 ± 1.45
18	749 ± 6.24	62.16 ± 2.37

24	757.66 ± 2.51	53.24 ± 4.44
30	743.33 ± 11.93	54.65 ± 2.67

The effect of seed aging time on the LPW and zeta potential of GNRs was also evaluated. However, this parameter does not show a significant effect on LPW (ANOVA p-value = 0.4223) (Fig. 3.16b) and zeta potential (ANOVA p-value = 0.4371) (Fig. 3.16b) of GNRs. The LPW of GNRs at every seed aging time point did not vary much (Fig. 3.15) although, the 30 min seed aging time was optimized because the LPW was maximum at that point (Table 3.7). Also, the zeta potential of GNRs at every time point was very stable (Avg. = >+40 mV) (Table 3.7).

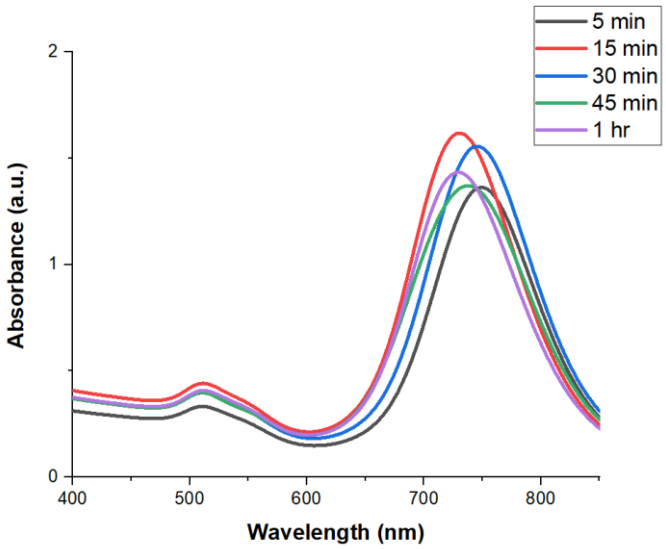

Figure 3.15 UV-visible spectra of GNRs at different seed aging time

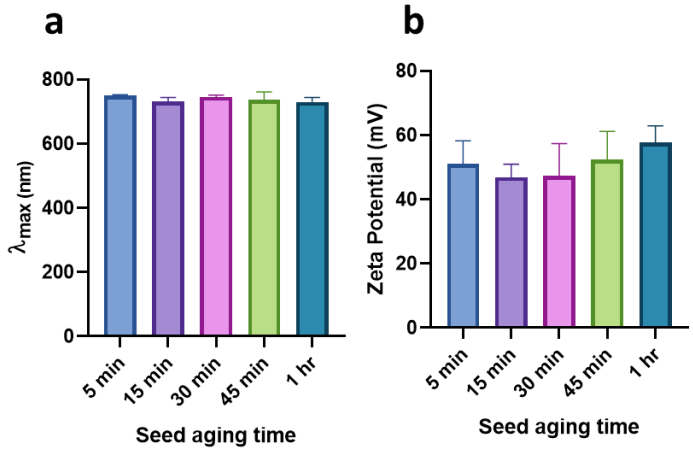

Figure 3.16 Effect of seed aging time on a) LPW and b) zeta potential of GNRs

Table 3.7 LPW and zeta potential of GNRs at different seed aging time

Seed Aging Time	LPW (nm)	Zeta Potential (mV)
5 min	749.33 ± 3.78	51.04 ± 7.19
15 min	730.66 ± 13.20	46.87 ± 4.07
30 min	745.33 ± 6.42	47.38 ± 9.97
45 min	736.66 ± 24.14	52.29 ± 8.84
1 hr	730 ± 14	57.61 ± 5.27

3.3.7. Effect of pH

pH is a very important factor for the synthesis of GNRs, as ascorbic acid reduction potential is low in acidic pH while it is high in basic conditions. Thus, the low reduction potential of ascorbic acid is vital in rod formation (Scarabelli et al., 2015). The pH above 6.6 does not support rod formation (Koeppl et al., 2011). Also, at basic pH, CTAB molecules get desorbed from the gold surface (Cheng et al., 2011). Herein, we have comprehensively studied the effect of a wide pH range on the synthesis of GNRs. In various studies, it was found that with the decrease in pH, the aspect ratio of GNRs increases (Cheng et al., 2011; Ye et al., 2013). A similar trend was observed in our study too. However, after pH 6, the longitudinal and transverse SPR bands of GNRs started merging and finally, at 11 pH, we observed only a single SPR band (Fig. 3.17) (Table 3.8). This was corroborated by the findings of Cheng et al. (Cheng et al., 2011). Further, on statistical analysis, it was also found that pH significantly affects the LPW (ANOVA p-value = <0.0001) (Fig 3.18a) and zeta potential (ANOVA p-value = 0.0334) (Fig. 3.18a) of the GNRs. Although the zeta potential of GNRs was above +40 mV at every pH (Fig. 3.18b) (Table 3.8). Notably, there was no significant difference in the LPW of GNRs at pH 2 and 3, but the absorbance of the longitudinal band was low at pH 2. Thus, pH 3 was optimized for the synthesis of GNRs.

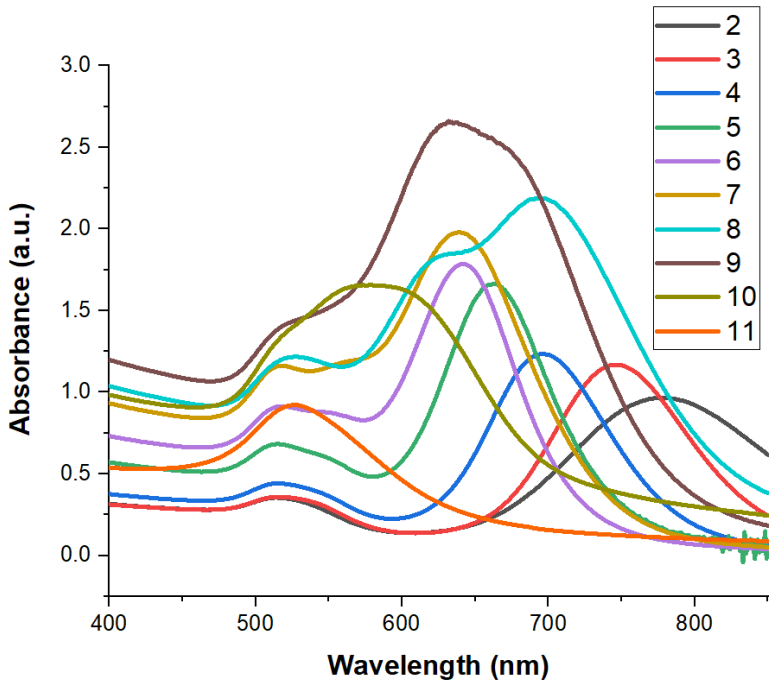

Figure 3.17 UV-visible spectra of GNRs at different pH

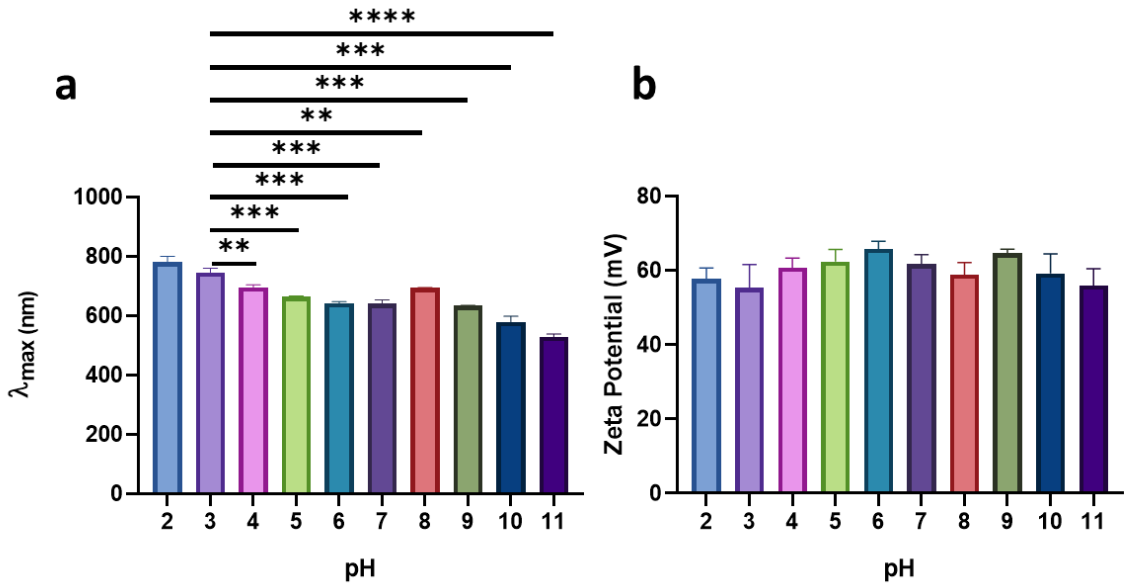

Figure 3.18 Effect of pH on a) LPW and b) zeta potential of GNRs

Table 3.8 LPW and zeta potential of GNRs at different pH

pH	LPW (nm)	Zeta Potential (mV)
2	779.66 ± 20.03	57.72 ± 2.93

3	745.33 ± 14.29	55.31 ± 6.24
4	695.66 ± 8.02	60.67 ± 2.64
5	664 ± 2.64	62.35 ± 3.28
6	641.33 ± 5.85	65.76 ± 2.07
7	639.66 ± 13.27	61.66 ± 2.56
8	694 ± 1	58.85 ± 3.26
9	632.66 ± 2.08	64.55 ± 1.16
10	No LPW Peak	59.17 ± 5.26
11	No LPW Peak	55.91 ± 4.49

3.3.8. Effect of time

The time of synthesis of GNRs also plays a role in their synthesis. It was observed that with the increase in time, there was a decrease in LPW of GNRs, but it was significant from the 8hr time point (Fig. 3.19) (Table 3.9). However, this parameter significantly affects the LPW (ANOVA p-value = 0.0043) of GNRs. But, based on an unpaired t-test, it was found that till 8 hr, there was no significant change in the LPW of GNRs synthesized at different time intervals (Fig. 3.20a). Further, the time of synthesis had an insignificant effect on the zeta potential (ANOVA p-value = 0.2652) of the GNRs (Fig. 3.20b). At every time point, the zeta potential of GNRs was found to be very stable (Table 3.9). As the synthesis of well-defined gold nanorods was observed at 2 hr, so it was finalized as the time of synthesis of GNRs.

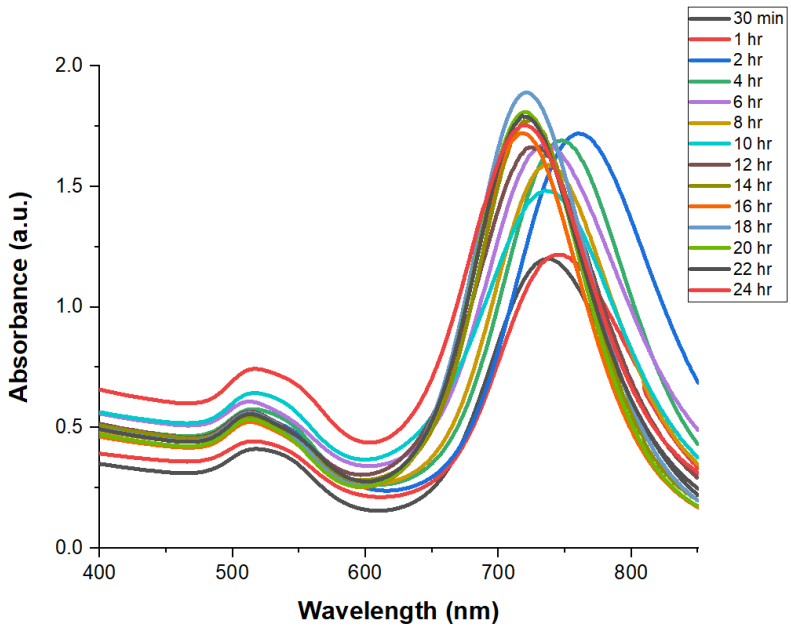

Figure 3.19 UV-visible spectra of GNRs at different time intervals

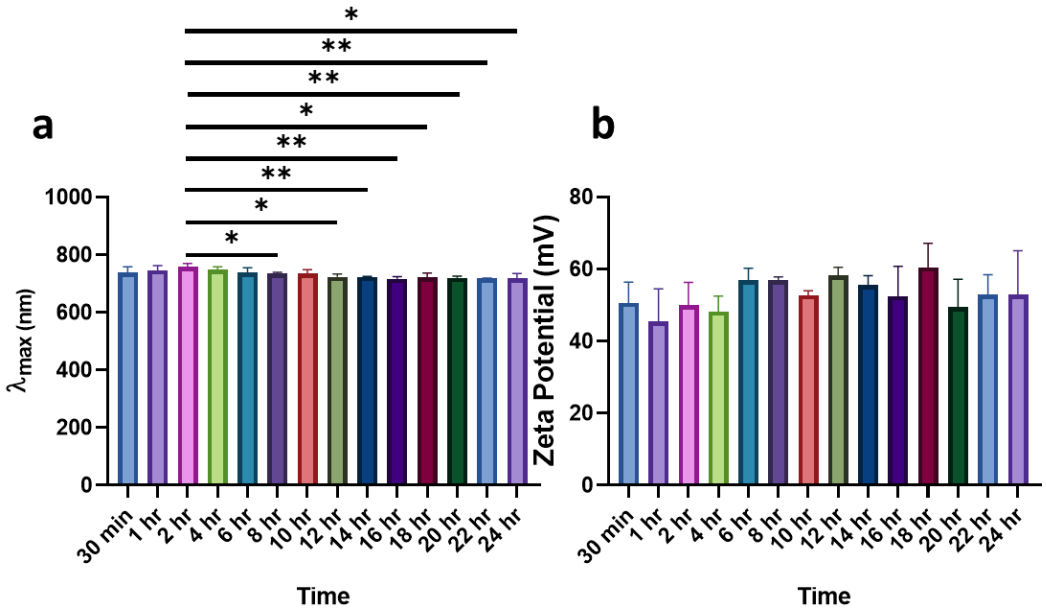

Figure 3.20 Effect of time on a) LPW and b) zeta potential of GNRs

Table 3.9 LPW and zeta potential of GNRs at different time intervals

Time	LPW (nm)	Zeta Potential (mV)
30 min	738 ± 20.29	50.6 ± 5.79
1 hr	746.66 ± 16.74	45.45 ± 9.03

2 hr	759 ± 11.35	49.98 ± 6.29
4 hr	747.66 ± 11.50	48.26 ± 4.25
6 hr	737.66 ± 18.17	56.88 ± 3.38
8 hr	735.66 ± 4.04	56.8 ± 1.05
10 hr	734.66 ± 14.04	52.66 ± 1.32
12 hr	723.66 ± 9.84	58.21 ± 2.30
14 hr	723.66 ± 1.52	55.49 ± 2.64
16 hr	717.33 ± 7.50	52.4 ± 8.36
18 hr	722 ± 14.93	60.41 ± 6.77
20 hr	720.66 ± 6.42	49.43 ± 7.73
22 hr	718.33 ± 1.52	52.9 ± 5.55
24 hr	718 ± 17.34	52.84 ± 12.25

3.3.9. Characterization of GNRs

At the final optimized values of the synthesis process of GNRs, they were synthesized and extensively characterized by various techniques.

3.3.9.1. UV-visible-NIR spectroscopy and zeta potential analysis

The synthesized GNRs capped with CTAB had a longitudinal SPR band around 751 nm, which was in the NIR region, and a transverse SPR band around 511 nm (Fig. 3.21). This finding was in line with the findings of Nikoobakth & El-Sayed (Nikoobakht & El-Sayed, 2003). The longitudinal SPR band was in the NIR region, which makes GNRs ideal for bioimaging applications as well as the band was sensitive to the change in the refractive index of the medium, thus, these GNRs can also be employed for biosensing applications. The zeta potential of GNRs was found to be +49.98 ± 6.29 mV (Fig. 3.22). The positive charge was due to the CTAB capping on their surface. This was supported by the findings of other studies also (J. He et al., 2018; Toh et al., 2013).

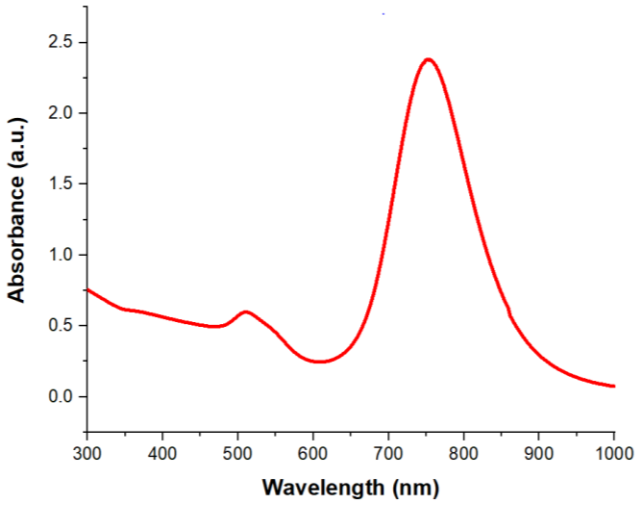

Figure 3.21 UV-visible-NIR spectrum of GNRs

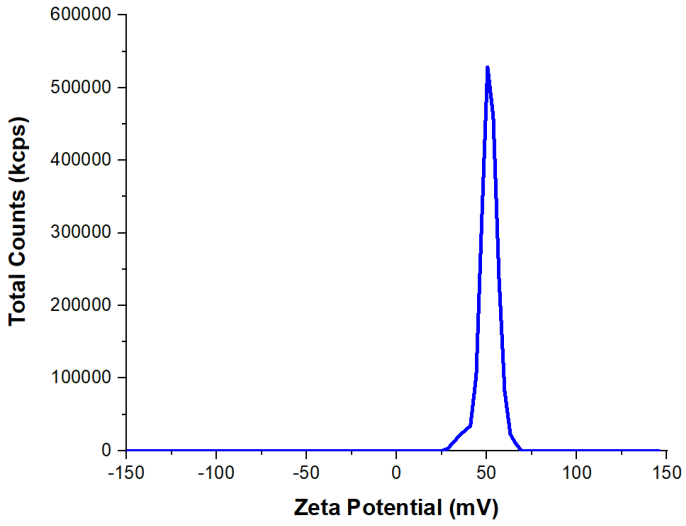

Figure 3.22 Zeta potential of GNRs

3.3.9.2. Electron microscopy analysis

The size of GNRs based on HRTEM investigation was found to be 41.72 ± 5 nm x 11 ± 2 nm (Fig. 3.23a). The FESEM investigation also supported the HRTEM data (Fig. 3.23b). The SAED pattern determined through HRTEM confirms the crystalline nature of the GNRs (Fig. 3.23c) (Anandhakumar et al., 2013; Kedawat et al., 2019). Further, the fringes were also recorded by the HRTEM analysis (Fig. 3.23d). The spacing between the fringes was found to be in accordance with the other studies (Si et al., 2012; J. Yin et al., 2017; L. Zhang et al., 2016). The d-spacing of GNRs was found to be 0.208 nm (Fig. 3.23d).

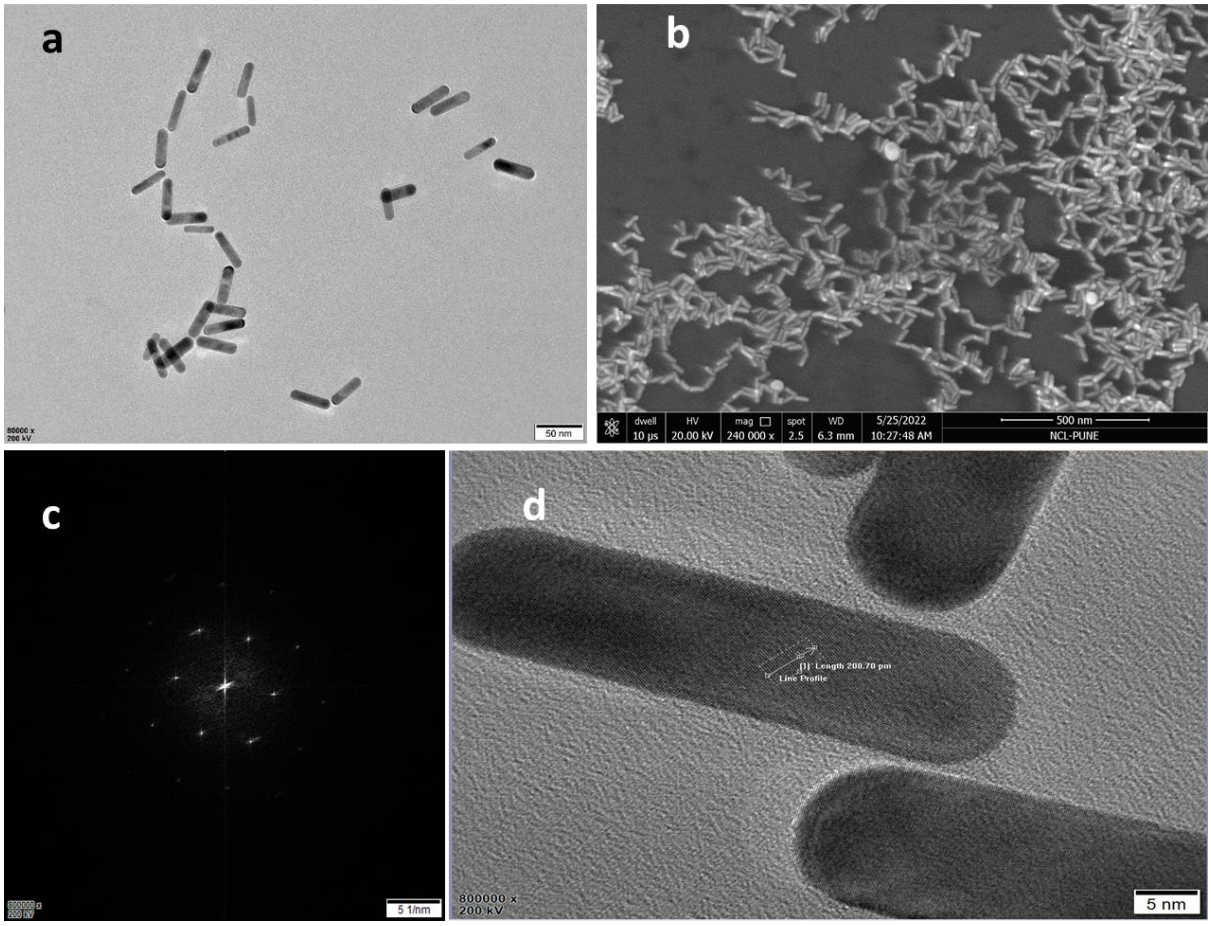

Figure 3.23 Electron microscopy analysis of GNRs a) HRTEM image, b) FESEM image, c) SAED pattern and d) fringes of GNRs

3.3.9.3. Elemental analysis

The EDX spectrum of GNRs recorded by HRTEM confirms the presence of elements gold (Au), carbon (C) and bromine (Br) (Fig. 3.24a). This was in accordance with the spectra of GNRs in other studies (Abareshi et al., 2021; Yan et al., 2016). Carbon and bromine were due to the CTAB on the surface of GNRs. However, the EDX spectrum was also acquired by using a concentrated sample of GNRs through FESEM. The EDX spectrum from FESEM also consists of oxygen (O) and nitrogen (N), which might be atmospheric and nitrogen was also due to the CTAB (Fig. 3.24b). Further, STEM mapping was also performed to analyze the elements present in GNRs (Fig. 3.25). It also supported the EDX spectrum.

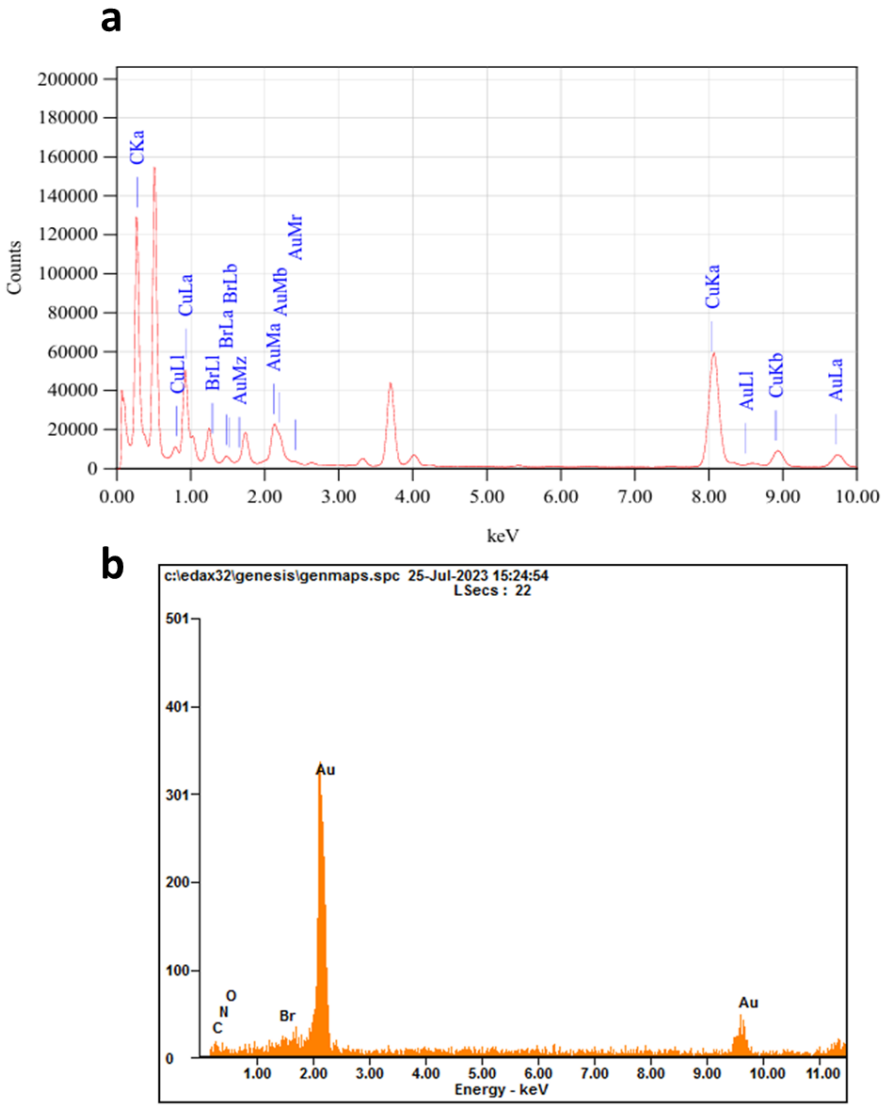

Figure 3.24 EDX spectra of GNRs a) from HRTEM and b) from FESEM

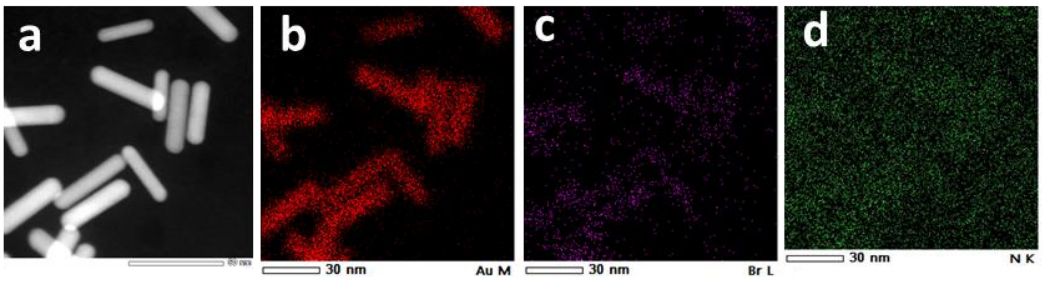

Figure 3.25 STEM mapping of GNRs a) STEM image, b) Au, c) Br and d) N

Further, the XPS analysis showed the peak around 83.98 eV and 87.68 eV corresponds to transitions Au $4f_{7/2}$ and Au $4f_{5/2}$ of Au^0 oxidation state, respectively (Fig. 3.26a, b) (L. Su et al., 2017). Additionally, the signal for Br 3d at 68.08 eV (Fig. 3.26a, c), Br 3p at 187.58 eV (Fig.

3.26a, d) Br 3s at 254.78 eV, C 1s at 285.08 eV and N 1s at 402.18 eV (Fig. 3.26a), was due to the presence of CTAB on the surface of GNRs (J. Cao et al., 2012; J. He et al., 2018; L. Su et al., 2017; Tao et al., 2018; Thierry et al., 2009).

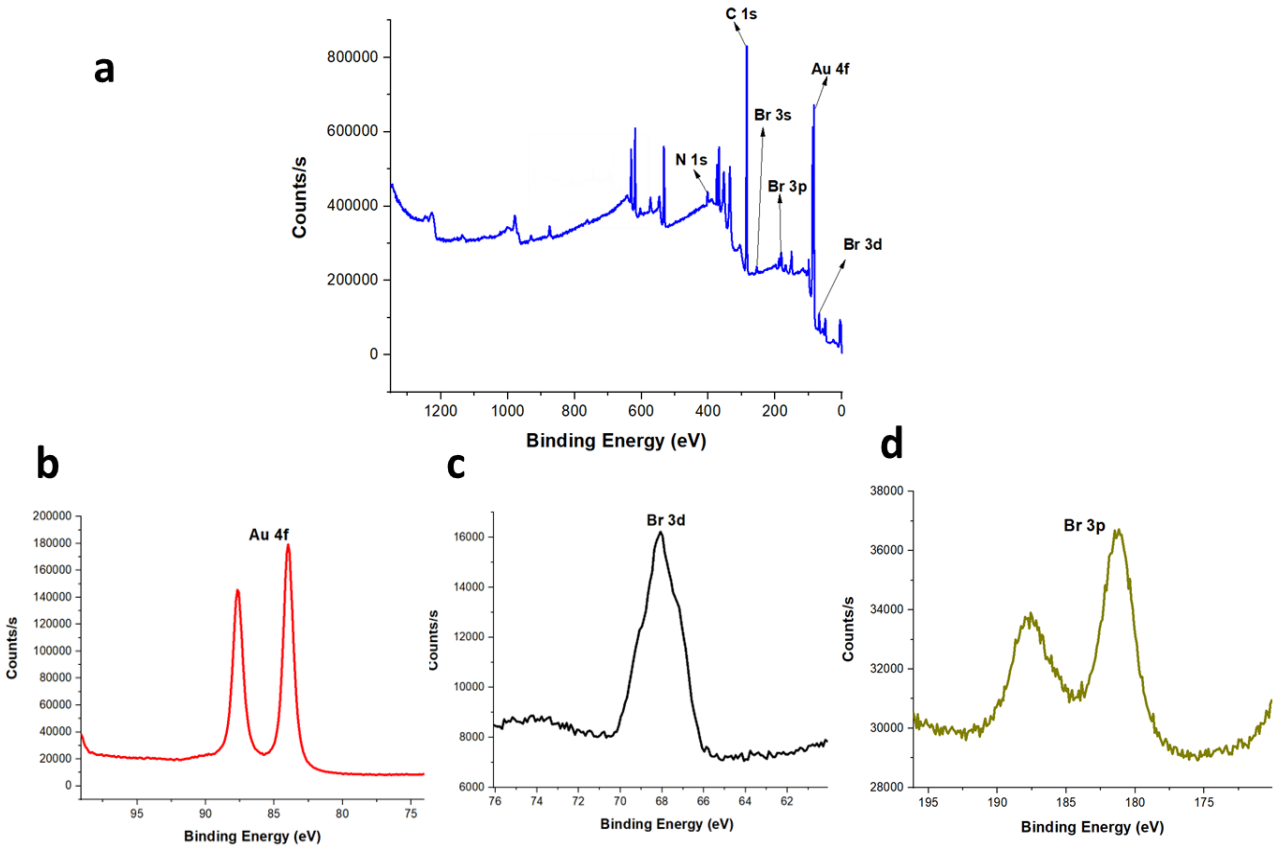

Figure 3.26 a) XPS spectrum of GNRs, b) XPS spectrum of Au 4f of GNRs, c) XPS spectrum of Br 3d of GNRs and d) XPS spectrum of Br 3p of GNRs

3.3.9.4. XRD analysis

The XRD pattern of GNRs is given in Figure 3.27. The peaks at 2Θ values 38.24°, 44.46°, 64.69° and 77.66° correspond to planes (111), (200), (220) and (311) respectively (Fig. 3.27). This was in agreement with the other reported findings (Abareshi et al., 2021; Marlinda et al., 2016; Yan et al., 2016).

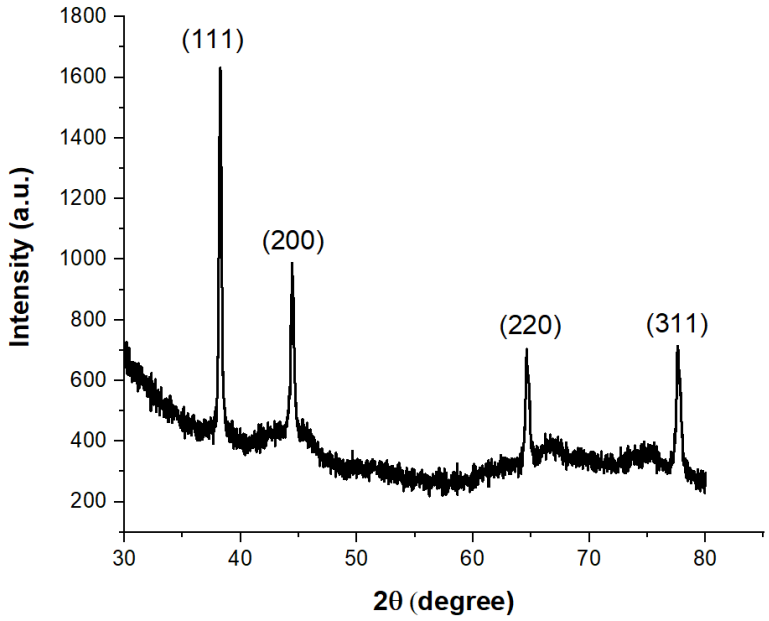

Figure 3.27 XRD spectrum of GNRs

3.3.9.5. FTIR analysis

The CTAB spectra showed strong symmetric and asymmetric C-H stretching at 2916 and 2849 cm^{-1} which was also preserved in the CTAB-coated GNRs at 2916 and 2853 cm^{-1}, but the intensity was reduced (Almada et al., 2017; J. He et al., 2018; Mehtala et al., 2014; G. Su et al., 2015), indicating the hydrophobic tail of CTAB was not interacting with GNRs (de Barros et al., 2016). The band around 1729 cm^{-1} in GNRs could be due to the carboxyl groups (G. Su et al., 2015). The peaks at 1484 and 1462 cm^{-1} in CTAB while the peak at 1469 cm^{-1} in GNRs were due to the C-H scissoring, which corresponds to the hydrocarbon tail of CTAB (Almada et al., 2017; de Barros et al., 2016; J. He et al., 2018; Mehtala et al., 2014). However, the intensity of the C-H scissoring peak was decreased in GNRs along with the shift compared to the CTAB. Further, the bands corresponding to $C\text{-}N^{+}$ stretching were at 962 and 910 cm^{-1} in CTAB (de Barros et al., 2016; J. He et al., 2018) which was shifted to 1021 cm^{-1} in GNRs (Hasannia et al., 2022), indicating CTAB was bound with the hydrophilic parts on the GNRs surface (de Barros et al., 2016). The peak around 1100 cm^{-1} in GNRs corresponds to C-O stretching (G. Su et al., 2015). The bending of more than 4 adjacent CH_2 groups was observed at 719 cm^{-1} in CTAB although it was shifted to 726 cm^{-1} in GNRs (Fig. 3.28) (Almada et al., 2017; de Barros et al., 2016; J. He et al., 2018; Mehtala et al., 2014).

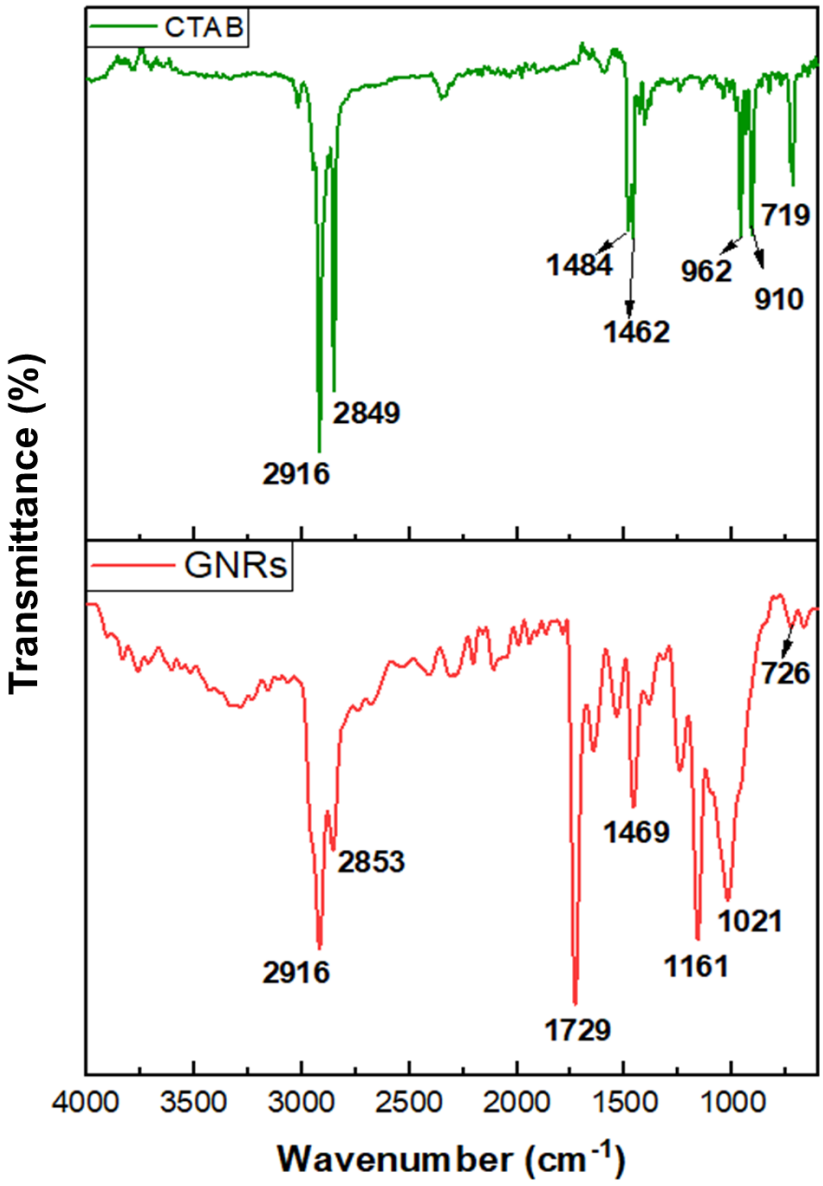

Figure 3.28 FTIR spectra of CTAB and GNRs

3.4. Conclusion

GNRs were widely synthesized by the seed-mediated growth method, and this study identifies the process parameter to synthesize GNRs for biosensing and bioimaging applications. 1 mM gold precursor concentration, 0.2 M CTAB, 250 µl $AgNO_3$ (4 mM), 75 µl ascorbic acid, and 12 µl seed aged for 30 minutes, were optimized to synthesize monodisperse and stable GNRs of aspect ratio around 3.8 in 2 hours at pH 3. Major factors that affect the synthesis of GNRs were found to be gold precursor concentration, CTAB concentration, silver nitrate concentration and its volume as well, ascorbic acid volume, seed

volume, and pH. However, synthesis time does not affect the synthesis process majorly and seed aging time showed an insignificant effect on the GNR synthesis process.

The analytical characterization techniques confirmed the synthesis of rod-shaped particles with transverse and longitudinal SPR bands having LPW in the NIR region and the zeta potential values tagged the particles with good stability. The HRTEM, FESEM, EDX, STEM mapping, XPS, XRD, and FTIR analysis corroborated the synthesis of CTAB-capped GNRs which comprise the crystalline structure. Thus, this study facilitates the synthesis of GNRs for biomedical or other applications by modulating the identified process parameters to attain the desired specifications.

CHAPTER 4

Optimization, Synthesis, and Characterization of MUA-modified GNRs (MUA-GNRs)

4.1. Introduction

GNRs synthesized by seed-mediated growth method consist of CTAB on their surface (J. Cao et al., 2012; Jain et al., 2019). However, CTAB is cytotoxic to most of the cells; thus, it cannot be used for biological applications (Azab et al.,2018; J. Cao et al., 2012; J. He et al., 2018; Jain et al., 2019; Shi et al., 2021; L. Su et al., 2017). Thus, it is necessary to remove or replace CTAB with other biocompatible substances to use GNRs for biological applications. Mainly, the free molecules of CTAB are toxic (J. Cao et al., 2012; L. Su et al., 2017), which are generally removed via centrifugation or dialysis still complete removal of CTAB is needed when the GNRs are intended to be used for sensing because it can impact the selectivity and sensitivity by interfering in the sensing process (Bao & Oluwafemi, 2023) and *in vivo* imaging or therapeutic applications (J. Cao et al., 2012; J. He et al., 2018). Additionally, the CTAB layer on the surface of GNRs averts facile functionalization with any ligands/ receptors required for biological studies (J. He et al., 2018).

We aspired to use GNRs for biosensing and bioimaging applications, so the CTAB layer on their surface needed to be replaced with the other biocompatible molecule. Herein, we have used alkanethiol ligand, i.e. 11- mercaptoundecaonic acid (11-MUA), to replace CTAB from the surface of GNRs by ligand exchange method (J. Cao et al., 2012; Shi et al., 2021; L. Su et al., 2017; J. Zhou et al., 2017). 11-MUA is a smaller molecule consisting of –SH at one end and –COOH group at another end. The -COOH group can be activated further with NHS–EDC carbodiimide reaction to covalently attach biological entities onto the surface of GNRs (J. Cao et al., 2012; H. Huang et al., 2012; Shi et al., 2021; Yüce & Kurt, 2017) and it is the most widely used molecule to replace CTAB on the surface of GNRs which provides good colloidal stability (Guerrini et al., 2018) and biocompatibility (Jain et al., 2019) to nanoparticles. The thiol group has an inherently stronger affinity for noble metals such as silver and gold. Therefore, the thiol group-containing molecules were explored to form a self-assembled monolayer (SAM) on the surface of gold nanoparticles (J. Cao et al., 2012; H. Huang et al., 2012; L. Su et al., 2017; Yüce & Kurt, 2017).

In this study, we optimized the process parameters of surface modification of GNRs with 11-MUA for its further functionalization for biosensing and bioimaging applications. Initially, we assessed the effect of solvents used to dissolve 11-MUA on the surface modification of GNRs. Further, we optimized the parameters like 11-MUA volume, time and stirring speed, which should be applied to modify the surface of GNRs based on the red shift in the LPW and zeta

potential evaluation. Finally, the 11-MUA modified GNRs were characterized as well as the modification was validated by various analytical techniques. This study allows us to examine the effects of different factors on the surface modification of GNRs with 11-MUA.

4.2. Method

The previously synthesized GNRs were surface-modified with 11-MUA by the protocol mentioned in section 2.2.2 of Chapter 2. We assessed the effect of the solvent used to dissolve 11-MUA on the surface modification of CTAB-GNRs. Further, the volume of 11-MUA, stirring speed and time were optimized.

4.2.1. Optimization of solvent

We varied the solvents used to dissolve 11-MUA and how those solvents affected the surface modification of GNRs based on LSPR analysis and zeta potential studies. The solvents were 70% ethanol, absolute ethanol, and alkaline aqueous solution.

4.2.2. Optimization of volume of 11-MUA

The 11-MUA volume used to surface modify 5 ml GNRs suspension synthesized in Chapter 1 was optimized by studying its effect on the red shift of LPW of GNRs and zeta potential analysis. The volumes used were 1 ml, 2 ml, and 3 ml.

4.2.3. Optimization of stirring speed

The stirring was varied at 600, 700, 800, and 900 rpm for surface modification of GNRs. the effect on stirring speed was analyzed by recording red shift in the LPW of GNRs as well as by zeta potential analysis.

4.2.4. Optimization of time of modification

The surface modification time was optimized by studying its effect on red shift of LPW of GNRs and the zeta potential of GNRs. The effect was studied at 6 hr, 8 hr, 10 hr, and 12 hr time points.

4.2.5. Characterization of 11-MUA modified GNRs

The MUA-GNRs were characterized by numerous analytical techniques. The optical LSPR properties of MUA-GNRs were assessed by UV-visible-NIR spectroscopy. Zeta potential was used to evaluate the surface modification and stability of MUA-GNRs. The morphology, shape, size and crystallinity were determined by electron microscopy studies. Further, the elemental

analysis and FTIR study were used to confirm the modification of GNRs with 11-MUA as well as to characterize the MUA-GNRs.

4.2.6. Stability of 11-MUA modified GNRs

The stability of MUA-GNRs was assessed in the resuspension medium i.e. borate buffer (pH 9), PBS (pH 7.4) and DI water. The stability was checked for 7 days by UV-visible analysis and zeta potential studies. This was done to fix the resuspension medium for further experiments. The intent was to use a biocompatible medium for bioimaging and biosensing studies.

4.3. Results and discussion

The process of surface modification of GNRs by replacing CTAB with 11-MUA was evaluated so that complete replacement of CTAB could be achieved. This not only produces biocompatible GNRs but also helps to form GNRs with -COOH group on their surface that can be used for further functionalization with other biomolecules for bioimaging, biosensing and other biomedical applications. Herein, as per our knowledge, no previous studies have comprehensively studied the effect of process factors on the surface modification of GNRs with 11-MUA.

4.3.1. Optimization of solvent

The solvents used to dissolve 11-MUA were absolute ethanol, 70% ethanol, and alkaline aqueous solvent. However, 11-MUA easily dissolves in alcoholic solvents, but the dissolution in alkaline solvents requires simultaneous sonication and stirring by adding 0.2 M NaOH. We optimized this parameter because as per reports, 11-MUA has more solubility in organic solvents (Charan et al., 2012; J. He et al., 2018; H. Huang et al., 2011, 2012; Toh et al., 2013; H. Zhang et al., 2016) compared to an aqueous solvent. However, there are also reports that used alkaline aqueous solvent or NaOH to dissolve 11-MUA (Ansar et al., 2018; Bai et al., 2017; J. Cao et al., 2012). Interestingly based on UV-visible analysis, it was observed that GNRs aggregated when alcoholic solvents were used; however, when the alkaline aqueous solvent was used, the proper red shift was observed in the LPW of CTAB-GNRs, due to the change in the refractive index of the medium (J. Cao et al., 2012; J. He et al., 2018; Toh et al., 2013) (Fig. 4.1). Further, in ethanolic solvents the zeta potential value does not state the stability of GNRs but in an alkaline aqueous solvent the zeta potential values state the good stability of MUA-GNRs as well as the change in charge of zeta potential from positive to

negative also confirms the replacement of CTAB with 11-MUA (Table 4.1) (J. He et al., 2018; L. Su et al., 2017; J. Wang et al., 2017). On the basis of statistical analysis, a significant difference was also observed in the zeta potential of MUA-GNRs when the surface modified by 11-MUA dissolved in different solvents (Fig. 4.2). Therefore, based on UV-visible and zeta potential studies, the alkaline aqueous solvent was used to dissolve 11-MUA for surface modification of GNRs.

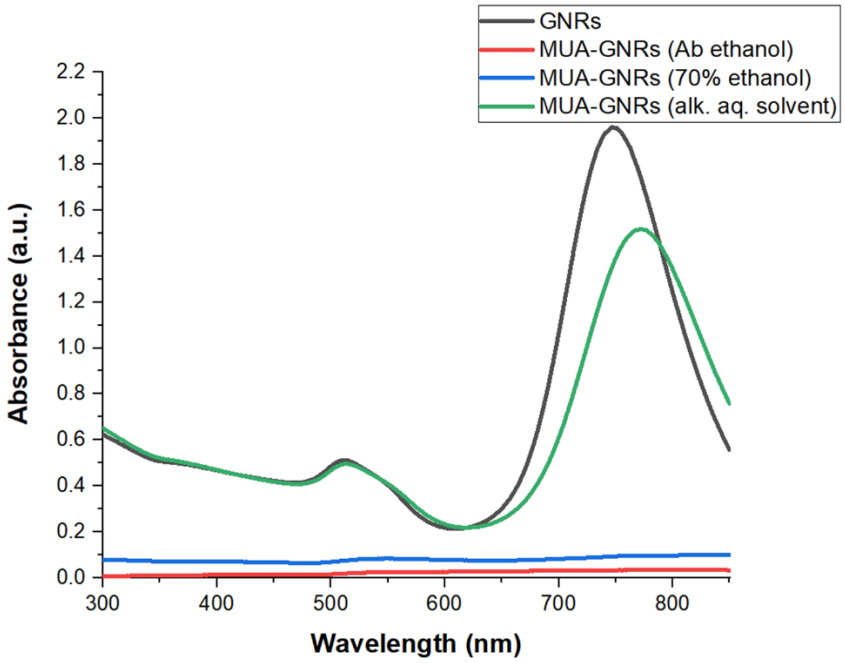

Figure 4.1 UV-visible spectra of MUA-GNRs modified using 11-MUA dissolved in different solvents

Table 4.1 Zeta potential of MUA-GNRs modified by using 11-MUA dissolved in various solvents

Solvents	Zeta Potential of GNRs (mV)	Zeta Potential of MUA-GNRs (mV)
Absolute ethanol	+49.51 ± 1.29	-2.97 ± 0.27
70% ethanol	+49.51 ± 1.29	-1.82 ± 0.32
Alkaline aqueous solvent	+49.51 ± 1.29	-36.91 ± 0.69

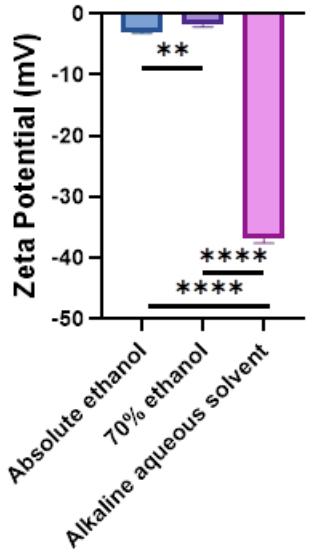

Figure 4.2 Effect of solvents used to dissolve 11-MUA on zeta potential of MUA-GNRs

4.3.2. Optimization of volume of 11-MUA

We optimized the volume of 11-MUA that should be used to surface modify 5 ml GNRs prepared in Chapter 3. This was elucidated based on the red shift in the LPW of GNRs and zeta potential analysis. The maximum red shift in the LPW was observed at 2 ml 11-MUA (Fig. 4.3) (Table 4.2). However, based on an unpaired t-test, there was no significant difference in the red shift at 1 ml and 2 ml 11-MUA volume, but the difference was significant between 2 ml and 3 ml (Fig. 4.4a). It was also found that this parameter had a significant effect on the red shift of LPW of GNRs (ANOVA p-value = 0.0324). The red shift in LPW was due to the change in the refractive index of the medium due to the ligand exchange, but the transverse plasmon wavelength (TPW) was insensitive to it (J. Cao et al., 2012; L. Su et al., 2017). Similarly, in our study, the LPW of GNRs was red shifted, but the TPW did not. The LSPR spectrum also confirms the stability and no sudden aggregation of GNRs after ligand exchange (L. Su et al., 2017).

Further, the zeta potential was altered from positive to negative, but it was above -30 mV after the surface modification of GNRs with 11-MUA (Table 4.2). Thus, the MUA-GNRs were found to have good electrostatic stability (Bhattacharjee, 2016; Honary & Zahir, 2013). Based on statistical analysis it was assessed that this factor does not significantly affect the zeta potential of MUA-GNRs (ANOVA p-value = 0.0521) (Fig. 4.2b). Finally, 2 ml 11-MUA was optimized to surface modify 5 ml GNRs.

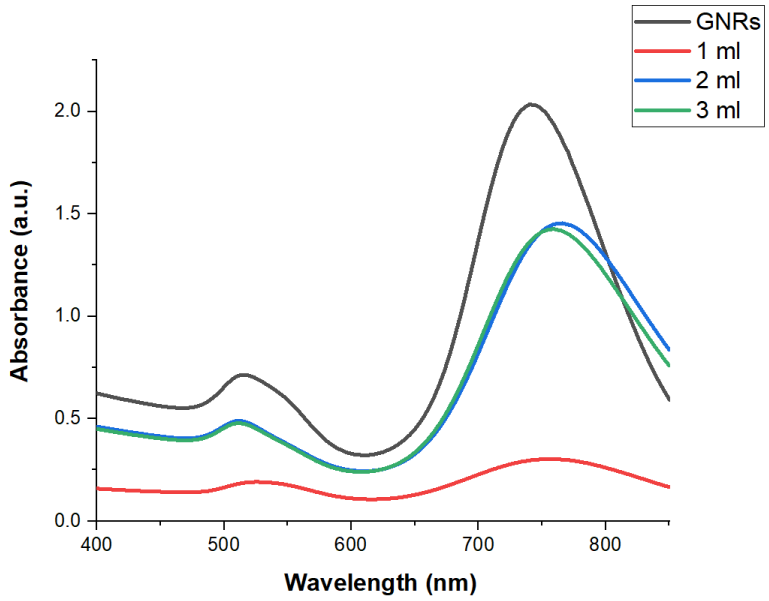

Figure 4.3 UV-visible spectra of MUA-GNRs modified at different volumes of 11-MUA

Table 4.2 Red shift in the LPW of GNRs and zeta potential of MUA-GNRs modified at different volumes of 11-MUA

Volume of 11-MUA (ml)	Red Shift in the LPW of GNRs (nm)	Zeta Potential of MUA-GNRs (mV)
1	17.33 ± 2.88	-31.02 ± 1.01
2	25 ± 4	-34.15 ± 1.10
3	18 ± 1	-32.32 ± 1.47

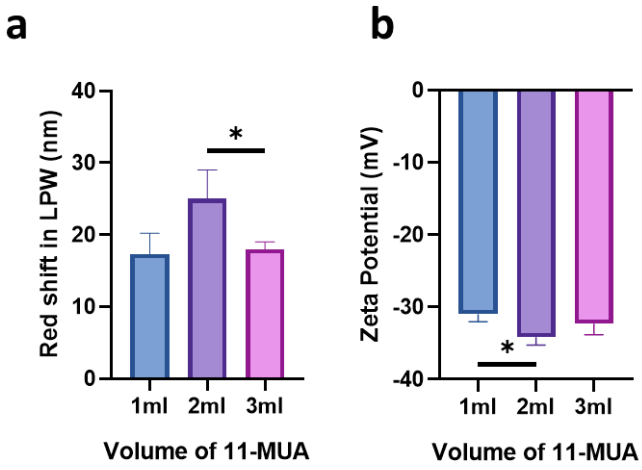

Figure 4.4 Effect of 11-MUA volumes on a) red shift in LPW of GNRs and b) zeta potential of MUA-GNRs

4.3.3. Optimization of stirring speed

On varying the stirring speed, the maximum red shift in the LPW of GNRs was observed at 800 rpm. Further, there was a decline in red shift of LPW of GNRs at 900 rpm (Fig. 4.5) (Table 4.3). The literature available mentioned vigorous stirring was required to replace CTAB from the surface of GNRs with 11-MUA. However, we have optimized the specific stirring speed (J. Cao et al., 2012; Jain et al., 2019). Also, it was worth noting that this parameter significantly affects the red shift in the LPW of GNRs (ANOVA p-value = 0.0012) (Fig. 4.6a) and the effect on zeta potential of MUA-GNRs was non-significant (ANOVA p-value = 0.1663) (Fig. 4.6b). Based on an unpaired t-test, there was a significant difference between LPW red shift at other stirring speeds compared to 800 rpm (Fig. 4.6a). The zeta potential of MUA-GNRs was very stable, as it was above -30 mV at every stirring point (Table 4.3). Herein, we have optimized 800 rpm for surface modification of GNRs with 11-MUA. Similarly, Oliveira et. al. used 800 rpm to modify citrate-capped spherical gold nanoparticles with 11-MUA (Oliveira et al., 2019).

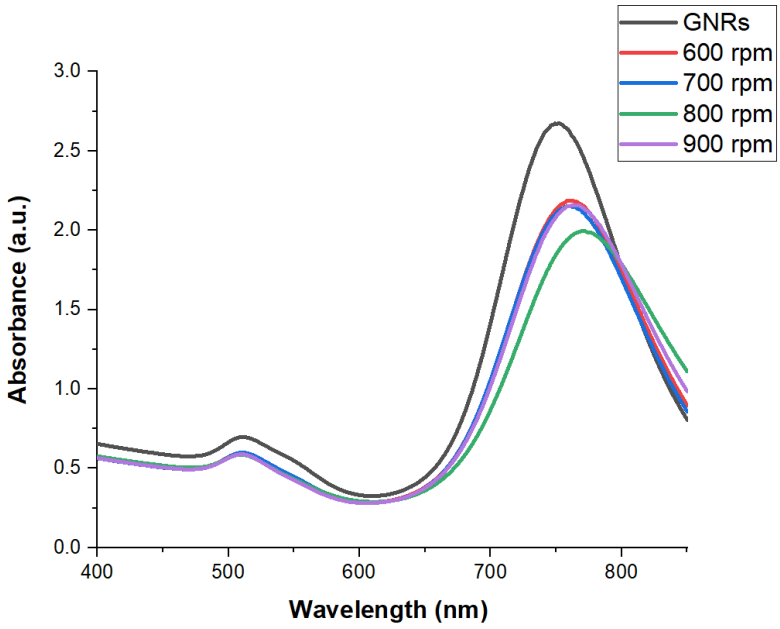

Figure 4.5 UV-visible spectra of MUA-GNRs modified at different stirring speeds

Table 4.3 Red shift in the LPW of GNRs and zeta potential of MUA-GNRs modified at different stirring speeds

Stirring speed (rpm)	Red Shift in the LPW of GNRs (nm)	Zeta Potential of MUA-GNRs (mV)
600	9 ± 1.73	-39.47 ± 1.43
700	8.66 ± 2.08	-38.33 ± 1.64

800	20 ± 3.60	-40.22 ± 1.27
900	10.66 ± 1.52	-37.24 ± 1.70

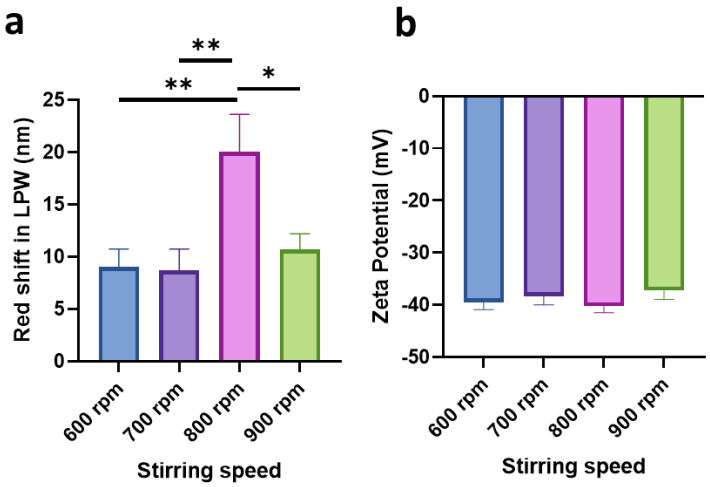

Figure 4.6 Effect of stirring speeds on a) red shift in LPW of GNRs and b) zeta potential of MUA-GNRs

4.3.4. Optimization of time of modification

The time of surface modification also had a significant (ANOVA p-value = 0.0030) role in the replacement of CTAB with 11-MUA from the surface of GNRs (Fig. 4.8a). When the time was varied, the maximum red shift in LPW of GNRs was noticed at 12 hr (Fig. 4.7) (Table 4.4); however, there was an insignificant difference in the red shift between 8 hr and 12 hr as well as 8 hr and 10 hr based on unpaired t-test. Also, by unpaired t-test, it was observed that there was a significant difference between the 8 hr when compared with 6 hr (Fig. 4.8a). Further, the zeta potential at every time point was above -30 mV, which confirms the modification of GNRs and electrostatic stability of MUA-GNRs (Table 4.4). This parameter does not affect the zeta potential of MUA-GNRs significantly (ANOVA p-value = 0.7688) (Fig. 4.8b). Thus, to keep it economical, we have selected 8 hr as the time for modification of GNRs with 11-MUA. Herein, we have optimized a specific time for the modification of GNRs with 11-MUA. However, other studies used overnight stirring (J. Cao et al., 2012; Jain et al., 2019) or incubation (J. He et al., 2018; H. Huang et al., 2011)

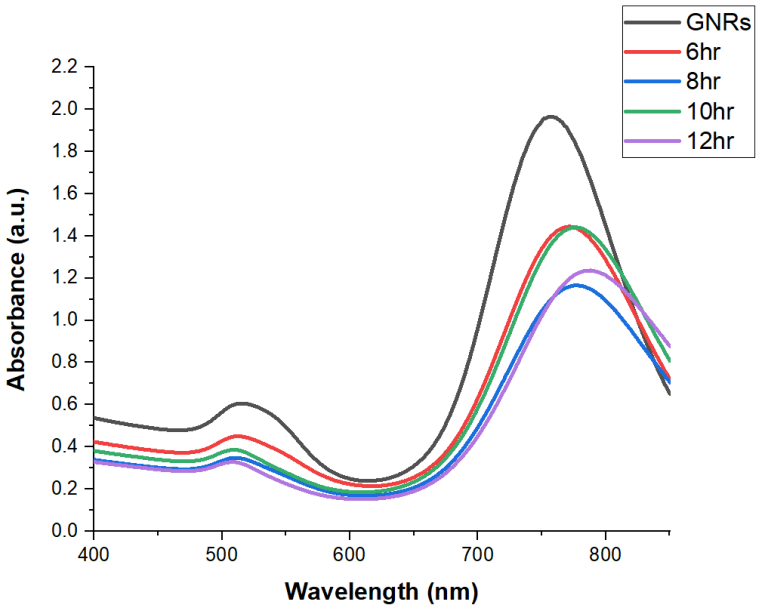

Figure 4.7 UV-visible spectra of MUA-GNRs modified at different time points

Table 4.4 Red shift in the LPW of GNRs and zeta potential of MUA-GNRs modified at different time points

Time (hr)	Red Shift in the LPW of GNRs (nm)	Zeta Potential of MUA-GNRs (mV)
6	12.66 ± 1.52	-34.85 ± 1.06
8	19.66 ± 3.78	-36.53 ± 2.96
10	18.66 ± 3.21	-35.14 ± 2.19
12	30.33 ± 5.50	-36.16 ± 2.36

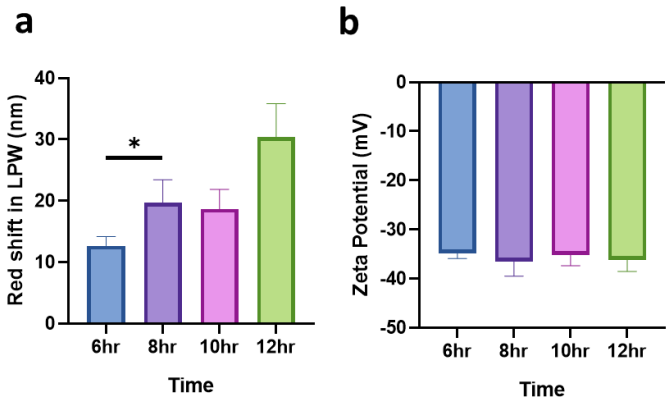

Figure 4.8 Effect of time of modification on a) red shift in LPW of GNRs and b) zeta potential of MUA-GNRs

4.3.5. Characterization of 11-MUA modified GNRs

The MUA-GNRs synthesized at the final optimized values of the surface modification process GNRs were extensively characterized by various techniques.

4.3.5.1. UV-visible-NIR spectroscopy and zeta potential analysis

As already discussed, the red shift in the LPW of GNRs was due to the change in the refractive index of the medium, which was due to the replacement of CTAB on the surface GNRs with the 11-MUA (J. Cao et al., 2012; J. He et al., 2018; Toh et al., 2013). Here, we have also detected a red shift of around 22 nm on the surface modification of GNRs with 11-MUA. The LPW of CTAB-GNRs was 751 nm, which shifted to 773 nm (Fig. 4.9). The LSPR spectrum of MUA-GNRs also shows that the MUA-GNRs were stable without any aggregation and no significant change in the TPW was detected after the formation of MUA-GNRs. These findings were in line with the other studies (J. Cao et al., 2012; J. He et al., 2018; L. Su et al., 2017).

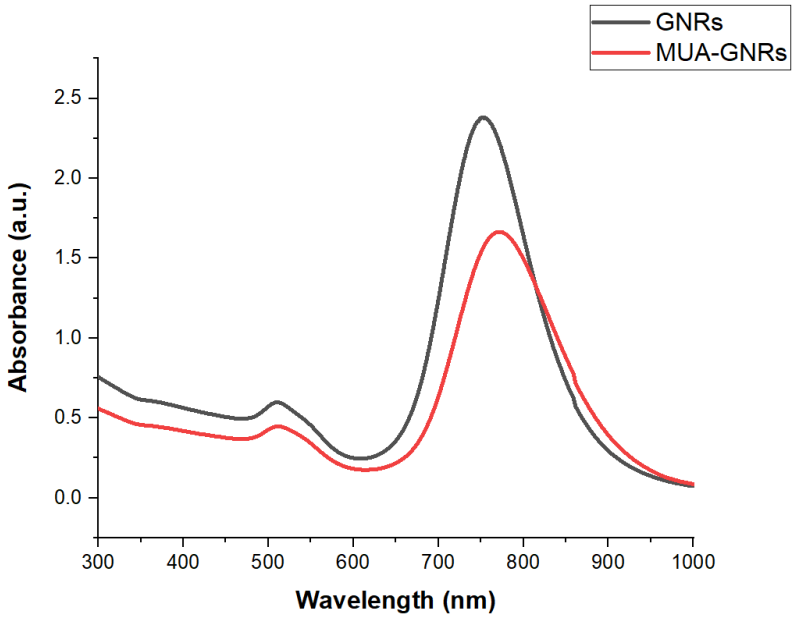

Figure 4.9 UV-visible-NIR spectra of GNRs and MUA-GNRs

Further, the change of surface charge of GNRs, determined by zeta potential analysis, from positive to negative also confirms the modification of CTAB-GNRs to MUA-GNRs (J. He et al., 2018; Jain et al., 2019; L. Su et al., 2017; J. Wang et al., 2017). The zeta potential of GNRs was around +49 mV and the zeta of MUA-GNRs was found to be -36.53 ± 2.96 mV (Fig. 4.10). The zeta potential value suggests the good colloidal stability of MUA-GNRs. Our result was

consistent with the other studies (Ansar et al., 2018; Charan et al., 2012; J. He et al., 2018; Jain et al., 2019; Morais et al., 2012; L. Su et al., 2017).

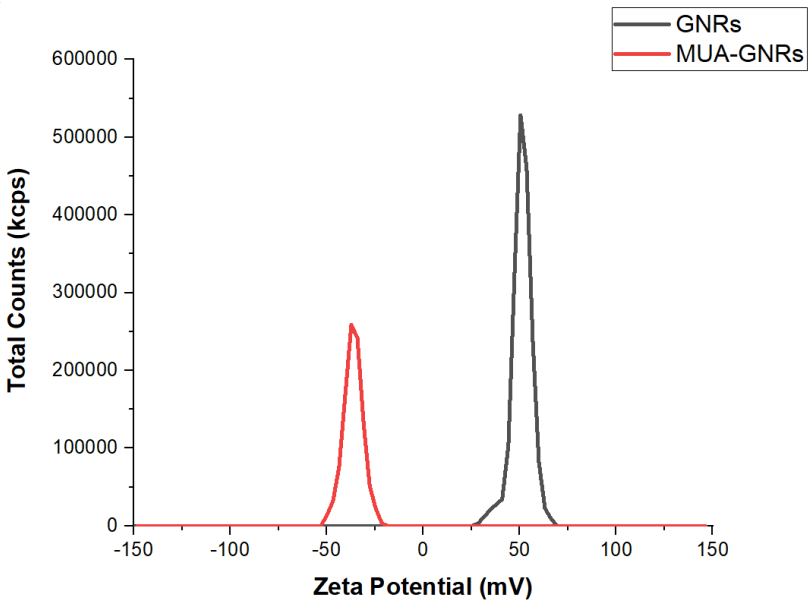

Figure 4.10 Zeta potential of GNRs and MUA-GNRs

4.3.5.2. Electron microscopy analysis

Based on HRTEM analysis, the size of MUA-GNRs was 42.97 ± 3.23 nm x 11.9 ± 1.76 nm (Fig. 4.11a). This finding was in agreement with the FESEM analysis (Fig. 4.11b). Further, the SAED pattern obtained by using HRTEM confirms the crystalline nature of MUA-GNRs (Fig 4.11c) (Anandhakumar et al., 2013; Kedawat et al., 2019). The fringes of MUA-GNRs were also captured by HRTEM. The d-spacing value was 0.209 nm. (Fig. 4.11d). The spacing between the fringes was found to be consistent with the other studies (Si et al., 2012; J. Yin et al., 2017; L. Zhang et al., 2016).

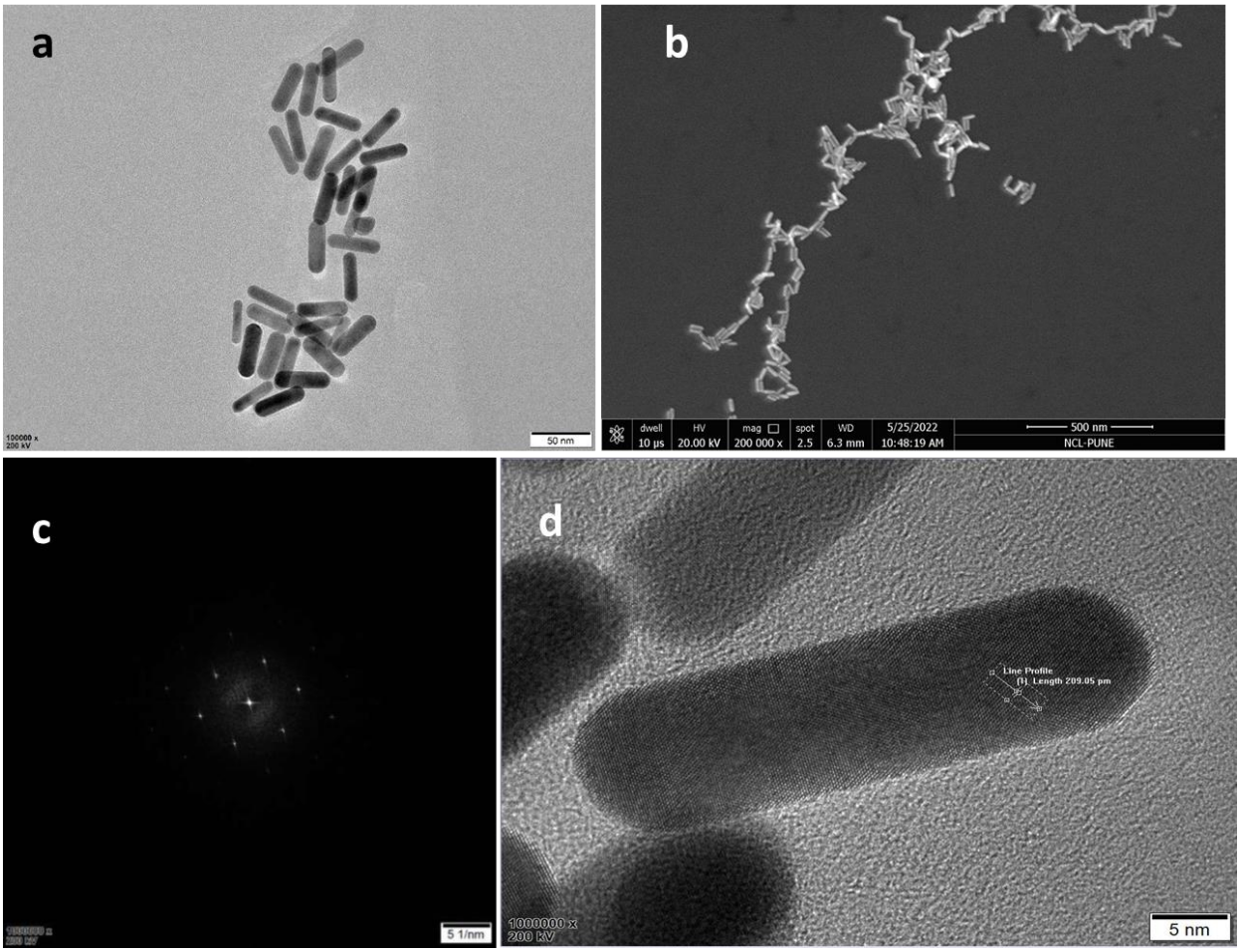

Figure 4.11 Electron microscopy analysis of MUA-GNRs a) HRTEM image, b) FESEM image, c) SAED pattern and d) fringes of MUA-GNRs

4.3.5.3. Elemental analysis

The EDX spectrum of MUA-GNRs was recorded using HRTEM. The spectrum confirms the modification of GNRs with 11-MUA by replacing CTAB, as there was gold (Au), carbon (C), oxygen (O) and sulfur (S) instead of bromine (Br). However, the copper (Cu) was present due to the copper grid used for the analysis (Fig. 4.12a). The EDX spectrum was also acquired using a concentrated MUA-GNRs sample through FESEM. It was in agreement with the EDX analysis from HRTEM (Fig. 4.12b). Further, STEM mapping was also performed to analyze the elements present in MUA-GNRs and to confirm the surface modification of GNRs with 11-MUA (Fig. 4.13). It also backs the EDX spectrum.

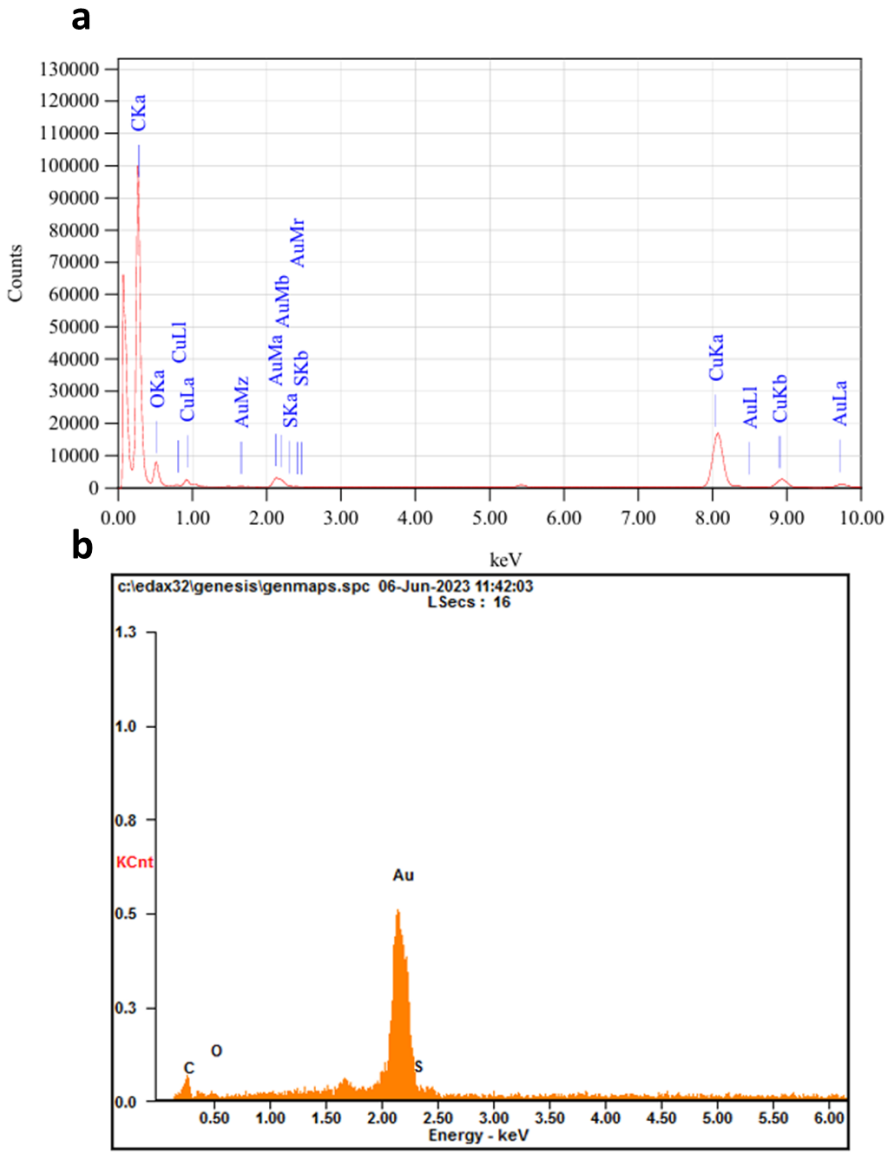

Figure 4.12 EDX spectra of MUA-GNRs a) from HRTEM and b) from FESEM

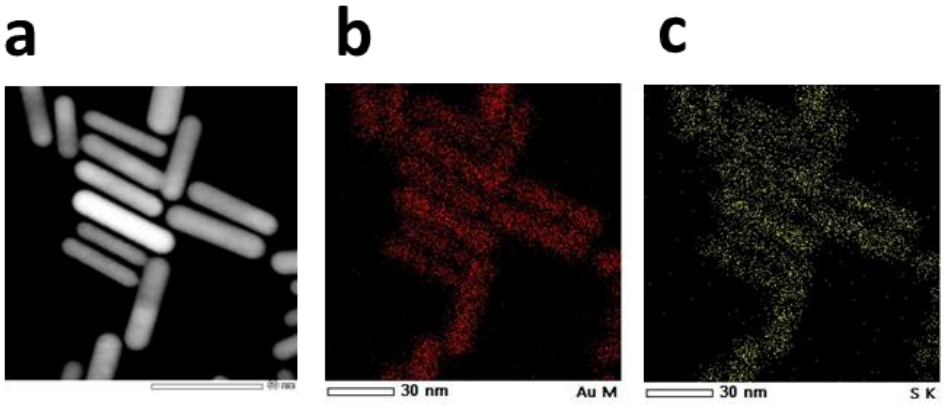

Figure 4.13 STEM mapping of MUA-GNRs a) STEM image, b) Au and c) S

Further, XPS analysis was also done to confirm the surface modification of GNRs with 11-MUA. However, the XPS spectrum of GNRs was already discussed in Chapter 3, section 3.3.9.3. Here, in the XPS spectrum of MUA-GNRs, the dual peak positioned around 83.88 eV and 87.58 eV links to transitions Au $4f_{7/2}$ and Au $4f_{5/2}$ of Au^0 oxidation state, respectively (L. Su et al., 2017). This was similar to the XPS spectrum of GNRs. However, in MUA-GNRs, there was the presence of sulfur (S), S 2p peak around 163.38 eV instead of bromine (Br) peaks in GNRs (Fig. 4.14a-c). This was due to the replacement of CTAB with 11-MUA (J. Cao et al., 2012; J. He et al., 2018; L. Su et al., 2017; Tao et al., 2018; Thierry et al., 2009; Toh et al., 2013).

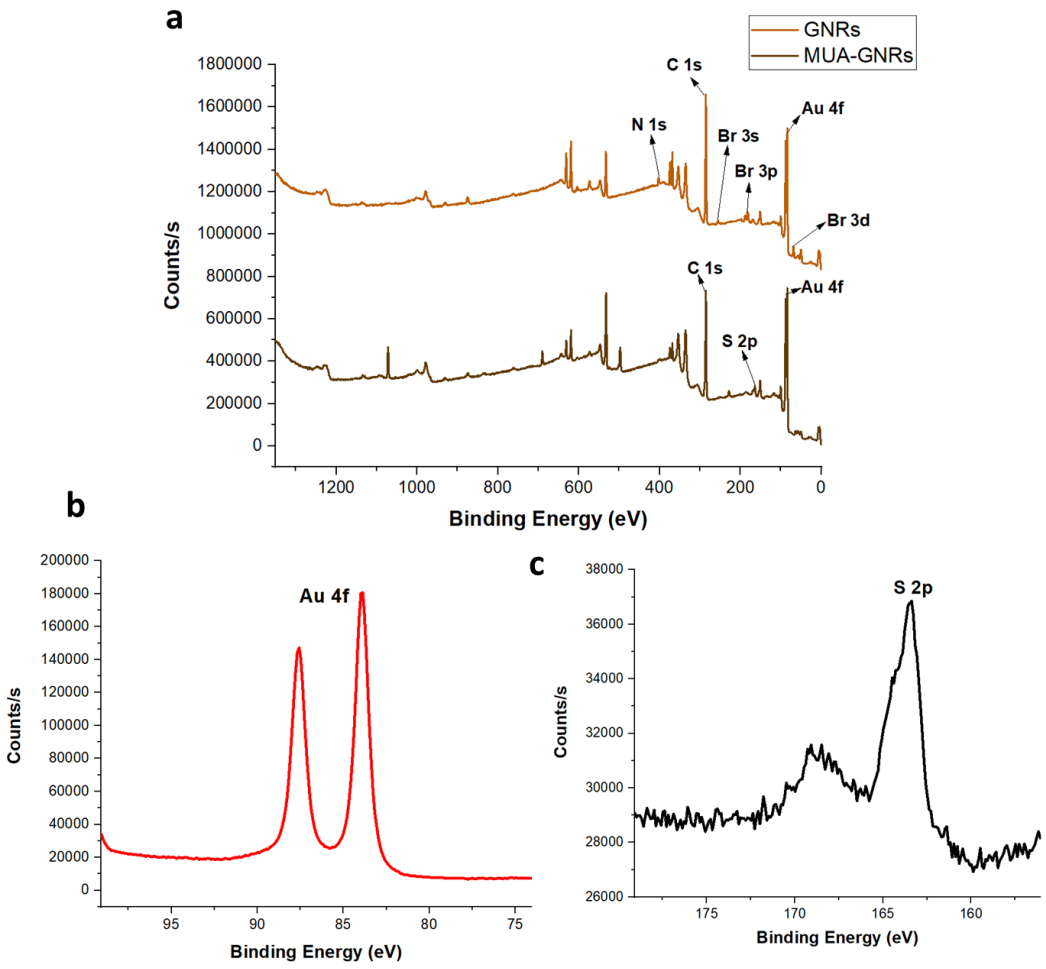

Figure 4.14 a) XPS spectra of GNRs and MUA-GNRs, b) XPS spectrum of Au 4f of MUA-GNRs and c) XPS spectrum of S 2p of MUA-GNRs

4.3.5.4. FTIR analysis

The MUA-GNRs exhibited broad and strong O-H absorptions from 11-MUA at 3200– 3600 cm^{-1} along with C-H stretching at 2918 and 2849 cm^{-1} (J. He et al., 2018; H. Huang et al.,

2011; Taheri et al., 2017). Similarly, C-H stretching was also observed in the 11-MUA at 2916 and 2848 cm^{-1}, but the intensity was higher than that of the MUA-GNRs. Further, in the 11-MUA, the -COOH stretching was observed at 1694 cm^{-1} (L. Su et al., 2017), while it was shifted in the MUA-GNRs. The MUA-GNRs showed strong C=O and C-O stretching at 1714 cm^{-1} and 1055 cm^{-1} (Hasannia et al., 2022; J. He et al., 2018; H. Huang et al., 2011; Vedhanayagam et al., 2022). The 11-MUA showed C-H scissoring modes around 1400 cm^{-1}(J. He et al., 2018). The peak at 2555 cm^{-1} in the 11-MUA spectrum disappeared in the spectrum MUA-GNRs, and the C-S stretching peak appeared at 702 cm^{-1}. This validated the presence of 11-MUA on the surface of GNRs by the formation of Au-S bonds (Fig. 4.15) (Y. Guo et al., 2012; Hasannia et al., 2022; Nikfarjam et al., 2017; L. Su et al., 2017; Vedhanayagam et al., 2022). Also, the peaks of CTAB mentioned in Figure 3.28 of Chapter 3 disappeared.

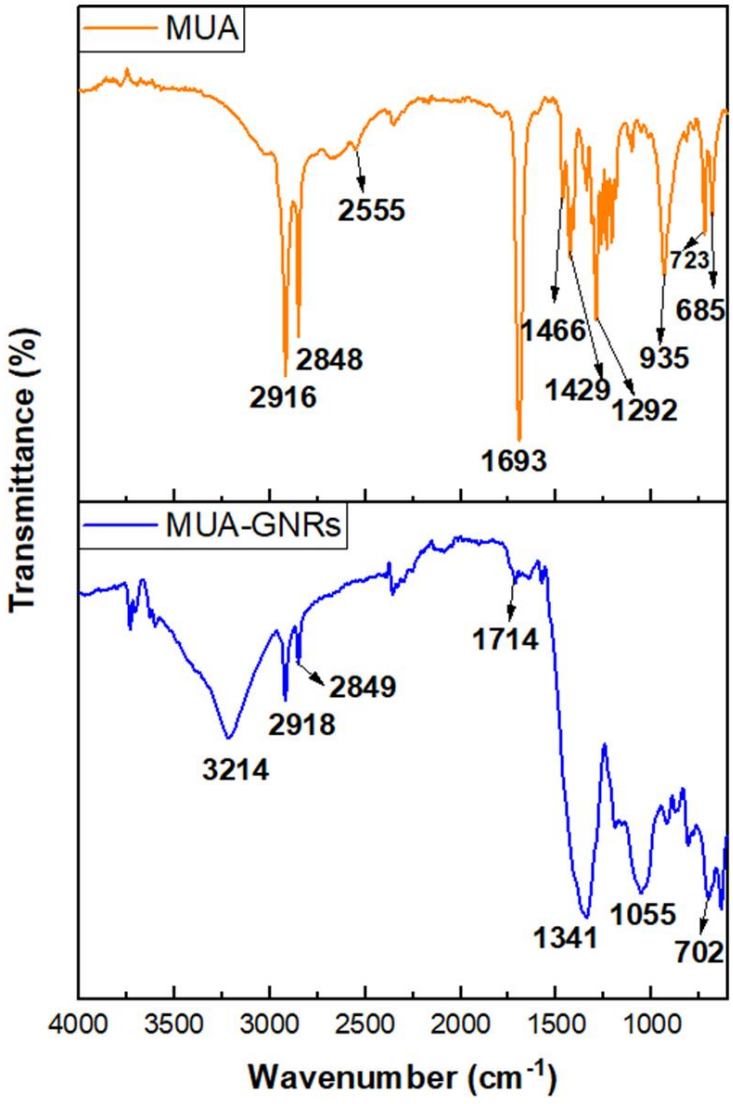

Figure 4.15 FTIR spectra of 11-MUA and MUA-GNRs

4.3.6. Stability of 11-MUA modified GNRs

The MUA-GNRs were found to be highly stable in a borate buffer (Fig.4.16a) however, the DI water also served as a suitable medium to keep MUA-GNRs stable (Fig.4.16b), based on UV-visible assessment. But, the MUA-GNRs were not stable in the PBS because the LSPR spectra of MUA-GNRs were not well defined and the longitudinal plasmon peaks were broadened (Fig.4.16c). Further, the zeta potential results were also supporting the UV-visible results (Fig. 4.17). Therefore, borate buffer and DI water were finalized as the dispersing medium for MUA-GNRs. Similarly, Cao et al. have also reported the stability of MUA-GNRs in borate buffer (pH 9) and instability in PBS. Contrary, to the findings of Cao et al. (J. Cao et al., 2012), we examined the good stability of MUA-GNRs in DI water also. Although, compared to DI water, MUA-GNRs were more stable in borate buffer.

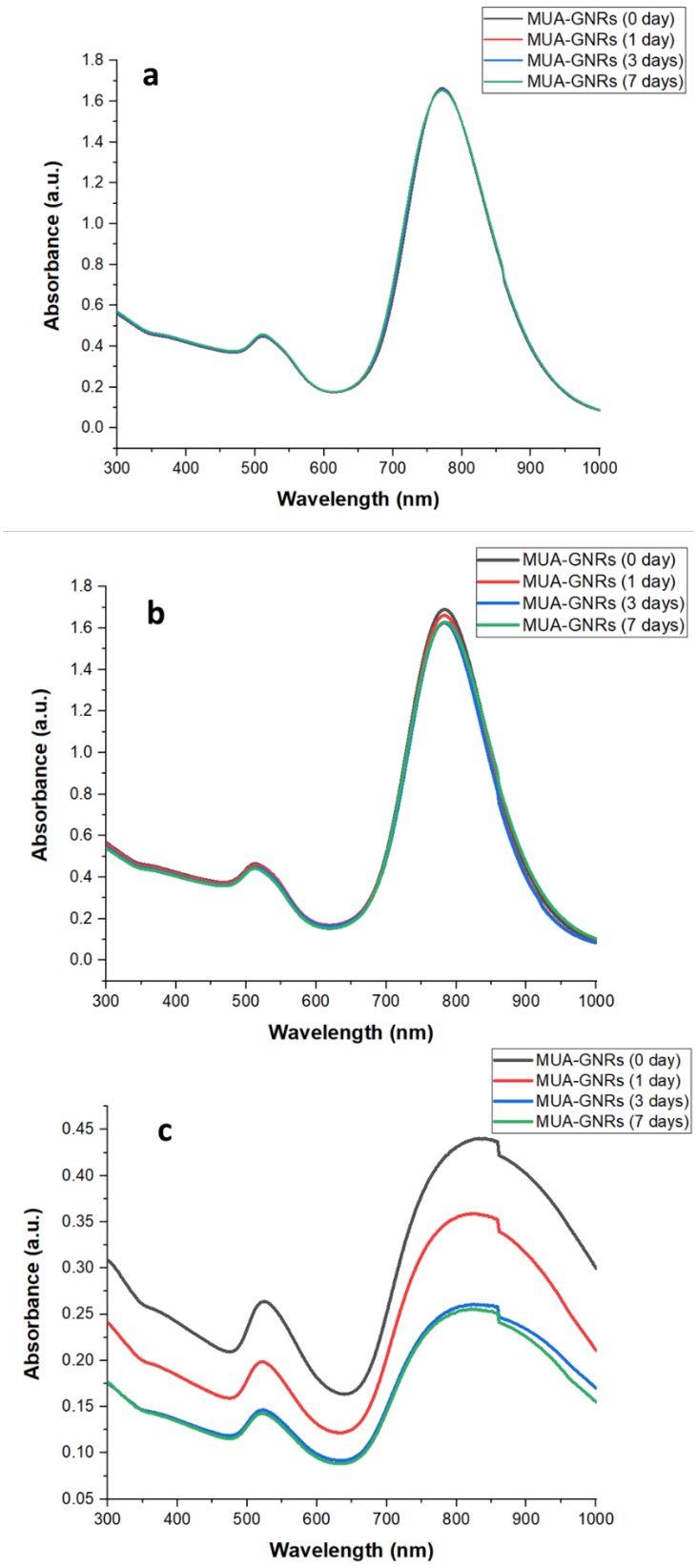

Figure 4.16 Stability studies of MUA-GNRs by UV-visible-NIR spectroscopy at different time points in a) borate buffer (pH 9), b) DI water and c) PBS (pH 7.4)

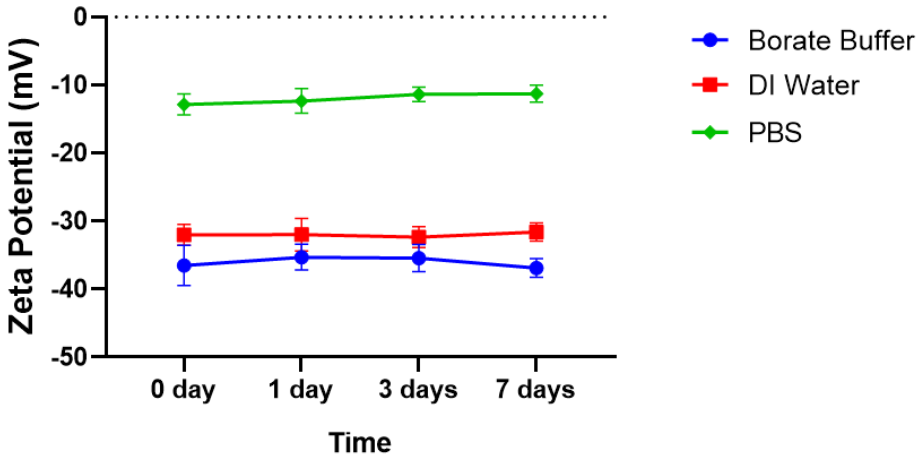

Figure 4.17 Zeta potential of MUA-GNRs at different time points in borate buffer (pH 9), DI water and PBS (pH 7.4)

4.4. Conclusion

This study identifies and comprehensively examines various parameters for surface-modifying GNRs with 11-MUA. We investigated various factors such as solvents used to dissolve 11-MUA, volume 11-MUA, stirring speed, and time of surface modification on the basis of red shift in the LPW of GNRs as well as zeta potential analysis. We optimized an alkaline aqueous solvent, 2 ml 11-MUA to modify 5 ml GNRs, 800 rpm stirring speed and 8 hr as the time required to modify GNRs. All these parameters were found to be significant for the exchange of CTAB with 11-MUA from the surface of GNRs. Although, these parameters did not have a significant effect on the zeta potential of MUA-GNRs.

Upon characterization, we confirmed that the MUA-GNRs were stable with zeta potential -36.53 ± 2.96 mV and a well-defined UV-Visible-NIR spectrum. The red shift of around 20 ± 4 nm in the LPW of MUA-GNRs was observed when compared with the LPW of CTAB-capped GNRs. The HRTEM, FESEM, SAED, EDX, STEM mapping, XPS, and FTIR analysis corroborated the synthesis of MUA-GNRs comprising the crystalline structure. The zeta potential, EDX, XPS, STEM mapping and FTIR studies also proved that the CTAB on the surface of GNRs was replaced by 11-MUA. Also, the MUA-GNRs were found to be highly stable in a borate buffer, although DI water can also be used as a medium to disperse them. Thus, this study imparted biocompatibility to GNRs. Also, the -COOH on the MUA-GNRs surface could be further explored to functionalize GNRs with any biological entities for numerous biological applications such as biosensing, bioimaging, targeted therapy, etc.

CHAPTER 5

Functionalization of GNRs and Development of LFA

CHAPTER 5A

Optimization, Synthesis and Characterization of TSH Antibody Functionalized GNRs

5A.1. Introduction

The two critical components of any biosensor are the receptor, which is a biological element specific to the analyte, and the transducer, which transduces recognition events into readable signals (Chamorro-Garcia & Merkoçi, 2016). Therefore, the LFAs are paper-based biosensors where the receptor tagged with the label undergoes binding with the analyte of interest, and qualitative or quantitative results are generated by interpreting the color development or using a reader to quantify the intensity of the color change (Z. Li et al., 2019; Mills et al., 2022; Posthuma-trumpie & Korf, 2009). Antibodies are mainly used as a recognition element in LFA; these are generally attached to the labels, which are color-generating substances (Parolo et al., 2013; Posthuma-trumpie & Korf, 2009). These labels are usually nanoparticles that have a specific color and in that specifically, gold nanoparticles are employed in LFAs (Chamorro-Garcia & Merkoçi, 2016; Parolo et al., 2013).

The antibodies are conjugated on the nanoparticle's surface by electrostatic interaction, or hydrophobic adsorption, or covalent binding (Lou et al., 2012). However, covalent functionalization of antibodies on nanoparticles is preferred over noncovalent because it leads to the proper orientation of the antibodies (Oliveira et al., 2019) and enhances the sensitivity and repeatability of antigen-antibody interaction (Busch et al., 2019; Mirshekari et al., 2024; Oliveira et al., 2019; Shahjahan et al., 2023). Further, noncovalent bonding is more straightforward but gets easily influenced by changes in external conditions like pH, ionic strength, etc. (Ahmad et al., 2022; Sanità et al., 2020), and also the orientation of the antibody is erroneous. Therefore, this results in poor selectivity and sensitivity of the conjugate (Shahjahan et al., 2023).

Herein, we have functionalized MUA-GNRs with TSH antibody, which was used as a conjugate for LFA preparation. The MUA-GNRs synthesized in Chapter 4 have a -COOH group on their surface which is activated by the EDC/NHS coupling reaction to form peptide bonds with the amine groups of the biomolecules (J. Cao et al., 2012; Mayer et al., 2008; Mirshekari et al., 2024; Panhwar et al., 2021; Sim et al., 2010; Y. Wang et al., 2013). This covalent coupling supports the formation of a consistent and stable bond between the nanoparticles and the antibody (Busch et al., 2019). The same approach was employed in this study to covalently functionalize TSH antibodies with GNRs for sensitive and selective detection of TSH. To ensure more attachment of the antibodies on the surface of GNRs and the stability of GNRs, we have optimized certain conditions, such as the concentration of antibodies and buffer appropriate for the process. Further, the Ab-GNRs were characterized,

and the bioconjugation was validated using various analytical techniques. Moreover, we have also tested the stability of the Ab-GNRs in resuspension buffer containing different percentages of sucrose (2, 5 and 10%). After this, a comprehensive stability study of MUA-GNRs and Ab-GNRs was performed based on UV-visible spectroscopy and zeta potential studies. These studies subsequently helped to enhance the performance of LFA designed for detecting TSH.

5A.2. Method

The formerly synthesized MUA-GNRs were functionalized with detection antibody (TSH antibody) by the protocol mentioned in section 2.2.3 of Chapter 2. We optimized the buffer for the reaction as well as the concentration of antibody required for functionalization and the concentration of sucrose should be added in the resuspension buffer to store Ab-GNRs based on UV-visible and zeta potential studies.

5A.2.1. Optimization of buffer

We have functionalized MUA-GNRs with TSH antibodies in borate buffer pH 9, in which the MUA-GNRs were already suspended. Next, we also used PSB pH 7.4 by suspending the MUA-GNRs in it during the experiment. The results were evaluated based on the LPSR spectrum and zeta potential analysis.

5A.2.2. Optimization of concentration of TSH antibody

We have varied the concentration of antibody that should be used to functionalize MUA-GNRs. The concentrations were 5 µg/ml, 25 µg/ml and 50 µg/ml. This parameter was also assessed based on the red shift in the LPW of MUA-GNRs and zeta potential analysis.

5A.2.3. Optimization of sucrose concentration in resuspension buffer

After the functionalization of MUA-GNRs with the TSH antibody, we optimized the percentage of sucrose that should be added to the resuspension buffer to keep the Ab-GNRs stable. This was assessed by resuspending Ab-GNRs in a resuspension buffer containing 2%, 5% and 10% sucrose and acquiring LSPR spectrum and zeta potential values after one day.

5A.2.4. Characterization of Ab-GNRs

The Ab-GNRs were characterized by numerous high-end analytical techniques. The optical LSPR properties of Ab-GNRs were assessed by UV-visible-NIR spectroscopy. A zeta potential study was used to evaluate the functionalization and stability of Ab-GNRs. Electron microscopy studies determined the morphology, shape, size and crystallinity. Further, the

elemental analysis and FTIR study were employed to simultaneously characterize and confirm the functionalization of GNRs with TSH antibodies.

5A.2.5. %BE of TSH antibodies on GNRs

The percent BE of TSH antibodies on the surface of GNRs was calculated by the Bradford assay described in Chapter 2, section 2.2.5.8.

5A.2.6. Stability studies

We evaluated the stability of MUA-GNRs in borate buffer and Ab-GNRs in resuspension buffer at different time intervals. MUA-GNRs and Ab-GNRs were stored at 4 ºC and LSPR spectrum and zeta potential values were recorded periodically.

5A.3. Results and discussion

The factors that could affect the functionalization of antibodies on the surface of MUA-GNRs were evaluated and the Ab-GNRs were synthesized. These Ab-GNRs were further used as a conjugate or label for sensing TSH through the LFA. Also, it was necessary to note that the covalent functionalization of antibodies with GNRs was achieved by forming peptide bonds (J. Cao et al., 2012; Mayer et al., 2008; Mirshekari et al., 2024; Panhwar et al., 2021; Sim et al., 2010; Y. Wang et al., 2013).

5A.3.1. Optimization of buffer

The reaction of antibody functionalization with MUA-GNRs was carried out in borate buffer pH 9, in which MUA-GNRs were already suspended and in PBS pH 7.4 to check their effect on the functionalization process. When the LSPR spectrum was acquired after the reaction in borate buffer pH 9, the LPW of Ab-GNRs was found to red shifted compared to the LPW of MUA-GNRs and the spectrum was well defined, which confirms the functionalization of GNRs with antibodies and stability of Ab-GNRs (Fig. 5A.1). This was supported by the findings of other researchers, where also the red shift in longitudinal SPR of GNRs was noticed after antibody conjugation (Busch et al., 2019; F. Cao et al., 2016; J. Cao et al., 2012; Tao et al., 2018). The red shift in LPW of MUA-GNRs after functionalization was due to the change in the dielectric constant of the medium (H. Zhang et al., 2016). Further, the zeta potential of Ab-GNRs was recorded as below -30 mV (Fig. 5A.2) (Table 5A.1). The zeta potential decreased after functionalization; this confirms the Ab conjugation with the MUA-GNRs. Although the

zeta potential value does not state the electrostatic stability of Ab-GNRs, the Ab-GNRs were still stable because antibodies provide steric stability to the GNRs (Ansar et al., 2018).

However, when the functionalization was performed in PBS, the GNRs were aggregated, which was confirmed from the LPSR spectra of the GNRs as there was no appearance of the transverse and longitudinal SPR peaks (Fig. 5A.1). Further, the zeta potential value was -6.33 ± 0.58 mV which signifies the electrostatic instability of the Ab-GNRs and they were also unstable sterically (Fig. 5A.2) (Table 5A.1). The functionalization was evaluated in PBS because there are many studies which have employed PBS for the functionalization of GNRs with antibodies (Eum et al., 2010; Mirshekari et al., 2024; Panhwar et al., 2021; Sim et al., 2010; X. Wang et al., 2017).

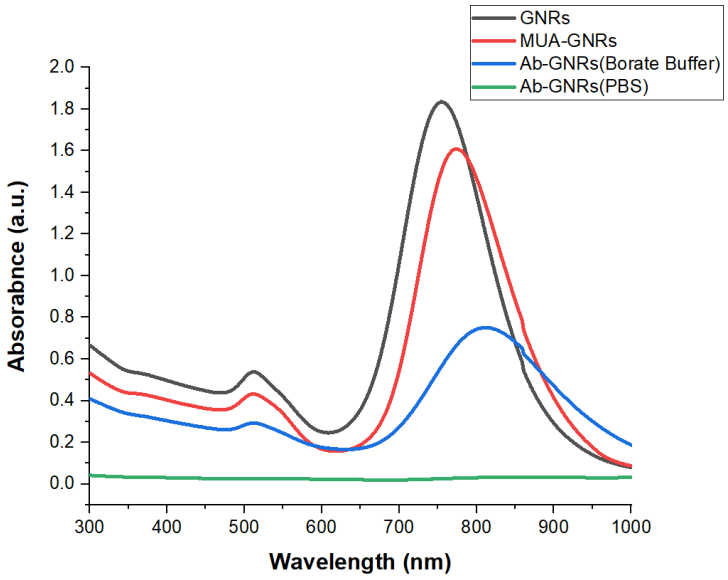

Figure 5A.1 UV-visible-NIR spectra of Ab-GNRs prepared in different buffers

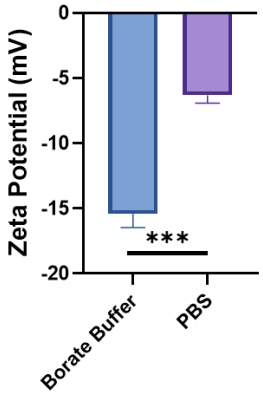

Figure 5A.2 Effect of buffers used for the functionalization process on the zeta potential of Ab-GNRs

Table 5A.1 Zeta potential of Ab-GNRs in different buffers used for the functionalization process

Buffer	Zeta Potential (mV)
Borate Buffer (pH 9)	-15.43 ± 1.05
PBS (pH 7.4)	-6.33 ± 0.58

5A.3.2. Optimization of concentration of TSH antibody

When the antibody concentration was varied, the maximum red shift in the LPW of MUA-GNRs was observed when 50 µg/ml TSH antibody was used to functionalize MUA-GNRs. Although, as the concentration of antibody decreased, the red shift also declined along with the absorbance (Fig. 5A.3) (Table 5A.2). The red shift in LPW of MUA-GNRs after functionalization was due to the change in the dielectric constant of the medium (H. Zhang et al., 2016). The decline in absorbance might be due to the small amount of antibody, which was not able to provide the proper steric stability to the MUA-GNRs; thus, the longitudinal SPR of the MUA-GNRs functionalized with 5 µg/ml antibody was broadened, and GNRs were aggregated (Shahjahan et al., 2023). However, the concentration of antibody had significantly affected the red shift in LPW of MUA-GNRs (ANOVA p-value = <0.0001) (Fig. 5A.4a). On the examination of zeta potential, it was found that the zeta potential values at all the concentrations of antibody were below -30 mV (Table 5A.2). Although, as per zeta potential data, the Ab-GNRs at all the antibody concentrations were electrostatically unstable, but the functionalization of antibodies on the surface of GNRs imparted steric stability to GNRs. Therefore, the Ab-GNRs were stable. Further, on statistics, it was found that this parameter had a significant effect on the zeta potential of the Ab-GNRs (ANOVA p-value = 0.0077) (Fig. 5A.4b). Finally, 50 µg/ml TSH antibody was optimized for functionalization of MUA-GNRs.

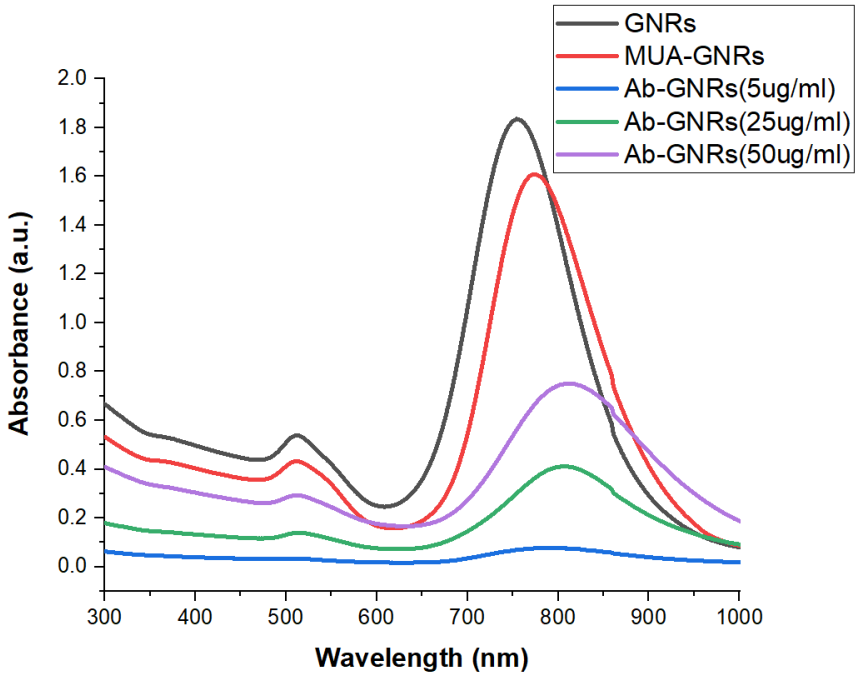

Figure 5A.3 UV-visible-NIR spectra of Ab-GNRs functionalized at different antibody concentrations

Table 5A.2 Red shift in the LPW of MUA-GNRs after antibody functionalization and zeta potential of Ab-GNRs functionalized at different antibody concentrations

Concentration of TSH antibody (µg/ml)	Red Shift in the LPW of GNRs (nm)	Zeta Potential of MUA-GNRs (mV)
5	13 ± 1.73	-11.26 ± 1.09
25	28 ± 3.6	-14.32 ± 1.06
50	41 ± 3	-15.43 ± 1.05

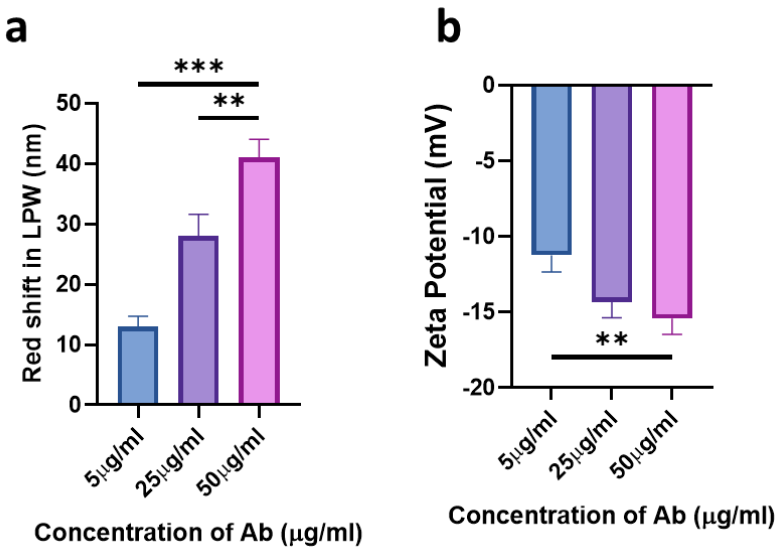

Figure 5A.4 Effect of concentrations of antibody on a) red shift in LPW of MUA-GNRs and b) zeta potential of Ab-GNRs

5A.3.3. Optimization of sucrose concentration in resuspension buffer

Based on the LSPR spectrum study, it was found that 10% sucrose concentration was not suitable for use in resuspension buffer, as the Ab-GNRs were aggregated. However, the Ab-GNRs were stable at 2% and 5% sucrose concentration (Fig. 5A.5). Further, the zeta potential of Ab-GNRs suspended in a buffer containing 10% sucrose was also decreased compared to the zeta potential of Ab-GNRs that were suspended in buffer containing 2% and 5% sucrose (Table 5A.3). This parameter significantly affects the zeta potential of Ab-GNRs (ANOVA p-value = 0.0004) (Fig. 5A.6). The UV-visible-NIR analysis and zeta potential study confirm that the Ab-GNRs were stable in buffer with 2% and 5% sucrose. We have finalized the 5% sucrose concentration. Sucrose maintains the stability of the antibodies when stored at lower temperatures, also after drying it keeps the antibodies in the glassy matrix by forming hydrogen bonds with them, thus, protecting them from degradation (Jonsson et al., 2024; J. Li et al., 2024; B. Wang et al., 2009). Therefore, the Ab-GNRs will be stable on LFA after drying. However, the proper sucrose concentration in the resuspension buffer should be maintained; otherwise, it can destabilize antibodies (Hauptmann et al., 2018; Svilenov et al., 2020).

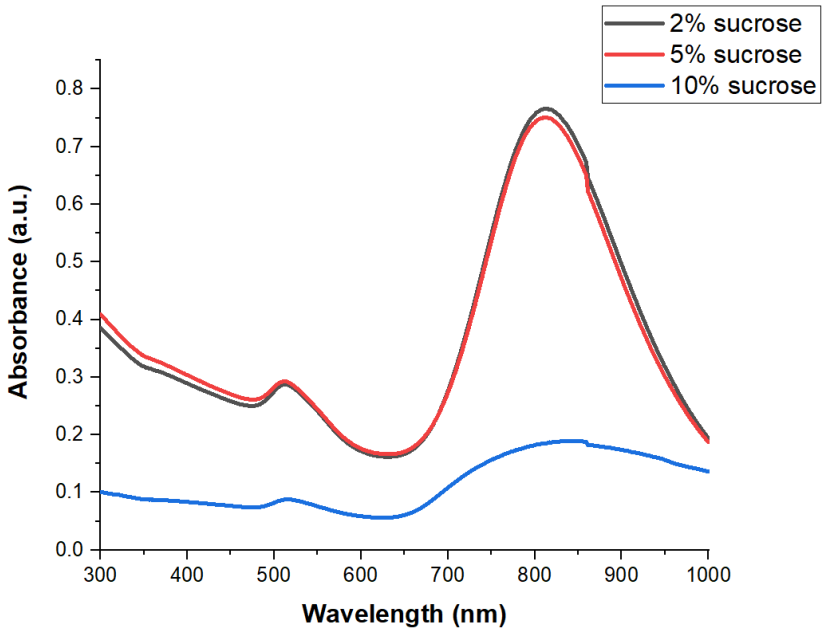

Figure 5A.5 UV-visible-NIR spectra of Ab-GNRs suspended in a resuspension buffer containing different concentrations of sucrose

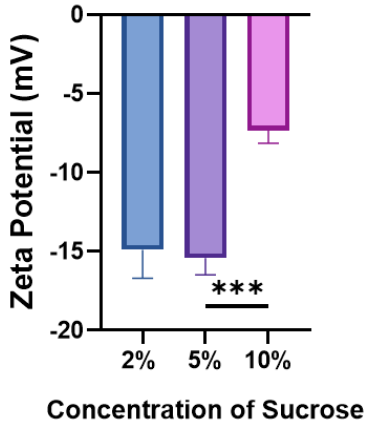

Figure 5A.6 Effect of concentrations of sucrose used in resuspension buffer on zeta potential of Ab-GNRs

Table 5A.3 Zeta potential of Ab-GNRs when suspended in resuspension buffer with different concentrations of sucrose

Sucrose Concentration (%)	Zeta Potential (mV)
2	-14.91 ± 1.77
5	-15.43 ± 1.05
10	-7.33 ± 0.8

5A.3.4. Characterization of Ab-GNRs

The following techniques fully characterized the finally synthesized Ab-GNRs-

5A.3.4.1. UV-Visible-NIR spectroscopy and zeta potential analysis

The LPW of Ab-GNRs was red shifted by around 41 nm compared to the LPW of MUA-GNRs. This res shift confirmed the binding of TSH antibodies on the surface of GNRs. This result was supported by the findings of other studies that have covalently functionalized GNRs with antibodies for biological applications (Busch et al., 2019; F. Cao et al., 2016; J. Cao et al., 2012; Tao et al., 2018; X. Wang et al., 2017). Also, the well-distributed LSPR spectrum with transverse and longitudinal peaks reveals that the GNRs were stable after conjugation with the antibody. The LPW of Ab-GNRs was around 814 nm (Fig. 5A.7). The figure 5A. 7 also contains the LSPR spectra of GNRs and MUA-GNRs to understand the red shift in LPW better.

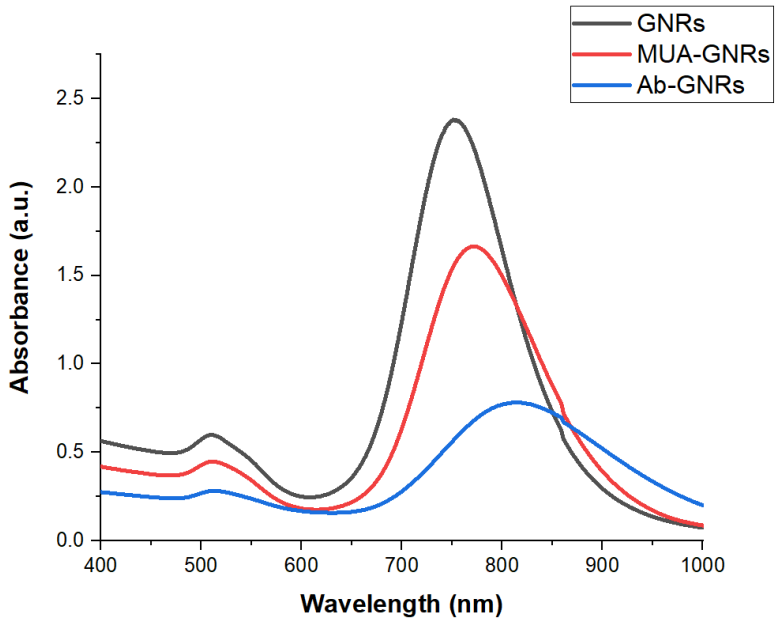

Figure 5A.7 UV-visible-NIR spectra of GNRs, MUA-GNRs and Ab-GNRs

The colloidal stability of Ab-GNRs, which was further used as a conjugate, was essential for the efficient performance of the LFA. The zeta potential of finally synthesized Ab-GNRs was -15.14 ± 0.78 mV (Fig. 5A.8). The decrease in the zeta potential of the Ab-GNRs compared to MUA-GNRs confirms the functionalization of GNRs with TSH antibodies. This finding was consistent with the other studies (Tao et al., 2018; X. Wang et al., 2017; F. Cao et al., 2016). However, the zeta potential value did not reveal the electrostatic stability of Ab-GNRs, but the bioconjugation of nanoparticles with antibodies led to their steric stability (Ansar et al., 2018).

Thus, the colloidal Ab-GNRs were stable. Figure 5A.8 also shows the zeta potential of GNRs and MUA-GNRs for better comparison of the change in surface charge of GNRs after conjugation with TSH antibodies.

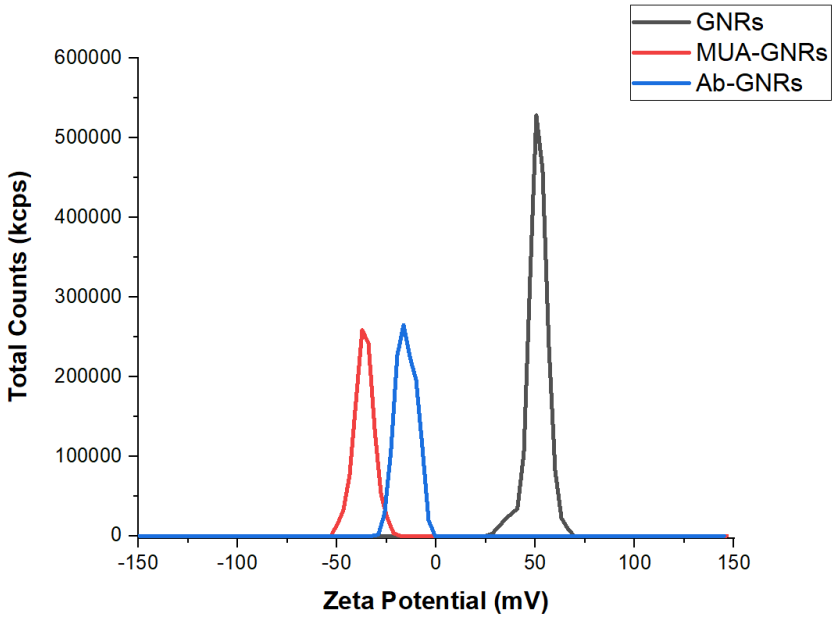

Figure 5A.8 Zeta potential of GNRs, MUA-GNRs and Ab-GNRs

5A.3.4.2. Electron microscopy analysis

The size of Ab-GNRs was determined by HRTEM studies. It was found to be 43.56 ± 5.16 nm x 11.59 ± 1.93 nm (Fig. 5A.9a). This confirms that the morphology of GNRs was maintained after the bioconjugation with the antibodies. Further, the FESEM results also supported the HRTEM results (Fig. 5A.9b). The crystalline nature of Ab-GNRs was very well confirmed by the SAED pattern, which was acquired through HRTEM (Fig. 5A.9c) (Mirshekari et al., 2024) The fringes of the Ab-GNRs were recorded. The d-spacing value of Ab-GNRs was found to be 0.208 nm (Fig. 5A.9d). This finding was in agreement with the d-spacing values of GNRs recorded in other studies (Si et al., 2012; J. Yin et al., 2017; L. Zhang et al., 2016).

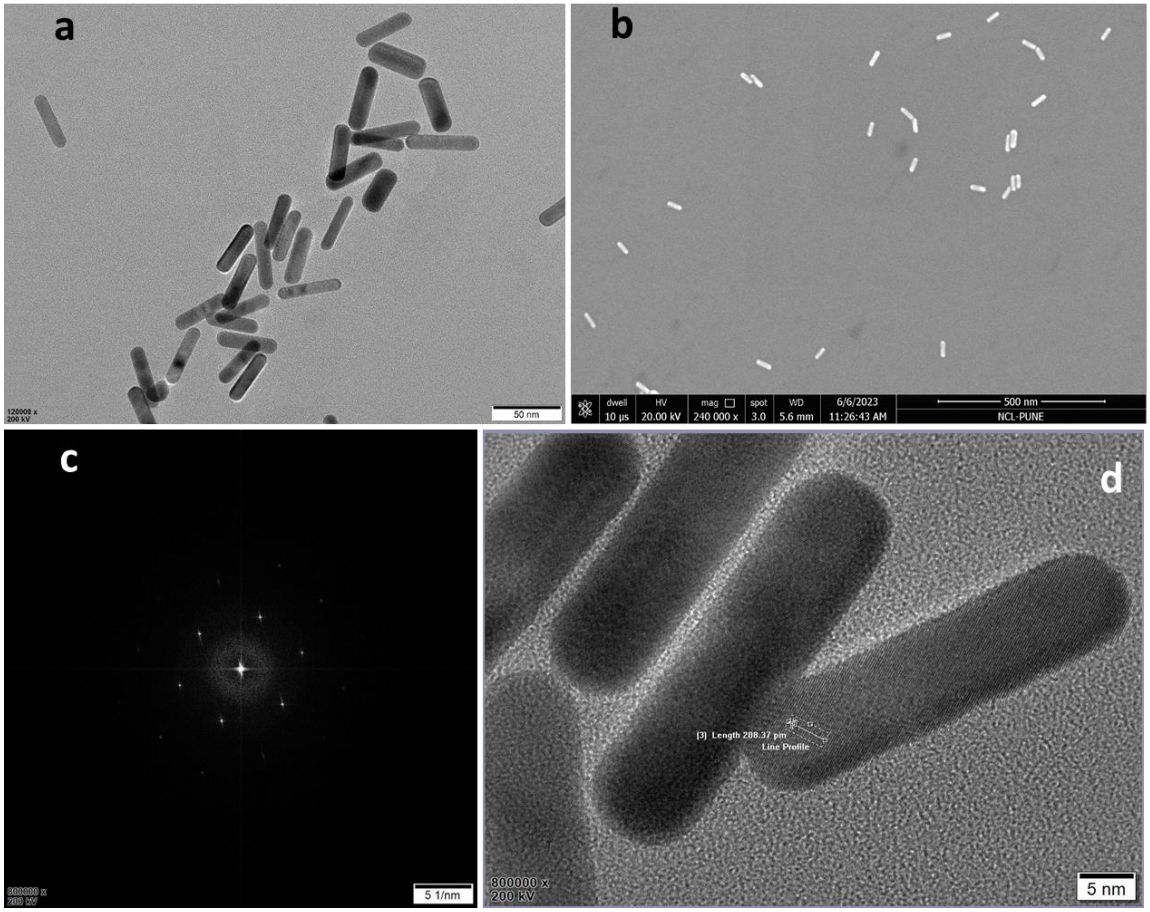

Figure 5A.9 Electron microscopy analysis of Ab-GNRs a) HRTEM image, b) FESEM image, c) SAED pattern and d) fringes of Ab-GNRs

5A.3.4.3. Elemental analysis

The EDX spectrum of Ab-GNRs shows the presence of gold (Au), carbon (C), sulfur (S), oxygen (O) and nitrogen (N) when acquired through both HRTEM (Fig. 5A.10a) and FESEM (Fig. 5A.10b). The additional appearance of nitrogen in EDX spectrum of Ab-GNRs compared to EDX of MUA-GNRs confirms that bioconjugation of TSH antibodies with the MUA-GNRs. The N was due to the amine groups present on the amino acids of antibodies which were responsible for forming peptide linkage with the -COOH group of MUA-GNRs (J. Cao et al., 2012; Mayer et al., 2008; Mirshekari et al., 2024; Panhwar et al., 2021; Sim et al., 2010; Y. Wang et al., 2013). Further, the STEM mapping also supports the elemental study performed by EDX spectroscopy (Fig. 5A.11).

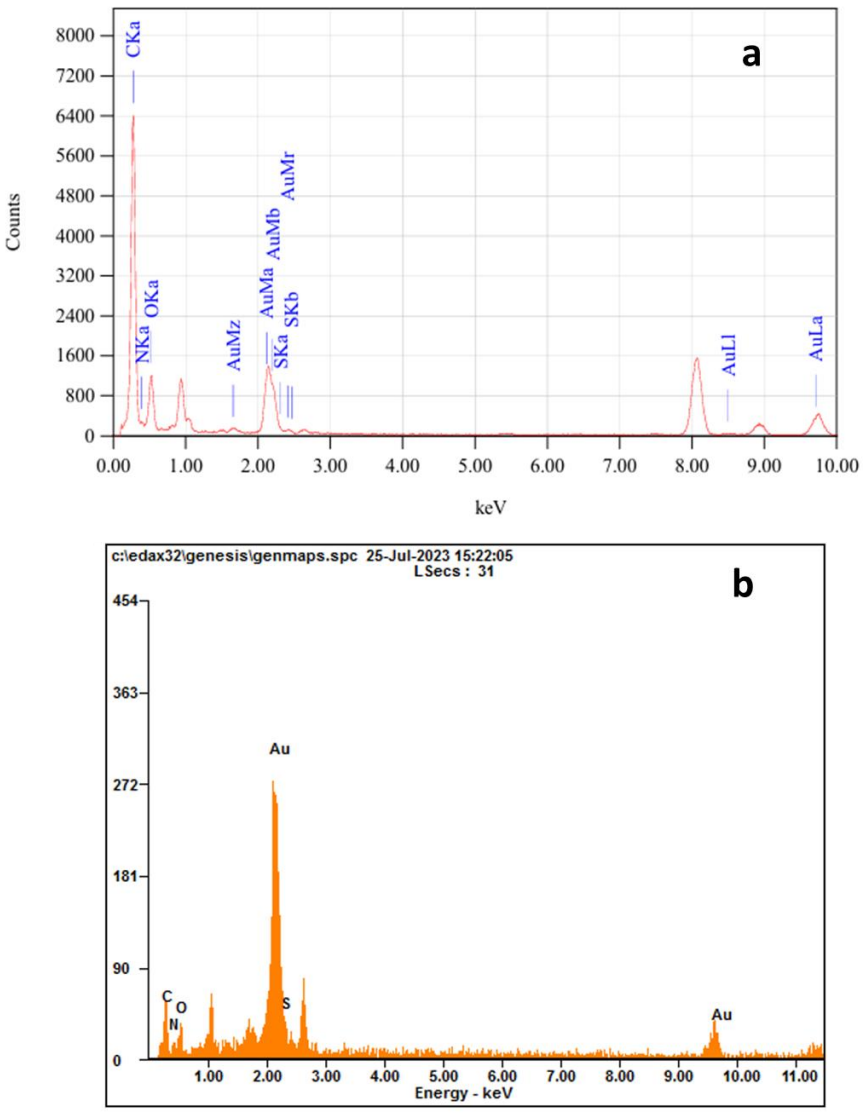

Figure 5A.10 EDX spectra of Ab-GNRs a) from HRTEM and b) from FESEM

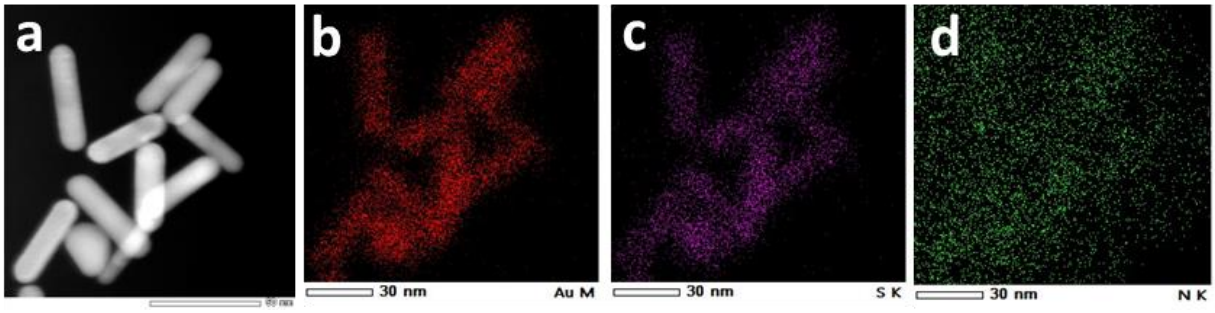

Figure 5A.11 STEM mapping of Ab-GNRs a) STEM image, b) Au, c) S and d) N

The XPS analysis was also performed to confirm the functionalization of GNRs with TSH antibody. The XPS results supported the EDX results. Here, in the XPS spectrum of Ab-GNRs, the dual peak positioned around 83.58 eV and 87.28 eV links to transitions Au $4f_{7/2}$ and

Au $4f_{5/2}$ of Au^0 oxidation state, respectively (L. Su et al., 2017). This data was similar to the XPS spectrum of GNRs and MUA-GNRs. The presence of nitrogen (N) signal along with Au, S, and C confirmed that the TSH antibodies were conjugated with the MUA-GNRs (Fig. 5A.12a-d). The N 1s peaks were at 399.68 eV and 402.58 eV (Fig. 5A.12a,d) (Mohtasebi et al., 2016; L. Su et al., 2017) and the S 2p peak was at 163.18 eV (Fig. 5A.12a, c) (L. Su et al., 2017). The sulfur was present due to 11-MUA and the amino acids in the antibody.

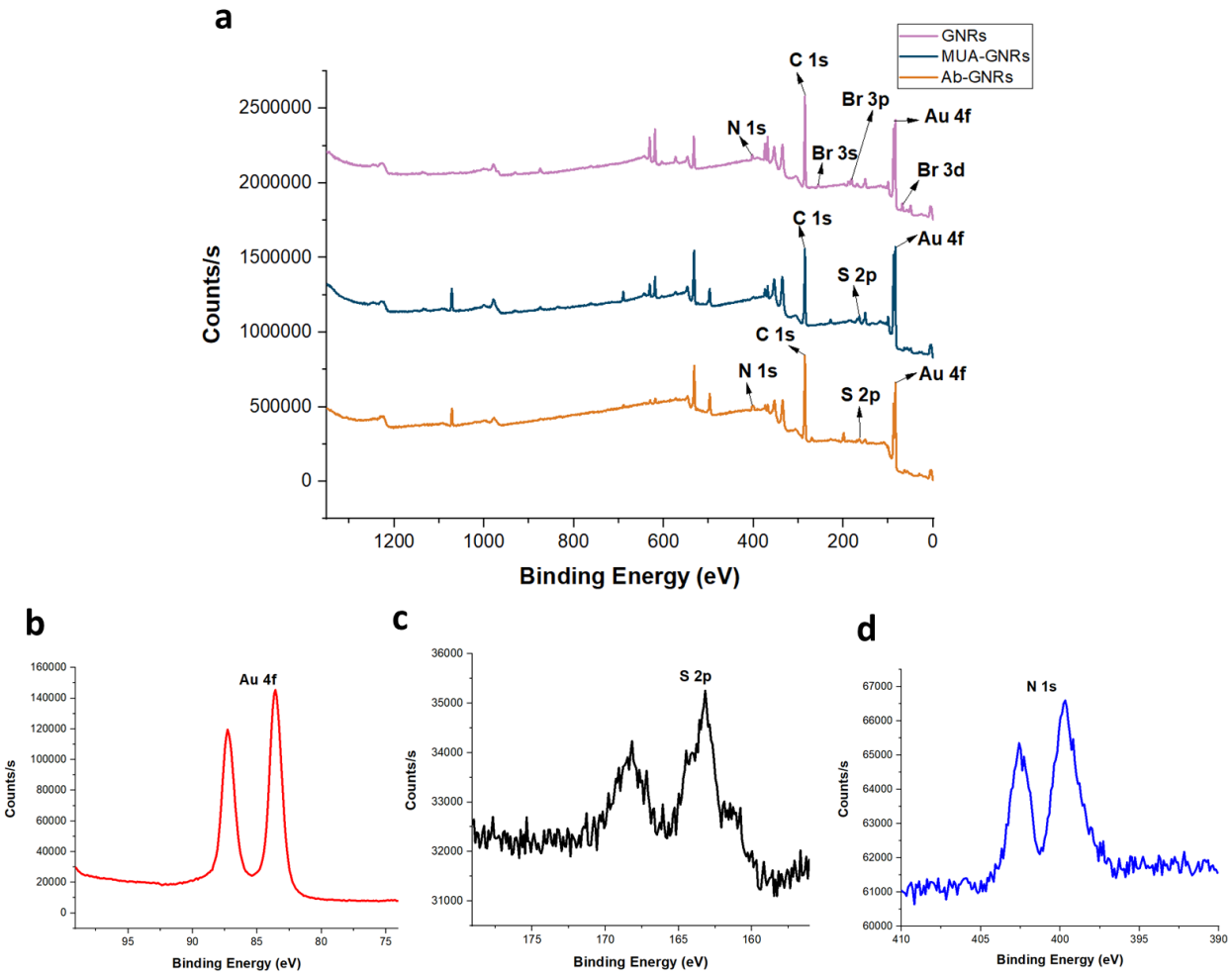

Figure 5A.12 a) XPS spectra of GNRs, MUA-GNRs and Ab-GNRs, b) XPS spectrum of Au 4f of Ab-GNRs, c) XPS spectrum of S 2p of Ab-GNRs and d) XPS spectrum of N 1s of Ab-GNRs

5A.3.4.4. FTIR analysis

The FTIR spectrum of Ab-GNRs had peaks at 1644, 1150, and 858 $cm^{-1,}$ which were the characteristic peaks of the IgG antibody, and the TSH antibody also belongs to the IgG class (H. Huang et al., 2011). IgG antibody's amide I and II regions were found at 1644 and 1533

cm^{-1} (Baird et al., 2020; Daniel-Da-Silva et al., 2009). Further, the peak at 1644 cm^{-1} may also correspond to N-H bending and carbonyl (C=O) group stretching vibration in the -CO-NH- (peptide bond), which were formed between GNRs and TSH antibodies, thus validating the conjugation (Fig. 5A.13) (Mirshekari et al., 2024; Y. Zhang et al., 2016).

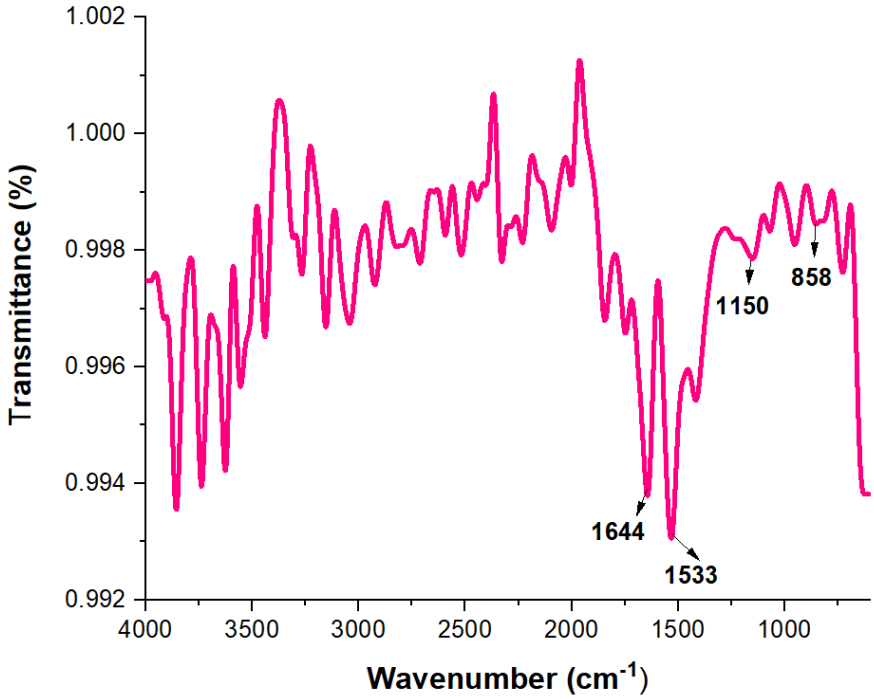

Figure 5A.13 FTIR spectrum of Ab-GNRs

5A.3.5. %BE of TSH antibodies on GNRs

The Bradford assay determined 83.38 ± 0.34 % BE of TSH antibodies on MUA-GNRs. Similarly, F. Cao et al. and Zhan et al. also used the Bradford assay to determine the %BE of antibodies on GNRs (F. Cao et al., 2016; Zhan et al., 2010).

5A.3.6. Stability studies

5A.3.6.1. Stability studies of MUA-GNRs

We studied the stability of MUA-GNRs suspended in 0.01 M borate buffer of pH 9 for 3 months and observed clear suspensions without any precipitate or aggregates during storage at 4°C. The LPW of MUA-GNRs did not change significantly after 3 months and the LSPR spectrum was also in its original form. This suggests that the structural integrity and stability of MUA-GNRs were maintained while storage (Fig. 5A.14). Our results were in agreement with those of Cao et al. They reported the stability of MUA-GNRs for 4 months. However, the small

decrease in absorbance could be due to the deposition of a small amount of MUA-GNRs (J. Cao et al., 2012). The zeta potential values also indicated the good colloidal stability of MUA-GNRs even at the end of 3 months. It was above -30 mV at all the time intervals (Fig. 5A.15).

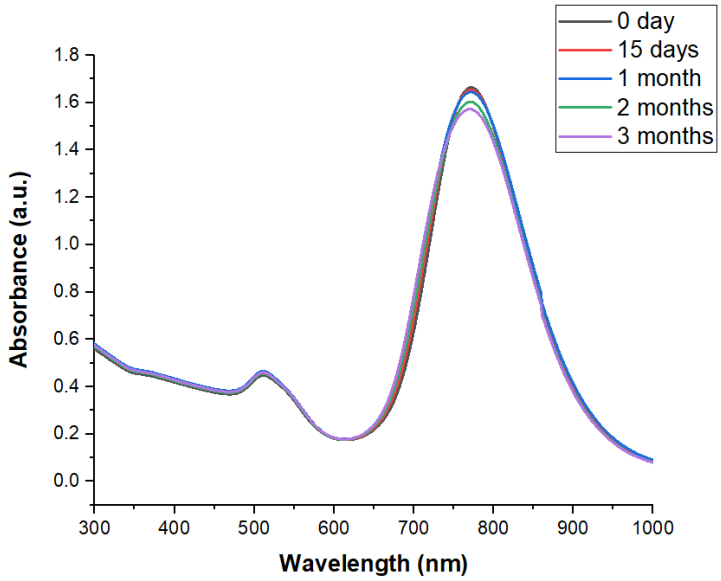

Figure 5A.14 LSPR spectra of MUA-GNRs when stored for 3 months at 4 °C

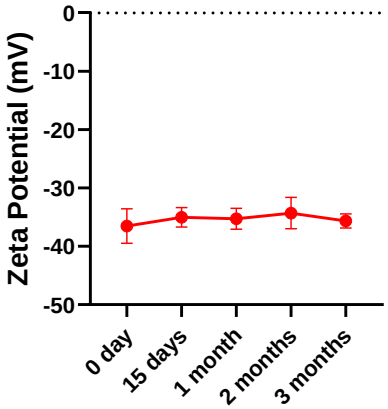

Figure 5A.15 Zeta potential of MUA-GNRs when stored for 3 months at 4 °C

5A.3.6.2. Stability studies of Ab-GNRs

The stability of Ab-GNRs was monitored for 1 month. It was suspended in the resuspension buffer that consisted of BSA as a blocking agent, which helps to block the nonspecific binding sites on the surface of GNRs to enhance the specificity of the conjugate towards the analyte for biosensing purposes (J. Cao et al., 2012; Jung et al., 2013; Z. Li et al., 2019; Y. Liu et al., 2021; Mirjalili et al., 2022; Panhwar et al., 2021; Preechakasedkit et al., 2012; Rodriguez-Quijada et al., 2023; Tan et al., 2021; Y. Zhang et al., 2020) and sucrose as a stabilizer (Jonsson et al.,

2024; J. Li et al., 2024; B. Wang et al., 2009). The clear suspension without aggregation was observed for 15 days; after that, the deposition of Ab-GNRs was visible. The LSPR spectrum was in its original form till 1 month; however, a sudden drop in the absorbance and little broadening of the longitudinal SPR band was noticed at 1 month time (Fig. 5A.16). This decline in absorbance means the color intensity of Ab-GNRs (conjugate) decreased which is not suitable for LFA purpose. Further, the zeta potential values were similar till 15 days but then declined (Fig. 5A.17). This might be due to the aggregation of Ab-GNRs. Hence, the Ab-GNRs were stable and structural integrity was maintained for 15 days when stored at 4 °C. However, the 15-day stability of Ab-GNRs was sufficient because it was further dried on the conjugate pad of LFA for their final use in detecting TSH. Further, in dry form, the sucrose will maintain the characteristics and functionality of Ab-GNRs.

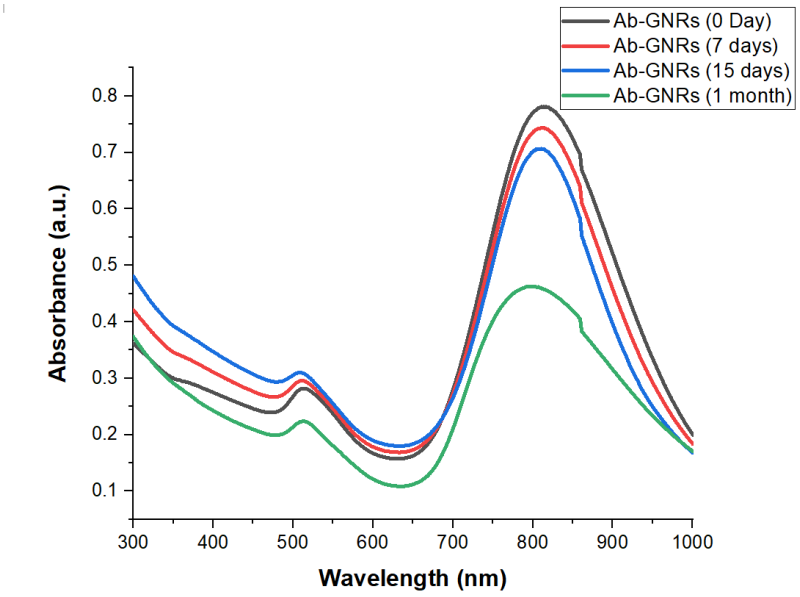

Figure 5A.16 LSPR spectra of Ab-GNRs when stored for 1 month at 4°C

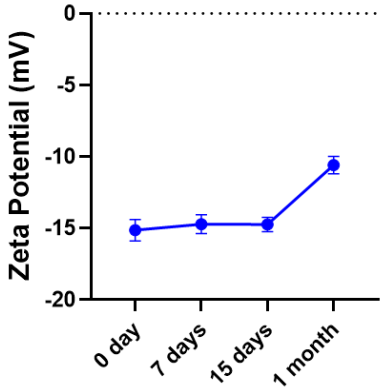

Figure 5A.17 Zeta potential of Ab-GNRs when stored for 1 month at 4 °C

5A.4. Conclusion

This study achieved the successful functionalization of MUA-GNRs with TSH antibodies. The functionalization is covalent, which is more stable than the electrostatic absorption. We optimized certain factors that could affect the stability and conjugation extent of the antibody on GNRs. Firstly, the buffer was fixed to functionalize MUA-GNRs with antibodies. The stability and structural integrity of GNRs were maintained when the functionalization process was performed in the borate buffer. Further, the antibody concentration for functionalization was fixed at 50 µg/ml. Lastly, to keep Ab-GNRs stable, the percentage of sucrose that should be added to the resuspension buffer of Ab-GNRs was optimized to 5%.

The characterization techniques not only revealed the characteristics of Ab-GNRs but also backed the functionalization of MUA-GNRs with TSH antibodies. The UV-visible-NIR spectra of Ab-GNRs in which the LPW was around 814 nm, which was around 41± 3 nm above the LPW of MUA-GNRs. The drop in zeta potential of Ab-GNRs compared to MUA-GNRs confirms the conjugation of antibodies. Further, HRTEM and FESEM analysis supports the appropriate size, shape and morphology of the Ab-GNRs. The SAED revealed the crystalline nature of Ab-of GNRs. The EDX, XPS and FTIR studies validated the bioconjugation of the MUA-GNRs with the TSH antibodies. Importantly, it was found that the MUA-GNRs and Ab-GNRs were stable in colloidal suspension for 3 months and 15 days, respectively, when stored at 4 ^{o}C. Thus, the overall results suggested the synthesis of robust Ab-GNRs, which were further employed as a label/conjugate for preparing LFA.

CHAPTER 5B

Preparation and Optimization of LFA

5B.1. Introduction

Nanobiosensors are rapidly progressing with the aim to solve several limitations of conventional tests. It is a sensor that integrates a biological element with a physiochemical transducer to produce a signal proportional to the analyte, which is then conveyed to a detector. It has served as a very potent developmental inroad in biosensor technology, which has been possible only due to the wonders of nanotechnological implications of the matter (P. Malik et al., 2013). Paper-based nanobiosensors mainly LFAs test strips, are gaining more importance these days due to their rapidity, sensitivity, selectivity, robustness, cost-effective and user-friendly nature (Bikkarolla et al., 2022; Bishop et al., 2019; Hsieh et al., 2017; Parolo & Merkoçi, 2013; Posthuma-trumpie & Korf, 2009). The lateral flow test strips are a paper-based platform for detecting and quantifying analytes in complex mixtures, where the sample is placed on a test device and the results are displayed within 10-20 min (Posthuma-trumpie & Korf, 2009).

LFA mainly works on the principle of competitive and sandwich assay (Parolo et al., 2020; Sajid et al., 2015). It can efficiently detect different types of analytes, such as pathogens, hormones, metabolites, and drugs, as well as analytes related to the environment (Posthuma-trumpie & Korf, 2009). The LFA bio-sensing platform mainly comprises four parts – sample pad, conjugate pad, test pad and absorbent pad (X. Ge et al., 2014; Parolo & Merkoçi, 2013; Sajid et al., 2015). The major components of the LFA are the reporter molecule or label and capture and detection antibody (Parolo et al., 2020). There are many types of labels that can be employed in LFA, such as gold nanoparticles, latex beads, quantum dots, liposomes, and magnetic nanoparticles. However, gold nanoparticles are generally preferred due to their intense color (Bikkarolla et al., 2022; Parolo & Merkoçi, 2013; Chamorro-Garcia & Merkoçi, 2016). Further, it has been found that GNRs may impactfully enhance the sensitivity of the LFA compared to the spherical gold nanoparticles (Bishop et al., 2019). Therefore, we explored GNRs as a potent label for the functioning of the LFA. It should also be noted that the commercially available TSH testing kits are qualitative and only used for the detection of hypothyroidism due to high TSH concentration in this condition, which is above 5 µIU/ml. However, in hyperthyroidism, the concentration of TSH reaches below 0.5 µIU/ml, which is difficult to elucidate by LFA (Choi et al., 2017).

Herein, we have used Ab-GNRs synthesized earlier as a label to detect TSH through LFA. In LFAs, the sample flows through the pads by the passive force, i.e. capillary action (Bishop et

al., 2019). Therefore, the detailed optimization of various fabrication components of LFA is required for sensitive assessment of the analyte of interest (Bikkarolla et al., 2022). Thus, we have optimized certain conditions like the OD of the label, the concentration of the capture antibody and the volume of sample needed for the LFA. Before this, we tested the sensitivity and selectivity of the label towards TSH by using LSPR sensing, i.e. the UV-visible-NIR spectroscopy analysis of the red shift in longitudinal SPR of Ab-GNRs after binding with the antigen, i.e. TSH. Further, the sensitivity and selectivity of the LFA for TSH were also assessed. This study helped us to enhance the performance of the LFA.

5B.2. Method

5B.2.1. Sensitivity and selectivity of the conjugate (Ab-GNRs) to detect TSH

The sensitivity and selectivity of the label or probe (Ab-GNRs) were tested initially by UV-visible-NIR spectroscopy by determining the red shift in the LPW of Ab-GNRs on binding with the antigen (TSH). For this, 500 µl of Ab-GNRs was mixed with different concentrations of 50µl TSH (0.01, 0.05, 0.1, 0.5, 1, 5, 10, 15 and 20 µIU/ml) and allowed to react for 20 min. Next, the mixture was centrifuged to remove unbound antigen at 8000 rpm for 15 min and the pellet was resuspended in 500 µl DI water to record the LSPR spectrum (Mirjalili et al., 2022; Salahvarzi et al., 2017). Further, to test the selectivity of the probe, it was mixed with FSH, LH and hCG hormones and the LSPR spectrum was recorded after centrifugation.

5B.2.2. Optimization and preparation of LFA

We have used the protocol reported by Parolo et al., 2020 for preparing LFAs (Parolo et al., 2020) The procedure was described in Chapter 2, Section 2.2.7.

5B.2.2.1. Optimization of OD of the label or conjugate (Ab-GNRs)

We varied the OD of conjugate at 5, 10 and 20. These OD's conjugate was sprayed on the conjugate pad, and after adding plain assay buffer, the intensity of the control was determined by visual examination.

5B.2.2.2. Optimization of concentration of capture antibody on the test line

The test line antibody concentration was varied from 1-3 mg/ml. For this, the different concentration of antibody was dispensed on the test line, and after the addition of TSH (10 µIU/ml), the intensity of color development at the test was observed.

5B.2.2.3. Optimization of sample volume

We checked the effect of sample volume on the performance of the LFA. For this, the LFA was tested with different sample volumes of 5 µIU/ml of TSH. The volumes were 30, 40 and 50 µl. Further, the color development at the test line was examined.

5B.2.2.4. Sensitivity of LFA

LFA with all the finally optimized parameters was tested for its sensitivity with different concentrations of TSH from (0.01 µIU/ml to 20 µIU/ml) and the color development at the test line was noticed.

5B.2.2.5. Selectivity testing of LFA

The selectivity of the prepared LFA was tested by adding 50 µl of FSH (15 mIU/ml), LH (25 mIU/ml) and hCG (100 mIU/ml) hormones to the sample pad and noticing the color development at the test line.

5B.2.2.6. Reproducibility of the LFA

The LFA was tested at various time points with different TSH concentrations to assess its reproducibility.

5B.3. Results and discussion

5B.3.1. Sensitivity and selectivity of the conjugate (Ab-GNRs) to detect TSH

Initially, UV-visible-NIR spectroscopy studies were performed to confirm the sensing potential of the conjugate (Ab-GNRs) towards the TSH. Herein, it was found that when Ab-GNRs were mixed with the increasing concentrations of TSH, there was an increase in red shift of the LPW of Ab-GNRs compared to unreacted Ab-GNRs (Fig. 5B.1a, b). This confirmed that the conjugate was efficient in detecting TSH. This shift in LPW was due to the change in the refractive index of the medium owing to the antigen-antibody binding interaction taking place at the surface of Ab-GNRs. Monitoring LSPR is the surface-sensitive optical technique to determine biomolecular interaction at the surface of nanoparticles (Salahvarzi et al., 2017). However, the limit of detection (LOD) or sensitivity of TSH, based on LSPR sensing, was 0.05 µIU/ml with an average red shift of 1.15 nm in the LPW of Ab-GNRs. Also, there was no shift in the LPW at 0.01 µIU/ml TSH concentration and it was also found that after 10 µIU/ml of TSH, the red shift in the LPW of GNRs was constant, which may be due to the saturation of antigen (TSH) binding sites on Ab-GNRs (Fig. 5B.1a, b). Similarly, Salahvarzi et al. used the

gold nanoparticles for LSPR sensing of TSH; their probe's LOD was 1.71 µIU/ml (Salahvarzi et al., 2017), which was much higher than the LOD of our Ab-GNRs. Our study was also consistent with the study of Mirjalili et al., where they used GNRs conjugated with antibodies for human serum albumin (HSA) LSPR sensing (Mirjalili et al., 2022)

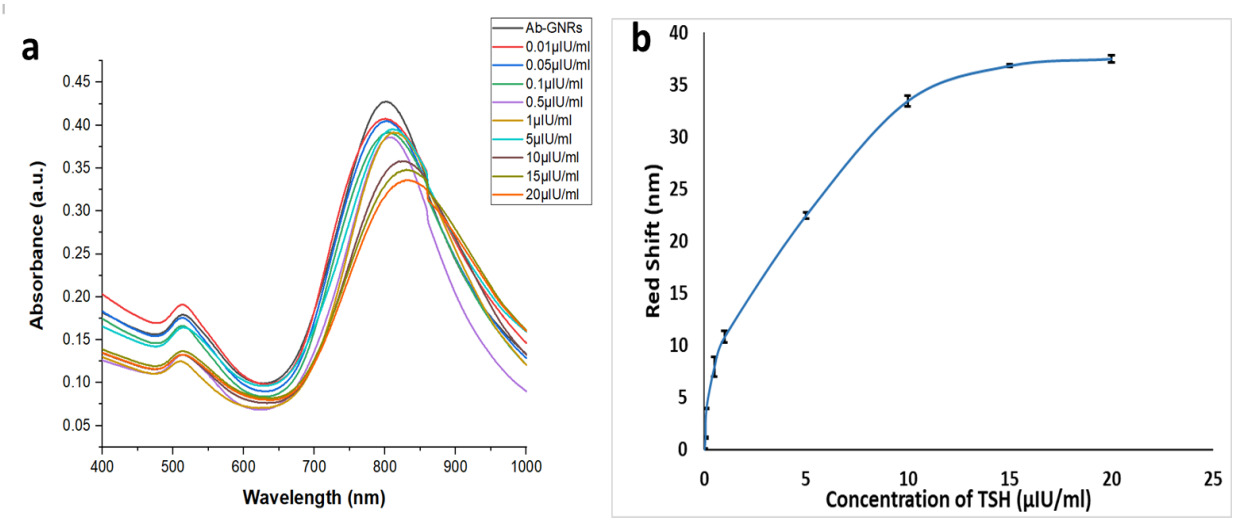

Figure 5B.1 a) Sensitivity testing of Ab-GNRs to detect TSH based on UV-visible-NIR spectroscopy analysis and b) Red shift in longitudinal SPR band of Ab-GNRs at different concentrations of TSH

Further, the specificity of the conjugate towards TSH was assessed by using 50 µl of FSH (15 mIU/ml), LH (25 mIU/ml) and hCG (100 mIU/ml) with Ab-GNRs instead of TSH. Based on LSPR analysis, no significant change in LPW of Ab-GNRs was observed when reacted with the other hormones (hCG, LH and FSH), which have α-subunit same as TSH (Fig. 5B.2a-c) (D. Wang et al., 2015; Wani et al., 2016). Thus, the conjugate was specific towards TSH only. Similarly, Mirjalili et al. also performed specificity testing based on LSPR studies (Mirjalili et al., 2022).

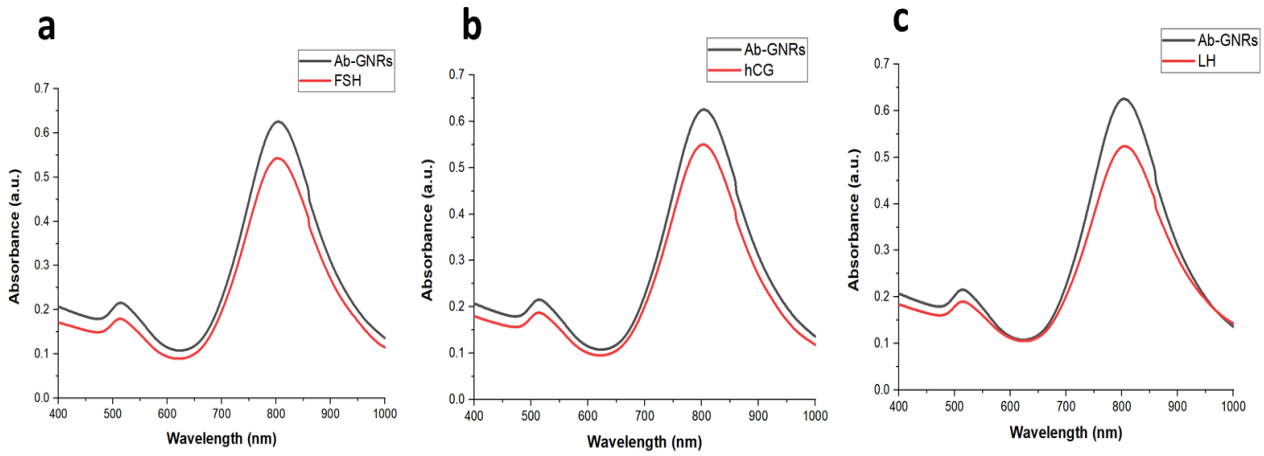

Figure 5B.2 Specificity testing of Ab-GNRs towards TSH by UV-visible-NIR spectroscopy analysis when tested with a) FSH, b) hCG and c) LH

5B.3.2. Optimization and preparation of LFA

The LFA was prepared and certain factors were optimized to enhance its performance. Firstly, the sample pad was soaked and treated with buffer and dried. After that, the conjugate of a particular OD was sprayed on the conjugate and dried. The test pad was prepared by dispensing a test line (mouse monoclonal TSH antibody (10-2429)) and control line (Anti-Mouse IgG (whole molecule) antibody produced in goat) and dried in a dehumidified environment. Further, all these pads, along with the absorbent pads, were assembled with overlapping of 1mm and cut into strips of 4 mm width.

The basic working of LFA involves binding of TSH present in the sample with the detection antibody present on GNRs at the conjugate pad, then this TSH-Ab-GNRs complex will flow through the test pad and TSH of the complex will be captured by the capture antibody at the test line which is also specific for TSH, leading to color development at the test line. Further, the unbound Ab-GNRs bind with the anti-mouse antibody, which is a secondary antibody for the primary detection antibody, leading to color development at the control line. Thus, the generation of color also happens at the control line when the analyte of interest is not present in the sample; this color formation confirms the proper functioning of the LFA (Parolo et al., 2020; Sajid et al., 2015).

5B.3.2.1. Optimization of OD of the label or conjugate (Ab-GNRs)

The OD of the conjugate was varied to enhance the performance of the LFA. We found that with the increase in OD of the conjugate, the intensity of the color at the control line also

increased (Fig. 5B.3). So, we finalized 20 OD of the conjugate for the LFA. We examined this parameter's effect only on the basis of color at the control line only, as we wanted to know the color intensity development when the OD of the conjugate was varied. So, a test line was not necessary for this factor.

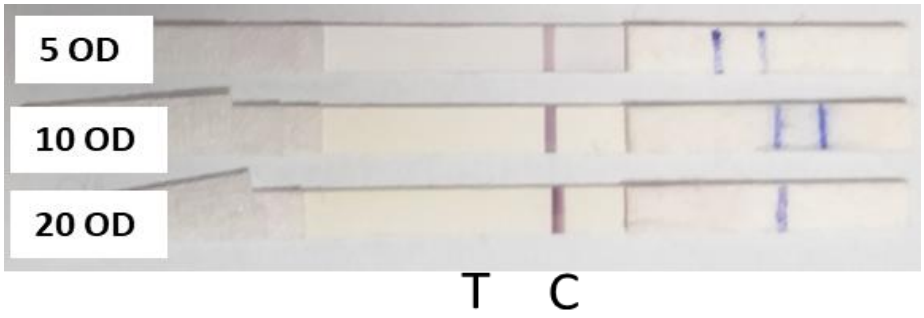

Figure 5B.3 Optimization of the OD of the conjugate for LFA

5B.3.2.2. Optimization of concentration of capture antibody on the test line

After preparing LFA with a test line comprised of different concentrations of capture antibody, it was tested with TSH. The test line with 3 mg/ml antibody concentration was found appropriate for the LFA because the color intensity at the test line was more compared to other antibody concentrations at the test line. Notably, the same concentration of TSH was used for the analysis of test lines prepared using different antibody concentrations (Fig. 5B.4). Therefore, 3 mg/ml capture antibody concentration was optimized for the LFA.

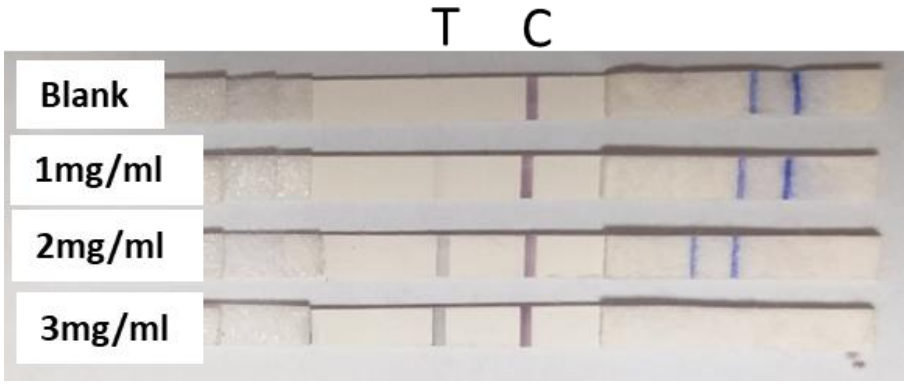

Figure 5B.4 Optimization of the concentration of capture antibody on the test line of LFA

5B.3.2.3. Optimization of sample volume

The sample volume was optimized to enhance the sensitivity of the LFA. For this, the TSH concentration was kept constant and the volume was varied. However, a more intense colored

test line was observed when the sample volume was 50 µl compared to 30 and 40 µl (Fig. 5B.5). Therefore, the 50 µl sample volume was fixed.

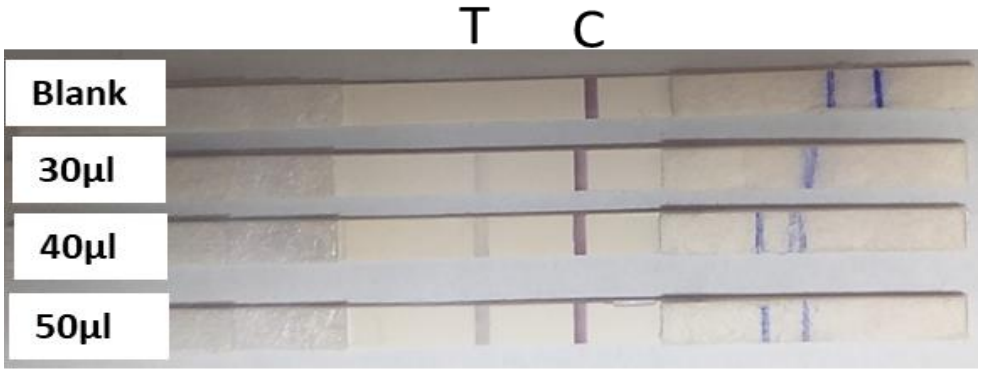

Figure 5B.5 Optimization of the sample volume for LFA

5B.3.2.4. Sensitivity of LFA

When the LFAs were tested with different concentrations of TSH, the color development at the test line was observed till 0.3 µIU/ml TSH concentration. Below 0.3 µIU/ml, no color was observed at the test line; however, from 0.3 µIU/ml as the concentration increased, the color intensity at the test line also increased (Fig. 5B.6). Thus, the LOD of the LFA was 0.3 µIU/ml. From this, we can say that the LFA could examine both hypothyroidism and hyperthyroidism semi-quantitatively. As, we observed a dark test line after 5 µIU/ml TSH concentration, so the appearance of the darker test line signifies hypothyroidism, as the concentration of TSH raches above 5 µIU/ml in case of hypothyroidism. While no appearance or very faint appearance of the test line indicates less concentration of TSH, which is related to the hyperthyroidism condition. In hyperthyroidism, TSH concentration reaches below 0.5 µIU/ml. Thus, our LFA device did not show color formation at the test line when the concentration of TSH reaches below 0.3 µIU/ml and it generates a very faint line when the concentration is below 0.5 µIU/ml. Similarly, You et al. achieved the same LOD for the estimation of TSH using AuNPs as the label for LFA, but their study involved the use of a cell phone to quantify the signal (You et al., 2013). In contrast, our study attained the same LOD with GNRs as a label without employing any quantification method. Also, Choi et al. prepared LFA for TSH detection using gold nanoparticles as labels. They found a LOD of 1.5 µIU/ml with the naked eye, which was much higher than our study (Choi et al., 2017). This indicates that GNRs are better labels than spherical gold nanoparticles as they enhanced the sensitivity of the LFA to detect TSH. In

another study, lab-on-chip was developed for sensing TSH; the LOD of the chip was 1.9 µIU/ml (Jung et al., 2013).

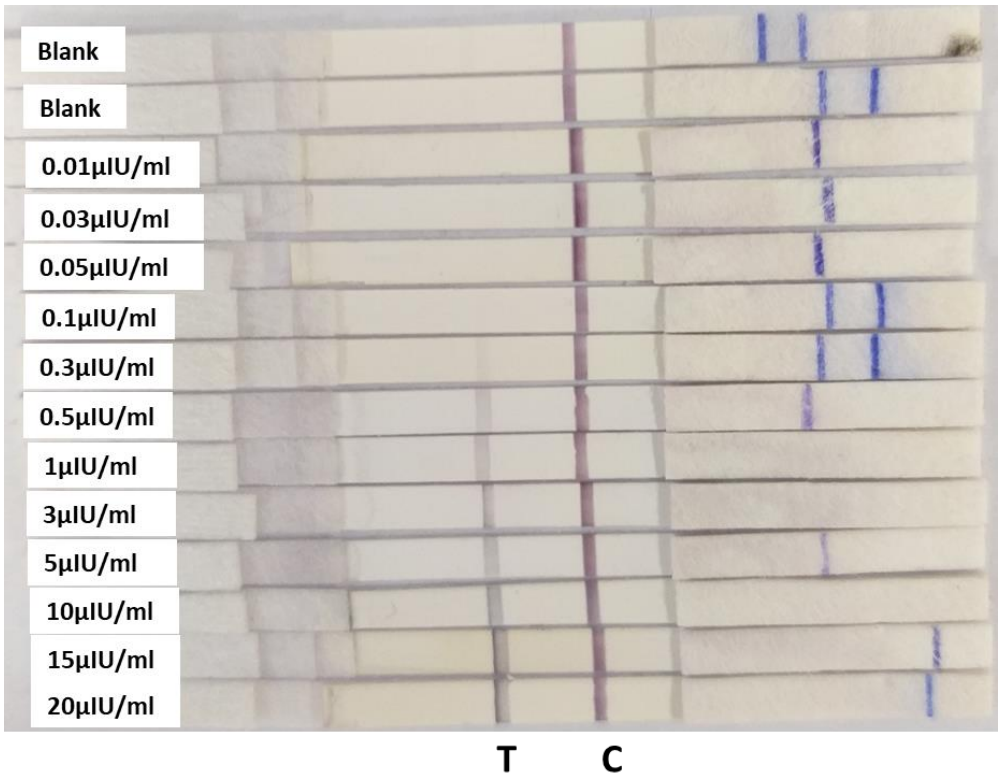

Figure 5B.6 Sensitivity testing of LFA

5B.3.2.5. Selectivity testing of LFA

The LFA device was tested with FSH, LH, and hCG due to its α subunit being similar to TSH. Although, no obvious color development at the test line was observed when the LFA was tested with a high concentration of all these three hormones individually (Fig. 5B.7). Thus, this shows that the chances of false positive results will be low.

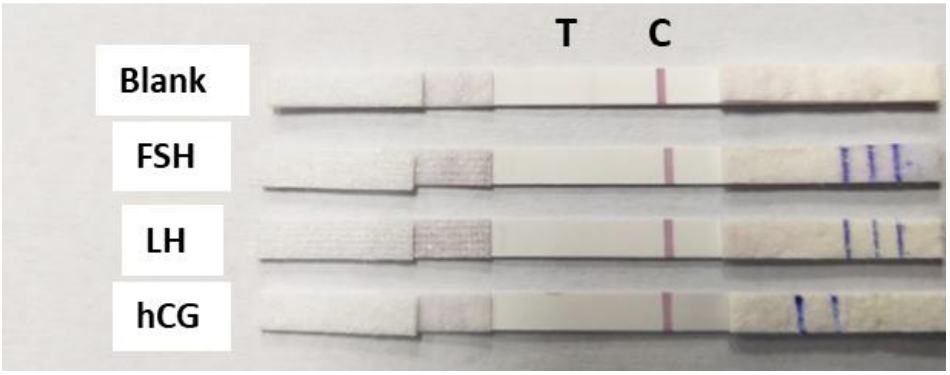

Figure 5B.7 Selectivity testing of the LFA

5B.3.2.6. Reproducibility of the LFA

When the LFA strips were tested at different time intervals, it was found that the strips could reproduce results till 3 months. Figure 5B.8 shows the reproducibility of the LFA when tested after 1 (Fig. 5B.8a), 2 (Fig. 5B.8b) and 3 months (Fig. 5B.8c).

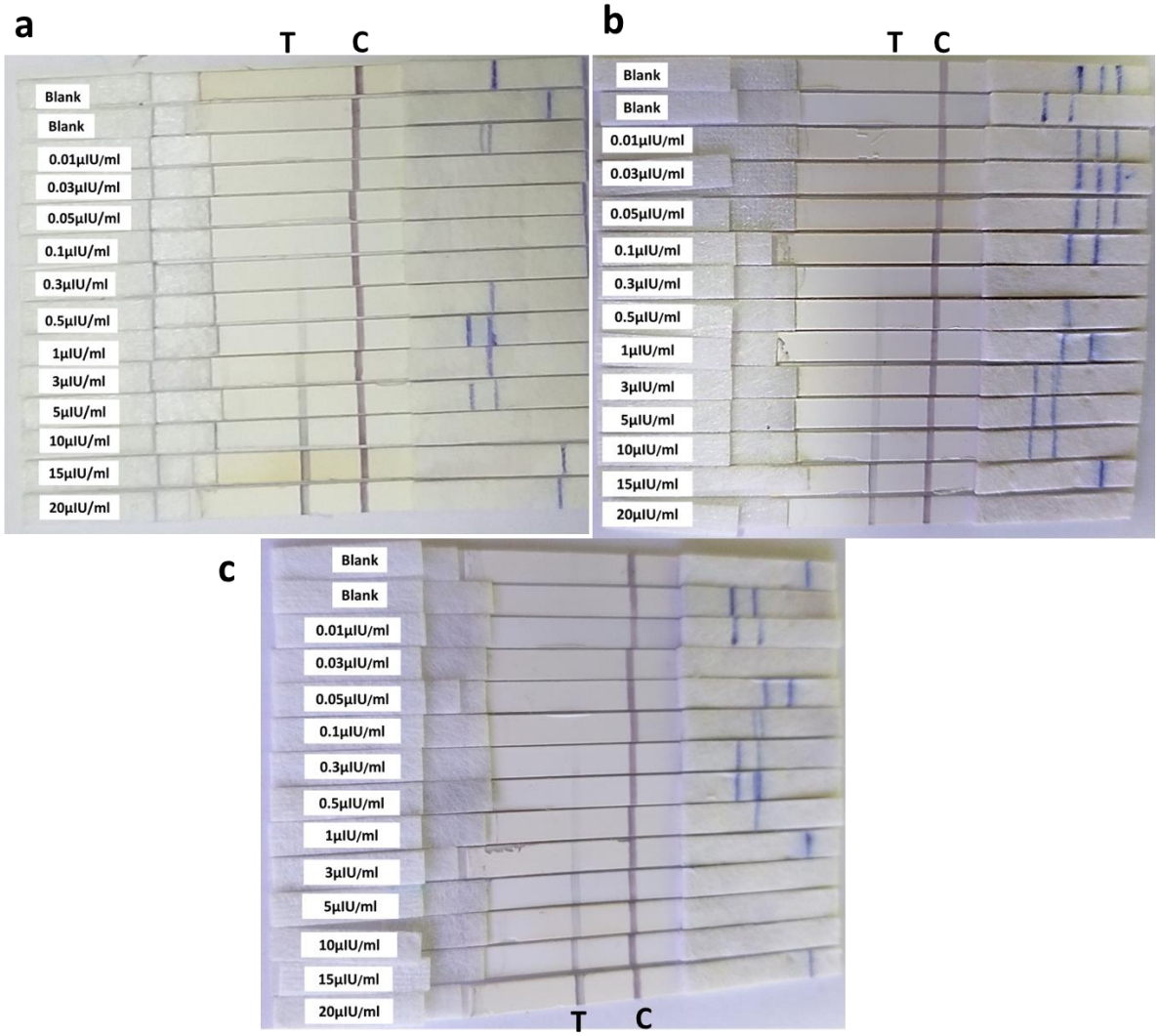

Figure 5B.8 Reproducibility of the LFA when tested after a) 1 month, b) 2 months and c) 3 months

5B.4. Conclusion

This study is proof of concept that GNRs are the potent label for LFA. We have successfully prepared fast, user-friendly and robust LFA by using GNRs as a reporter or label or conjugate to detect TSH. Firstly, the sensing potential of the conjugate was confirmed by a UV-visible-NIR spectroscopy study which determined the binding between TSH and TSH antibodies

attached to the surface of GNRs. The red shift in the LPW of Ab-GNRs validated this binding. Also, the UV-visible-NIR study revealed that the Ab-GNRs were specific towards TSH sensing. Further, the different parts of the LFA, i.e. sample pad, test pad, conjugate pad and absorbent pad, were prepared and assembled, and the performance of the LFA to detect TSH was assessed. It was observed that by optimizing the OD of the conjugate, the concentration of the capture antibody and the sample volume, the sensitivity of the LFA was enhanced. The LOD of the LFA was found to be 0.3 μIU/ml, and the LFA was specific towards TSH; it did not show any cross-reactivity with the hormones FSH, LH and hCG. Additionally, this LFA device could function effectively till 3 months when kept in a desiccated environment.

The LFA was capable of semi-quantitatively elucidating hypothyroidism and hypothyroidism based on the TSH without using any quantification method. As, the normal range of TSH in normal adult humans is 0.5-5 μIU/ml. Therefore, when the concentration of TSH in the sample is below 0.3 μIU/ml, there will be no appearance of the test line signifying hyperthyroidism or the appearance of a very faint test line will also confirm hyperthyroidism as it was observed that below 0.5 μIU/ml TSH concentration, the LFA device generates very faint test line. While when the concentration of TSH is above 5 μIU/ml in the sample, a darker test line will appear, leading to the determination of hypothyroidism. Conclusively, GNRs acted as a potent and sensitive label for LFA; they can also be employed for sensing other infectious and noninfectious diseases as well as environmental analytes.

CHAPTER 6

Functionalized GNRs for Bioimaging Studies

CHAPTER 6A

Optimization, Synthesis and Characterization of γPGA Functionalized GNRs

6A.1. Introduction

Another aspect of the work was to employ GNRs for bioimaging studies. GNRs are a potent bioimaging contrast agent due to their LSPR property. The SPR band in the NIR region is advantageous for enhancing the *in vivo* imaging activity of GNRs because of minimal NIR light absorption by water and human tissues (Kim et al., 2023; Haine & Niidome, 2017; Varma et al., 2025). In addition to this, other attributes like long blood circulation time, enhanced light scattering, good photostability, ease of surface functionalization, etc., also contribute in making GNRs efficient bioimaging agents (Rizwan Younis et al., 2021; Varma et al., 2025; J. Zhou et al., 2017). Although, it is very necessary to make GNRs biocompatible and stable before employing them for bioimaging studies due to the presence of cytotoxic CTAB on their surface (Gui & Cui, 2012; J. He et al., 2018). Also, functionalization helps the nanoparticles to escape the RES clearance and boost their circulation time, which is a significant requirement for various *in vivo* and *in vitro* therapeutic and bioimaging studies (Dreaden et al., 2011; Gao & Chen, 2023).

In this study, we have surface-coated GNRs and MUA-GNRs with a biologically synthesized anionic polymer, i.e. γPGA, by using *Bacillus paralicheniformis* NCIM 5769 (P. G. Nair et al., 2021). γPGA is a non-toxic, water-soluble, biodegradable, nonimmunogenic and biocompatible polymer (Ajayeoba et al., 2019; Khalil et al., 2018; Z. Li et al., 2017). γPGA can be synthesized by chemical method, microbial fermentation and an enzymatic conversion method. However, microbial fermentation is the major preferred method for γPGA synthesis (Cai et al., 2024). γPGA is a homopolyamide made up of D and L glutamic residues, which are connected by the amide linkage (Ajayeoba et al., 2019; Hejazi et al., 2023; Khalil et al., 2018). γPGA can be used for drug delivery (Ajayeoba et al., 2019; Khalil et al., 2018), wound healing (P. G. Nair et al., 2021), agricultural (Cai et al., 2024), and many other applications (Cai et al., 2024; Z. Li et al., 2017). The γPGA has a free -COOH group at its side chain (Cai et al., 2024; Khalil et al., 2018), which can form an electrostatic bond with positively charged CTAB-GNRs (Vigderman et al., 2012; J. Zhou et al., 2017). Further, γPGA was also used to coat MUA-GNRs; thus, it could form weak interactions like hydrogen bonding with MUA-GNRs (March & Brown, 2024). Therefore, functionalizing GNRs with γPGA aimed to aid GNRs with the properties of γPGA, to augment their biocompatibility, stability and biomedical imaging potential of GNRs by avoiding their RES clearance.

Herein, we have optimized the various parameters that affect the surface coating of GNRs and MUA-GNRs with γPGAs procured from National Collection of Industrial Microorganisms

(NCIM). We initially screened three types of γPGA synthesized using different substrates for coating GNRs and a standard commercially available γPGA procured from Sigma. Further, we have finalized γPGA synthesized using tomato waste as a substrate and optimized its concentration and volume needed for effective surface coating of GNRs based on UV-visible-NIR and zeta potential studies. The γPGA-GNRs and γPGA-MUA-GNRs were characterized and the coating of γPGA was also validated by employing various high-end analytical techniques. Additionally, we also assessed the stability of functionalized and non-functionalized GNRs to determine any structural variation during storage over a period of time. This functionalization of GNRs and their stability investigation was required to utilize them for further *in vitro* studies.

6A.2. Method

To functionalize GNRs and MUA-GNRs, we have taken four types [γPGA (Sucrose), γPGA (Jaggery), γPGA (Tomato waste) and γPGA (Commercial)] of γPGA. The first 3 were biologically synthesized by using different substrates taken from the NCIM, CSIR-National Chemical Laboratory, Pune, India 411008. Further, we have used the protocol mentioned in Chapter 2, Section 2.2.4. for functionalization

6A.2.1. Screening of different types of γPGA for functionalization and optimization of the concentration of γPGA

We prepared three groups of GNRs: 1) GNRs, 2) MUA-GNRs in DI water, and 3) MUA-GNRs in 0.01 M borate buffer. GNRs from each group were functionalized with all four types of γPGA at three different concentrations (0.1 mg/ml, 0.5 mg/ml and 1 mg/ml). The functionalization was confirmed by observing the red shift in the UV-vis-NIR spectra of GNRs as well as zeta potential measurements.

6A.2.2. Optimization of volume of γPGA

To study the effect of the volume of γPGA on the functionalization of 5 ml GNRs, at different volumes of γPGA, i.e. 0.75, 1, 1.25 and 1.5 ml, the red shift in LPW and zeta potential of GNRs and MUA-GNRs suspended in DI water were studied.

6A.2.3. Characterization of γPGA-GNRs and γPGA-MUA-GNRs

The γPGA-GNRs and γPGA-MUA-GNRs were characterized by numerous analytical techniques. The LSPR spectra and the surface charge were investigated by the UV-visible-NIR

spectroscopy and zeta potential analysis, respectively. The electron microscopy (HRTEM & FESEM) studies were employed to reveal the structural information of the GNRs. The validation of functionalization was achieved by FTIR and XPS studies.

6A.2.4. Stability studies

The stability of GNRs, MUA-GNRs, γPGA-GNRs and γPGA-MUA-GNRs, which were suspended in DI water and stored at 4 ^{o}C, was checked for 3 months. It was determined by acquiring LSPR spectra and zeta potential measurements periodically.

6A.3. Results and discussion

6A.3.1. Screening of different types of γPGA for functionalization and optimization of the concentration of γPGA

Initially, we tested four types of γPGA for the functionalization of GNRs, MUA-GNRs in DI water and MUA-GNRs in borate buffer at different concentrations of γPGA. The γPGA synthesized using jaggery and sucrose as the substrate did not show appropriate results for all three groups of GNRs. The LSPR spectra revealed the aggregations and distortion of the structure of GNRs at all the concentrations of γPGA (jaggery) (Fig. 6A.1a-f) and γPGA (sucrose) (Fig. 6A.2a-f). Further, the zeta potential values also signify the instability of the GNRs. Although, the change of zeta potential of GNRs from positive to negative due to the free -COOH group of γPGA which confirms the coating of γPGA (J. He et al., 2018; Jain et al., 2019; L. Su et al., 2017; J. Wang et al., 2017). Also, in the case of MUA-GNRs, the zeta potential decreased below -30 mV, which validated the coating of MUA-GNRs with γPGA.

However, when γPGA synthesized using tomato waste was used to functionalize all the groups of GNRs, an appropriate red shift in LPW of GNRs and MUA-GNRs in DI water was observed at 1mg/ml concentration of γPGA (Fig. 6A.3a-f). Thereafter, on investigating zeta potential, it was found that GNRs and MUA-GNRs were moderately stable electrostatically at 1mg/ml concentration of γPGA. However, the γPGA coating provided steric stability to different types of GNRs. Although, the results for MUA-GNRs in borate buffer reveal a very less red shift in the LPW of MUA-GNRs (borate buffer) and instability of the γPGA-MUA-GNRs. We have also used standard γPGA (commercial) to functionalize all the groups of GNRs. This γPGA did not show adequate results for MUA-GNRs in borate buffer, as aggregations were observed at all the concentrations of γPGA. Although, the red shift in the LPW was observed at 1 and 0.5 mg/ml γPGA concentration in GNRs and at 1 mg/ml concentration in MUA-GNRs in DI water

groups (Fig. 6A.4a-f). Comparatively, the shift was lesser than the γPGA (tomato waste). The zeta potential reveals the instability of the γPGA (commercial) functionalized GNRs for every group. Tables 6A.1, 6A.2, 6A.3 and 6A.4 thoroughly summarize the UV-visible-NIR spectroscopy results and the zeta potential results (Table 6A.1, 6A.2, 6A.3 and 6A.4). Notably, we have selected 1 mg/ml γPGA (tomato waste) to functionalize 1ml GNRs and MUA-GNRs (DI water), as more red shift was recorded in the LPW and the zeta potential revealed more stability of different GNRs than the GNRs functionalized by using other three types of γPGA. We have omitted the MUA-GNRs (borate buffer) group because we wanted to use these γPGA further functionalized GNRs for *in vitro* studies, and borate buffer can interfere in the study.

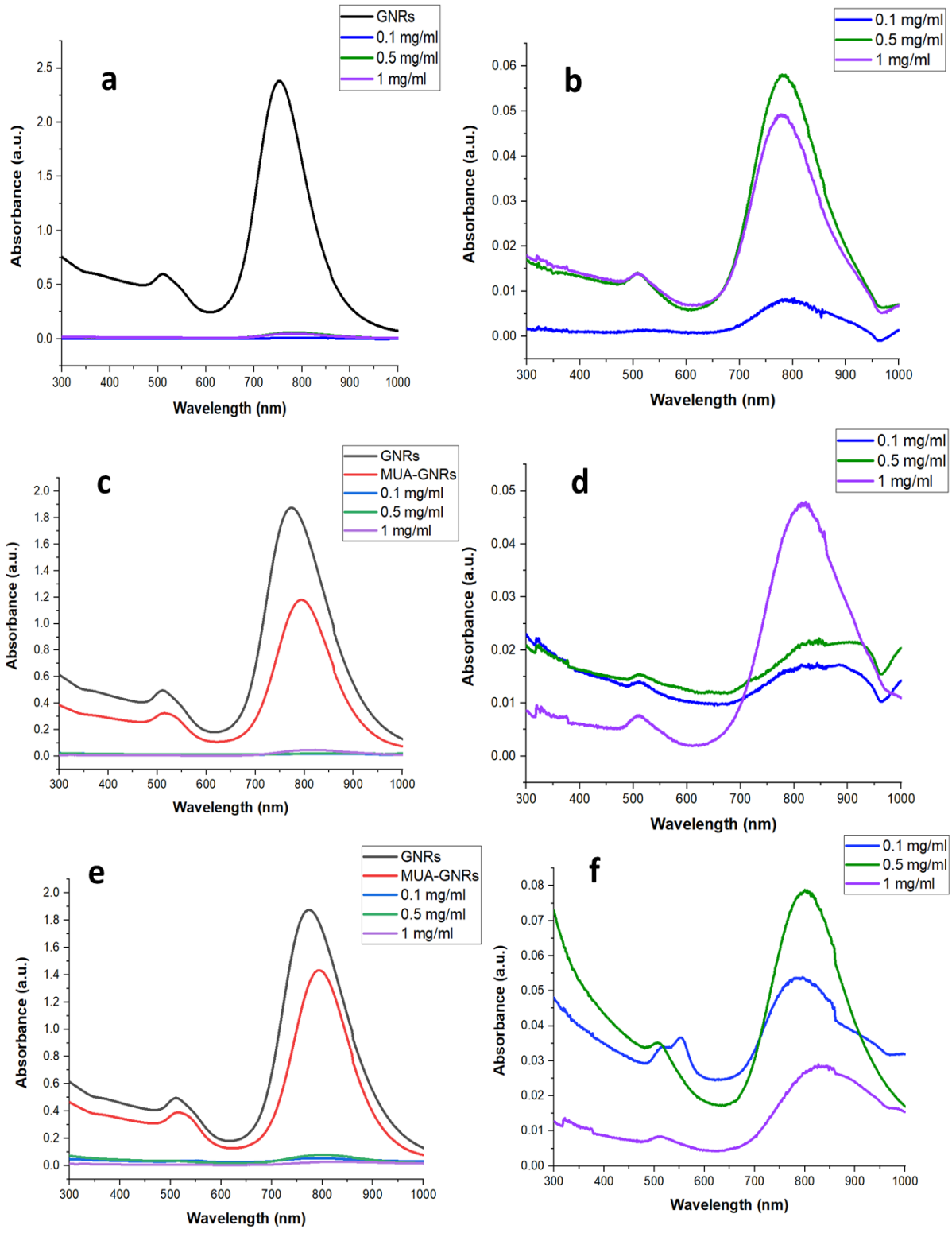

Figure 6A.1 UV-visible-NIR spectra of a) γPGA-GNRs, b) zoomed spectra of γ-PGA-GNRs, c) γPGA-MUA-GNRs (DI water), d) zoomed spectra of γPGA-MUA-GNRs (DI water), e) γPGA-MUA-GNRs (borate buffer) and f) zoomed spectra of γPGA-MUA-GNRs (borate buffer) functionalized using different concentrations of γPGA (jaggery)

Table 6A.1 Summary of functionalization results by using γPGA (Jaggery)

Groups	Samples	λmax of GNR	λmax of MUA-GNR	Avg. λmax of GNR after functionalization with γPGA (Jaggery)	Conclusion	Zeta Potential (mV)
GNRs directly after synthesis	γPGA (Jaggery) 1 mg/ml	751 nm	-	778 nm	Red shift & low absorbance	-24.71 ± 1.29
	γPGA (Jaggery) 0.5 mg/ml	751 nm	-	780 nm	Reds shift & low absorbance	-23.14 ± 0.28
	γPGA (Jaggery) 0.1 mg/ml	751 nm	-	Aggregations	Aggregations	-10.69 ± 0.85
MUA-GNRs functionalized with γPGA (Jaggery) in DI water	γPGA (Jaggery) 1 mg/ml	772 nm	793 nm	822 nm	Red shift & low absorbance	-21.39 ± 1.3
	γPGA (Jaggery) 0.5 mg/ml	772 nm	793 nm	Aggregations	Aggregations	-15.14 ± 0.33
	γPGA (Jaggery) 0.1 mg/ml	772 nm	793 nm	Aggregations	Aggregations	-7.33 ± 1.11
MUA-GNRs functionalized with γPGA (Jaggery) in 0.01M borate buffer	γPGA (Jaggery) 1 mg/ml	772 nm	793 nm	827 nm	Reds shift & low absorbance	-16.64 ± 2.02
	γPGA (Jaggery) 0.5 mg/ml	772 nm	793 nm	800 nm	Reds shift & low absorbance	-11.37 ± 1.21
	γPGA (Jaggery) 0.1 mg/ml	772 nm	793 nm	786 nm	Blue shift & low absorbance	-6.68 ± 1.16

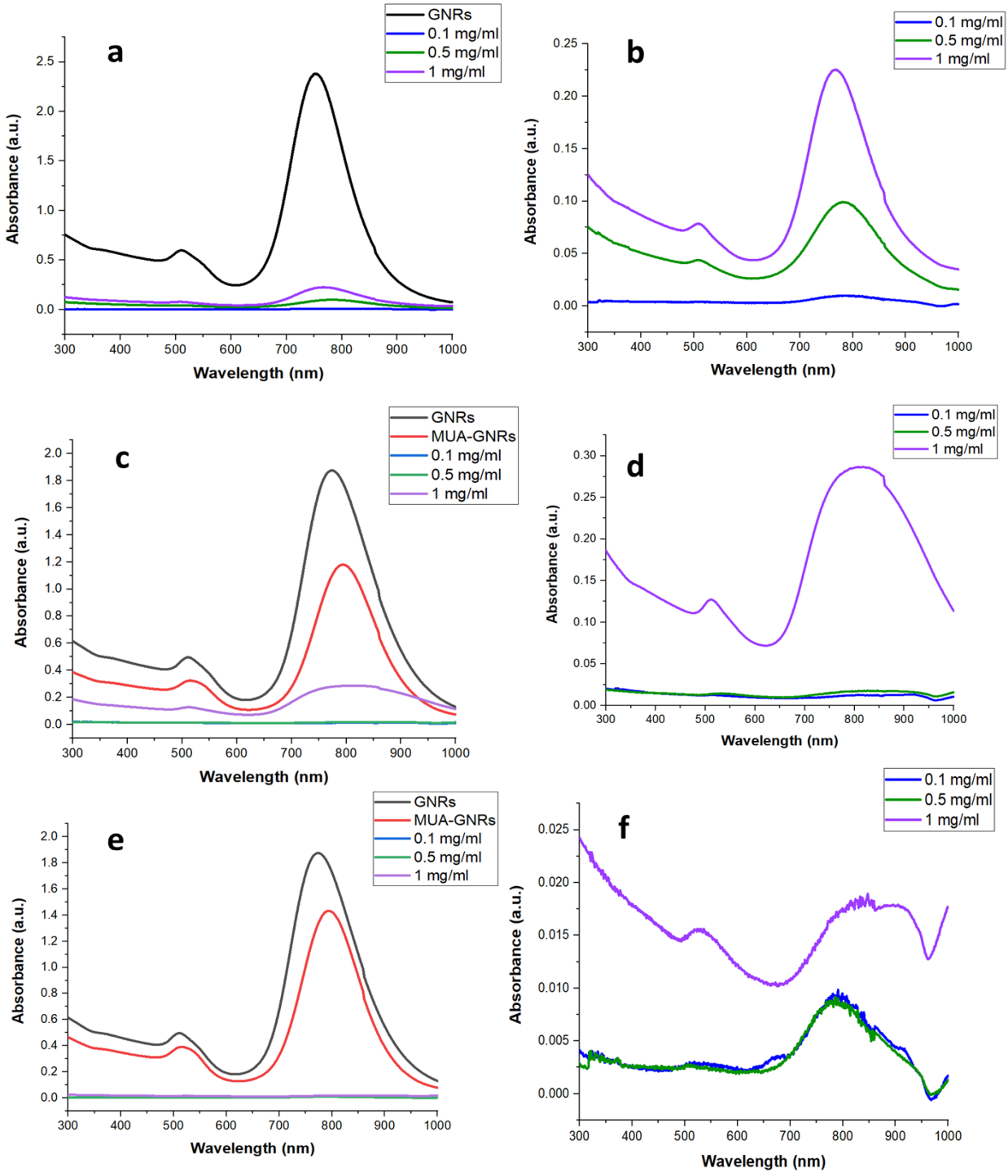

Figure 6A.2 UV-visible-NIR spectra of a) γPGA-GNRs, b) zoomed spectra of γPGA-GNRs, c) γPGA-MUA-GNRs (DI water), d) zoomed spectra of γPGA-MUA-GNRs (DI water), e) γPGA-MUA-GNRs (borate buffer) and f) zoomed spectra of γPGA-MUA-GNRs (borate buffer) functionalized using different concentrations of γPGA (sucrose)

Table 6A.2 Summary of functionalization results by using γPGA (Sucrose)

Groups	Samples	λmax of GNR	λmax of MUA-GNR	Avg. λmax of GNR after functionalization with γPGA (Sucrose)	Conclusion	Zeta Potential (mV)
GNRs directly after synthesis	γPGA (Sucrose) 1mg/ml	751 nm	-	768 nm	Red shift	-22.44 ± 1.67
	γPGA (Sucrose) 0.5 mg/ml	751 nm	-	780 nm	Reds shift & low absorbance	-17.72 ± 1.38
	γPGA (Sucrose) 0.1 mg/ml	751 nm	-	Aggregations	Aggregations	-11.26 ± 0.98
MUA-GNRs functionalized with γPGA (Sucrose) in DI water	γPGA (Sucrose) 1mg/ml	772 nm	793 nm	810 nm	Red shift	-19.4 ± 1.38
	γPGA (Sucrose) 0.5 mg/ml	772 nm	793 nm	Aggregations	Aggregations	-14.31 ± 1.04
	γPGA (Sucrose) 0.1 mg/ml	772 nm	793 nm	Aggregations	Aggregations	-10.85 ± 1.71
MUA-GNRs functionalized with γPGA (Sucrose) in 0.01M borate buffer	γPGA (Sucrose) 1mg/ml	772 nm	793 nm	Aggregations	Aggregations	-10.08 ± 0.89
	γPGA (Sucrose) 0.5 mg/ml	772 nm	793 nm	Aggregations	Aggregations	-10.46 ± 1.13
	γPGA (Sucrose) 0.1 mg/ml	772 nm	793 nm	Aggregations	Aggregations	-7.63 ± 1.29

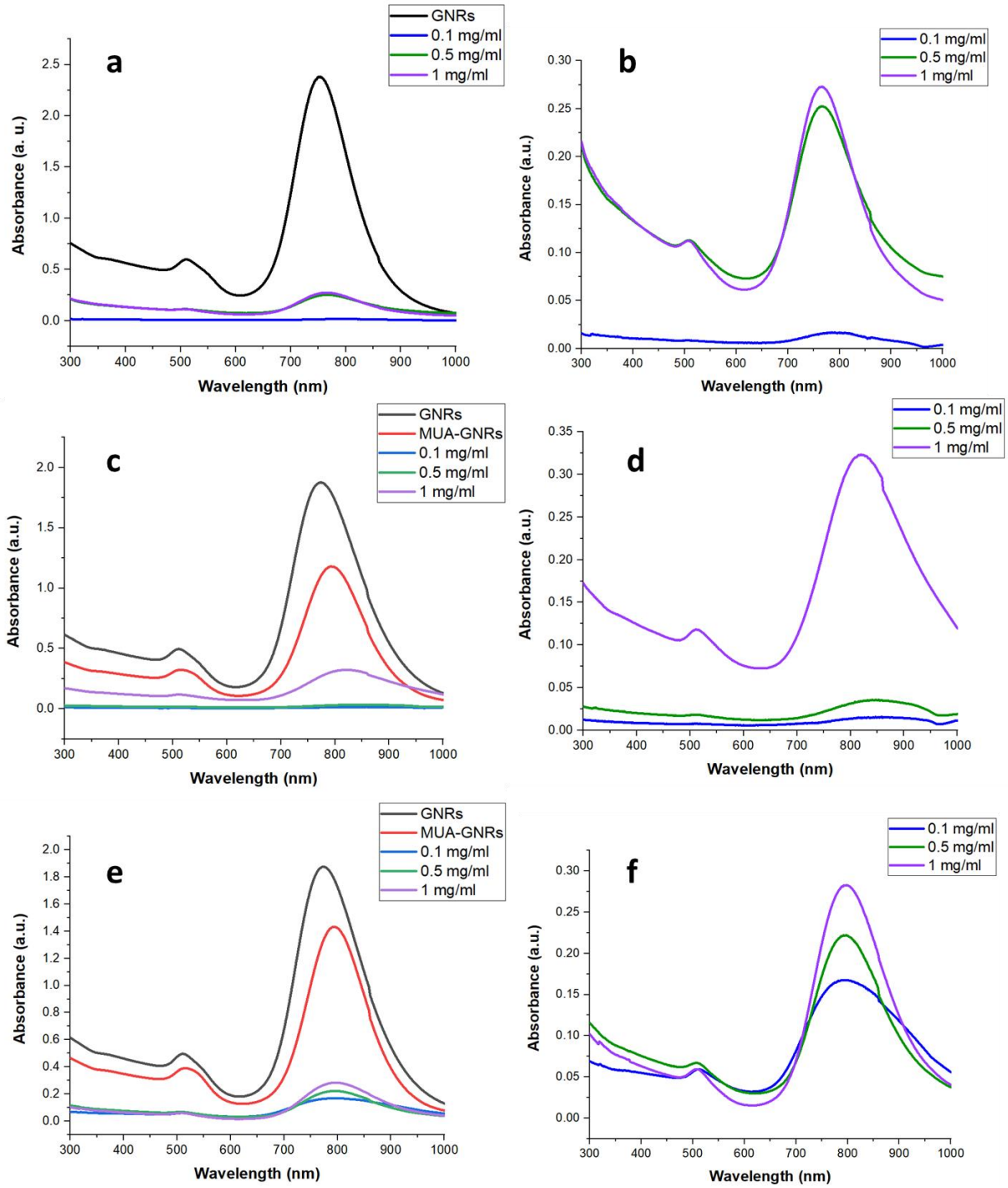

Figure 6A.3 UV-visible-NIR spectra of a) γPGA-GNRs, b) zoomed spectra of γPGA-GNRs, c) γPGA-MUA-GNRs (DI water), d) zoomed spectra of γPGA-MUA-GNRs (DI water), e) γPGA-MUA-GNRs (borate buffer) and f) zoomed spectra of γPGA-MUA-GNRs (borate buffer) functionalized using different concentrations of γPGA (tomato waste)

Table 6A.3 Summary of functionalization results by using γPGA (Tomato waste)

Groups	Samples	λmax of GNR	λmax of MUA-GNR	Avg. λmax of GNR after functionalization with γPGA (Tomato waste)	Conclusion	Zeta Potential (mV)
GNRs directly after synthesis	γPGA (Tomato waste) 1 mg/ml	751 nm	-	766 nm	Red shift	-26.75 ± 1.62
	γPGA (Tomato waste) 0.5 mg/ml	751 nm	-	766 nm	Red shift	-25.49 ± 0.70
	γPGA (Tomato waste) 0.1 mg/ml	751 nm	-	Aggregations	Aggregations	-18.49 ± 1.3
MUA-GNRs functionalized with γPGA (Tomato waste) in DI water	γPGA (Tomato waste) 1 mg/ml	772 nm	793 nm	819 nm	Red shift	-26.4 ± 1.33
	γPGA (Tomato waste) 0.5mg/ml	772 nm	793 nm	Aggregations	Aggregations	-22.6 ± 1.16
	γPGA (Tomato waste) 0.1 mg/ml	772 nm	793 nm	Aggregations	Aggregations	-19.61 ± 1.07
MUA-GNRs functionalized with γPGA (Tomato waste) in 0.01M borate buffer	γPGA (Tomato waste) 1 mg/ml	772 nm	793 nm	798 nm	Red shift	-20.89 ± 1.01
	γPGA (Tomato waste) 0.5 mg/ml	772 nm	793 nm	798 nm	Red shift	-17.41 ± 0.83
	γPGA (Tomato waste) 0.1 mg/ml	772 nm	793 nm	792 nm	Blue shift	-14.74 ± 0.98

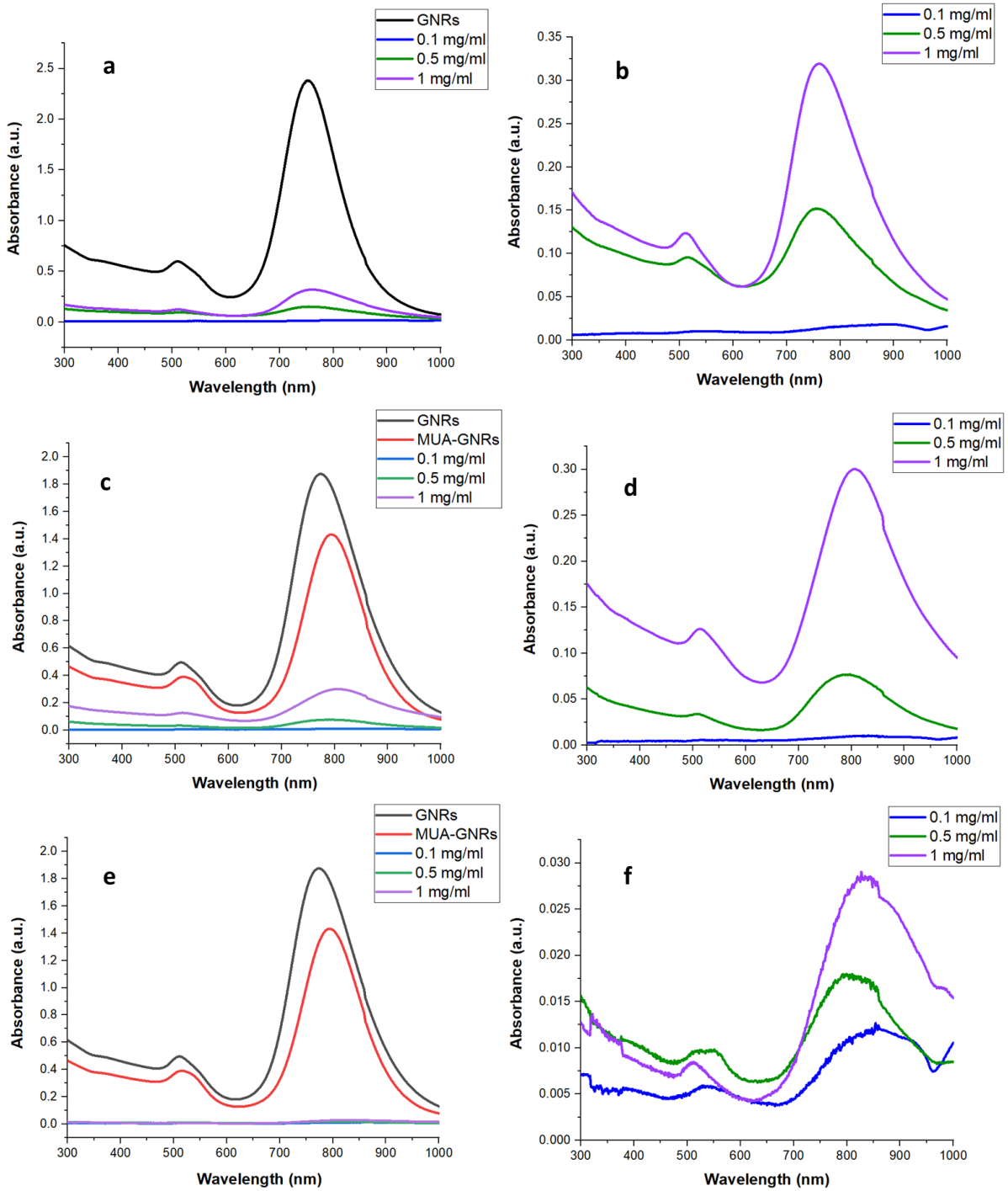

Figure 6A.4 UV-visible-NIR spectra of a) γPGA-GNRs, b) zoomed spectra of γPGA-GNRs, c) γPGA-MUA-GNRs (DI water), d) zoomed spectra of γPGA-MUA-GNRs (DI water), e) γPGA-MUA-GNRs (borate buffer) and f) zoomed spectra of γPGA-MUA-GNRs (borate buffer) functionalized using different concentrations of γPGA (commercial)

Table 6A.4 Summary of functionalization results by using γPGA (Commercial)

Groups	Samples	λmax of GNR	λmax of MUA-GNR	Avg. λmax of GNR after functionalization with γPGA (Commercial)	Conclusion	Zeta Potential (mV)
GNRs directly after synthesis	γPGA (Commercial) 1 mg/ml	751 nm	-	760 nm	Red shift	-22.74 ± 0.93
	γPGA (Commercial) 0.5 mg/ml	751 nm	-	754 nm	Red shift & low absorbance	-22.19 ± 1.61
	γPGA (Commercial) 0.1 mg/ml	751 nm	-	Aggregations	Aggregations	-14.75 ± 1.29
MUA-GNRs functionalized with γPGA (Commercial) in DI water	γPGA (Commercial) 1 mg/ml	772 nm	793 nm	806 nm	Red shift	-21.56 ± 2.18
	γPGA (Commercial) 0.5 mg/ml	772 nm	793 nm	790 nm	Red shift & low absorbance	-20.3 ± 1.05
	γPGA (Commercial) 0.1 mg/ml	772 nm	793 nm	Aggregations	Aggregations	-19.18 ± 0.83
MUA-GNRs functionalized with γPGA (Commercial) in 0.01M borate buffer	γPGA (Commercial) 1 mg/ml	772 nm	793 nm	Aggregations	Aggregations	-17.87 ± 0.99
	γPGA (Commercial) 0.5 mg/ml	772 nm	793 nm	Aggregations	Aggregations	-15.53 ± 1.17
	γPGA (Commercial) 0.1 mg/ml	772 nm	793 nm	Aggregations	Aggregations	-14.75 ± 1.39

6A.3.2. Optimization of volume of γPGA

In the case of GNRs, on varying the volume of γPGA, the maximum red shift in the LPW was observed at 0.75 ml γPGA (Fig. 6A.5a, b), but based on unpaired t-test, there was no significant difference between the red shift of LPW of GNRs after functionalization with 1 ml and 0.75ml γPGA (Fig. 6A.6a). However, when the absorbance was examined, it was found that as the volume of γPGA increases, there was an increase in the absorbance of the γPGA-GNRs (Fig. 6A.5a, b). Further, based on an unpaired t-test, it was observed that there was a significant difference between the absorbance at 0.75 ml and 1ml volume of γPGA (Fig. 6A.6b). Based on one-way ANOVA study, it was concluded that the volume of γPGA had a significant impact on the red shift of LPW of GNRs (ANOVA p-valu e= 0.0001) as well as the absorbance (ANOVA p-value = <0.0001) at the LPW. Thus, this parameter significantly affects the functionalization of GNRs with γPGA.

Furthermore, zeta potential analysis confirms the functionalization of GNRs with γPGA as it changed from positive to negative (J. He et al., 2018; Jain et al., 2019; L. Su et al., 2017; J. Wang et al., 2017). Zeta potential shows the stability of functionalized γPGA-GNRs at every volume of γPGA except at 0.75 ml as it was below -25 mV at 0.75 ml (Fig. 6A.6c). Also, one-way ANOVA analysis revealed that the parameter significantly affects the zeta potential of γPGA-GNRs (ANOVA p-value = 0.0110). Herein, the zeta potential at 1.25 ml γPGA was highest, but on performing an unpaired t-test, an insignificant difference was observed between the zeta potential at 1 ml and 1.25 ml γPGA volumes (Fig. 6A.6c) (Table 6A.5). Therefore, based on LSPR spectra and zeta potential studied 1 ml volume of γPGA was optimized. Table 6A.5 summarizes the red shift in the LPW of GNRs and zeta potential measurements of GNRs after functionalization with different volumes of γPGA (Table 6A.5).

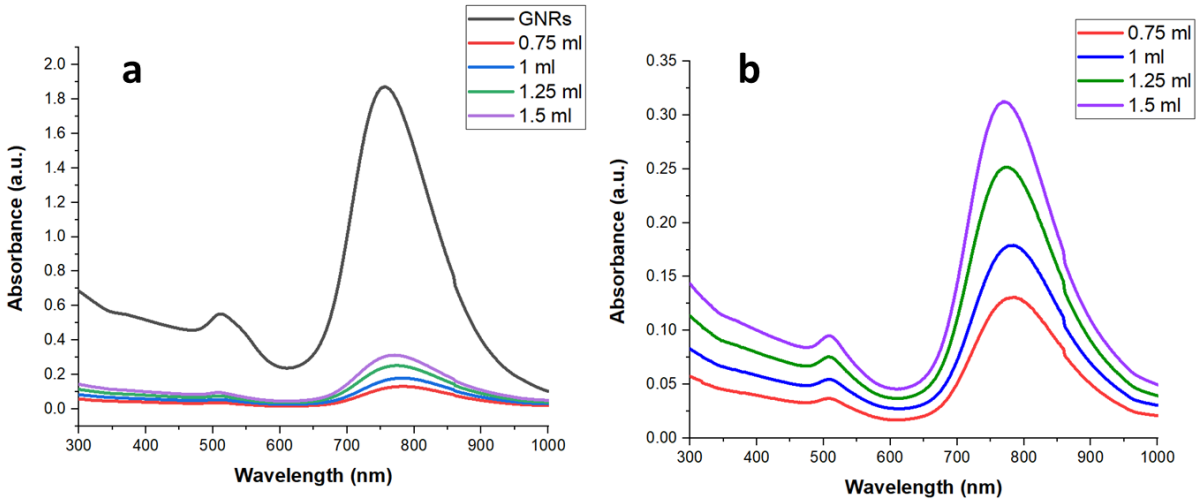

Figure 6A.5 UV-visible-NIR spectra of γPGA-GNRs functionalized at different volumes of γPGA a) with spectra of GNRs and b) zoomed spectra of only γPGA-GNRs

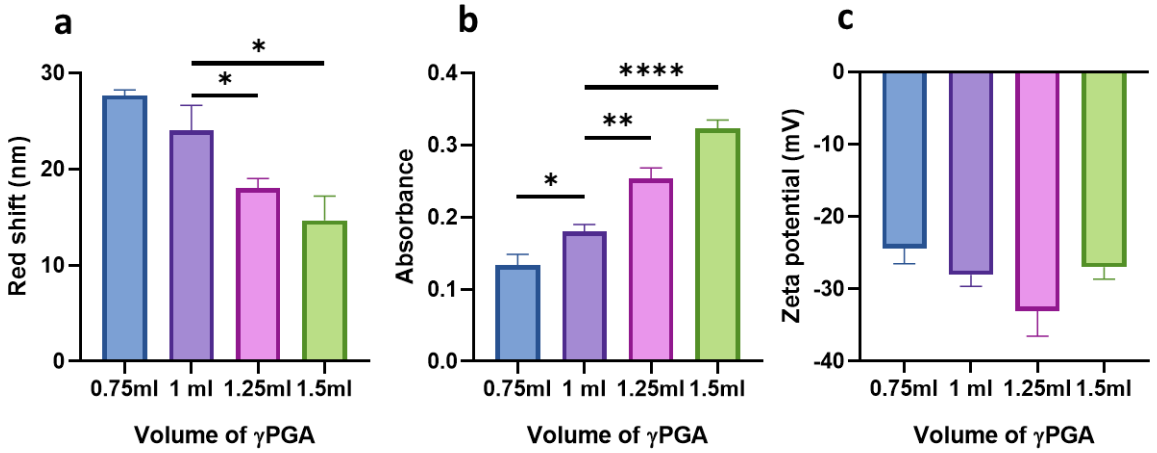

Figure 6A.6 Effect of γPGA volumes on a) red shift in LPW of GNRs, b) absorbance of γPGA-GNRs at LPW and c) zeta potential of γPGA-GNRs

Table 6A.5 Red shift in the LPW of GNRs after functionalization with γPGA and zeta potential of γPGA-GNRs functionalized at different volumes of γPGA

Volume of γPGA (ml)	Red Shift in the LPW of GNRs (nm)	Zeta Potential of γPGA-GNRs (mV)
0.75	27.66 ± 0.57	-24.39 ± 2.11
1	24 ± 2.64	-28.06 ± 1.58
1.25	18 ± 1	-33.09 ± 3.45
1.5	14.66 ± 2.51	-27 ± 1.65

Furthermore, the volume of γPGA was also optimized for functionalizing MUA-GNRs dispersed in DI water. On varying the volume of γPGA, the maximum red shift in the LPW of MUA-GNRs was found at 0.75 ml γPGA after that, there was a decrease in red shift with increase in volume of γPGA (Fig. 6A.7a, b) (Table 6A.6). However, the absorbance at LPW was maximum at 1 ml and 1.5 ml volumes of γPGA (Fig. 6A.7a, b). On statistical analysis, it was found that this parameter significantly affects the red shift of LPW of MUA-GNRs (ANOVA p-value = <0.0001) as well as the absorbance (ANOVA p-value = <0.0001) at the LPW (Fig. 6A.8a, b). Thus, this parameter significantly affects the functionalization of GNRs with γPGA. But it should also be noted that there was no significant difference in the red shift of LPW at 1 ml and 0.75 ml of γPGA. The zeta potential analysis confirms the functionalization of MUA-GNRs with γPGA as it decreased compared to the zeta potential of MUA-GNRs at all the volumes of γPGA. Zeta potential shows the stability of functionalized γPGA-MUA-GNRs at every volume of γPGA except at 0.75 ml as it was below -25 mV at 0.75 ml (Fig. 6A.8c) (Table 6A.6). Also, one-way ANOVA analysis revealed that the parameter significantly affects the zeta potential of γPGA-MUA-GNRs (ANOVA p-value = <0.0001). Although the zeta potential at 1.5 ml γPGA was maximum but based on the LSPR study, the red shift in the LPW was minimum at 1.5 ml. Therefore, on compiling the results of LSPR spectra and zeta potential analysis, 1 ml volume of γPGA was optimized.

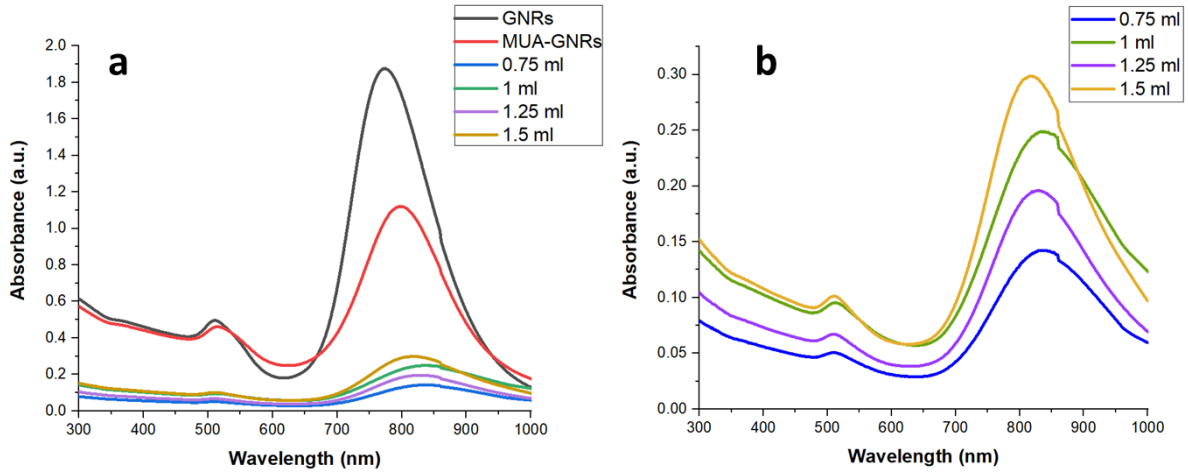

Figure 6A.7 UV-visible-NIR spectra of γPGA-MUA-GNRs functionalized at different volumes of γPGA a) with spectra of GNRs & MUA-GNRs and b) zoomed spectra of only γPGA-MUA-GNRs

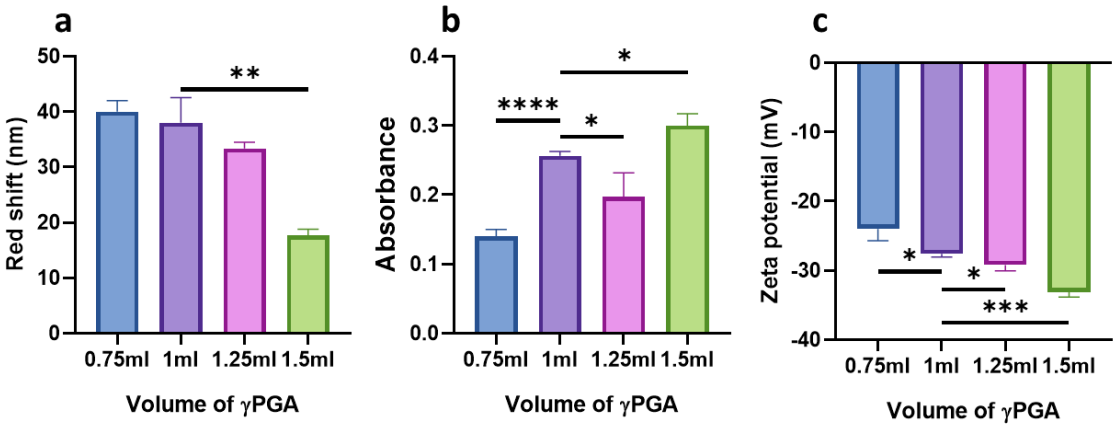

Figure 6A.8 Effect of γPGA volumes on a) red shift in LPW of MUA-GNRs, b) absorbance of γPGA-MUA-GNRs at LPW and c) zeta potential of γPGA-MUA-GNRs

Table 6A.6 Red shift in the LPW of MUA-GNRs after functionalization with γPGA and zeta potential of γPGA-MUA-GNRs functionalized at different volumes of γPGA

Volume of γPGA (ml)	Red Shift in the LPW of MUA-GNRs (nm)	Zeta Potential of γPGA-MUA-GNRs (mV)
0.75	40 ± 2	-23.98 ± 1.70
1	38 ± 4.58	-27.59 ± 0.44
1.25	33.33 ± 1.15	-29.20 ± 0.85
1.5	17.66 ± 1.15	-33.13 ± 0.67

6A.3.3. Characterization of γPGA-GNRs and γPGA-MUA-GNRs

The γPGA functionalized GNRs and MUA-GNRs were extensively characterized by various techniques.

6A.3.3.1. UV-visible-NIR spectroscopy and zeta potential analysis

The UV-visible-NIR spectroscopy revealed the red shift in the LPW of GNRs and MUA-GNRs when functionalized with the γPGA. It was due to the change in local dielectric permittivity of the medium because of γPGA (Guan et al., 2014; J. Y. Liu et al., 2019). The LPW of GNRs, MUA-GNRs, γPGA-GNRs and γPGA-MUA-GNRs was around 745 nm, 765 nm, 770 nm and 804 nm, respectively (Fig. 6A.9). Similarly, Guan et. al and Liu et al. also found the red shift the SPR spectra of nanoparticles after functionalization with PGA (Guan et al., 2014; J. Y. Liu

et al., 2019). The average red shift in the LPW of γPGA-GNRs and γPGA-MUA-GNRs was 24 ± 2.64 nm and 38 ± 4.58 nm, respectively (Fig. 6A.9).

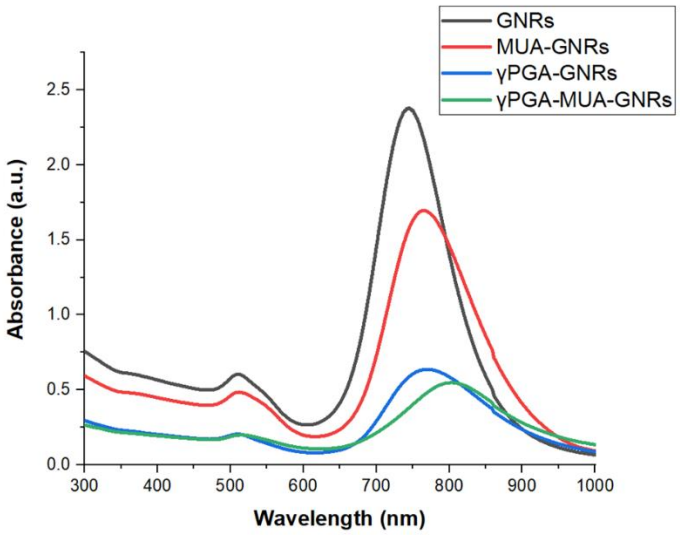

Figure 6A.9 UV-visible-NIR spectra of GNRs, MUA-GNRs, γPGA-GNRs and γPGA-MUA-GNRs

The zeta potential study confirmed the functionalization of GNRs and MUA-GNRs with γPGA. In case of functionalization of GNRs, the zeta potential altered from positive to negative after coating of γPGA. It was due to the anionic nature of γPGA due to the free -COOH group (Cai et al., 2024; Khalil et al., 2018; J. Y. Liu et al., 2019). The zeta potential of γPGA-GNRs was -28.06 ± 1.58 mV (Fig. 6A.10); this was corroborated by the findings of Liu et. al. (J. Y. Liu et al., 2019). Further, on functionalizing MUA-GNRs with γPGA, the zeta potential was negative only, but it got decreased compared to the zeta potential of MUA-GNRs. This decrease confirmed the attachment of γPGA on the surface of MUA-GNRs. Many studies reported the decrease in zeta potential on functionalizing GNRs with polymers (Du et al., 2019; Niidome et al., 2006; Z. Zhang & Lin, 2014). The zeta potential of γPGA-MUA-GNRs was -27.59 ± 0.44 mV (Fig. 6A.10). As, the zeta potential was above -25 mV for both γPGA-GNRs and γPGA-MUA-GNRs. Therefore, both γPGA-GNRs and γPGA-MUA-GNRs were found to have moderate stability (Bhattacharjee, 2016; Honary & Zahir, 2013).

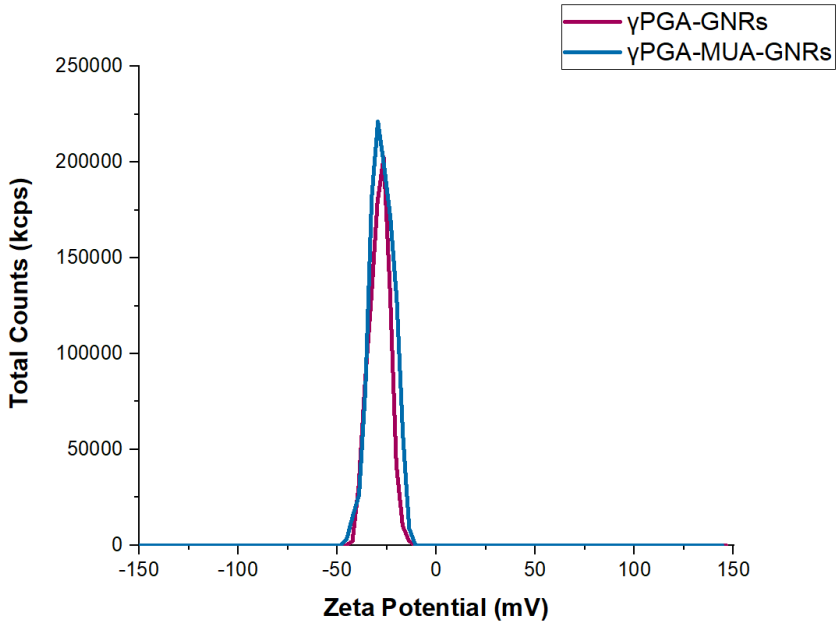

Figure 6A.10 Zeta potential of γPGA-GNRs and γPGA-MUA-GNRs

6A.3.3.2. Electron microscopy analysis

Based on HRTEM analysis, the size of γPGA-GNRs and γPGA-MUA-GNRs were found to be as 43.22 ± 3.8 nm x 12.2 ± 1.58 nm (Fig. 6A.11a) and 45.71 ± 3.29 nm x 12.9 ± 1.84 nm (Fig. 6A.12a), respectively. This finding was corroborated by the FESEM results of γPGA-GNRs (Fig. 6A.11b) and γPGA-MUA-GNRs (Fig. 6A.12b). Further, the SAED pattern obtained by using HRTEM confirms the crystalline nature of γPGA-GNRs (Fig. 6A.11c) and γPGA-MUA-GNRs (Fig. 6A.12c) (Anandhakumar et al., 2013; Kedawat et al., 2019). The fringes of γPGA-GNRs and γPGA-MUA-GNRs were also observed by HRTEM. The d-spacing value of γPGA-GNRs was around 0.208 nm (Fig. 6A.11d) and of γPGA-MUA-GNRs was around 0.211 nm (Fig. 6A.12d). These d-spacing findings aligned with the other studies (Si et al., 2012; J. Yin et al., 2017; L. Zhang et al., 2016).

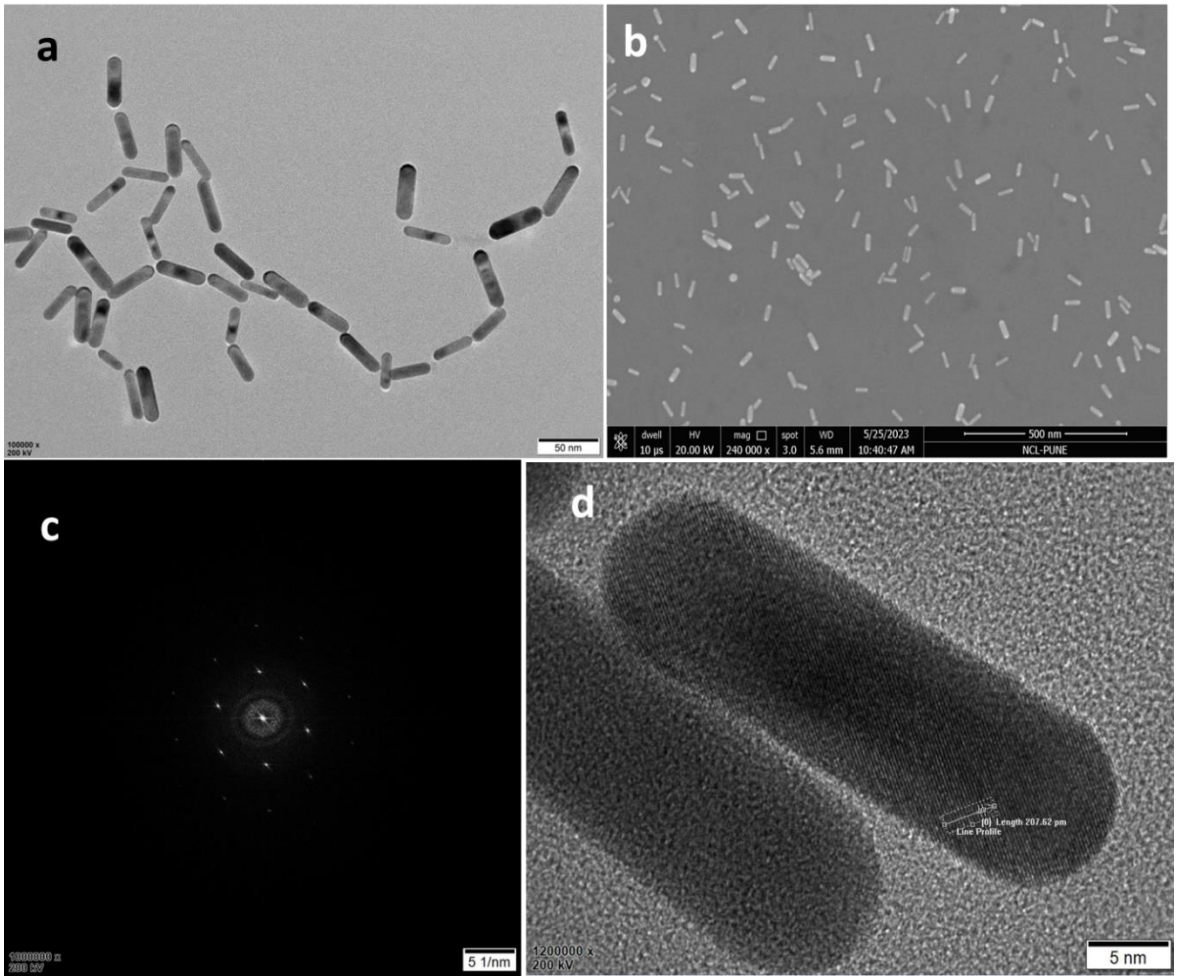

Figure 6A.11 Electron microscopy analysis of γPGA-GNRs a) HRTEM image, b) FESEM image, c) SAED pattern, and d) fringes of γPGA-GNRs

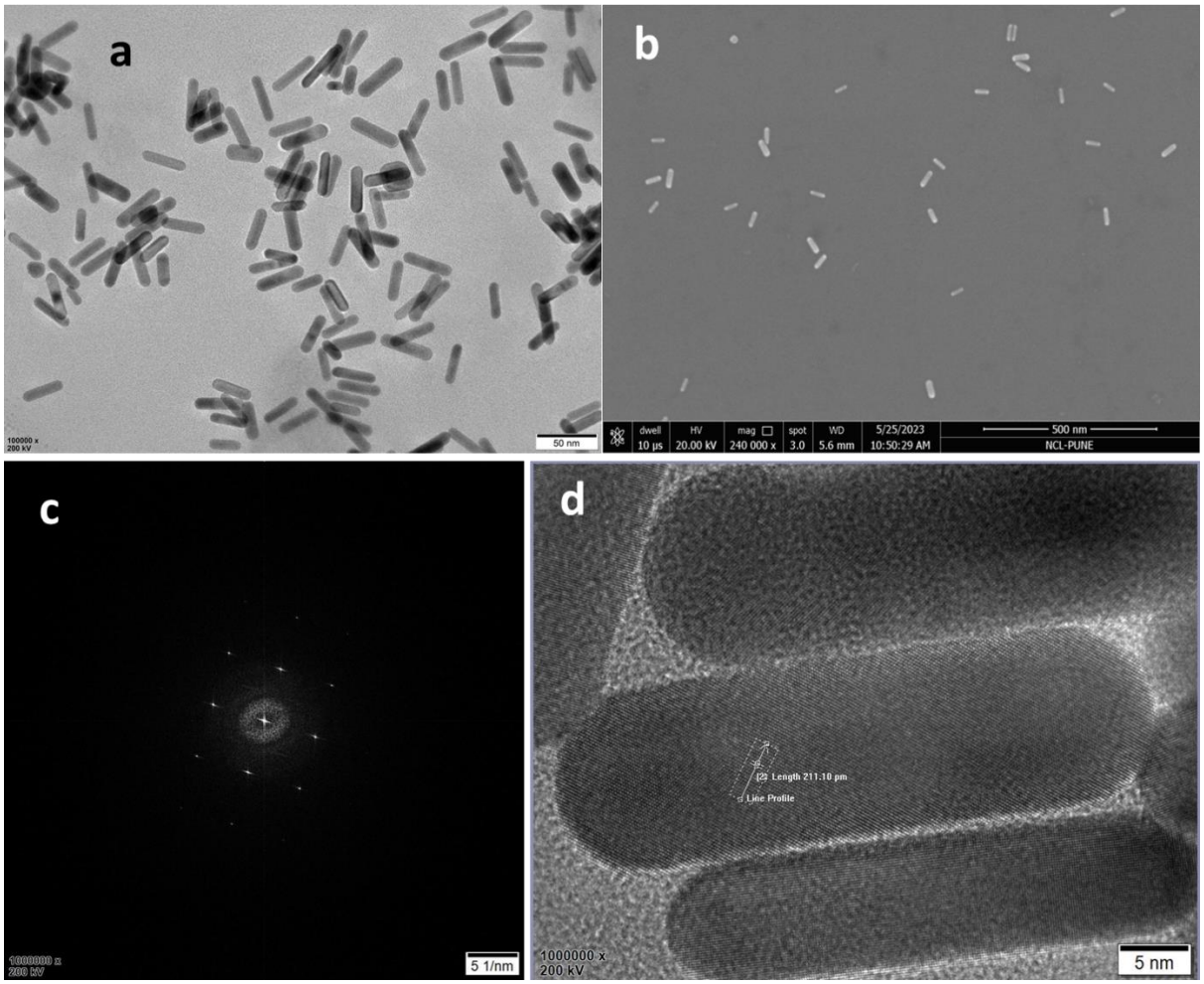

Figure 6A.12 Electron microscopy analysis of γPGA-MUA-GNRs a) HRTEM image, b) FESEM image, c) SAED pattern and d) fringes of γPGA-MUA-GNRs

6A.3.3.3. Elemental analysis

On recording the EDX spectrum of γPGA-GNRs, the presence of gold (Au), carbon (C), oxygen (O), nitrogen (N) and bromine (Br) was observed. However, these elements were also present in the GNRs. But, here, interestingly, the intensity of the bromine peak decreased. Thus, this decrease in the intensity of the Br peak might be due to the masking of Br because of the functionalization with γPGA (Fig. 6A.13a). Similarly, in the EDX spectrum of γPGA-GNRs generated through FESEM, there was also a decrease in the intensity of Br was observed (Fig. 6A.13b) compared to the EDX spectrum of GNRs, shown in Chapter 3, Figure 3.24. The STEM mapping study also supports the findings of EDX studies (Fig. 6A.14).

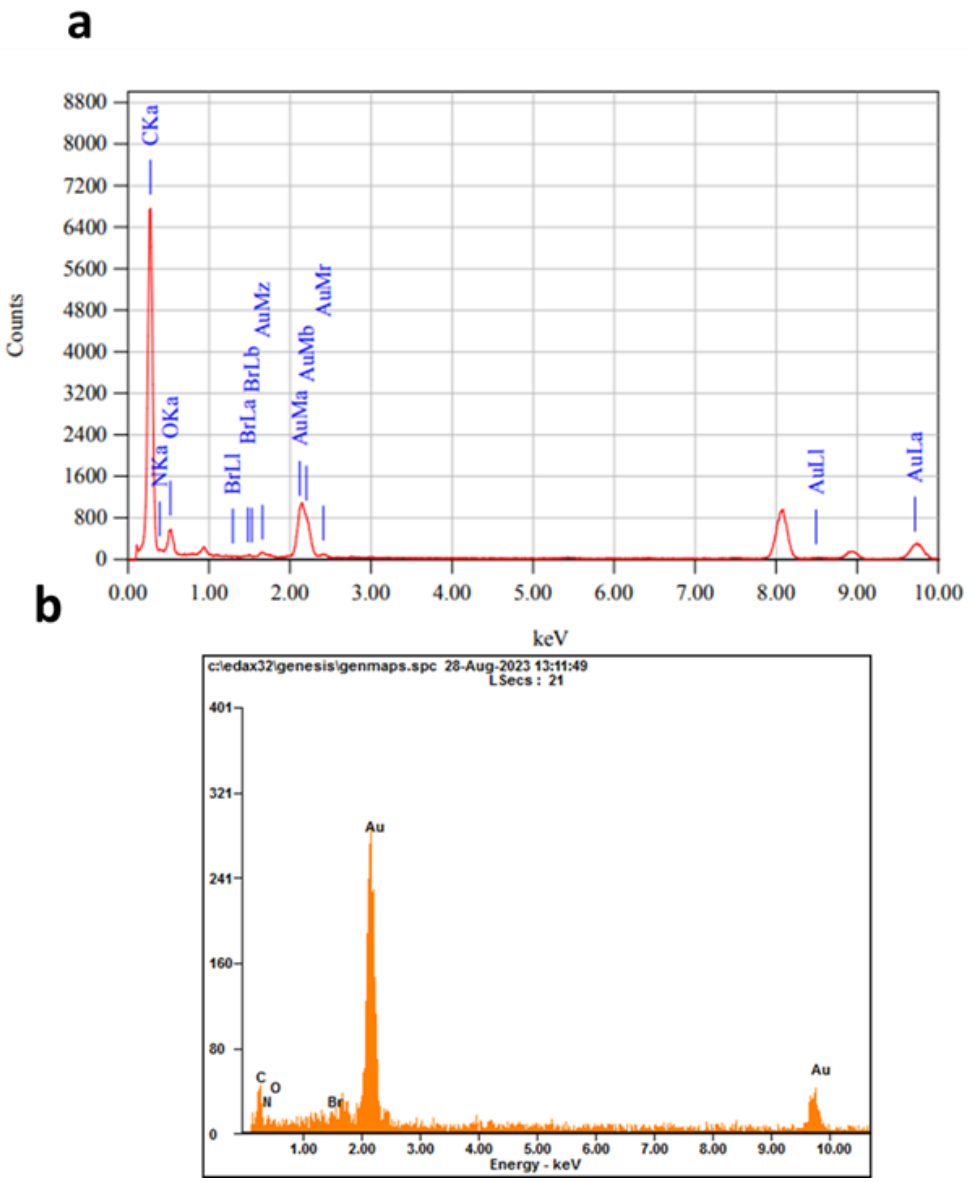

Figure 6A.13 EDX spectra of γPGA-GNRs a) from HRTEM and b) from FESEM

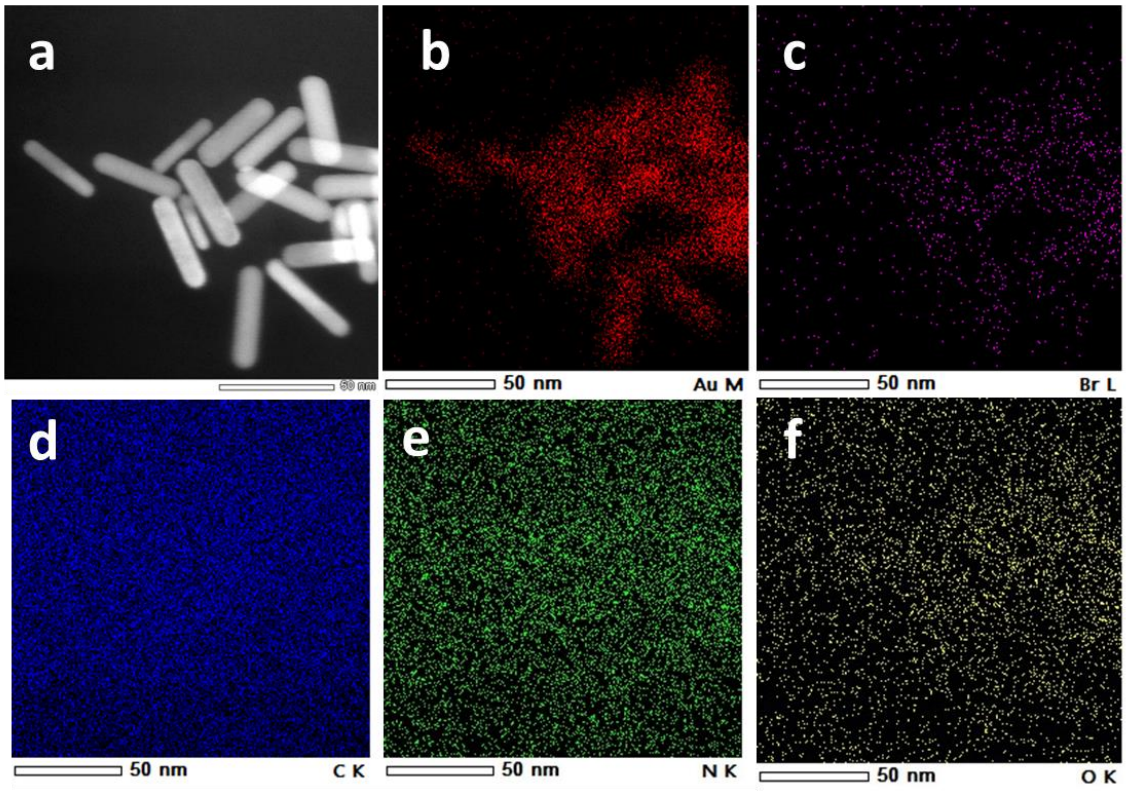

Figure 6A.14 STEM mapping of γPGA-GNRs a) STEM image, b) Au, c) Br, d) C, e) N and f) O

Further, the EDX spectrum of γPGA-MUA-GNRs acquired through HRTEM showed the presence of gold (Au), carbon (C), oxygen (O), nitrogen (N) and sulfur (S) (Fig. 6A.15a). Therefore, the presence of nitrogen was due to γPGA which confirms the functionalization of MUA-GNRs with γPGA, and nitrogen was also absent in EDX spectrum of MUA-GNRs, shown in Chapter 4, Figure 4.12. The results of the EDX spectrum of HRTEM were also supported by the results of the EDX spectrum of γPGA-MUA-GNRs acquired through FESEM (Fig. 6A.15b). Further, the elemental analysis was also confirmed by the STEM mapping study (Fig. 6A.16).

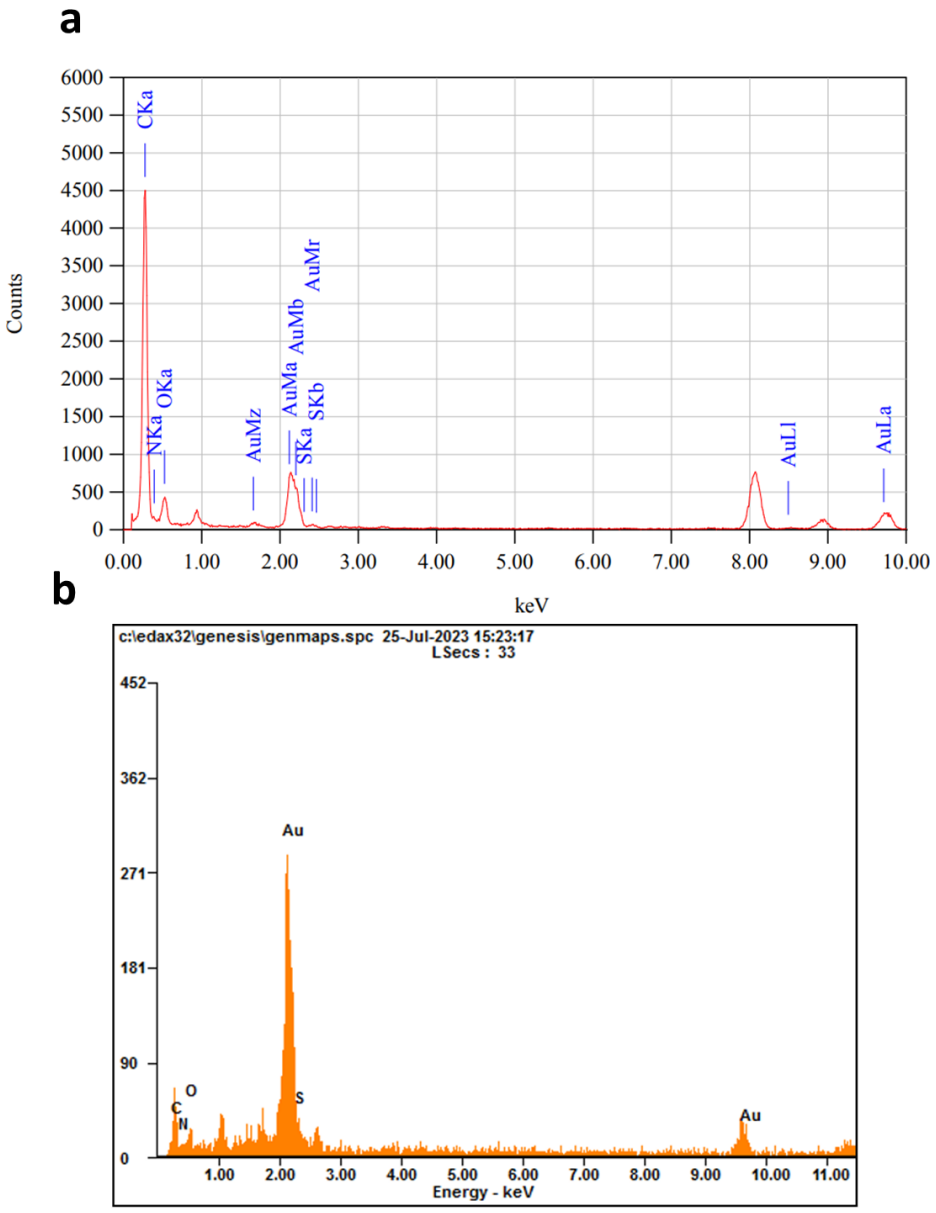

Figure 6A.15 EDX spectra of γPGA-MUA-GNRs a) from HRTEM and b) from FESEM

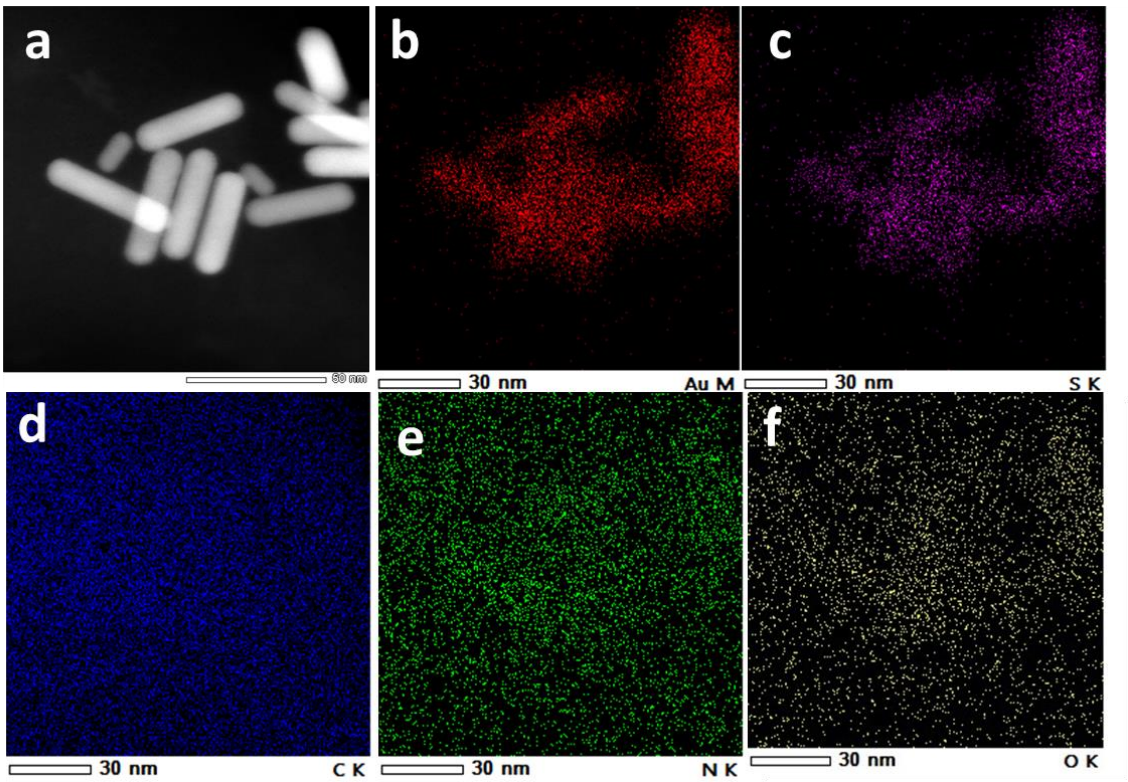

Figure 6A.16 STEM mapping of γPGA-MUA-GNRs a) STEM image, b) Au, c) S, d) C, e) N, and f) O

The XPS spectra of γPGA-GNRs and γPGA-MUA-GNRs were in line with the EDX analysis. The transitions Au $4f_{7/2}$ and Au $4f_{5/2}$ of Au^0 oxidation state were found at 84.08eV and 87.68 eV in γPGA-GNRs and at 84.08 eV and 87.68 eV in γPGA-MUA-GNRs, respectively (L. Su et al., 2017) (Fig. 6A.17a-c). Further, the Br 3p, Br 3d and Br 3s were found at 187.47 eV, 67.18 eV and 254.38 eV in γPGA-GNRs (Fig. 6A.17a,b). The bromine was due to the CTAB. However, in γPGA-MUA-GNRs, CTAB was replaced by 11-MUA so S 2p was found at 163.28 eV (Fig. 6A.17a,c) (J. Cao et al., 2012; J. He et al., 2018; L. Su et al., 2017; Tao et al., 2018; Thierry et al., 2009; Toh et al., 2013). Furthermore, both γPGA-GNRs and γPGA-MUA-GNRs have shown the presence of N 1s at 399.98 eV and 402.08 eV in γPGA-GNRs and at 399.98 eV in γPGA-MUA-GNRs (Fig. 6A.17a-c) (Mohtasebi et al., 2016; L. Su et al., 2017). Thus, the presence of a nitrogen signal confirmed the functionalization of GNRs and MUA-GNRs with γPGA.

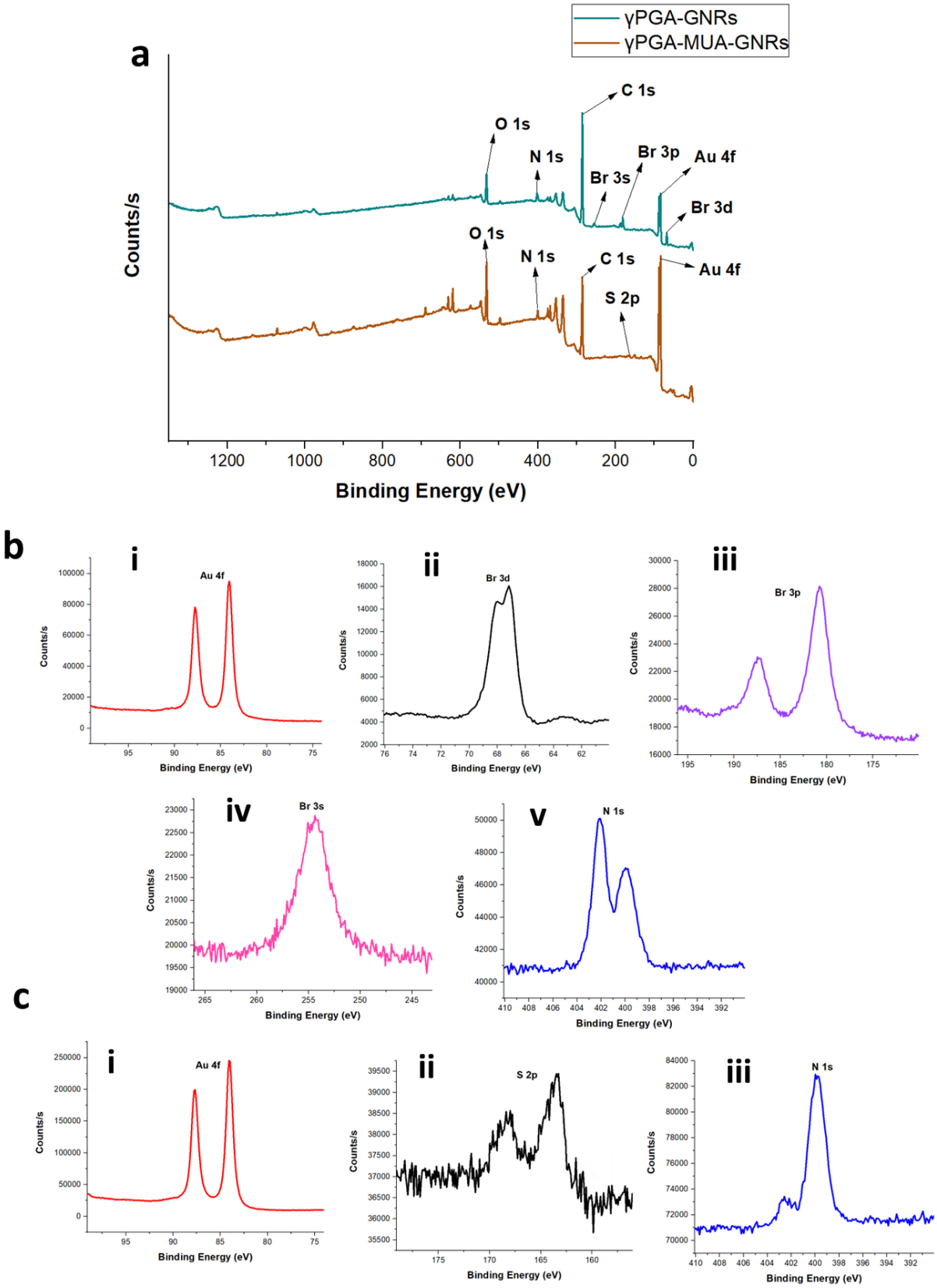

Figure 6A.17 a) XPS spectra of γPGA-GNRs and γPGA-MUA-GNRs, b) XPS spectra of (i-v) Au 4f, Br 3d, Br 3p, Br 3s and N 1s in γPGA-GNRs and c) XPS spectra of (i-iii) Au 4f, S 2p and N 1s in γPGA-MUA-GNRs

6A.3.3.4. FTIR analysis

FTIR measurements were carried out for the analysis of the binding of γPGA on GNRs and MUA-GNRs. Firstly, we determined the FTIR spectra of γPGA. The broad peak at 3275 cm^{-1} was due to the amine N-H stretching (Ajayeoba et al., 2019; Guan et al., 2014; L. L. Wang et al., 2017). Further, the peak at 2934 cm^{-1} C-H stretching vibrations of alkyl chains (Ajayeoba et al., 2019; P. G. Nair et al., 2021). The intense peak at 1572 cm^{-1} corresponds to -COOH asymmetric stretching (Anju et al., 2017; Guan et al., 2014; L. L. Wang et al., 2017). However, it also signifies an amide II bond (P. G. Nair et al., 2021; L. L. Wang et al., 2017). Next, the peak at 1400 cm^{-1} was assigned to the symmetric bending of the carboxylate anion (Guan et al., 2014; L. L. Wang et al., 2017). The peak at 1400 cm^{-1} could also be due to the CH_2 bending deformation (Hejazi et al., 2023). The spectra of γPGA-GNRs and γPGA-MUA-GNRs revealed the functionalization of GNRs and MUA-GNRs with γPGA. This can be validated by the presence of peaks around 3300 cm^{-1} and 3200 cm^{-1}in both γPGA-GNRs and γPGA-MUA-GNRs which were due to N-H bending (P. G. Nair et al., 2021) and amine N-H stretching (Ajayeoba et al., 2019; Guan et al., 2014) of γPGA, respectively. Furthermore, the peak of γPGA at 1572 cm^{-1} shifted to around 1600 cm^{-1} in both γPGA-GNRs and γPGA-MUA-GNRs corresponds to an α-helix structure that can be allocated to amide I or amide II in the spectrum for surface fastened peptides (Fig. 6A.18) (Guan et al., 2014). These findings suggest that the surface of GNRs and MUA-GNRs were successfully coated with the γPGA.

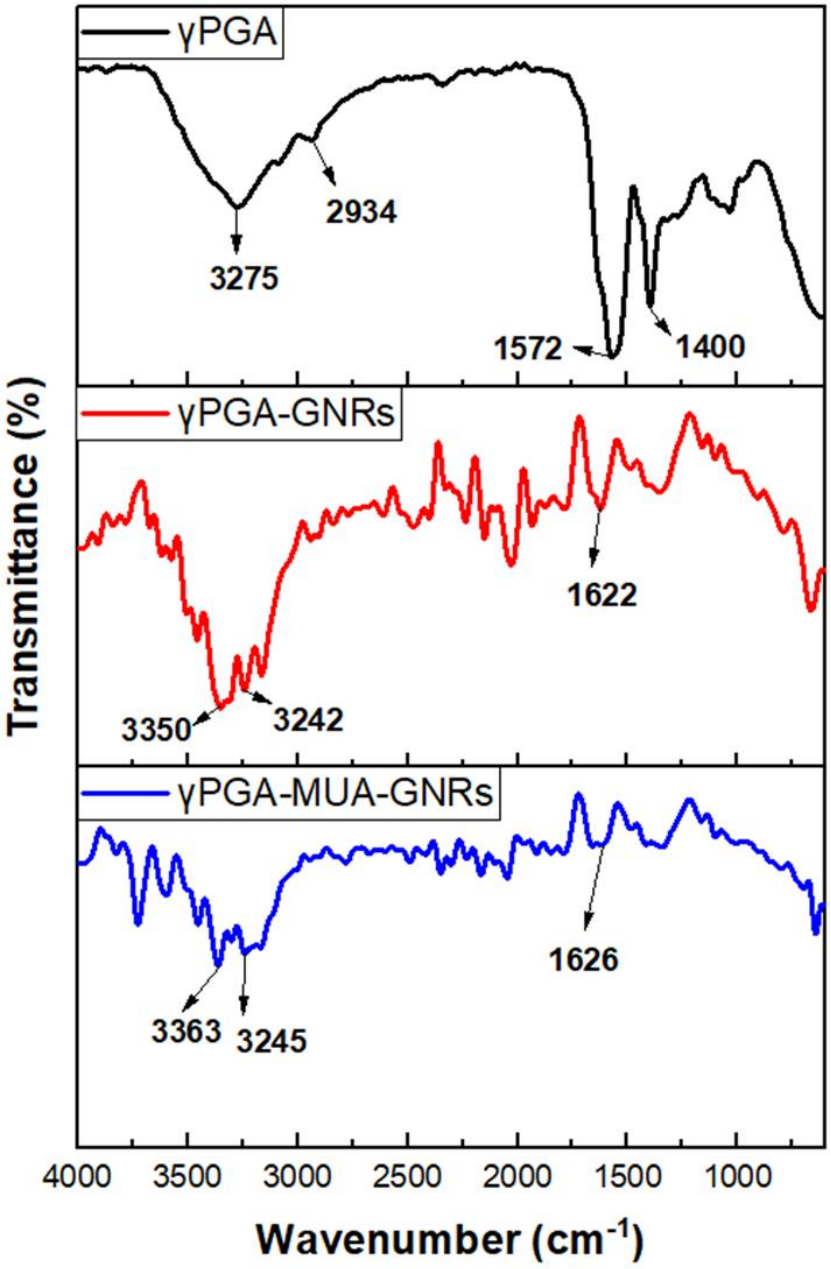

Figure 6A.18 FTIR spectra of γPGA, γPGA-GNRs and γPGA-MUA-GNRs

6A.3.4. Stability studies

Before proceeding for *in vitro* studies, we assessed the stability of GNRs, MUA-GNRs, γPGA-GNRs and γPGA-MUA-GNRs for 3 months based on LSPR spectra and zeta potential determination.

We studied the stability of GNRs and γPGA-GNRs suspended in DI water for 3 months and noticed clear suspensions without any precipitate or aggregates during storage at 4 ^{o}C. The LPW of GNRs (Fig. 6A.19a) and γPGA-GNRs (Fig. 6A.19b) did not change significantly after

3 months and the LSPR spectrum was also in its original form. This suggests that GNRs and γPGA-GNRs maintained their structural integrity and stability (Fig. 6A.19a, b). However, there was a little decrease in the absorbance of LSPR spectra of γPGA-GNRs after 1 month this may be due to some deposition of γPGA-GNRs. Further, the zeta potential values for both the GNRs and γPGA-GNRs at different time intervals were also consistent, suggesting good colloidal stability of the GNRs and γPGA-GNRs while storage (Fig. 6A.20).

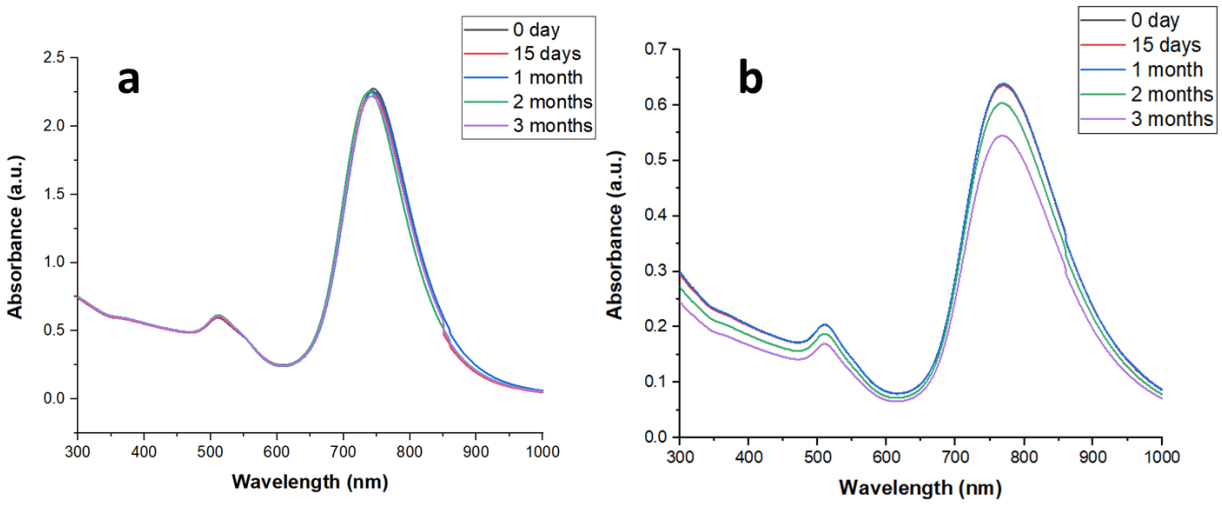

Figure 6A.19 LSPR spectra of a) GNRs and b) γPGA-GNRs when stored for 3 months at 4 ºC

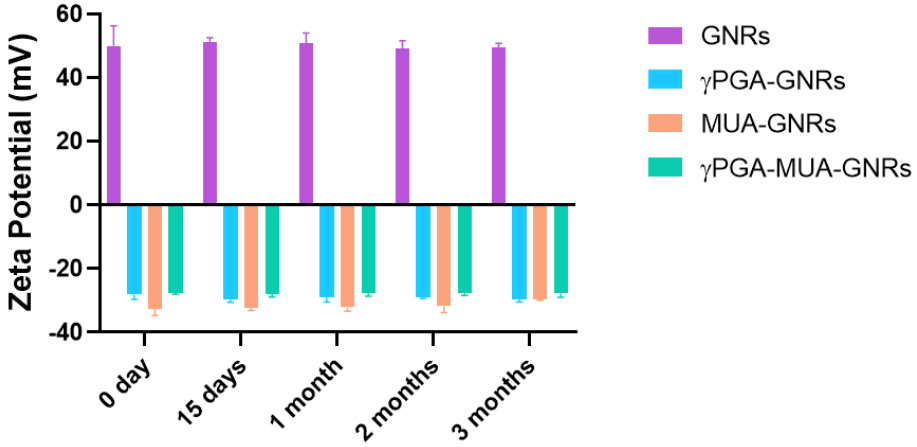

Figure 6A.20 Zeta potential of GNRs, MUA-GNRs, γPGA-GNRs and γPGA-MUA-GNRs when stored for 3 months at 4 ºC

When the stability of MUA-GNRs and γPGA-MUA-GNRs were assessed for 3 months, insignificant change was observed in the LPW of MUA-GNRs and γPGA-MUA-GNRs.

However, with time, there was a little decrease in absorbance of the LSPR spectra of MUA-GNRs and γPGA-MUA-GNRs; this may be due to some deposition of MUA-GNRs and γPGA-MUA-GNRs but there was no change or disorientation of the LSPR spectrum, which validated the structural integrity of both MUA-GNRs and γPGA-MUA-GNRs (Fig. 6A.21a, b). Also, the suspensions of MUA-GNRs and γ-PGA-MUA-GNRs were found to be clear. The zeta potential results also backed the LSPR analysis, as there was no significant change in the zeta potential values till 3 months. Thus, this confirms the good colloidal stability of MUA-GNRs and γPGA-MUA-GNRs for 3 months during storage (Fig. 6A.20).

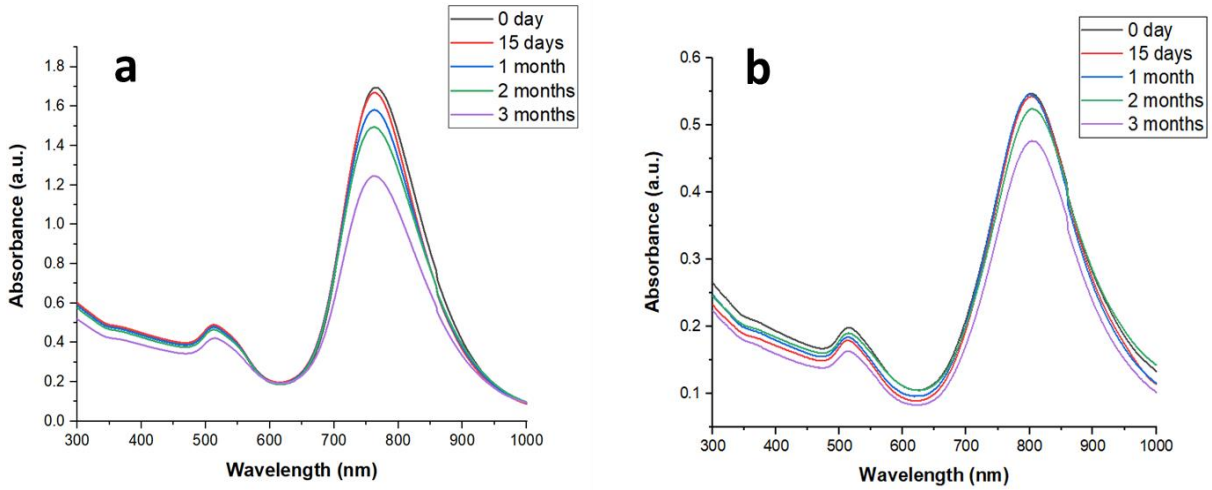

Figure 6A.21 LSPR spectra of a) MUA-GNRs and b) γPGA-MUA-GNRs when stored for 3 months at 4 °C

6A.4. Conclusion

The study successfully achieved the functionalization of GNRs and MUA-GNRs with the γPGA procured from NCIM, which was synthesized by using *Bacillus paralicheniformis* NCIM 5769 (P. G. Nair et al., 2021). Firstly, we have finalized which type of γPGA was suitable to functionalize the GNRs; herein, we have simultaneously screened the various types of γPGA and also optimized the concentration of γPGA appropriate for functionalizing GNRs and MUA-GNRs. Thus, based on UV-visible-NIR spectroscopy and zeta potential study, it was found that γPGA synthesized using tomato waste as substrate at 1 mg/ml had given good results for functionalization of GNRs and MUA-GNRs in DI water. Afterwards, we optimized the volume of γPGA to functionalize 5 ml GNRs and MUA-GNRs at 1 ml. Furthermore, the γPGA-GNRs and γPGA-MUA-GNRs were characterized and functionalization was validated using various techniques.

The UV-Visible-NIR spectroscopy revealed the red shift of 24 ± 2.64nm and 38 ± 4.58nm in the LPW of GNRs and MUA-GNRs, respectively, after functionalization with γPGA, and the zeta potential of GNRs was changed to negative after coating with γPGA as well as the zeta potential of γPGA-MUA-GNRs was decreased compared to the zeta potential of MUA-GNRs. Therefore, these studies primarily confirmed the functionalization of GNRs and MUA-GNRs with γPGA. Further, HRTEM and FESEM analysis supports the well-defined size, shape and morphology of the γPGA-GNRs and γPGA-MUA-GNRs. The SAED analysis shown the crystalline nature of both γPGA-GNRs and γPGA-MUA-GNRs. Also, the EDX, XPS and FTIR studies authenticated the functionalization of the GNRs and MUA-GNRs with γPGA. Subsequently, based on stability studies, the GNRs, MUA-GNRs, γPGA-GNRs and γPGA-MUA-GNRs were found to be highly stable and structural integrity was also maintained during storage at 4 ^{o}C. Thus, the results indicate the synthesis of robust and biocompatible GNRs for bioimaging studies.

CHAPTER 6B

In vitro Efficacy and Bioimaging Studies

6B.1. Introduction

Breast cancer is the second most common cancer around the world, with around 2.3 million cases in the year 2022 (International Agency for Research on Cancer, 2024). Due to its intricate characteristics, the early diagnosis of breast cancer is highly required for effective treatment and cure, as well as to avoid relapses. The commonly used imaging techniques are not sensitive enough to detect small lesions in case of metastasis (Mu et al., 2017). Therefore, combining two or more imaging modalities for the diagnosis of breast cancer will not only help to overcome the limitations imaging techniques but will also enhance the quality of diagnosis and therapy used for cancer. This combination of imaging techniques is known as multimodal imaging (Y. Huang et al., 2012; Morato et al., 2021; Rieffel et al., 2015; Varma et al., 2025; H. Wang et al., 2024). Multimodal imaging helps acquire more precise information from the molecular and cellular levels without using invasive tumor characterization and diagnosis techniques (Shahbazi-Gahrouei et al., 2019b). Although, this multimodal approach can be achieved by combining the scanners or imaging systems or preparing the multifunctional contrast agents so that the same agent can be employed in different imaging techniques (Burke et al., 2017; Rieffel et al., 2015; Varma et al., 2025).

Herein, we have employed γPGA functionalized GNRs as a multimodal contrast agent or imaging probe for both CT and PAI of breast tumor. GNRs are the promising contrast agent for PAI due to their properties like strong absorption coefficient, LSPR, absorption in NIR region and great photothermal conversion ability (X. Li et al., 2020; Z. Y. Ma et al., 2013; Zeng et al., 2022). Further, gold is a very good CT contrast agent due to its higher X-ray absorption coefficient than iodine (L. Li et al., 2023).

In this chapter, we first assessed the GNRs' stability in media, followed by cytotoxic activity, cellular uptake, and hemolysis activity of the functionalized GNRs to establish their biocompatibility. The cell viability assay and cellular uptake studies were carried out on breast cancer cell line MCF-7 and MDA-MB-231 as well as on the nontumorigenic breast cell line MCF-10A. MCF-7 is a less aggressive and non-invasive Luminal A model with ER+ and PR+ status (Comşa et al., 2015), while the MDA-MB-231 is a TNBC model with p53 mutation (Z. Huang et al., 2020), with invasive and aggressive attributes (Chavez et al., 2010). Further, the MCF-10A is a human mammary gland epithelial cell line (Cowell et al., 2005). We investigated the cytotoxicity of GNRs, MUA-GNRs, γPGA-GNRs and γPGA-MUA-GNRs in all the above-mentioned three cell lines. Thereafter, we determined the uptake of different types

of GNRs-based imaging probes in the cell lines for 24 hr by using ICP-MS. Also, the hemolytic activity of the GNRs was investigated. Therefore, all these studies helped to determine the *in vitro* efficacies of different GNRs-based probes. Lastly, the dual-modal CT and photoacoustic bioimaging potential of GNRs-based probes were determined by performing phantom, CT and PAI studies with them. Phantom imaging means testing the relationship between the contrast agent concentrations and the signal strength according to the imaging modality. This is the most common method to compare the imaging potential of the contrast agents with the conventional ones (Rieffel et al., 2015).

6B.2. Method

We synthesized non-functionalized and functionalized GNRs using at optimized values mentioned in the prior chapters. Afterwards, we investigated their stability in media, cell viability, cell uptake, and hemolytic activity as per protocol mentioned in Chapter 2, Sections 2.2.6 and 2.2.8. Further, the CT and PAI potential of GNRs-based probes was examined according to the method given in Chapter 2, Section 2.2.9.

6B.3. Results and discussion

6B.3.1. Stability studies

The stability of GNRs, MUA-GNRs, γPGA-GNRs and γPGA-MUA-GNRs were assessed in media containing fetal bovine serum (FBS) before commencing the *in vitro* studies, based on UV-visible-NIR spectroscopy and zeta potential analysis. The zeta potential of GNRs was decreased and changed to negative (Fig. 6B.1), although the UV-visible-NIR spectra at various time points suggest the structural integrity of GNRs in media (Fig. 6B.2a). Thus, the change in zeta potential was due to the adsorption of serum proteins on the surface of GNRs (Alkilany et al., 2009; Hauck et al., 2008). Similarly, a slight decrease in the zeta potential of the other three functionalized groups of GNRs was also noticed owing to the adsorption of serum proteins on the surface of all the groups of GNRs (Fig. 6B.1) (Alkilany et al., 2009; Hauck et al., 2008). These changes in zeta potential were inconsistent in all the groups of GNRs due to the difference in species of serum proteins coated on the surface of all the groups of GNRs. This difference was due to the variation in surface chemistry among the GNR groups (Hauck et al., 2008). Further, the UV-visible-NIR spectra validates that the structural integrity of the different types of GNRs were maintained in media, too, without any aggregations (Fig. 6B.2a-d). This finding was in

agreement with the findings of Zhan et al., who showed the stability of GNRs in DMEM by UV-visible analysis (Zhan et al., 2010).

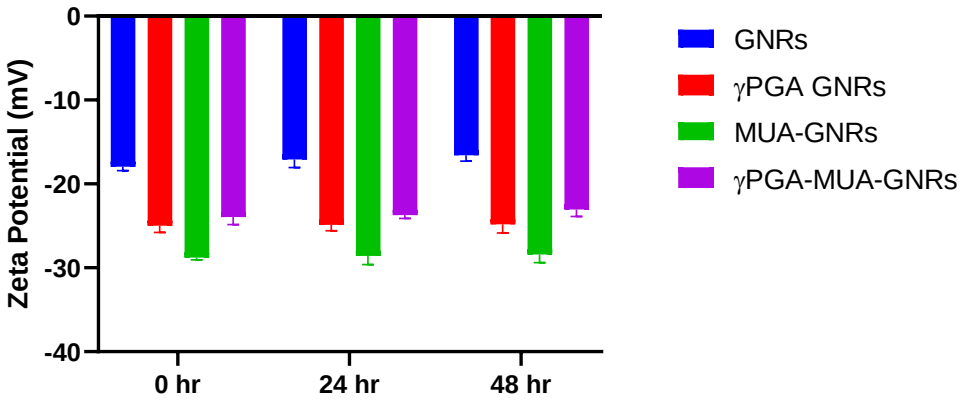

Figure 6B.1 Zeta potential of GNRs, MUA-GNRs, γPGA-GNRs and γPGA-MUA-GNRs in DMEM at various time points

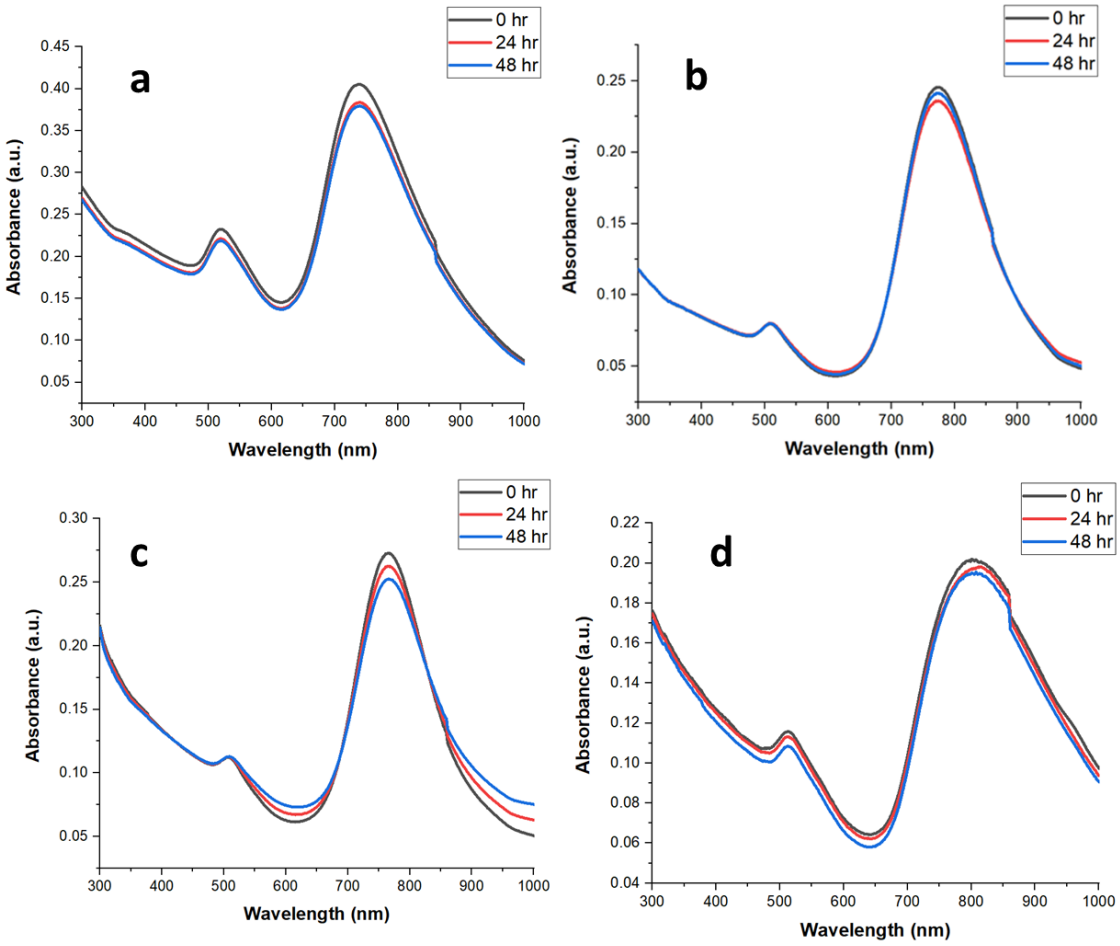

Figure 6B.2 UV-visible-NIR spectra of a) GNRs, b) γPGA-GNRs, c) MUA-GNRs and d) γPGA-MUA-GNRs in DMEM at various time points

6B.3.2. Cell viability assay

The cell viability of MCF-7, MDA-MB-231 and MCF-10A was assessed for 48 hr after treatment with plain γPGA, CTAB and 11-MUA and GNRs based probes.

6B.3.2.1. Cell viability study in MCF-7 cell line

On treating MCF-7 cells with different concentrations of γPGA, the cell viability was found to be more than 99%, even at the highest concentration of 50 μM, suggesting that γPGA is biocompatible. Further, the 11-MUA was also found to be biocompatible as the cell viability was more than 87% at 50 μM concentration (Fig. 6B.3). The CTAB showed its cytotoxic effects, resulting in a drastic decline in cell viability to around 12% at its highest concentration (Fig. 6B.3). Therefore, the plain GNRs were also found cytotoxic to MCF-7 cell lines because they contain CTAB on their surface, which imparts cytotoxicity potential to the plain GNRs (F. Xia et al., 2022; L. Zhang et al., 2018). However, the toxicity of GNRs increased as the concentration of equivalent gold increased shown a dose-dependent effect. Interestingly, the viability of γPGA-GNRs treated cells was more than that of the plain GNRs treated cells; this suggested that the γPGA enhanced the biocompatibility of GNRs. At 50 μM, the viability was around 2 times higher in γPGA-GNRs treated cells compared to GNRs treated cells (Fig. 6B.3). Furthermore, the MUA-GNRs and γPGA-MUA-GNRs were found to be more biocompatible than the GNRs and γPGA-GNRs. This was due to the absence of CTAB in MUA-GNRs and γPGA-MUA-GNRs. At 50 μM concentration, the viability for MUA-GNRs and γPGA-MUA-GNRs was around 87% and 91%, respectively (Fig. 6B.3). Thus, it could be concluded that GNRs attained good biocompatibility when CTAB was replaced with 11-MUA and further functionalized with γPGA. Similarly, many studies revealed great cell viability in MCF-7 cells when treated with GNRs functionalized with different biocompatible molecules (H. Guo et al., 2021; F. Xia et al., 2022; Zhan et al., 2010; L. Zhang et al., 2018). The IC_{50} of all the groups was given in Table 6B.1 (Table 6B.1).

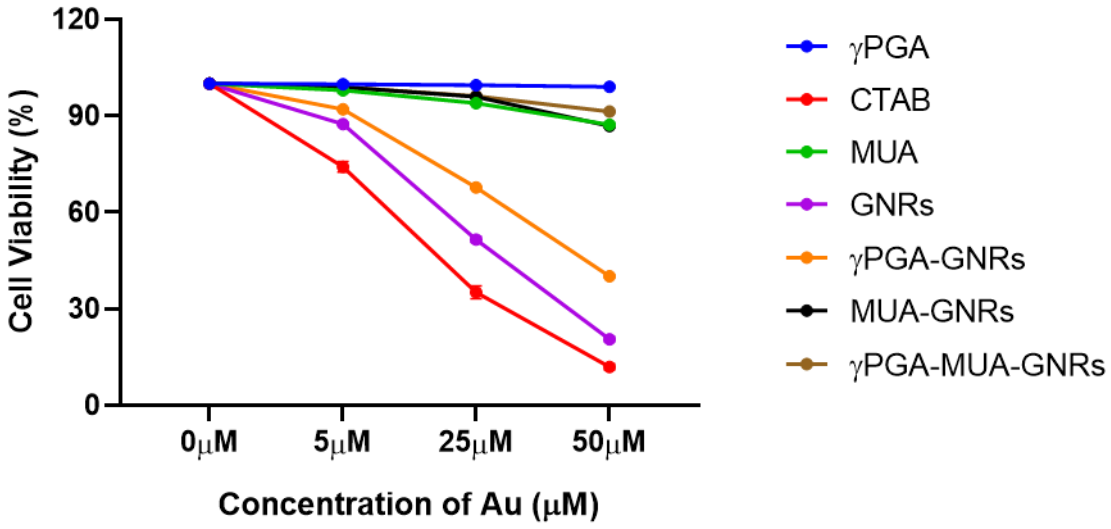

Figure 6B.3 Cell viability percentage of MCF-7 cells when treated with different groups

Table 6B.1 IC_{50} of different groups in MCF-7 cells

Groups	IC_{50} (μM)
γPGA	5453.43 ± 442.75
CTAB	12.2 ± 0.83
MUA	349.45 ± 12.35
GNRs	21.95 ± 0.5
γPGA-GNRs	42.23 ± 0.5
MUA-GNRs	371.49 ± 7.96
γPGA-MUA-GNRs	548.93 ± 4.49

6B.3.2.2. Cell viability study in MDA-MB-231 cell line

Herein, γPGA and 11-MUA were found to be biocompatible with the viability maintained at around 99% and 89%, respectively, even at their highest concentration (Fig. 6B.4). Although, the CTAB, GNRs and γPGA-GNRs were found to be cytotoxic. γPGA-GNRs were less toxic than GNRs due to the presence of highly biocompatible γPGA on its surface. At, 50 μM

concentration, the cell viability in the γPGA-GNRs group was maintained at about 43% compared to 23% in the GNRs group (Fig. 6B.4). However, the presence of CTAB on GNRs and γPGA-GNRs was responsible for their toxicity (T. Guo et al., 2017; Joshi et al., 2013; R. et al. et al., 2020).

Thus, replacing CTAB with biocompatible 11-MUA and further coating it with γPGA greatly enhanced the biocompatibility of GNRs. This was supported by the finding that the cell viability was maintained at about 90% and 93% for groups MUA-GNRs and γPGA-MUA-GNRs, respectively, even at their maximal concentration (Fig. 6B.4). Similarly, many other studies have also found the enhancement in the viability of cells on functionalizing GNRs with biocompatible molecules (T. Guo et al., 2017; Joshi et al., 2013; R. et al. et al., 2020; L. Xie et al., 2023). Yao et al. also found that functionalized GNRs were biocompatible in the MDA-MB-231 cell line (Yao et al., 2021). Table 6B.2 summarizes the IC_{50} of the groups in MDA-MB-231 cells (Table 6B.2).

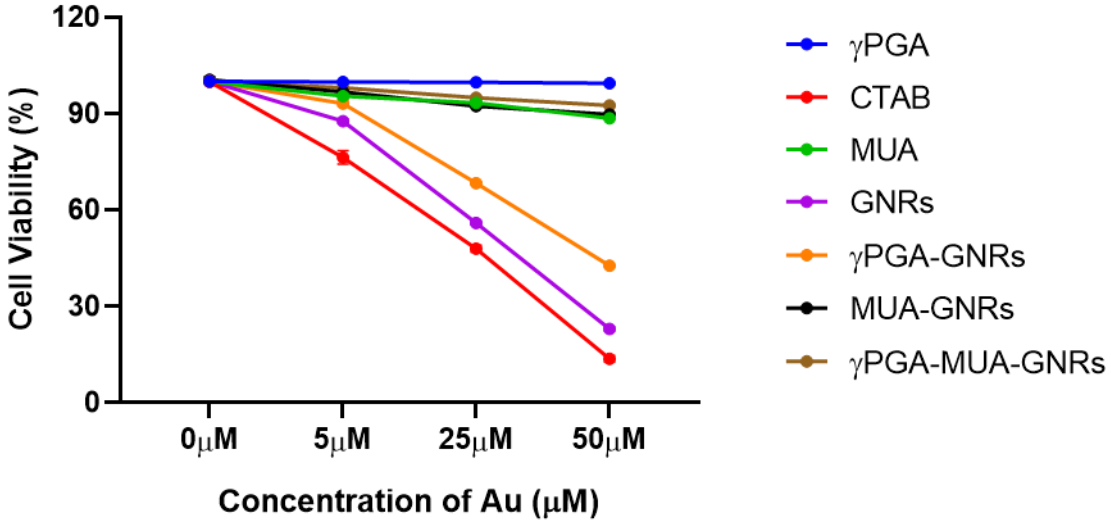

Figure 6B.4 Cell viability percentage of MDA-MB-231 cells when treated with different groups

Table 6B.2 IC_{50} of different groups in MDA-MB-231 cells

Groups	IC_{50} (μM)
γPGA	7920.71 ± 1735.29
CTAB	16.28 ± 0.75

MUA	367.49 ± 10.76
GNRs	24.63 ± 0.49
γPGA-GNRs	45.14 ± 0.58
MUA-GNRs	388.87 ± 12.94
γPGA-MUA-GNRs	571.13 ± 6.61

6B.3.2.3. Cell viability study in MCF-10A cell line

We have tested the toxicity of various groups on normal breast epithelial cell line to prove the biocompatibility of the various groups. The plain γPGAand11- MUA maintained cell viability at around 99% and 90%, respectively, even at their maximal concentration (Fig. 6B.5). Although CTAB has shown its cytotoxic effect (T. Guo et al., 2017; Joshi et al., 2013; R. et al. et al., 2020) by reducing the cell viability to around 14% at 50μM of its concentration (Fig. 6B.5). Further, the GNRs and γPGA-GNRs were found more cytotoxic than the MUA-GNRs and γPGA-MUA-GNRs, owing to the fact that GNRs and γPGA-GNRs had CTAB on them. Although, CTAB was replaced with 11-MUA in groups MUA-GNRs and γPGA-MUA-GNRs. Moreover, the cell viability was maintained around 25%, 43%, 90% and 93% with the groups GNRs, γPGA-GNRs, MUA-GNRs and γPGA-MUA-GNRs, respectively, at their maximal concentration (Fig. 6B.5). However, it was evident that the γPGA functionalization enhanced the biocompatibility of GNRs. Thus, γPGA-MUA-GNRs was a biocompatible probe for the bioimaging application. Similarly, many studies have proved the biocompatibility of GNRs in normal cell lines after functionalizing them with biocompatible molecules (Chauhan et al., 2018; F. Xia et al., 2022; Yue et al., 2019). An et al. have shown that neutral and anionic GNRs do not have evident toxic effects on normal cell lines (An et al., 2019). Similarly, GNRs in this study were also anionic and did not have a toxic effect on MCF-10A cells. Table 6B.3 illustrates the IC_{50} of various groups in MCF-10A cells.

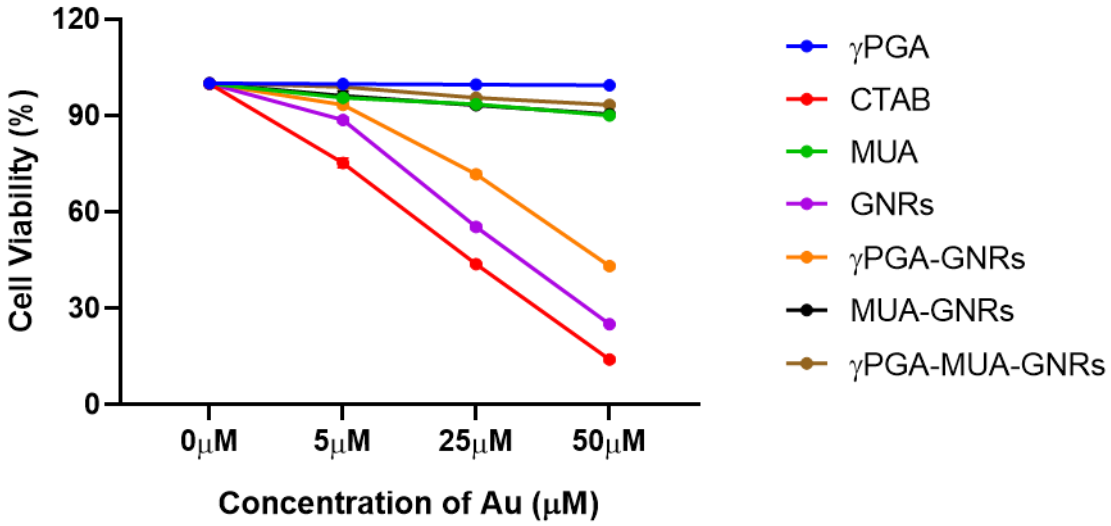

Figure 6B.5 Cell viability percentage of MCF-10A cells when treated with different groups

Table 6B.3 IC_{50} of different groups in MCF-10A cells

Groups	**IC_{50} (μM)**
γPGA	8053.19 ± 215.17
CTAB	14.88 ± 0.58
MUA	416.84 ± 15.19
GNRs	25.38 ± 0.54
γPGA-GNRs	48.47 ± 1.15
MUA-GNRs	424.87 ± 19.3
γPGA-MUA-GNRs	653.14 ± 9.65

6B.3.3. Cellular uptake study

We have quantified the amount of gold present in various cell lines MCF-7, MDA-MB-231 and MCF-10A at various time points through ICP-MS. We treated all the cell lines with 1000 ng gold, and uptake was determined at 30 min, 3 hr, 6 hr, 12 hr and 24 hr. With

the increase in incubation time, the mass of uptake of gold gradually increased for all the groups (GNRs, MUA-GNRs, γPGA-GNRs and γPGA-MUA-GNRs) in all the cell lines.

In the MCF-7 cell line, the total uptake of GNRs was around 36.3% at the end of 24 hr. However, the uptake at 12 and 24 hr was similar, i.e. around 10.78% and 10.67%. Further, the total uptake of MUA-GNRs was more than the plain GNRs, i.e. 51.45%; this may be due to the more biocompatibility of MUA-GNRs compared to GNRs. The CTAB on the surface of GNRs also caused cell death due to its toxicity. Interestingly, it was observed that the total uptake of γPGA-GNRs was around 1.65 times more than the plain GNRs; this might be due to the presence of biocompatible γPGA on the surface of GNRs. Lastly, the maximum uptake was observed for γPGA-MUA-GNRs, i.e. 67.05%, at the end of 24 hr. This group was the most biocompatible group and the γPGA enhaced its uptake. Although, in all the groups, the uptake became almost constant after 12 hr (Fig. 6B.6) (Table 6B.4). Similarly, Nair et al. used PEG-modified GNRs to study their uptake in MCF-7 cell lines (R. V. Nair et al., 2020). Ma et al. also demonstrated the efficient uptake of GNR-capped magnetic core/mesoporous silica shell nanoparticles by MCF-7 cells (M. Ma et al., 2012).

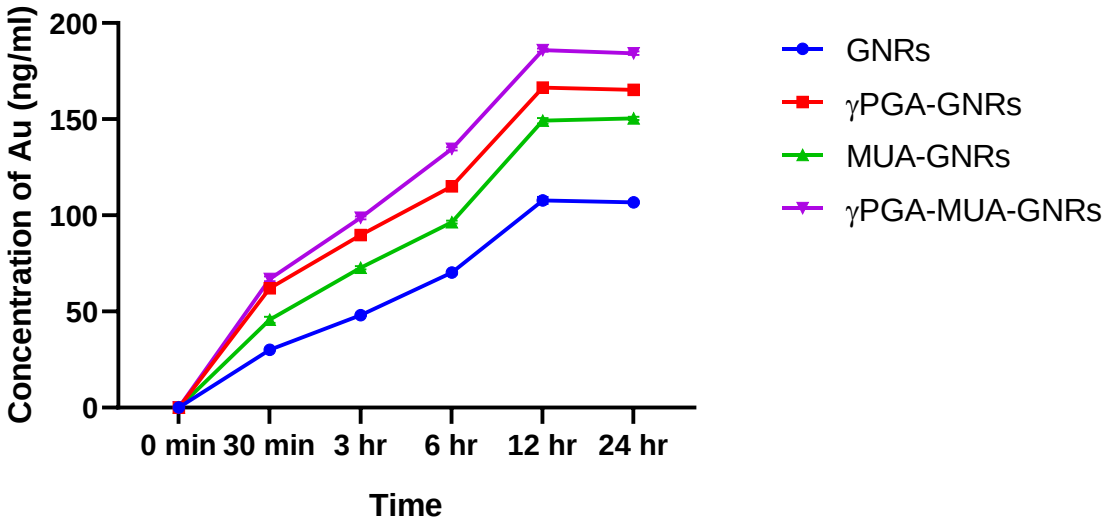

Figure 6B.6 Cellular uptake analysis in MCF-7 cell line using ICP-MS

Further, in MDA-MB-231 cells, the uptake trend was similar to the MCF-7 cells. Here, also after 12 hr, the uptake became constant. The total uptake of GNRs, γPGA-GNRs, MUA-GNRs, and γPGA-MUA-GNRs was around 32.89%, 55.63%, 47.53% and 63.63%, respectively. Similar to MCF-7 cells, here also, the uptake was enhanced for γPGA functionalized groups, and it was minimal for plain GNRs due to the presence of CTAB on them, which

was cytotoxic (Fig. 6B.7) (Table 6B.4). Although CTAB was also in the γPGA-GNRs group but it was masked by γPGA, thus leading to a decrease in its cytotoxic effect and increase in its uptake. Zhou et al. also found a time-dependent uptake of GNRs in MDA-MB-231, which was faster at the initial stage and later slowly reached equilibrium (T. Zhou et al., 2014). Similarly, Zhang et al. also demonstrate the uptake of GNRs by MDA-MB-231 cells through an ICP-MS study (W. Zhang et al., 2012)

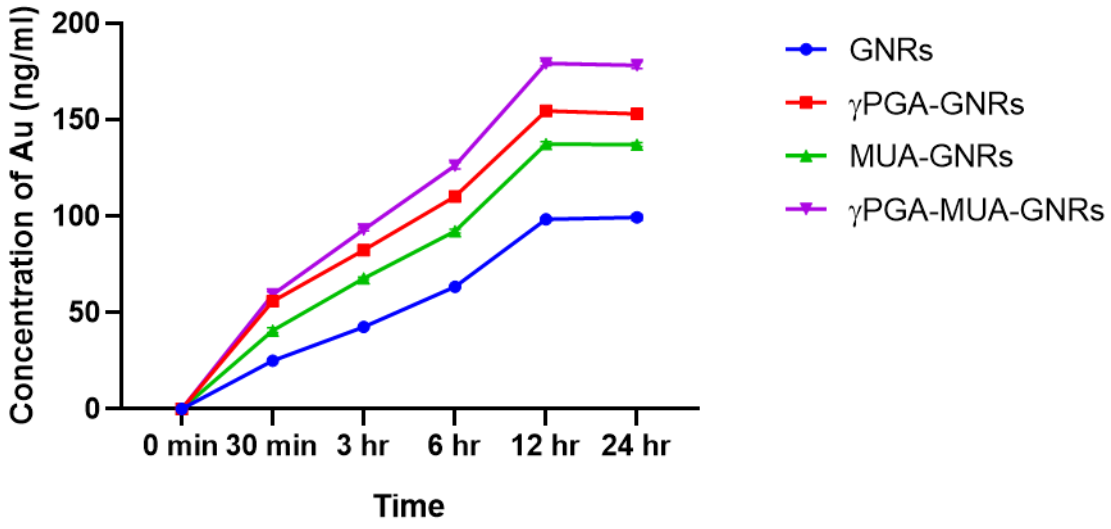

Figure 6B.7 Cellular uptake analysis in MDA-MB-231 cell line using ICP-MS

We also investigated the cellular uptake of various GNRs in MCF-10A cells, which are normal breast epithelial cells. However, the uptake of all the groups of GNRs was lower here compared to the cancerous cells, which might be due to the slow growth rate of the normal cells. The total uptake of GNRs, γPGA-GNRs, MUA-GNRs, and γPGA-MUA-GNRs was around 19.73%, 37.72%, 29.66% and 42.55%, respectively. Although, the uptake trend was identical to the MCF-7 and MDA-MB-231 cells for all the groups of GNRs. Here also, the γPGA functionalization enhanced the uptake efficiency of GNRs, and the uptake of γPGA-MUA-GNRs was maximum due to its more biocompatibility (Fig. 6B.8) (Table 6B.4).

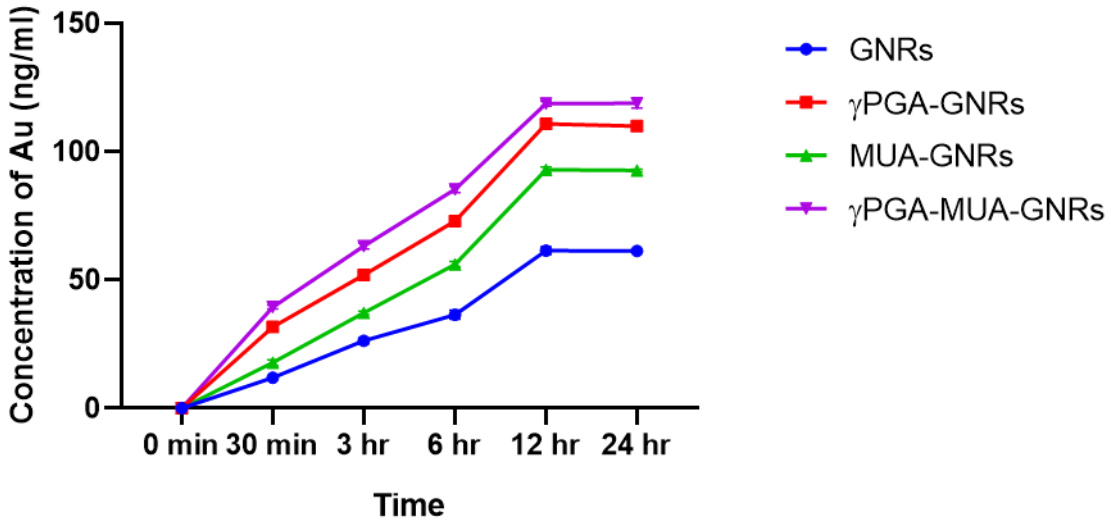

Figure 6B.8 Cellular uptake analysis in MCF-10A cell line using ICP-MS

Table 6B.4 % uptake of various groups of GNRs by MCF-7, MDA-MB-231 and MCF-10A cells at different time intervals

Groups	Avg. % uptake in 30 min	Avg. % uptake in 3 hr	Avg. % uptake in 6 hr	Avg. % uptake in 12 hr	Avg. % uptake in 24 hr
			MCF-7		
GNRs	3	4.81	7.02	10.78	10.67
γPGA-GNRs	6.21	8.97	11.51	16.63	16.52
MUA-GNRs	4.57	7.27	9.64	14.91	15.04
γPGA-MUA-GNRs	6.69	9.86	13.46	18.59	18.43
			MDA-MB-231		
GNRs	2.51	4.25	6.34	9.84	9.93
γPGA-GNRs	5.6	8.24	11.02	15.45	15.3
MUA-GNRs	4.08	6.77	9.22	13.73	13.70
γPGA-MUA-GNRs	5.93	9.31	12.62	17.93	17.83
			MCF-10A		
GNRs	1.18	2.63	3.64	6.14	6.13
γPGA-GNRs	3.17	5.19	7.29	11.08	10.99
MUA-GNRs	1.78	3.71	5.61	9.29	9.27
γPGA-MUA-GNRs	3.95	6.31	8.53	11.87	11.88

Cells have receptors that recognize proteins in the serum-containing media, thus leading to receptor-mediated uptake of GNRs (Alkilany et al., 2009). Many studies have demonstrated the receptor-mediated uptake of GNRs by the cells (Alkilany et al., 2009; An et al., 2019; M. Ma et al., 2012; X. Xie et al., 2017; T. Zhou et al., 2014). Therefore, in our study, it was also found that all the groups of GNRs had negative surface charges due to the functional groups as well as the serum proteins attached to their surface (Alkilany et al., 2009; Hauck et al., 2008) might be leading to the receptor assisted endocytosis of all the groups of GNRs. Although, many factors control the binding of serum proteins on the surface of GNRs. The factors are properties of GNRs, protein concentration, and protein binding affinity (Hauck et al., 2008).

Further, the studies revealed that the uptake of cationic nanoparticles was more than the anionic and neutral (Ratto et al., 2016; D. Zhang et al., 2018). However, in our case, the GNRs have a negative charge due to the serum proteins on them. An et al. reported cytotoxicity of cationic GNRs on normal cells compared to the anionic and neutral. Also, they reported that the uptake of anionic GNRs was significantly more than that of neutral GNRs (An et al., 2019). Our study corroborated this because the uptake of GNRs, which had zeta towards the neutral side, was lesser than the other groups of GNRs. Moreover, the initial surface charge is not the only predictor of cytotoxicity and cellular uptake of GNRs. Indeed, the uptake is also ruled by the type of protein adsorbed on the surface and its orientations because, by the presentation of different faces of the proteins to cells, different receptor-based endocytic pathways could be explored for cellular uptake of GNRs (Alkilany et al., 2009). Furthermore, the higher uptake of γPGA-GNRs compared to GNRs could be due to the masking of CTAB on the surface of GNRs with the polymer, making the γPGA-GNRs more biocompatible and less cytotoxic for the cells (Alkilany et al., 2009).

6B.3.4. Hemolysis assay

The biocompatibility of GNRs, γPGA-GNRs, MUA-GNRs, and γPGA-MUA-GNRs were also assessed by the hemolysis assay at various concentrations. Here, we have used triton -x as the positive control and PBS as the negative control. The aim was to determine the effect of surface functionalization of GNRs on hemolysis. Plain GNRs had shown hemolysis after 5 μM gold concentration, suggesting the non-biocompatibility of the GNRs. GNRs showed around 96.26% hemolysis at 25 μM gold concentration. This could be due to the presence of CTAB on their surface (Fig. 6B.9a & Fig. 6B.10a). Further, γPGA-GNRs had shown around 5.94% hemolysis at 100 μM gold concentration, which

validated the fact that γPGA provided biocompatibility to the GNRs by masking CTAB present on their surface (Fig. 6B.9b & Fig. 6B.10b). The MUA-GNRs and γPGA-MUA-GNRs groups were found to be more biocompatible with negligible hemolysis of < 3% at their maximal concentration (Fig. 6B.9c, d & Fig. 6B.10c, d). This might be because there was no CTAB in these groups, as 11-MUA replaced it. The comparative hemolytic analysis of all the groups of GNRs was given in Figure 6B.11 (Fig. 6B.11). The functionalization enhances the hemocompatibility of GNRs; this was also observed in other studies (H. Guo et al., 2021; Hou et al., 2022; Prasad et al., 2018).

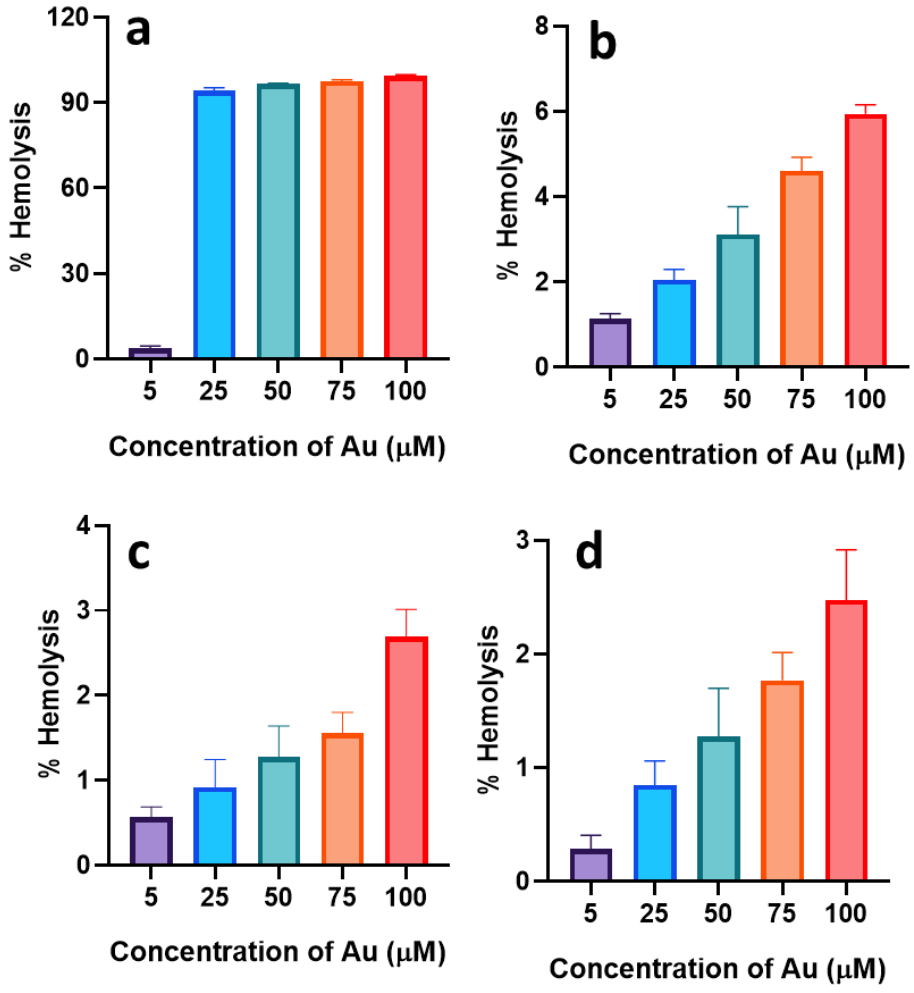

Figure 6B.9 % hemolysis shown by a) GNRs, b) γPGA-GNRs, c) MUA-GNRs and d) γPGA-MUA-GNRs

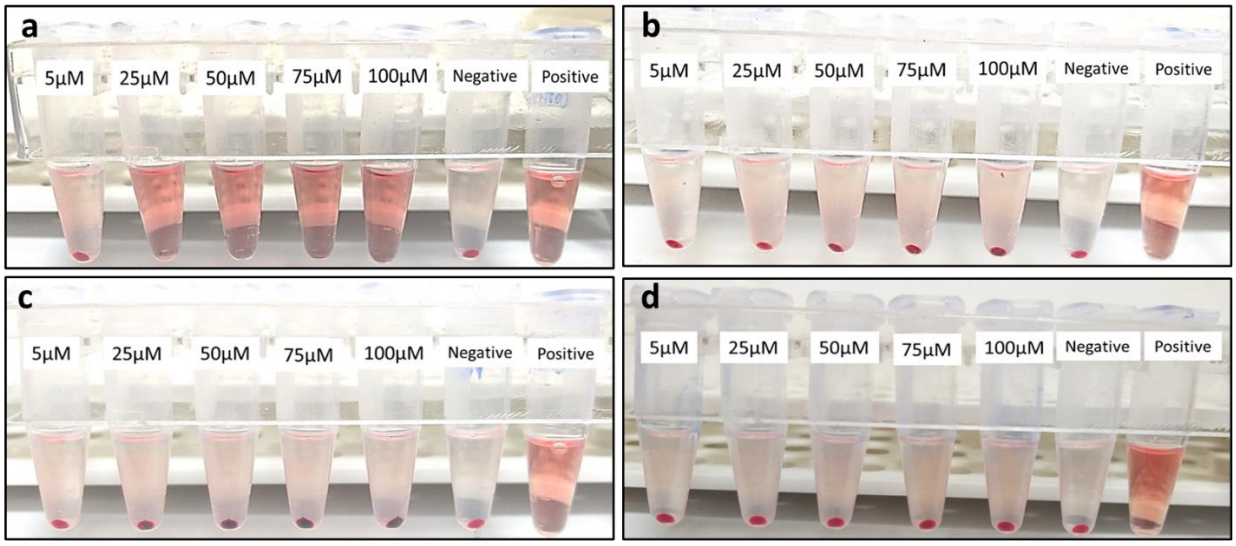

Figure 6B.10 Digital photographs showing hemolyzed and precipitated RBCs during hemolysis study with a) GNRs, b) γPGA-GNRs, c) MUA-GNRs and d) γPGA-MUA-GNRs

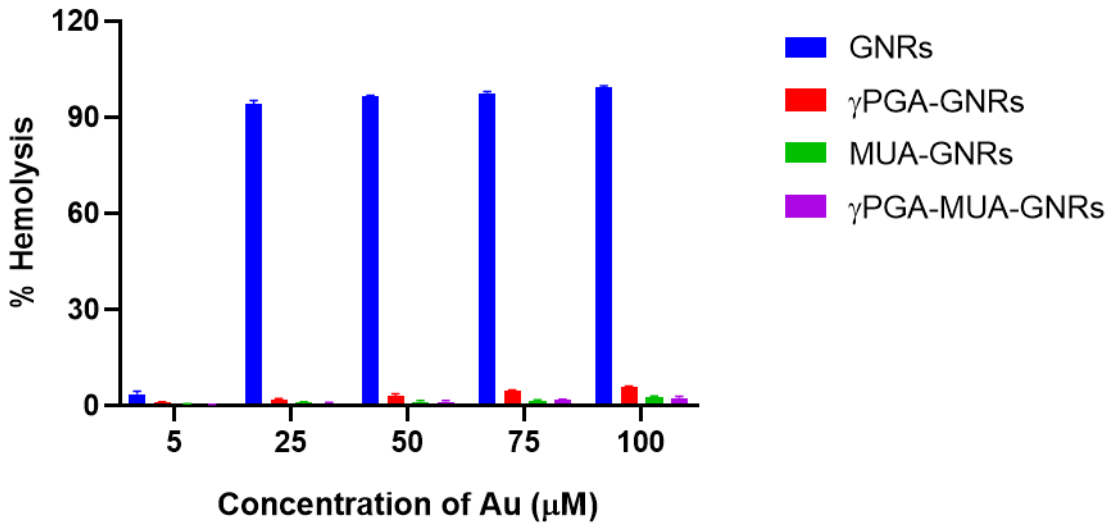

Figure 6B.11 Comparative % hemolytic activity of GNRs, γPGA-GNRs, MUA-GNRs, and γPGA-MUA-GNRs

6B.3.5. Phantom CT imaging study

CT imaging is one of the most common techniques for clinical diagnosis and medical research. It offers advantages like high resolution and deep tissue penetration imaging (Shang et al., 2017). CT imaging uses X-rays to irradiate body parts under examination, generating various grey-scale image contrast distribution maps, which help to investigate the condition (F.

Xia et al., 2022). GNRs are potent CT contrast agents owing to their strong ability to attenuate X-rays (P. Huang et al., 2011; F. Xia et al., 2022) due to the high atomic number (79) of gold element (F. Xia et al., 2022). Thus, we investigated the CT contrast ability by evaluating the Hounsfield unit (HU) of GNRs, γPGA-GNRs, MUA-GNRs, and γPGA-MUA-GNRs. The HU value of all the groups of GNRs was taken with different Au concentrations in water. The concentration for GNRs and γPGA-GNRs were 2, 4, 8, 12 and 24 μM, as it was below IC_{50} of these GNRs groups. Although the concentration range for MUA-GNRs and γPGA-MUA-GNRs was 100-500 μM, considering the IC_{50} of these groups.

The photographs acquired for all the groups of GNRs at different Au concentrations have shown that the CT image's brightness increased with the increase in Au concentrations. Further, the linear correlation was noticed in the HU values of various GNR groups and their concentrations (Fig. 6B.12a, b & Fig. 6B.13 a, b). Thus, this proves that GNRs were the efficient CT contrast probes. When the HU values of GNRs and γPGA-GNRs were compared, no significant difference was observed (Fig. 6B.12a, b). Similarly, the CT intensity of MUA-GNRs and γPGA-MUA-GNRs were also similar (Fig. 6B.13a, b). Therefore, the functionalization did not affect the CT contrast ability of GNRs and the extensively biocompatible γPGA-MUA-GNRs among all the groups of GNRs could be used as a potential CT contrast agent. Interestingly, it was also observed that the CT intensity of all the groups of GNRs was slightly better than the CT intensity of the clinically used contrast agent, iohexol, at the same concentrations. The HU value of GNRs and γPGA-GNRs at maximal concentration was around 6.3 and 6.97, respectively; however, the HU value of iohexol was around 5.87 at the same concentration (Fig. 6B.12a-c). Similarly, the HU value of MUA-GNRs and γPGA-MUA-GNRs at maximal concentration was around 145.55 and 147.63, respectively; however, at the same concentration, the HU value of iohexol was around 141.96 (Fig. 6B.13a-c).

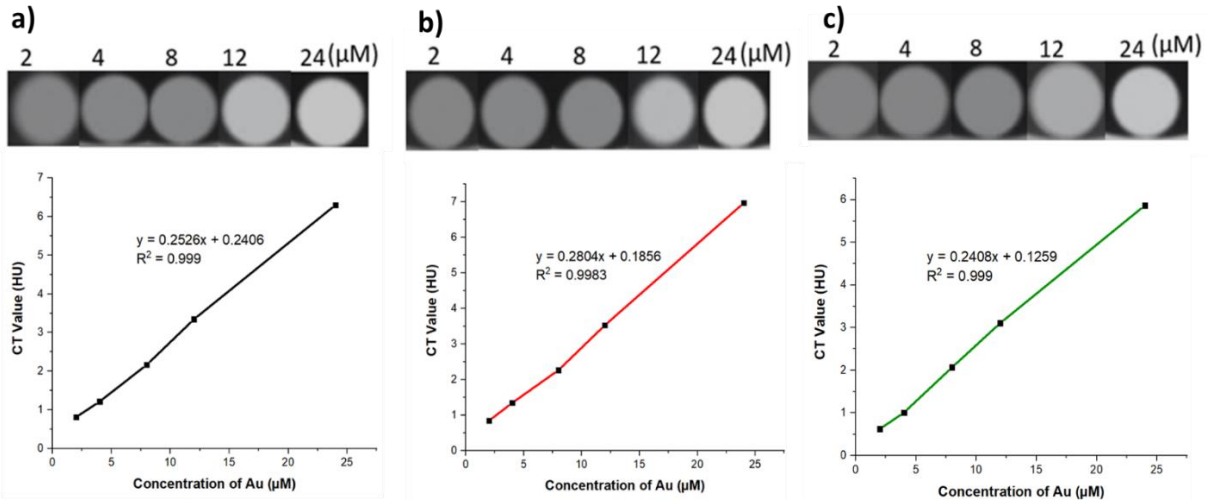

Figure 6B.12 Phantom CT images and HU values of a) GNRs, b) γPGA-GNRs and c) iohexol at various concentrations

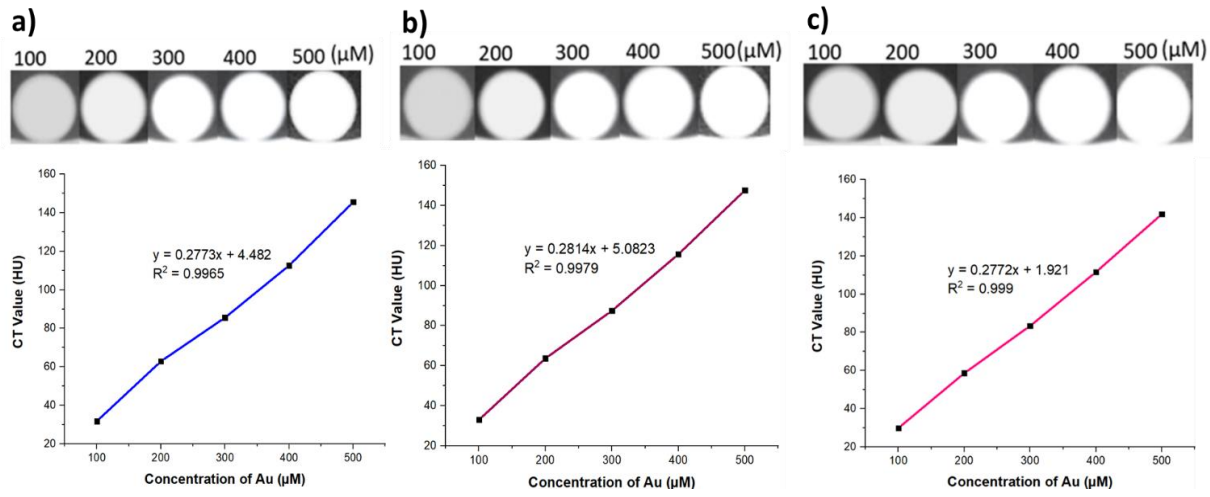

Figure 6B.13 Phantom CT images and HU values of a) MUA-GNRs, b) γPGA-MUA-GNRs and c) iohexol at various concentrations

6B.3.6. Phantom PAI study

PAI is an efficient optical bioimaging modality with higher imaging depth and spatial resolution than other optical imaging techniques. It works on the photoacoustic effect due to the absorption of light by the photoacoustic agents (Shang et al., 2017). Gold-based nanomaterials, specifically GNRs, are promising contrast agents for PAI owing to their attributes like strong absorption coefficient, LSPR properties, NIR region absorption ability and great photothermal conversion ability (T. Guo et al., 2017; X. Li et al., 2020; Z. Y. Ma et al., 2013; Qin et al., 2013; Zeng et al., 2022). Thus, we measured the PA signal of GNRs, γPGA-GNRs, MUA-GNRs, and γPGA-MUA-GNRs. The PA intensity of all the groups of GNRs

was evaluated with different Au concentrations in water. The concentration for GNRs and γPGA-GNRs were 2, 4, 8, 12 and 24 μM; however, the concentration range for MUA-GNRs and γPGA-MUA-GNRs was 100-500 μM, considering the IC_{50} of these groups.

The photographs developed for all the groups of GNRs at different Au concentrations have shown that the photoacoustic intensity increased with the increase in Au concentrations. However, due to the very low concentrations, the change was not evident for GNRs, γPGA-GNRs and standard (2, 4, 8, 12 and 24 μM). Nevertheless, the linear correlation was seen in the photoacoustic intensity of various GNR groups and their concentrations (Fig. 6B.14a, b & Fig. 6B.15 a, b). Therefore, this proves that GNRs were the efficient PAI probes. Further, an insignificant difference was detected when the photoacoustic intensity of GNRs and γPGA-GNRs was compared (Fig. 6B.14a, b). Likewise, the photoacoustic intensity of MUA-GNRs and γPGA-MUA-GNRs were also comparable (Fig. 6B.15a, b). Hence, it was confirmed that the functionalization did not affect the photoacoustic contrast ability of GNRs, and the more biocompatible γPGA-MUA-GNRs among all the groups of GNRs could be used as a promising PAI probe. Remarkably, it was also noted that the photoacoustic intensity of all the groups of GNRs was slightly better than the intensity of the standard photoacoustic imaging agent, methylene blue, at the same concentrations. The photoacoustic intensity of GNRs and γPGA-GNRs at 780 nm and at their maximal concentration was around 0.1962 and 0.1996, respectively; however, at the same concentration, the photoacoustic intensity of standard was around 0.1924 (Fig. 6B.14a-c). Similarly, the photoacoustic intensity of MUA-GNRs and γPGA-MUA-GNRs at maximal concentration was around 2.4324 and 2.4535, respectively, although the photoacoustic intensity of methylene blue was around 2.3358 (Fig. 6B.15a-c).

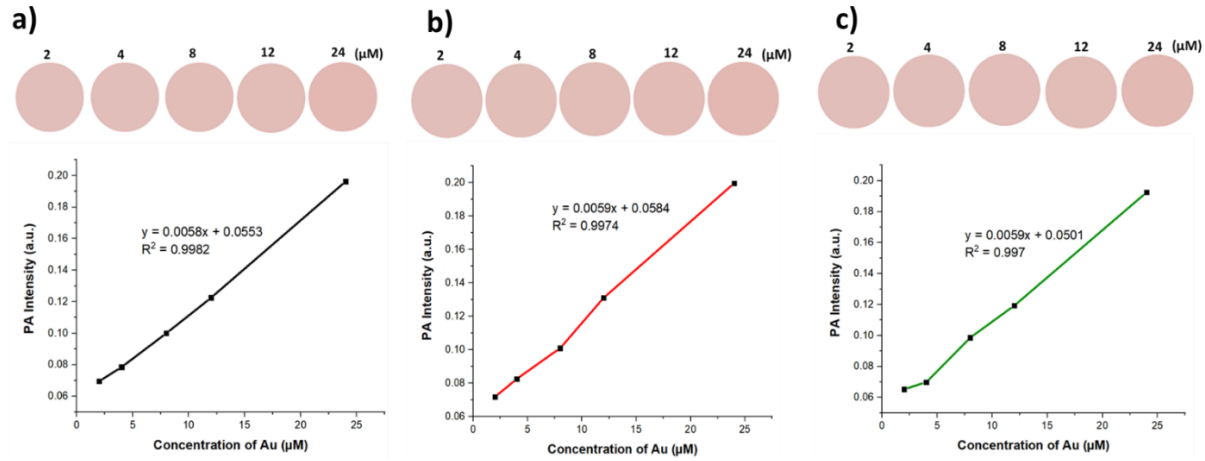

Figure 6B.14 Phantom photoacoustic images and PA intensity of a) GNRs, b) γPGA-GNRs and c) methylene blue at various concentrations

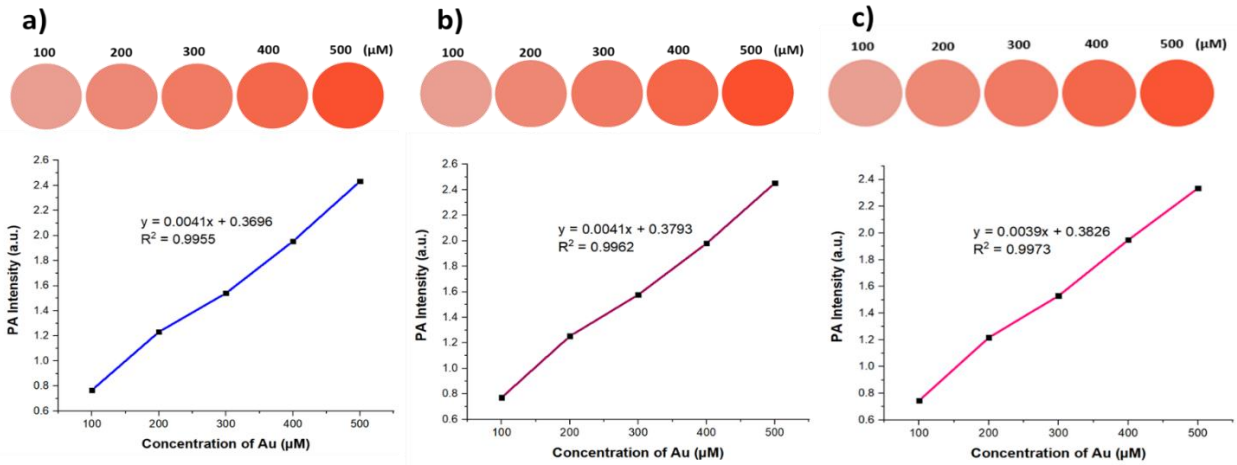

Figure 6B.15 Phantom photoacoustic images and PA intensity of a) MUA-GNRs, b) γPGA-MUA-GNRs and c) methylene blue at various concentrations

6B.4. Conclusion

The GNRs, γPGA-GNRs, MUA-GNRs, and γPGA-MUA-GNRs maintained their structural integrity in the DMEM with the adsorption of serum proteins on their surface. The *in vitro* efficacy studies defined the robust efficacy of the groups of GNRs synthesized. The cell viability assay established the great biocompatibility of the γPGA-MUA-GNRs in both cancerous and normal breast cell lines. Also, the MUA-GNRs and γPGA-MUA-GNRs do not have inherent cytotoxic potential, making them the biocompatible multimodal imaging probe. The biocompatibility was further established by the hemolytic assay. The γPGA-GNRs, MUA-GNRs, and γPGA-MUA-GNRs showed great hemocompatibility with less than 6% hemolysis at their highest concentration. The cellular uptake studies showed

higher uptake of γPGA-MUA-GNRs compared to other groups of GNRs in all three cell lines. However, the uptake was slow in normal breast epithelial MCF-10A cells compared to the cancerous MCF-7 and MDA-MB-231 cells. After γPGA-MUA-GNRs, the next highest uptake was of γPGA-GNRs. These studies validated that the functionalization of GNRs by replacing CTAB with 11-MUA and then by coating biocompatible γPGA on their surface enhances the biocompatibility, stability and cellular uptake efficiency of the GNRs for the bioimaging application.

This robust and biocompatible γPGA-MUA-GNRs was found to have dual-modal CT and PAI contrast properties, which combine the advantages of high spatial/ density resolution and high sensitivity. By comparing the CT and PA intensity of GNRs, γPGA-GNRs, MUA-GNRs, and γPGA-MUA-GNRs, it was also established that the functionalization did not affect the CT and PAI contrast potential of GNRs. The contrast intensity was similar for the plain and functionalized GNRs at different concentrations of Au and also a good linear relationship was recorded between the CT and PA intensity and the concentrations of all the groups of GNRs based on Au content. Notably, the various types of GNRs were found to be slightly better than the standard CT and PAI contrast agents. Thus, the *in vitro* efficacy studies and phantom CT and PAI studies confirmed the great dual-modal cancer imaging potential of biocompatible γPGA-MUA-GNRs. This novel multimodal GNRs-based imaging probe will not only subjugate the side effects of conventional CT and PAI contrast agents but will also enhance the sensitivity of cancer diagnosis.

CHAPTER 7

Conclusions & Future Prospects

7.1. Conclusions

GNRs were extensively synthesized by the seed-mediated growth method, and the process parameter for synthesizing GNRs for biosensing and bioimaging applications was identified. We optimized 1 mM gold precursor concentration, 0.2 M CTAB, 250 µl $AgNO_3$ (4 mM), 75 µl ascorbic acid, 12 µl seed volume, 30 minutes seed aging time, pH 3, and time of synthesis 2 hr for synthesizing monodisperse and stable GNRs of aspect ratio around 3.8. The major factors that affect the synthesis of GNRs are gold precursor concentration, CTAB concentration, silver nitrate concentration and its volume, ascorbic acid volume, seed volume, and pH. Though, synthesis time and seed aging time showed an insignificant effect on the GNR synthesis process.

The analytical characterization techniques confirmed the synthesis of rod-shaped particles with transverse and longitudinal SPR bands with LPW (around 751 nm) in the NIR region and the zeta potential +49.98 ± 6.29 mV, validating the good stability. The GNRs were of size 41.72 ± 5 nm x 11 ± 2 nm elucidated by HRTEM and corroborated by FESEM too. The EDX, STEM mapping, XPS, and FTIR analysis substantiated the synthesis of CTAB-capped GNRs. The XRD and SAED analysis confirmed the crystalline structure.

Further, to replace cytotoxic CTAB from the surface of GNRs with 11-MUA, we optimized an alkaline aqueous solvent for dissolving MUA; 2 ml 11-MUA to modify 5 ml GNRs; 800 rpm stirring speed and 8 hr as the time required to modify GNRs. All these parameters were found to be significant for the exchange of CTAB with 11-MUA from the surface of GNRs. Although, these parameters did not have a significant effect on the zeta potential of MUA-GNRs. The replacement was confirmed by the red shift in the LPW of GNRs as well as by the change of zeta potential from positive to negative due to the free -COOH group in 11-MUA. Upon characterization, we confirmed that the MUA-GNRs were stable with zeta potential -36.53 ± 2.96 mV and a well-defined UV-Visible-NIR spectrum. The red shift of around 20 ± 4 nm in the LPW of MUA-GNRs was observed when compared with the LPW of CTAB-capped GNRs. The size of MUA-GNRs observed by HRTEM was 42.97 ± 3.23 nm x 11.9 ± 1.76 nm, similar to what was marked in FESEM analysis. The EDX, STEM mapping, XPS and FTIR analysis corroborated the synthesis of MUA-GNRs, and the SAED pattern elucidated their crystalline nature. Also, the MUA-GNRs were highly stable in borate buffer pH 9, although DI water can also be used as a dispersing medium. However, PBS cannot be used as the dispersing medium as MUA-GNRs lost their structural integrity and stability in PBS. These MUA-GNRs are used

to further functionalize GNRs, specifically for biosensing and multimodal bioimaging applications.

For the biosensing study, the MUA-GNRs were covalently functionalized with TSH antibodies by the EDC/NHS linking method. We optimized certain factors that could affect the stability and conjugation extent of the antibody on GNRs. Firstly, the borate buffer of pH 9 was optimized as the reaction medium instead of PBS because the stability and structural integrity of GNRs were maintained when the functionalization process was performed in the borate buffer. Thereafter, the antibody concentration was fixed at 50 µg/ml. Lastly, to keep Ab-GNRs stable, the percentage of sucrose that should be added to the resuspension buffer of Ab-GNRs was optimized to 5%. Furthermore, the characterization techniques also backed the functionalization of MUA-GNRs with TSH antibodies. The UV-visible-NIR spectrum of Ab-GNRs was red shifted by around 41± 3nm compared to the spectrum of MUA-GNRs and the zeta potential decreased to -15.14 ± 0.78 mV, which confirmed the conjugation of antibody on the surface of GNRs. Further, the size of Ab-GNRs was found to be 43.56 ± 5.16 nm x 11.59 ± 1.93 nm by HRTEM, which was also supported by the FESEM study. The SAED revealed the crystalline nature of Ab-of GNRs. The EDX, XPS and FTIR studies corroborated the bioconjugation of the MUA-GNRs with the TSH antibody. The % binding efficiency of the TSH antibody was 83.38 ± 0.34 %. Notably, it was found that the MUA-GNRs and Ab-GNRs were stable in colloidal suspension for 3 months and 15 days, respectively, when stored at 4 ^{o}C. This stability of Ab-GNRs was more than enough to prepare LFA.

These Ab-GNRs were employed as labels for the biosensing of TSH by LFA. However, before preparing LFA, the sensing potential and specificity of Ab-GNRs toward TSH were established by a UV-visible-NIR spectroscopy study. We quantified the red shift in the UV-visible-NIR spectrum of Ab-GNRs at different concentrations of TSH, as the longitudinal SPR of GNRs is sensitive to changes in the refractive index of the medium, thus making them a potent biosensing agent. Further, the fast, user-friendly and robust LFA was prepared by optimizing certain factors. We optimized 20 OD of the conjugate, 3 mg/ml as the capture antibody concentration and 50 µl as the sample volume. The LOD of the LFA was found to be 0.3 µIU/ml, and the LFA was specific towards TSH; it did not show any cross-reactivity with the hormones FSH, LH and hCG. Additionally, this LFA can provide reproducible results for 3 months when stored in a desiccated environment. The LFA could semi-quantitatively elucidate the hypothyroidism and hypothyroidism based on the TSH. As the normal range of TSH in

adult humans is 0.5-5 µIU/ml, therefore when the concentration in the sample is below 0.3 µIU/ml, there will be no appearance of the test line and if it is between 0.5-0.3 µIU/ml, a very faint test line will form, as from 0.5 µIU/ml the clear test line appeared on the device. Thus, by this hyperthyroidism could be estimated. However, when the concentration of TSH is above 5 µIU/ml, the darker test line will appear, leading to the detection of hypothyroidism. Hence, our study proved that the GNRs can be employed as an adequate label for LFA. Along with this, the developed device could concurrently detect hypothyroidism and hyperthyroidism without involving the use of any quantification method.

Further, for bioimaging applications, GNRs and MUA-GNRs were functionalized with the γPGA obtained from NCIM, which was synthesized by using *Bacillus paralicheniformis* NCIM 5769. Initially, on screening three types of γPGA bioproduced by using different substrates as well as the commercially available one, γPGA produced from tomato waste as a substrate had given adequate results, so, it was finalized for functionalization of GNRs. We optimized 1 mg/ml γPGA concentration and 1 ml γPGA volume to functionalize 5 ml GNRs and MUA-GNRs. Upon characterization, the UV-Visible-NIR spectroscopy revealed the red shift of 24 ± 2.64 nm and 38 ± 4.58 nm in the LPW of GNRs and MUA-GNRs, respectively, and zeta potential of γPGA-GNRs and γPGA-MUA-GNRs were -28.06 ± 1.58 mV and -27.59 ± 0.44 mV, respectively. Thus, the change in zeta potential after functionalization and the shift in LPW confirmed the coating of γPGA on GNRs and MUA-GNRs. The EDX, XPS and FTIR studies also validated the functionalization of the GNRs and MUA-GNRs with γPGA. The size of γPGA-GNRs and γPGA-MUA-GNRs, based on HRTEM, were 43.22 ± 3.8 nm x 12.2 ± 1.58 nm and 45.71 ± 3.29 nm x 12.9 ± 1.84 nm, respectively, FESEM also corroborated this. The SAED confirmed the crystalline nature of both γPGA-GNRs and γPGA-MUA-GNRs. Furthermore, the stability studies revealed the excellent stability of the GNRs, MUA-GNRs, γPGA-GNRs and γPGA-MUA-GNRs for 3 months at 4 ^{o}C.

The GNRs, γPGA-GNRs, MUA-GNRs, and γPGA-MUA-GNRs were also stable in the *in vitro* culture media. The cell viability assay established the great biocompatibility of the γPGA-MUA-GNRs in both cancerous (MCF-7 & MDA-MB-231) and normal breast (MCF-10A) cell lines. The γPGA-MUA-GNRs were also found to be hemocompatible with <3% hemolysis at maximal concentration. The cellular uptake studies showed higher uptake of γPGA functionalized GNRs compared to other groups of GNRs in all three cell lines. Thus, γPGA coating enhanced the cellular uptake efficiency of the GNRs. Moreover,

this robust and biocompatible γPGA-MUA-GNRs was found to be an excellent dual-modal CT imaging and PAI contrast agent for the bioimaging of cancer. A good linear relationship was recorded between the CT and PA intensity and the concentrations (based on Au content) of γPGA-MUA-GNRs. Also, the CT imaging and PAI contrast property of γPGA-MUA-GNRs were found to be better than the clinically used CT imaging and PAI contrast agents. This probe combines the advantages of CT imaging, i.e. high spatial/ density resolution, and PAI, i.e. high sensitivity.

Our study is a proof of concept and concurs with the hypothesis that the functionalized GNRs are promising labels for LFA and a competent multimodal bioimaging probe. The Ab-GNRs were established as a potent, sensitive and robust label for detecting TSH through LFAs, and the highly biocompatible γPGA-MUA-GNRs exhibited outstanding dual-modal CT imaging and PAI contrast properties. Therefore, the functionalized GNRs demonstrated exceptional diagnostic capabilities to detect and diagnose various biological conditions accurately.

7.2. Future prospects

This proof-of-concept study highlights the proficient TSH sensing potential of stable Ab-GNRs as a label in LFA. Also, it demonstrates the multimodal imaging capability of biocompatible γPGA-MUA-GNRs. Upon this groundwork, we lay out the envisioned roadmap for subsequent investigations.

- The various other factors to enhance the sensitivity of the LFA can be optimized. The factors could be types of paper, assay buffers, etc. Also, the real sample analysis from individuals of different age groups, genders, geographical areas, and medical conditions can validate the LFA for further steps of clinical translation.
- Multiplex LFA can be prepared for complete thyroid function tests on a single device. Multiplexing will help to determine TSH, T4 and T3 simultaneously.
- The robust and stable GNRs can be used as label for preparing LFA for a wide array of biological and environmental indicators following specific functionalization at the optimized parameters outlined in this study.
- The γPGA-MUA-GNRs can be further evaluated by various *in vitro* assays such as receptor-specific assays, determining the uptake mechanism of the GNRs, cell cycle analysis, cell apoptosis assay, etc. Also, the efficacy of this imaging probe can be assessed on 3D spheroid models. These assays back the efficiency of the functionalized GNRs.

- Subsequently, the probe can be investigated for *in vivo* efficacy studies to determine their nonspecific accumulation, accumulation in the tumor, pharmacokinetics and pharmacodynamics, etc.
- γPGA-MUA-GNRs can be functionalized with the specific targeting ligand depending on the type of cancer, to achieve more precise targeted multimodal bioimaging of various cancers. Also, the targeted γPGA-MUA-GNR can be employed for simultaneous targeted therapy and diagnosis of any biological condition.
- This GNRs-based probe can also be utilized for personalized treatment and diagnosis to treat any diseases when tailored according to the unique genetics and medical profile of the patient.

BIBLIOGRAPHY

Abareshi, A., Arshadi Pirlar, M., Houshiar, M. (2021). Experimental and theoretical investigation of the photothermal effect in gold nanorods. *New Journal of Chemistry*, *45*(1), 298–303. https://doi.org/10.1039/d0nj04580b

Agarwal, A., Shao, X., Rajian, J. R., Zhang, H., Chamberland, D. L., Kotov, N. A., Wang, X. (2011). Dual-mode imaging with radiolabeled gold nanorods. *Journal of Biomedical Optics, 16*(5), 051307. https://doi.org/10.1117/1.3580277

Ahmad, F., Salem-Bekhit, M. M., Khan, F., Alshehri, S., Khan, A., Ghoneim, M. M., Wu, H. F., Taha, E. I., Elbagory, I. (2022). Unique properties of surface-functionalized nanoparticles for bio-application: Functionalization mechanisms and importance in application. *Nanomaterials*, 12(8), 1333. https://doi.org/10.3390/nano12081333

Ajayeoba, T. A., Dula, S., Ijabadeniyi, O. A. (2019). Properties of poly-γ-glutamic acid producing-Bacillus species isolated from Ogi liquor and lemon-Ogi liquor. *Frontiers in Microbiology*, *10*, 771. https://doi.org/10.3389/fmicb.2019.00771

Ali, M. R. K., Snyder, B., El-Sayed, M. A. (2012). Synthesis and optical properties of small Au nanorods using a seedless growth technique. *Langmuir, 28*(25), 9807–9815. https://doi.org/10.1021/la301387p

Alkilany, A. M., Nagaria, P. K., Hexel, C. R., Shaw, T. J., Murphy, C. J., Wyatt, M. D. (2009). Cellular uptake and cytotoxicity of gold nanorods: Molecular origin of cytotoxicity and surface effects. *Small, 5*(6), 701–708. https://doi.org/10.1002/smll.200801546

Almada, M., Leal-Martínez, B. H., Hassan, N., Kogan, M. J., Burboa, M. G., Topete, A., Valdez, M. A., Juárez, J. (2017). Photothermal conversion efficiency and cytotoxic effect of gold nanorods stabilized with chitosan, alginate and poly(vinyl alcohol). *Materials Science and Engineering C, 77*, 583–593. https://doi.org/10.1016/j.msec.2017.03.218

Alshangiti, D. M., Ghobashy, M. M., Alqahtani, H. A., El-Damhougy, T. K., Madani, M. (2023). The energetic and physical concept of gold nanorod-dependent fluorescence in cancer treatment and development of new photonic compounds|review. *RSC Advances 13*(46), 32223–32265. https://doi.org/10.1039/d3ra05487j

An, L., Wang, Y., Lin, J., Tian, Q., Xie, Y., Hu, J., Yang, S. (2019). Macrophages-mediated delivery of small gold nanorods for tumor hypoxia photoacoustic imaging and enhanced photothermal therapy. *ACS Applied Materials and Interfaces, 11*(17), 15251–15261. https://doi.org/10.1021/acsami.9b00495

Anandhakumar, S., Rajaram, R., Mathiyarasu, J. (2013). Unusual seedless approach to gold nanoparticle synthesis: Application to selective rapid naked eye detection of mercury(ii). *Analyst, 139*(14), 3356–3359. https://doi.org/10.1039/c4an00480a

Anju, A. J., Binod, P., Pandey, A. (2017). Production and characterization of microbial poly-γ-glutamic acid from renewable resources. *Indian Journal of Experimental Biology, 55*(7), 405-410.

Ansar, S. M., Chakraborty, S., Kitchens, C. L. (2018). pH-responsive mercaptoundecanoic acid functionalized gold nanoparticles and applications in catalysis. *Nanomaterials, 8*(5), 339. https://doi.org/10.3390/nano8050339

Attia, A. B. E., Balasundaram, G., Moothanchery, M., Dinish, U. S., Bi, R., Ntziachristos, V., Olivo, M. (2019). A review of clinical photoacoustic imaging: Current and future trends. *Photoacoustics, 16*, 100144. https://doi.org/10.1016/j.pacs.2019.100144

Avitabile, E., Bedognetti, D., Ciofani, G., Bianco, A., Delogu, L. G. (2018). How can nanotechnology help the fight against breast cancer? *Nanoscale 10*(25), 11719–11731. https://doi.org/10.1039/c8nr02796j

Awad, H., Abdallah, T., Easawi, K., Negm, S., Talaat, H. (2020). Gold nanorods as contrast agent for photoacoustic imaging (PAI) of breast cancer. *IOP Conference Series: Materials Science and Engineering, 956*(1), 012014. https://doi.org/10.1088/1757-899X/956/1/012014

Azab, M. M., Cherif, R., Finnie, A. L., Abou El-Alamin, M. M., Sultan, M. A., Wark, A. W. (2018). Optimized polydopamine coating and DNA conjugation onto gold nanorods for single nanoparticle bioaffinity measurements. *Analyst, 143*(7), 1635-1643.https://doi.org/10.1039/C7AN02019H

Bahadır, E. B., Sezgintürk, M. K. (2016). Lateral flow assays: Principles, designs and labels. *TrAC - Trends in Analytical Chemistry, 82*, 286–306. https://doi.org/10.1016/j.trac.2016.06.006

Bai, Z., Ren, X., Gong, Z., Hao, C., Chen, Y., Wan, P., Meng, X. (2017). 11-Mercaptoundecanoic acid functionalized gold nanoclusters as fluorescent probes for the sensitive detection of Cu2+ and Fe3+ ions. *Chinese Chemical Letters, 28*(9), 1901–1904. https://doi.org/10.1016/j.cclet.2017.05.005

Baird, G., Farrell, C., Cheung, J., Semple, A., Blue, J., Ahl, P. L. (2020). FTIR spectroscopy detects intermolecular β-sheet formation above the high temperature Tm for two monoclonal antibodies. *Protein Journal, 39*(4), 318–327. https://doi.org/10.1007/s10930-020-09907-y

Bao, Y., Oluwafemi, A. (2023). Recent advances in surface modified gold nanorods and their improved sensing performance. *Chemical Communications*, 60(5), 469–481. https://doi.org/10.1039/d3cc04056a

Bhattacharjee, S. (2016). DLS and zeta potential - What they are and what they are not? *Journal of Controlled Release, 235*, 337–351. https://doi.org/10.1016/j.jconrel.2016.06.017

Bikkarolla, S. K., McNamee, S. E., Vance, P., McLaughlin, J. (2022). High-sensitive detection and quantitative analysis of thyroid-stimulating hormone using gold-nanoshell-based lateral flow immunoassay device. *Biosensors, 12*(3), 182. https://doi.org/10.3390/bios12030182

Billot, L., Lamy de la Chapelle, M., Grimault, A. S., Vial, A., Barchiesi, D., Bijeon, J. L., Adam, P. M., Royer, P. (2006). Surface enhanced Raman scattering on gold nanowire arrays: Evidence of strong multipolar surface plasmon resonance enhancement. *Chemical Physics Letters, 422*(4–6), 303–307. https://doi.org/10.1016/j.cplett.2006.02.041

Biris, A.S., Kumpuris, A.G., Nima, Z., inventors; University of Arkansas, assignee (2021). Nanocomposites and methods of making same. United States patent US 11,119,099.

Biris, A.S., Nima, Z., Xu, Y., inventors; University of Arkansas, assignee (2020). Nanocomposites, methods of making same, and applications of same for multicolor

surface enhanced Raman spectroscopy (SERS) detections. United States patent US 10,830,767.

Bishop, J. D., Hsieh, H. V., Gasperino, D. J., Weigl, B. H. (2019). Sensitivity enhancement in lateral flow assays: A systems perspective. *Lab on a Chip*, *19*(15), 2486–2499. https://doi.org/10.1039/c9lc00104b

Bose, T., Latawiec, D., Mondal, P. P., Mandal, S. (2014). Overview of nano-drugs characteristics for clinical application: The journey from the entry to the exit point. *Journal of Nanoparticle Research, 16*(8), 1-25. https://doi.org/10.1007/s11051-014-2527-7

Boyer, J. C., Manseau, M. P., Murray, J. I., Van Veggel, F. C. J. M. (2010). Surface modification of upconverting NaYF4 nanoparticles with PEG-phosphate ligands for NIR (800 nm) biolabeling within the biological window. *Langmuir, 26*(2), 1157–1164. https://doi.org/10.1021/la902260j

Boyes, S.G., Rowe, M.D., inventors; Colorado School of Mines, assignee (2019). Gold/lanthanide nanoparticle conjugates and uses thereof. United States patent US 10,406,111.

Boyne, D. A., Chipara, A. C., Griep, M. H. (2016). Transverse axis morphological control for tailored gold nanorod (GNR) synthesis. *RSC Advances, 6*(68), 63634–63641. https://doi.org/10.1039/c6ra12058j

Bradford, M. M. (1976). A rapid and sensitive method for the quantitation of microgram quantities of protein utilizing the principle of protein-dye binding. *Analytical Biochemistry, 72*(1-2), 248-254. https://doi.org/10.1016/0003-2697(76)90527-3

Burke, B. P., Cawthorne, C., Archibald, S. J. (2017). Multimodal nanoparticle imaging agents: Design and applications. *Philosophical Transactions of the Royal Society A: Mathematical, Physical and Engineering Sciences, 375*(2107), 2017026. https://doi.org/10.1098/rsta.2017.0261

Busch, R. T., Karim, F., Weis, J., Sun, Y., Zhao, C., Vasquez, E. S. (2019). Optimization and structural stability of gold nanoparticle-antibody bioconjugates. *ACS Omega, 4*(12), 15269–15279. https://doi.org/10.1021/acsomega.9b02276

Cai, M., Han, Y., Zheng, X., Xue, B., Zhang, X., Mahmut, Z., Wang, Y., Dong, B., Zhang, C., Gao, D., Sun, J. (2024). Synthesis of poly-γ-glutamic acid and its application in biomedical materials. *Materials, 17*(1), 15. https://doi.org/10.3390/ma17010015

Calatayud, D. G., Lledos, M., Casarsa, F., Pascu, S. I. (2023). Functional diversity in radiolabeled nanoceramics and related biomaterials for the multimodal imaging of tumors. *ACS Bio and Med Chem Au, 3*(5), 389–417. https://doi.org/10.1021/acsbiomedchemau.3c00021

Cao, F., Yao, Q., Wang, X. (2016). GNR@mSiO 2 -TDM1 conjugates as multimodal platform for breast cancer therapy as well as enhanced photoacoustic agent. In *Photonic Therapeutics and Diagnostics XII* (Vol. 9689, pp. 449-455). SPIE. https://doi.org/10.1117/12.2212140

Cao, J., Galbraith, E. K., Sun, T., Grattan, K. T. V. (2012). Effective surface modification of gold nanorods for localized surface plasmon resonance-based biosensors. *Sensors and Actuators, B: Chemical, 169*, 360–367. https://doi.org/10.1016/j.snb.2012.05.019

Cao, J., Sun, T., Grattan, K. T. V. (2014). Gold nanorod-based localized surface plasmon resonance biosensors: A review. *Sensors and Actuators, B: Chemical, 195*, 332–351. https://doi.org/10.1016/j.snb.2014.01.056

Chamorro-Garcia, A., Merkoçi, A. (2016). Nanobiosensors in diagnostics. *Nanobiomedicine, 3*, 1849543516663574. https://doi.org/10.1177/1849543516663574

Chang, C. W., Wang, C. H., Peng, C. A. (2009). Gold nanorods modified with chitosan as photothermal agents. In *13th International Conference on Biomedical Engineering: ICBME 2008 3–6 December 2008 Singapore* (pp. 874-877). Springer Berlin Heidelberg.

Chang, S. S., Shih, C. W., Chen, C. D., Lai, W. C., Wang, C. R. C. (1999). The shape transition of gold nanorods. *Langmuir, 15*(3), 701–709. https://doi.org/10.1021/la980929l

Charan, S., Sanjiv, K., Singh, N., Chien, F. C., Chen, Y. F., Nergui, N. N., Huang, S. H., Kuo, C. W., Lee, T. C., Chen, P. (2012). Development of chitosan oligosaccharide-modified gold nanorods for in vivo targeted delivery and noninvasive imaging by NIR irradiation. *Bioconjugate Chemistry, 23*(11), 2173–2182. https://doi.org/10.1021/bc3001276

Chauhan, D. S., Prasad, R., Devrukhkar, J., Selvaraj, K., Srivastava, R. (2018). Disintegrable NIR light triggered gold nanorods supported liposomal nanohybrids for cancer theranostics. *Bioconjugate Chemistry, 29*(5), 1510–1518. https://doi.org/10.1021/acs.bioconjchem.7b00801

Chavez, K. J., Garimella, S. V., Lipkowitz, S. (2010). Triple negative breast cancer cell lines: One tool in the search for better treatment of triple negative breast cancer. *Breast Disease, 32*(1–2), 35–48. https://doi.org/10.3233/BD-2010-0307

Chen, D., Dougherty, C. A., Yang, D., Wu, H., Hong, H. (2016). Radioactive nanomaterials for multimodality imaging. *Tomography, 2*(1), 3–16. https://doi.org/10.18383/j.tom.2016.00121

Chen, H., Shao, L., Ming, T., Sun, Z., Zhao, C., Yang, B., Wang, J. (2010). Understanding the photothermal conversion efficiency of gold nanocrystals. *Small, 6*(20), 2272–2280. https://doi.org/10.1002/smll.201001109

Chen, J., Dai, T., Yu, J., Dai, X., Chen, R., Wu, J., Li, N., Fan, L., Mao, Z., Sheng, G., Li, L. (2020). Integration of antimicrobial peptides and gold nanorods for bimodal antibacterial applications. *Biomaterials Science, 8*(16), 4447–4457. https://doi.org/10.1039/d0bm00782j

Cheng, J., Ge, L., Xiong, B., He, Y. (2011). Investigation of pH effect on gold nanorod synthesis. *Journal of the Chinese Chemical Society, 58*(6), 822–827. https://doi.org/10.1002/jccs.201190128

Chithrani, B. D., Ghazani, A. A., Chan, W. C. W. (2006). Determining the size and shape dependence of gold nanoparticle uptake into mammalian cells. *Nano Letters, 6*(4), 662–668. https://doi.org/10.1021/nl052396o

Choi, S., Hwang, J., Lee, S., Lim, D. W., Joo, H., Choo, J. (2017). Quantitative analysis of thyroid-stimulating hormone (TSH) using SERS-based lateral flow

immunoassay. *Sensors and Actuators, B: Chemical, 240*, 358–364. https://doi.org/10.1016/j.snb.2016.08.178

Comşa, Ş., Cimpean, A. M., Raica, M. (2015). The story of MCF-7 breast cancer cell line: 40 years of experience in research. *Anticancer Research, 35*(6), 3147–3154.

Cowell, J. K., LaDuca, J., Rossi, M. R., Burkhardt, T., Nowak, N. J., Matsui, S. I. (2005). Molecular characterization of the t(3;9) associated with immortalization in the MCF10A cell line. *Cancer Genetics and Cytogenetics, 163*(1), 23–29. https://doi.org/10.1016/j.cancergencyto.2005.04.019

Daniel-Da-Silva, A. L., Fateixa, S., Guiomar, A. J., Costa, B. F. O., Silva, N. J. O., Trindade, T., Goodfellow, B. J., Gil, A. M. (2009). Biofunctionalized magnetic hydrogel nanospheres of magnetite and κ-carrageenan. *Nanotechnology, 20*(35), 355602. https://doi.org/10.1088/0957-4484/20/35/355602

Das, P., Fatehbasharzad, P., Colombo, M., Fiandra, L., Prosperi, D. (2019). Multifunctional magnetic gold nanomaterials for cancer. *Trends in Biotechnology, 37*(9), 995–1010. https://doi.org/10.1016/j.tibtech.2019.02.005

de Barros, H. R., Piovan, L., Sassaki, G. L., de Araujo Sabry, D., Mattoso, N., Nunes, Á. M., Meneghetti, M. R., Riegel-Vidotti, I. C. (2016). Surface interactions of gold nanorods and polysaccharides: From clusters to individual nanoparticles. *Carbohydrate Polymers, 152*, 479–486. https://doi.org/10.1016/j.carbpol.2016.07.018

Dey, M. K., Iftesum, M., Devireddy, R., Gartia, M. R. (2023). New technologies and reagents in lateral flow assay (LFA) designs for enhancing accuracy and sensitivity. *Analytical Methods, 15*(35), 4351–4376). https://doi.org/10.1039/d3ay00844d

Dreaden, E. C., Mac key, M. A., Huang, X., Kang, B., El-Sayed, M. A. (2011). Beating cancer in multiple ways using nanogold. *Chemical Society Reviews, 40*(7), 3391–3404. https://doi.org/10.1039/c0cs00180e

Du, X., Lin, W. C., Shou, Q., Liang, X., Liu, H. (2019). pH optimization for high-efficiency PEGylation of gold nanorods. *Colloid and Polymer Science, 297*(6), 891–902. https://doi.org/10.1007/s00396-019-04511-8

Erathodiyil, N., Ying, J. Y. (2011). Functionalization of inorganic nanoparticles for bioimaging applications. *Accounts of chemical research*, *44*(10), 925-935. https://doi.org/10.1021/ar2000327

Eum, N. S., Yeom, S. H., Kwon, D. H., Kim, H. R., Kang, S. W. (2010). Enhancement of sensitivity using gold nanorods-Antibody conjugator for detection of E. coli O157:H7. *Sensors and Actuators, B: Chemical, 143*(2), 784–788. https://doi.org/10.1016/j.snb.2009.09.054

Eustis, S., El-Sayed, M. (2005). Aspect ratio dependence of the enhanced fluorescence intensity of gold nanorods: Experimental and simulation study. *Journal of Physical Chemistry B, 109*(34), 16350–16356. https://doi.org/10.1021/jp052951a

Feng, Y., Spezia, M., Huang, S., Yuan, C., Zeng, Z., Zhang, L., Ji, X., Liu, W., Huang, B., Luo, W., Liu, B., Lei, Y., Du, S., Vuppalapati, A., Luu, H. H., Haydon, R. C., He, T. C., Ren, G. (2018). Breast cancer development and progression: Risk factors, cancer stem cells, signaling pathways, genomics, and molecular pathogenesis. Genes and Diseases, 5(2), 77–106. https://doi.org/10.1016/j.gendis.2018.05.001

Ferlay J, Ervik M, Lam F, Laversanne M, Colombet M, Mery L, Piñeros M, Znaor A, Soerjomataram I, Bray F (2024). Global Cancer Observatory: Cancer Today. Lyon, France: International Agency for Research on Cancer. Available from: https://gco.iarc.who.int/today, accessed [10 February 2025].

Gaiduk, A., Yorulmaz, M., Ruijgrok, P. V, Orrit, M. (2010). Room-temperature detection of a single molecule's absorption by photothermal contrast. *Science, 330*(6002), 353–356. https://doi.org/10.1126/science.1195475

Gao, Q., Chen, F. (2023). Multimodal radiolabeled gold nanoparticle molecular probes: synthesis, imaging, and applications. *Journal of Radioanalytical and Nuclear Chemistry, 332*(6), 1625–1645. https://doi.org/10.1007/s10967-023-08895-4

Ge, X., Asiri, A. M., Du, D., Wen, W., Wang, S., Lin, Y. (2014). Nanomaterial-enhanced paper-based biosensors. *TrAC - Trends in Analytical Chemistry, 58*, 31–39. https://doi.org/10.1016/j.trac.2014.03.008

Ge, X., Fu, Q., Su, L., Li, Z., Zhang, W., Chen, T., Yang, H., Song, J. (2020). Light-activated gold nanorod vesicles with NIR-II fluorescence and photoacoustic

imaging performances for cancer theranostics. *Theranostics, 10*(11), 4809–4821. https://doi.org/10.7150/thno.44376

Ghosh, A., Banerjee, A., Srivastava, R. (2023). Nanomaterial-based lateral flow assays for point-of-care diagnostic tests. In *Surface Engineering and Functional Nanomaterials for Point-of-Care Analytical Devices* (pp. 323–344). Springer Nature Singapore. https://doi.org/10.1007/978-981-99-3025-8_14

Gong, T., Olivo, M., Dinish, U. S., Goh, D., Kong, K. V., Yong, K. T. (2013). Engineering bioconjugated gold nanospheres and gold nanorods as label-free plasmon scattering probes for ultrasensitive multiplex dark-field imaging of cancer cells. *Journal of Biomedical Nanotechnology, 9*(6), 985–991. https://doi.org/10.1166/jbn.2013.1603

Guan, H., Wang, W., Liu, X., Liang, J. (2014). Real-time visualization of colorimetric probe for pH-sensitive based on poly-(γ-glutamic acid)-functionalized gold nanoparticles. *Colloids and Surfaces A: Physicochemical and Engineering Aspects, 448*(1), 147–153. https://doi.org/10.1016/j.colsurfa.2014.02.026

Guerrini, L., Alvarez-Puebla, R. A., Pazos-Perez, N. (2018). Surface modifications of nanoparticles for stability in biological fluids. *Materials, 11*(7), 1154. https://doi.org/10.3390/ma11071154

Gui, C., Cui, D. X. (2012). Functionalized gold nanorods for tumor imaging and targeted therapy. *Cancer Biology and Medicine, 9*(4), 221–233. https://doi.org/10.7497/j.issn.2095-3941.2012.04.002

Guo, H., Ruan, F., Lu, L., Hu, J., Pan, J., Yang, Z., Ren, B. (2009). Correlating the shape, surface plasmon resonance, and surface-enhanced Raman scattering of gold nanorods. *Journal of Physical Chemistry C, 113*(24), 10459–10464. https://doi.org/10.1021/jp9019427

Guo, H., Yi, S., Feng, K., Xia, Y., Qu, X., Wan, F., Chen, L., Zhang, C. (2021). In situ formation of metal organic framework onto gold nanorods/mesoporous silica with functional integration for targeted theranostics. *Chemical Engineering Journal, 403*, 126432. https://doi.org/10.1016/j.cej.2020.126432

Guo, T., Lin, Y., Li, Z., Chen, S., Huang, G., Lin, H., Wang, J., Liu, G., Yang, H. H. (2017). Gadolinium oxysulfide-coated gold nanorods with improved stability and dual-modal magnetic resonance/photoacoustic imaging contrast enhancement for cancer theranostics. *Nanoscale, 9*(1), 56–61. https://doi.org/10.1039/c6nr08281e

Guo, Y., Wang, Z., Shao, H., Jiang, X. (2012). Stable fluorescent gold nanoparticles for detection of Cu2+ with good sensitivity and selectivity. *Analyst, 137*(2), 301–304. https://doi.org/10.1039/c1an15877e

Maurya, H. (2018). Thyroid function disorders among the indian population. *Annals of Thyroid Research, 4*(3), 172–173. https://doi.org/10.26420/annalsthyroidres.2018.1044

Haine, A. T., & Niidome, T. (2017). Gold nanorods as nanodevices for bioimaging, photothermal therapeutics, and drug delivery. *Chemical and Pharmaceutical Bulletin*, *65*(7), 625-628. https://doi.org/10.1248/cpb.c17-00102

Han, S., Lee, D., Kim, S., Kim, H. H., Jeong, S., Kim, J. (2022). Contrast agents for photoacoustic imaging: A review focusing on the wavelength range. *Biosensors, 12*(8), 594. https://doi.org/10.3390/bios12080594

Hasannia, M., Abnous, K., Taghdisi, S. M., Nekooei, S., Ramezani, M., Alibolandi, M. (2022). Synthesis of doxorubicin-loaded peptosomes hybridized with gold nanorod for targeted drug delivery and CT imaging of metastatic breast cancer. *Journal of Nanobiotechnology, 20*(1), 391. https://doi.org/10.1186/s12951-022-01607-2

Hauck, T. S., Ghazani, A. A., Chan, W. C. W. (2008). Assessing the effect of surface chemistry on gold nanorod uptake, toxicity, and gene expression in mammalian cells. *Small, 4*(1), 153–159. https://doi.org/10.1002/smll.200700217

Hauptmann, A., Podgoršek, K., Kuzman, D., Srčič, S., Hoelzl, G., Loerting, T. (2018). Impact of buffer, protein concentration and sucrose addition on the aggregation and particle formation during freezing and thawing. *Pharmaceutical Research, 35*(5), 1-16. https://doi.org/10.1007/s11095-018-2378-5

He, G. S., Zhu, J., Yong, K. T., Baev, A., Cai, H. X., Hu, R., Cui, Y., Zhang, X. H., Prasad, P. N. (2010). Scattering and absorption cross-section spectral measurements of

gold nanorods in water. *Journal of Physical Chemistry C, 114*(7), 2853–2860. https://doi.org/10.1021/jp907811g

He, J., Unser, S., Bruzas, I., Cary, R. J., Shi, Z., Mehra, R., Aron, K., Sagle, L. (2018). The facile removal of CTAB from the surface of gold nanorods. *Colloids and Surfaces B: Biointerfaces, 163*, 140–145. https://doi.org/10.1016/j.colsurfb.2017.12.019

Heidari, Z., Sariri, R., Salouti, M. (2014). Gold nanorods-bombesin conjugate as a potential targeted imaging agent for detection of breast cancer. *Journal of Photochemistry and Photobiology B: Biology, 130*, 40–46. https://doi.org/10.1016/j.jphotobiol.2013.10.019

Hejazi, S., Restaino, O. F., Sabbah, M., Zannini, D., Di Girolamo, R., Marotta, A., D'Ambrosio, S., Krauss, I. R., Giosafatto, C. V. L., Santagata, G., Schiraldi, C., Porta, R. (2023). Physicochemical characterization of chitosan/poly-γ-glutamic acid glass-like materials. *International Journal of Molecular Sciences, 24*(15), 12495. https://doi.org/10.3390/ijms241512495

Honary, S., Zahir, F. (2013). Effect of zeta potential on the properties of nano-drug delivery systems - A review (Part 2). *Tropical Journal of Pharmaceutical Research, 12*(2), 265–273. https://doi.org/10.4314/tjpr.v12i2.20

Hou, S., Zhang, Y., Lian, M., Xie, X., Lu, Q., Zhang, Q. (2022). Drug self-framework delivery system-coated gold nanorods for multi-modal imaging and combination therapy for breast cancer. *Chemical Communications, 59*(13), 1809–1812. https://doi.org/10.1039/d2cc05341a

Hsieh, H. V., Dantzler, J. L., Weigl, B. H. (2017). Analytical tools to improve optimization procedures for lateral flow assays. *Diagnostics, 7*(2), 29. https://doi.org/10.3390/diagnostics7020029

Hu, X., Wang, T., Wang, L., Dong, S. (2007). Surface-enhanced Raman scattering of 4-aminothiophenol self-assembled monolayers in sandwich structure with nanoparticle shape dependence: Off-surface plasmon resonance condition. *Journal of Physical Chemistry C, 111*(19), 6962–6969. https://doi.org/10.1021/jp0712194

Huang, G., Yang, S., Yuan, Y., Xing, D. (2011). Combining x-ray and photoacoustics for in vivo tumor imaging with gold nanorods. *Applied Physics Letters, 99*(12). https://doi.org/10.1063/1.3643033

Huang, H., Huang, S., Yuan, S., Qu, C., Chen, Y., Xu, Z., Liao, B., Zeng, Y., Chu, P. K. (2011). High-sensitivity biosensors fabricated by tailoring the localized surface plasmon resonance property of core-shell gold nanorods. *Analytica Chimica Acta, 683*(2), 242–247. https://doi.org/10.1016/j.aca.2010.10.033

Huang, H., Liu, F., Huang, S., Yuan, S., Liao, B., Yi, S., Zeng, Y., Chu, P. K. (2012). Sensitive and simultaneous detection of different disease markers using multiplexed gold nanorods. *Analytica Chimica Acta, 755*, 108–114. https://doi.org/10.1016/j.aca.2012.10.020

Huang, L., Ao, L., Hu, D., Wang, W., Sheng, Z., Su, W. (2016). Magneto-plasmonic nanocapsules for multimodal-imaging and magnetically guided combination cancer therapy. *Chemistry of Materials, 28*(16), 5896–5904. https://doi.org/10.1021/acs.chemmater.6b02413

Huang, P., Bao, L., Zhang, C., Lin, J., Luo, T., Yang, D., He, M., Li, Z., Gao, G., Gao, B., Fu, S., Cui, D. (2011). Folic acid-conjugated Silica-modified gold nanorods for X-ray/CT imaging-guided dual-mode radiation and photo-thermal therapy. *Biomaterials, 32*(36), 9796–9809. https://doi.org/10.1016/j.biomaterials.2011.08.086

Huang, X., Neretina, S., El-Sayed, M. A. (2009). Gold nanorods: From synthesis and properties to biological and biomedical applications. *Advanced Materials, 21*(48), 4880–4910. https://doi.org/10.1002/adma.200802789

Huang, Y., He, S., Cao, W., Cai, K., Liang, X. J. (2012). Biomedical nanomaterials for imaging-guided cancer therapy. *Nanoscale, 4*(20), 6135–6149. https://doi.org/10.1039/c2nr31715j

Huang, Z., Yu, P., Tang, J. (2020). Characterization of triple-negative breast cancer MDA-MB-231 cell spheroid model. *OncoTargets and Therapy, 13*, 5395–5405. https://doi.org/10.2147/OTT.S249756

Hue, D. T., Thu Huong, T. T., Thu Ha, P. T., Trang, T. T., Ha Lien, N. T., Xuan Hoa, V. (2021). The dependence of medium refractive index on optical properties of gold nanorods and their SERS application. *AIP Advances, 11*(5). https://doi.org/10.1063/5.0052882

Jain, V., Bhagat, S., Singh, M., Bansal, V., Singh, S. (2019). Unveiling the effect of 11-MUA coating on biocompatibility and catalytic activity of a gold-core cerium oxide-shell-based nanozyme. *RSC Advances, 9*(57), 33195–33206. https://doi.org/10.1039/c9ra05547a

Jana, N. R., Gearheart, L., Murphy, C. J. (2001). Seed-mediated growth approach for shape-controlled synthesis of spheroidal and rod-like gold nanoparticles using a surfactant template. *Advanced Materials, 13*(18), 1389–1393. https://doi.org/10.1002/1521-4095(200109)13:18<1389::AID-ADMA1389>3.0.CO;2-F

Jang, B., Kim, Y. S., Choi, Y. (2011). Effects of gold Nanorod concentration on the depth-related temperature increase during hyperthermic ablation. *Small, 7*(2), 265–270. https://doi.org/10.1002/smll.201001532

Jenkins, S. V., Nima, Z. A., Vang, K. B., Kannarpady, G., Nedosekin, D. A., Zharov, V. P., Griffin, R. J., Biris, A. S., Dings, R. P. M. (2017). Triple-negative breast cancer targeting and killing by EpCAM-directed, plasmonically active nanodrug systems. *Npj Precision Oncology, 1*(1), 27. https://doi.org/10.1038/s41698-017-0030-1

Jeong, J. H., Kim, T. K., Oh, S. W., Choi, E. Y. (2013). Fluorescence immunochip assay for thyroid stimulating hormone in whole blood. *Biochip Journal, 7*(4), 408–414. https://doi.org/10.1007/s13206-013-7413-3

John, C. L., Strating, S. L., Shephard, K. A., Zhao, J. X. (2013). Reproducibly synthesize gold nanorods and maintain their stability. *RSC Advances, 3*(27), 10909–10918. https://doi.org/10.1039/c3ra41521j

Jonsson, O., Lundell, A., Rosell, J., You, S., Ahlgren, K., Swenson, J. (2024). Comparison of sucrose and trehalose for protein stabilization using differential scanning calorimetry. *Journal of Physical Chemistry B, 128*(20), 4922–4930. https://doi.org/10.1021/acs.jpcb.4c00022

Joshi, P. P., Yoon, S. J., Hardin, W. G., Emelianov, S., Sokolov, K. V. (2013). Conjugation of antibodies to gold nanorods through fc portion: Synthesis and molecular specific imaging. *Bioconjugate Chemistry, 24*(6), 878–888. https://doi.org/10.1021/bc3004815

Jung, W., Han, J., Kai, J., Lim, J. Y., Sul, D., Ahn, C. H. (2013). An innovative sample-to-answer polymer lab-on-a-chip with on-chip reservoirs for the POCT of thyroid stimulating hormone (TSH). *Lab on a Chip, 13*(23), 4653–4662. https://doi.org/10.1039/c3lc50403d

Kedawat, G., Sharma, I., Nagpal, K., Kumar, M., Gupta, G., Gupta, B. K. (2019). Studies of ultrafast transient absorption spectroscopy of gold nanorods in an aqueous solution. *ACS Omega, 4*(7), 12626–12631. https://doi.org/10.1021/acsomega.9b01157

Kesharwani, P., Ma, R., Sang, L., Fatima, M., Sheikh, A., Abourehab, M. A. S., Gupta, N., Chen, Z. S., Zhou, Y. (2023). Gold nanoparticles and gold nanorods in the landscape of cancer therapy. *Molecular Cancer, 22*(1), 98. https://doi.org/10.1186/s12943-023-01798-8

Key, J., Leary, J. F. (2014). Nanoparticles for multimodal in vivo imaging in nanomedicine. *International Journal of Nanomedicine*, 9(1), 711–726. https://doi.org/10.2147/IJN.S53717

Khalil, I. R., Khechara, M. P., Kurusamy, S., Armesilla, A. L., Gupta, A., Mendrek, B., Khalaf, T., Scandola, M., Focarete, M. L., Kowalczuk, M., Radecka, I. (2018). Poly-Gamma-Glutamic Acid (γ-PGA)-based encapsulation of adenovirus to evade neutralizing antibodies. *Molecules, 23*(10), 2565. https://doi.org/10.3390/molecules23102565

Khan, N. U., Lin, J., Younas, M. R., Liu, X., Shen, L. (2021). Synthesis of gold nanorods and their performance in the field of cancer cell imaging and photothermal therapy. *Cancer Nanotechnology, 12*(1), 1-33. https://doi.org/10.1186/s12645-021-00092-w

Kim, M. J., Jung, D. H., Lee, C. Y., Hong, S., Heo, J. H., Lee, J. H. (2023). Structurally engineered silica shells on gold nanorods for biomedical applications. *Small Structures, 4*(9), 2300047. https://doi.org/10.1002/sstr.202300047

Koeppl, S., Solenthaler, C., Caseri, W., Spolenak, R. (2011). Towards a reproducible synthesis of high aspect ratio gold nanorods. *Journal of Nanomaterials*, *2011*(1), 515049. https://doi.org/10.1155/2011/515049

Lee, K. S., El-Sayed, M. A. (2005). Dependence of the enhanced optical scattering efficiency relative to that of absorption for gold metal nanorods on aspect ratio, size, end-cap shape, and medium refractive index. *Journal of Physical Chemistry B, 109*(43), 20331–20338. https://doi.org/10.1021/jp054385p

Li, G., Chen, Y., Zhang, L., Zhang, M., Li, S., Li, L., Wang, T., Wang, C. (2018). Facile approach to synthesize gold nanorod@polyacrylic acid/ calcium phosphate yolk–shell nanoparticles for dual-mode imaging and pH/NIR-responsive drug delivery. *Nano-Micro Letters, 10*(1), 1–11. https://doi.org/10.1007/s40820-017-0155-3

Li, J. L., Gu, M. (2010). Surface plasmonic gold nanorods for enhanced two-photon microscopic imaging and apoptosis induction of cancer cells. *Biomaterials, 31*(36), 9492–9498. https://doi.org/10.1016/j.biomaterials.2010.08.068

Li, J., Wang, H., Wang, L., Yu, D., Zhang, X. (2024). Stabilization effects of saccharides in protein formulations: A review of sucrose, trehalose, cyclodextrins and dextrans. *European Journal of Pharmaceutical Sciences, 192*, 106625. https://doi.org/10.1016/j.ejps.2023.106625

Li, L., Wang, Z., Guo, H., Lin, Q. (2023). Nanomaterials: a promising multimodal theranostics platform for thyroid cancer. *Journal of Materials Chemistry B, 11*(32), 7544–7566. https://doi.org/10.1039/d3tb01175e

Li, M., Yang, J., Yao, X., Li, X., Xu, Z., Tang, S., Sun, B., Lin, S., Yang, C., Liu, J. (2023). Multifunctional mesoporous silica-coated gold nanorods mediate mild photothermal heating-enhanced gene/immunotherapy for colorectal cancer. *Pharmaceutics, 15*(3), 854. https://doi.org/10.3390/pharmaceutics15030854

Li, Q., Cao, Y. (2012). Preparation and characterization of gold nanorods. In *Nanorods* (p. 159). IntechOpen, Shanghai, China.

Li, X., Cai, Z., Jiang, L. P., He, Z., Zhu, J. J. (2020). Metal-ligand coordination nanomaterials for biomedical imaging. *Bioconjugate Chemistry, 31*(2), 332–339. https://doi.org/10.1021/acs.bioconjchem.9b00642

Li, Z., Chen, H., Wang, P. (2019). Lateral flow assay ruler for quantitative and rapid point-of-care testing. *Analyst, 144*(10), 3314–3322. https://doi.org/10.1039/c9an00374f

Li, Z., He, G., Hua, J., Wu, M., Guo, W., Gong, J., Zhang, J., Qiao, C. (2017). Preparation of γPGAhydrogels and swelling behaviors in salt solutions with different ionic valence numbers. *RSC Advances, 7*(18), 11085–11093. https://doi.org/10.1039/c6ra26419k

Liao, J., Qi, T., Chu, B., Peng, J., Luo, F., Qian, Z. (2014). Multifunctional nanostructured materials for multimodal cancer imaging and therapy. *Journal of Nanoscience and Nanotechnology, 14*(1), 175–189. https://doi.org/10.1166/jnn.2014.9049

Liao, S., Yue, W., Cai, S., Tang, Q., Lu, W., Huang, L., Qi, T., Liao, J. (2021). Improvement of gold nanorods in photothermal therapy: Recent progress and perspective. *Frontiers in Pharmacology*, *12,* 664123. https://doi.org/10.3389/fphar.2021.664123

Liu, J. Y., Ma, W., Kou, W., Shang, L., Huang, R., Zhao, J. (2019). Poly-amino acids coated gold nanorod and doxorubicin for synergistic photodynamic therapy and chemotherapy in ovarian cancer cells. *Bioscience Reports, 39*(12), 1–11. https://doi.org/10.1042/BSR20192521

Liu, M., Anderson, R. C., Lan, X., Conti, P. S., Chen, K. (2020). Recent advances in the development of nanoparticles for multimodality imaging and therapy of cancer. *Medicinal Research Reviews, 40*(3), 909–930. https://doi.org/10.1002/med.21642

Liu, Y., Jiang, T., Liu, Z. (2022). Metal-organic frameworks for bioimaging: Strategies and challenges. *Nanotheranostics, 6*(2), 143–160. https://doi.org/10.7150/ntno.63458

Liu, Y., Zhan, L., Qin, Z., Sackrison, J., Bischof, J. C. (2021). Ultrasensitive and highly specific lateral flow assays for point-of-care diagnosis. *ACS Nano, 15*(3), 3593–3611. https://doi.org/10.1021/acsnano.0c10035

Lou, S., Ye, J. Y., Li, K. Q., Wu, A. (2012). A gold nanoparticle-based immunochromatographic assay: The influence of nanoparticulate size. *Analyst, 137*(5), 1174–1181. https://doi.org/10.1039/c2an15844b

Luo, L., Sun, W., Feng, Y., Qin, R., Zhang, J., Ding, D., Shi, T., Liu, X., Chen, X., Chen, H. (2020). Conjugation of a scintillator complex and gold nanorods for dual-modal image-guided photothermal and X-ray-induced photodynamic therapy of tumors. *ACS Applied Materials and Interfaces, 12*(11), 12591–12599. https://doi.org/10.1021/acsami.0c01189

Luo, T., Huang, P., Gao, G., Shen, G., Fu, S., Cui, D., Zhou, C., Ren, Q. (2011). Mesoporous silica-coated gold nanorods with embedded indocyanine green for dual mode X-ray CT and NIR fluorescence imaging. *Optics express*, *19*(18), 17030-17039. https://doi.org/10.1364/OE.19.017030

Ma, M., Chen, H., Chen, Y., Wang, X., Chen, F., Cui, X., Shi, J. (2012). Au capped magnetic core/mesoporous silica shell nanoparticles for combined photothermo-/chemo-therapy and multimodal imaging. *Biomaterials, 33*(3), 989–998. https://doi.org/10.1016/j.biomaterials.2011.10.017

Ma, Z. Y., Xia, H. X., Liu, Y. P., Liu, B., Chen, W., Zhao, Y. Di. (2013). Applications of gold nanorods in biomedical imaging and related fields. *Chinese Science Bulletin, 58*(21), 2530–2536. https://doi.org/10.1007/s11434-013-5720-7

Malik, N., Arfin, T., & Khan, A. U. (2019). Chapter 13 - Graphene nanomaterials: chemistry and pharmaceutical perspectives. In *Nanomaterials for Drug Delivery and Therapy* (pp. 373–402). William Andrew Publishing. https://doi.org/https://doi.org/10.1016/B978-0-12-816505-8.00002-3

Malik, P., Katyal, V., Malik, V., Asatkar, A., Inwati, G., Mukherjee, T. K. (2013). Nanobiosensors: Concepts and variations. *ISRN Nanomaterials, 2013*(1), 327435. https://doi.org/10.1155/2013/327435

March, J., Brown, W. H., (2025, January 28). Carboxylic acid. *Encyclopedia Britannica*. https://www.britannica.com/science/carboxylic-acid

Marlinda, A. R., Pandikumar, A., Jayabal, S., Yusoff, N., Suriani, A. B., Huang, N. M. (2016). Voltammetric determination of nitric oxide using a glassy carbon electrode modified with a nanohybrid consisting of myoglobin, gold nanorods, and reduced graphene oxide. *Microchimica Acta, 183*(11), 3077–3085. https://doi.org/10.1007/s00604-016-1922-4

Mayer, K. M., Lee, S., Liao, H., Rostro, B. C., Fuentes, A., Scully, P. T., Nehl, C. L., Hafner, J. H. (2008). A label-free immunoassay based upon localized surface plasmon resonance of gold nanorods. *ACS Nano, 2*(4), 687–692. https://doi.org/10.1021/nn7003734

Mehtala, J. G., Zemlyanov, D. Y., Max, J. P., Kadasala, N., Zhao, S., Wei, A. (2014). Citrate-stabilized gold nanorods. *Langmuir, 30*(46), 13727–13730. https://doi.org/10.1021/la5029542

Messersmith, P.B., Black IV, K.C.L., Yi, J., Rivera, J.G., inventors; Northwestern University, assignee (2014). Multifunctional metal nanoparticles having a polydopamine-based surface and methods of making and using the same. United States patent US 8,784,895.

Mills, C., Dillon, M. J., Kulabhusan, P. K., Senovilla-Herrero, D., Campbell, K. (2022). Multiplex lateral flow assay and the sample preparation method for the simultaneous detection of three marine toxins. *Environmental Science and Technology, 56*(17), 12210–12217. https://doi.org/10.1021/acs.est.2c02339

Mirjalili, S., Tohidi Moghadam, T., H. Sajedi, R. (2022). Facile and rapid detection of microalbuminuria by antibody-functionalized gold nanorods. *Plasmonics, 17*(3), 1269–1277. https://doi.org/10.1007/s11468-022-01606-x

Mirshekari, H., Dabirmanesh, B., Daneshjou, S., Khajeh, K. (2024). Fabrication and evaluation of a plasmonic biosensor based on silica-coated gold nanorods for highly-sensitive detection of anti-Müllerian hormone. *Colloids and Interface Science Communications, 61*, 100795. https://doi.org/10.1016/j.colcom.2024.100795

Mohd-Zahid, M. H., Mohamud, R., Che Abdullah, C. A., Lim, J., Alem, H., Wan Hanaffi, W. N., Iskandar, Z. A. (2019). Colorectal cancer stem cells: A review of targeted drug delivery by gold nanoparticles. *RSC Advances, 10*(2), 973–985. https://doi.org/10.1039/c9ra08192e

Mohtasebi, A., Chowdhury, T., Hsu, L. H. H., Biesinger, M. C., Kruse, P. (2016). Interfacial charge transfer between phenyl-capped aniline tetramer films and iron oxide surfaces. *Journal of Physical Chemistry C, 120*(51), 29248–29263. https://doi.org/10.1021/acs.jpcc.6b09950

Morais, T., Soares, M. E., Duarte, J. A., Soares, L., Maia, S., Gomes, P., Pereira, E., Fraga, S., Carmo, H., Bastos, M. D. L. (2012). Effect of surface coating on the biodistribution profile of gold nanoparticles in the rat. *European Journal of Pharmaceutics and Biopharmaceutics, 80*(1), 185–193. https://doi.org/10.1016/j.ejpb.2011.09.005

Morato, Y. L., Paredes, K. O., Chamizo, L. L., Marciello, M., Filice, M. (2021). Recent advances in multimodal molecular imaging of cancer mediated by hybrid magnetic nanoparticles. *Polymers, 13*(17), 2989. https://doi.org/10.3390/polym13172989

Moudgil, A., Salve, R., Gajbhiye, V., Chaudhari, B. P. (2023). Challenges and emerging strategies for next generation liposomal based drug delivery: An account of the breast cancer conundrum. *Chemistry and Physics of Lipid, 250*, 105258. https://doi.org/10.1016/j.chemphyslip.2022.105258

Mu, Q., Wang, H., Zhang, M. (2017). Nanoparticles for imaging and treatment of metastatic breast cancer. *Expert Opinion on Drug Delivery 14*(1), 123–136. https://doi.org/10.1080/17425247.2016.1208650

Nag, S., Mitra, O., Tripathi, G., Adur, I., Mohanto, S., Nama, M., Samanta, S., Gowda, B. H. J., Subramaniyan, V., Sundararajan, V., Kumarasamy, V. (2024). Nanomaterials-assisted photothermal therapy for breast cancer: State-of-the-art advances and future perspectives. *Photodiagnosis and Photodynamic Therapy*, *45*, 103959. https://doi.org/10.1016/j.pdpdt.2023.103959

Nair, P. G., Joseph, E., Killi, N., Konchada, S., Nisal, A., Gundloori, R. V. N., Dharne, M. S. (2021). One-pot bioconversion of tomato waste into poly-gamma-glutamic acid (γ-PGA) biopolymer by a novel biocatalyst. *ACS Sustainable Chemistry and Engineering, 9*(43), 14330–14334. https://doi.org/10.1021/acssuschemeng.1c05362

Nair, R. V., Nair, L. V., Govindachar, D. M., Santhakumar, H., Nazeer, S. S., Rekha, C. R., Shenoy, S. J., Periyasamy, G., Jayasree, R. S. (2020). Luminescent gold nanorods to enhance the near-infrared emission of a photosensitizer for targeted cancer imaging and dual therapy: Experimental and theoretical approach. *Chemistry - A European Journal, 26*(13), 2826–2836. https://doi.org/10.1002/chem.201904952

Niidome, T., Yamagata, M., Okamoto, Y., Akiyama, Y., Takahashi, H., Kawano, T., Katayama, Y., Niidome, Y. (2006). PEG-modified gold nanorods with a stealth character for in vivo applications. *Journal of Controlled Release, 114*(3), 343–347. https://doi.org/10.1016/j.jconrel.2006.06.017

Nikfarjam, A., Rezayan, A. H., Mohammadkhani, G., Mohammadnejad, J. (2017). Label-free detection of digoxin using localized surface plasmon resonance-based nanobiosensor. *Plasmonics, 12*(1), 157–164. https://doi.org/10.1007/s11468-016-0243-0

Nikoobakht, B., El-Sayed, M. A. (2003). Preparation and growth mechanism of gold nanorods (NRs) using seed-mediated growth method. *Chemistry of Materials, 15*(10), 1957–1962. https://doi.org/10.1021/cm0207321

Nilsson, M., Fagman, H. (2017). Development of the thyroid gland. *Development (Cambridge), 144*(12), 2123–2140. https://doi.org/10.1242/dev.145615

Núñez, C., Estévez, S. V., del Pilar Chantada, M. (2018). Inorganic nanoparticles in diagnosis and treatment of breast cancer. *Journal of Biological Inorganic Chemistry 23*(3), 331–345. https://doi.org/10.1007/s00775-018-1542-z

Oliveira, J. P., Prado, A. R., Keijok, W. J., Antunes, P. W. P., Yapuchura, E. R., Guimarães, M. C. C. (2019). Impact of conjugation strategies for targeting of antibodies in gold nanoparticles for ultrasensitive detection of 17β-estradiol. *Scientific Reports, 9*(1), 13859. https://doi.org/10.1038/s41598-019-50424-5

Orendorff, C. J., Murphy, C. J. (2006). Quantitation of metal content in the silver-assisted growth of gold nanorods. *Journal of Physical Chemistry B, 110*(9), 3990–3994. https://doi.org/10.1021/jp0570972

Pallares, R. M., Su, X., Lim, S. H., Thanh, N. T. K. (2015). Fine-tuning of gold nanorod dimensions and plasmonic properties using the Hofmeister effects. *Journal of Materials Chemistry C, 4*(1), 53–61. https://doi.org/10.1039/c5tc02426a

Panhwar, S., ilhan, H., Aftab, A., Muqeet, M., Keerio, H. A., Solangi, G. S., Suludere, Z., Tamer, U. (2021). High-performance E. coli antibody-conjugated gold nanorods for the selective electrochemical detection of pathogens in drinking water. *Journal*

of Electronic Materials, 50(12), 7119–7125. https://doi.org/10.1007/s11664-021-09247-2

Park, J., Park, B., Yeong Kim, T., Jung, S., June Choi, W., Ahn, J., Hee Yoon, D., Kim, J., Jeon, S., Lee, D., Yong, U., Jang, J., Jong Kim, W., Kyun Kim, H., Jeong, U., Ham Kim, H., Kim, C. (2021). Quadruple ultrasound, photoacoustic, optical coherence, and fluorescence fusion imaging with a transparent ultrasound transducer. *Proceedings of the National Academy of Sciences*, *118*(11), e1920879118. https://doi.org/10.1073/pnas.1920879118

Park, S. B., Shin, J. H. (2022). Pressed lateral flow assay strips for flow delay-induced signal enhancement in lateral flow assay strips. *Biochip Journal, 16*(4), 480–489. https://doi.org/10.1007/s13206-022-00085-w

Parolo, C., de la Escosura-Muñiz, A., Merkoçi, A. (2013). Enhanced lateral flow immunoassay using gold nanoparticles loaded with enzymes. *Biosensors and Bioelectronics, 40*(1), 412–416. https://doi.org/10.1016/j.bios.2012.06.049

Parolo, C., Merkoçi, A. (2013). Paper-based nanobiosensors for diagnostics. *Chemical Society Reviews, 42*(2), 450–457. https://doi.org/10.1039/c2cs35255a

Parolo, C., Sena-Torralba, A., Bergua, J. F., Calucho, E., Fuentes-Chust, C., Hu, L., Rivas, L., Álvarez-Diduk, R., Nguyen, E. P., Cinti, S., Quesada-González, D., Merkoçi, A. (2020). Tutorial: design and fabrication of nanoparticle-based lateral-flow immunoassays. *Nature Protocols, 15*(12), 3788–3816. https://doi.org/10.1038/s41596-020-0357-x

Pérez-Juste, J., Pastoriza-Santos, I., Liz-Marzán, L. M., Mulvaney, P. (2005). Gold nanorods: Synthesis, characterization and applications. *Coordination Chemistry Reviews, 249*(17-18), 1870–1901. https://doi.org/10.1016/j.ccr.2005.01.030

Pham, N., Fahs, A., Pimental, D., Sandman, J., Stich, A., Spudich, T., Blankson, G. (2022). The design, development, and optimization of a lateral flow assay to detect the presence of myoglobin. *Journal of Undergraduate Chemistry Research, 21*(3), 64.

Polyak, K. (2011). Heterogeneity in breast cancer. *Journal of Clinical Investigation, 121*(10), 3786–3788. https://doi.org/10.1172/JCI60534

Posthuma-Trumpie, G. A., Korf, J., van Amerongen, A. (2009). Lateral flow (immuno) assay: its strengths, weaknesses, opportunities and threats. A literature survey. *Analytical and bioanalytical chemistry*, *393*, 569-582.https://doi.org/10.1007/s00216-008-2287-2

Prasad, R., Agawane, S. B., Chauhan, D. S., Srivastava, R., Selvaraj, K. (2018). In vivo examination of folic acid-conjugated gold-silica nanohybrids as contrast agents for localized tumor diagnosis and biodistribution. *Bioconjugate Chemistry, 29*(12), 4012–4019. https://doi.org/10.1021/acs.bioconjchem.8b00522

Preechakasedkit, P., Pinwattana, K., Dungchai, W., Siangproh, W., Chaicumpa, W., Tongtawe, P., Chailapakul, O. (2012). Development of a one-step immunochromatographic strip test using gold nanoparticles for the rapid detection of Salmonella typhi in human serum. *Biosensors and Bioelectronics, 31*(1), 562–566. https://doi.org/10.1016/j.bios.2011.10.031

Qin, H., Zhou, T., Yang, S., Chen, Q., Xing, D. (2013). Gadolinium(III)-gold nanorods for MRI and photoacoustic imaging dual-modality detection of macrophages in atherosclerotic inflammation. *Nanomedicine, 8*(10), 1611–1624. https://doi.org/10.2217/nnm.12.168

Ratto, F., Centi, S., Avigo, C., Borri, C., Tatini, F., Cavigli, L., Kusmic, C., Lelli, B., Lai, S., Colagrande, S., Faita, F., Menichetti, L., Pini, R. (2016). A robust design for cellular vehicles of gold nanorods for multimodal imaging. *Advanced Functional Materials, 26*(39), 7178–7185. https://doi.org/10.1002/adfm.201600836

Rieffel, J., Chitgupi, U., Lovell, J. F. (2015). Recent advances in higher-order, multimodal, biomedical imaging agents. *Small, 11*(35), 4445–4461. https://doi.org/10.1002/smll.201500735

Rizwan, M., Mohd-Naim, N. F., Ahmed, M. U. (2018). Trends and advances in electrochemiluminescence nanobiosensors. *Sensors, 18*(1), 166. https://doi.org/10.3390/s18010166

Rizwan Younis, M., He, G., Gurram, B., Lin, J., Huang, P. (2021). Recent advances in gold nanorods-based cancer theranostics. *Advanced NanoBiomed Research, 1*(12), 2100029. https://doi.org/10.1002/anbr.202100029

Rodriguez-Quijada, C., Lyons, C., Sanchez-Purra, M., Santamaria, C., Leonardo, B. M., Quinn, S., Tlusty, M. F., Shiaris, M., Hamad-Schifferli, K. (2023). Gold nanoparticle paper immunoassays for sensing the presence of Vibrio parahaemolyticus in oyster hemolymph. *ACS Omega, 8*(22), 19494–19502. https://doi.org/10.1021/acsomega.3c00853

Rossi, F., Trakoolwilaiwan, T., Gigli, V., Tortolini, C., Lenzi, A., Isidori, A. M., Thanh, N. T. K., Antiochia, R. (2024). Progress in nanoparticle-based electrochemical biosensors for hormone detection. *Nanoscale, 16*(39), 18134-18164. https://doi.org/10.1039/D4NR02075H

Sajid, M., Kawde, A. N., Daud, M. (2015). Designs, formats and applications of lateral flow assay: A literature review. *Journal of Saudi Chemical Society, 19*(6), 689–705. https://doi.org/10.1016/j.jscs.2014.09.001

Salahvarzi, A., Mahani, M., Torkzadeh-Mahani, M., Alizadeh, R. (2017). Localized surface plasmon resonance based gold nanobiosensor: Determination of thyroid stimulating hormone. *Analytical Biochemistry, 516*, 1–5. https://doi.org/10.1016/j.ab.2016.10.003

Sanità, G., Carrese, B., Lamberti, A. (2020). Nanoparticle surface functionalization: How to improve biocompatibility and cellular internalization. *Frontiers in Molecular Biosciences, 7*, 587012. https://doi.org/10.3389/fmolb.2020.587012

Saravanakumar, K., Sathiyaseelan, A., Park, S., Kim, S. R., Priya, V. V., Wang, M. H. (2022). Monoclonal antibody functionalized, and L-lysine α-oxidase loaded PEGylated-chitosan nanoparticle for HER2/Neu targeted breast cancer therapy. *Pharmaceutics, 14*(5), 927. https://doi.org/10.3390/pharmaceutics14050927

Sau, T. K., Murphy, C. J. (2004). Seeded high yield synthesis of short Au nanorods in aqueous solution. *Langmuir, 20*(15), 6414–6420. https://doi.org/10.1021/la049463z

Scarabelli, L., Sánchez-Iglesias, A., Pérez-Juste, J., Liz-Marzán, L. M. (2015). A “tips and tricks” practical guide to the synthesis of gold nanorods. *Journal of Physical Chemistry Letters, 6*(21), 4270–4279. https://doi.org/10.1021/acs.jpclett.5b02123

Sena-Torralba, A., Álvarez-Diduk, R., Parolo, C., Piper, A., Merkoçi, A. (2022). Toward next generation lateral flow assays: Integration of nanomaterials. *Chemical Reviews, 122*(18), 14881–14910. https://doi.org/10.1021/acs.chemrev.1c01012

Sequeira-Antunes, B., Ferreira, H. A. (2023). Nucleic acid aptamer-based biosensors: A review. *Biomedicines, 11*(12), 3201. https://doi.org/10.3390/biomedicines11123201

Shahbazi-Gahrouei, D., Khaniabadi, P. M., Khaniabadi, B. M., Shahbazi-Gahrouei, S. (2019a). Medical imaging modalities using nanoprobes for cancer diagnosis: A literature review on recent findings. *Journal of Research in Medical Sciences, 24*(1), 38. https://doi.org/10.4103/jrms.JRMS_437_18

Shahbazi-Gahrouei, D., Moradi Khaniabadi, P., Shahbazi-Gahrouei, S., Khorasani, A., Mahmoudi, F. (2019b). A literature review on multimodality molecular imaging nanoprobes for cancer detection. *Polish Journal of Medical Physics and Engineering, 25*(2), 57–68. https://doi.org/10.2478/pjmpe-2019-0009

Shahjahan, T., Javed, B., Sharma, V., Tian, F. (2023). pH and NaCl optimisation to improve the stability of gold and silver nanoparticles' anti-zearalenone antibody conjugates for immunochromatographic assay. *Methods and Protocols, 6*(5), 93. https://doi.org/10.3390/mps6050093

Shang, W., Zeng, C., Du, Y., Hui, H., Liang, X., Chi, C., Wang, K., Wang, Z., Tian, J. (2017). Core–shell gold nanorod@metal–organic framework nanoprobes for multimodality diagnosis of glioma. *Advanced Materials, 29*(3). https://doi.org/10.1002/adma.201604381

Shen, J., Kim, H. C., Mu, C., Gentile, E., Mai, J., Wolfram, J., Ji, L. N., Ferrari, M., Mao, Z. wan, Shen, H. (2014). Multifunctional gold nanorods for siRNA gene silencing and photothermal therapy. *Advanced Healthcare Materials, 3*(10), 1629–1637. https://doi.org/10.1002/adhm.201400103

Sheng, Y., Lin, M., Li, X., Hao, H., Lin, X., Sun, H., Zhang, H. (2014). Enhancement of the 808 nm photothermal effect of gold nanorods by thiol-induced self-assembly. *Particle and Particle Systems Characterization, 31*(7), 788–793. https://doi.org/10.1002/ppsc.201300351

Shi, X., Perry, H. L., Wilton-Ely, J. D. E. T. (2021). Strategies for the functionalisation of gold nanorods to reduce toxicity and aid clinical translation. *Nanotheranostics, 5*(2), 155–165. https://doi.org/10.7150/ntno.56432

Shukla, S., Leem, H., Kim, M. (2011). Development of a liposome-based immunochromatographic strip assay for the detection of Salmonella. *Analytical and Bioanalytical Chemistry, 401*(8), 2581–2590. https://doi.org/10.1007/s00216-011-5327-2

Si, S., Leduc, C., Delville, M. H., Lounis, B. (2012). Short gold nanorod growth revisited: The critical role of the bromide counterion. *ChemPhysChem, 13*(1), 193–202. https://doi.org/10.1002/cphc.201100710

Sim, H. R., Wark, A. W., Lee, H. J. (2010). Attomolar detection of protein biomarkers using biofunctionalized gold nanorods with surface plasmon resonance. *Analyst, 135*(10), 2528–2532. https://doi.org/10.1039/c0an00457j

Smitha, S. L., Gopchandran, K. G., Smijesh, N., Philip, R. (2013). Size-dependent optical properties of Au nanorods. *Progress in Natural Science: Materials International, 23*(1), 36–43. https://doi.org/10.1016/j.pnsc.2013.01.005

Singh, R. (2020). Surgical anatomy of thyroid gland - A comprehensive review. *Basic Sciences of Medicine, 9*(1), 10–14. https://doi.org/10.5923/j.medicine.20200901.03

Song, N., Zhang, Z., Liu, P., Dai, D., Chen, C., Li, Y., Wang, L., Han, T., Yang, Y. W., Wang, D., Tang, B. Z. (2021). Pillar[5]arene-modified gold nanorods as nanocarriers for multi-modal imaging-guided synergistic photodynamic-photothermal therapy. *Advanced Functional Materials, 31*(21), 2009924. https://doi.org/10.1002/adfm.202009924

Su, G., Yang, C., Zhu, J. J. (2015). Fabrication of gold nanorods with tunable longitudinal surface plasmon resonance peaks by reductive dopamine. *Langmuir, 31*(2), 817–823. https://doi.org/10.1021/la504041f

Su, L., Hu, S., Zhang, L., Wang, Z., Gao, W., Yuan, J., Liu, M. (2017). A fast and efficient replacement of CTAB with MUA on the surface of gold nanorods assisted by a

water-immiscible ionic liquid. *Small, 13*(11), 1602809. https://doi.org/10.1002/smll.201602809

Svilenov, H. L., Kulakova, A., Zalar, M., Golovanov, A. P., Harris, P., Winter, G. (2020). Orthogonal techniques to study the effect of pH, sucrose, and arginine salts on monoclonal antibody physical stability and aggregation during long-term storage. *Journal of Pharmaceutical Sciences, 109*(1), 584–594. https://doi.org/10.1016/j.xphs.2019.10.065

Taheri, R. A., Rezayan, A. H., Rahimi, F., Mohammadnejad, J., Kamali, M. (2017). Evaluating the potential of an antibody against recombinant OmpW antigen in detection of Vibrio cholerae by surface plasmon resonance (SPR) biosensor. *Plasmonics, 12*(5), 1493–1504. https://doi.org/10.1007/s11468-016-0411-2

Tan, E., Frew, E., Cooper, J., Humphrey, J., Holden, M., Mand, A. R., Li, J., Anderson, S., Bi, M., Hatler, J., Person, A., Mortari, F., Gould, K., Barry, S. (2021). Use of lateral flow immunoassay to characterize SARS-COV-2 RBD-specific antibodies and their ability to react with the UK, SA and BR P.1 variant RBDs. *Diagnostics, 11*(7), 1190. https://doi.org/10.3390/diagnostics11071190

Tao, Y., Yang, J., Chen, L., Huang, Y., Qiu, B., Guo, L., Lin, Z. (2018). Dialysis assisted ligand exchange on gold nanorods: Amplification of the performance of a lateral flow immunoassay for E. coli O157:H7. *Microchimica Acta, 185*(7), 1-9. https://doi.org/10.1007/s00604-018-2897-0

Taub, N., Krichevski, O., Markovich, G. (2003). Growth of gold nanorods on surfaces. *Journal of Physical Chemistry B, 107*(42), 11579–11582. https://doi.org/10.1021/jp036144s

Taylor, P. N., Albrecht, D., Scholz, A., Gutierrez-Buey, G., Lazarus, J. H., Dayan, C. M., Okosieme, O. E. (2018). Global epidemiology of hyperthyroidism and hypothyroidism. *Nature Reviews Endocrinology, 14*(5), 301–316. https://doi.org/10.1038/nrendo.2018.18

Tetyana, P., Shumbula, P. M., Njengele-Tetyana, Z. (2021). Biosensors: Design, development and applications. In *Nanopores* (p. Ch. 3). IntechOpen. https://doi.org/10.5772/intechopen.97576

Thierry, B., Ng, J., Krieg, T., Griesser, H. J. (2009). A robust procedure for the functionalization of gold nanorods and noble metal nanoparticles. *Chemical Communications, 13*, 1724–1726. https://doi.org/10.1039/b820137d

Thomas, N., Mani, E. (2016). An analytical solution to the kinetics of growth of gold nanorods. *RSC Advances, 6*(36), 30028–30036. https://doi.org/10.1039/C5RA24411K

Thomas, R., Park, I. K., Jeong, Y. Y. (2013). Magnetic iron oxide nanoparticles for multimodal imaging and therapy of cancer. *International Journal of Molecular Sciences, 14*(8), 15910–15930. https://doi.org/10.3390/ijms140815910

Toh, Y. R., Yu, P., Wen, X., Tang, J., Hsieh, T. shih. (2013). Induced pH-dependent shift by local surface plasmon resonance in functionalized gold nanorods. *Nanoscale Research Letters, 8*(1), 1–7. https://doi.org/10.1186/1556-276X-8-103

Truong, P. L., Kim, B. W., Sim, S. J. (2012). Rational aspect ratio and suitable antibody coverage of gold nanorod for ultra-sensitive detection of a cancer biomarker. *Lab on a Chip, 12*(6), 1102–1109. https://doi.org/10.1039/c2lc20588b

Turashvili, G., Brogi, E. (2017). Tumor heterogeneity in breast cancer. *Frontiers in Medicine, 4*, 227. https://doi.org/10.3389/fmed.2017.00227

Unnikrishnan, A., Bantwal, G., John, M., Kalra, S., Sahay, R., Tewari, N. (2013). Prevalence of hypothyroidism in adults: An epidemiological study in eight cities of India. *Indian Journal of Endocrinology and Metabolism, 17*(4), 647. https://doi.org/10.4103/2230-8210.113755

Varma, S., Bamb, A. L., Haldar, N., Gajbhiye, V., Amalnerkar, D., Chaudhari, B. P. (2025). Gold nanorods (GNRs): A golden nano compass to navigate breast cancer by multimodal imaging approaches. *Journal of Biomedical Materials Research Part B: Applied Biomaterials, 113*(2), e35543. https://doi.org/10.1002/jbm.b.35543

Vedhanayagam, M., Andra, S., Muthalagu, M., Sreeram, K. J. (2022). Influence of functionalized gold nanorods on the structure of cytochrome –C: An effective bio-nanoconjugate for biomedical applications. *Inorganic Chemistry Communications, 146*, 110182. https://doi.org/10.1016/j.inoche.2022.110182

Venkatesan, R., Pichaimani, A., Hari, K., Balasubramanian, P. K., Kulandaivel, J., Premkumar, K. (2013). Doxorubicin conjugated gold nanorods: A sustained drug delivery carrier for improved anticancer therapy. *Journal of Materials Chemistry B, 1*(7), 1010–1018. https://doi.org/10.1039/c2tb00078d

Vigderman, L., Khanal, B. P., Zubarev, E. R. (2012). Functional gold nanorods: Synthesis, self-assembly, and sensing applications. *Advanced Materials, 24*(36), 4811–4841. https://doi.org/10.1002/adma.201201690

Von Maltzahn, G., Park, J. H., Agrawal, A., Bandaru, N. K., Das, S. K., Sailor, M. J., Bhatia, S. N. (2009). Computationally guided photothermal tumor therapy using long-circulating gold nanorod antennas. *Cancer Research, 69*(9), 3892–3900. https://doi.org/10.1158/0008-5472.CAN-08-4242

Walls, G. V., Mihai, R. (2017). Thyroid gland embryology, anatomy, and physiology. *Endocrine Surgery in Children, 2*(9), 3–15. https://doi.org/10.1007/978-3-662-54256-9_1

Wang, B., Tchessalov, S., Cicerone, M. T., Warne, N. W., Pikal, M. J. (2009). Impact of sucrose level on storage stability of proteins in freeze-dried solids: II. Correlation of aggregation rate with protein structure and molecular mobility. *Journal of Pharmaceutical Sciences, 98*(9), 3145–3166. https://doi.org/10.1002/jps.21622

Wang, C., Bao, C., Liang, S., Fu, H., Wang, K., Deng, M., Liao, Q., Cui, D. (2014). RGD-conjugated silica-coated gold nanorods on the surface of carbon nanotubes for targeted photoacoustic imaging of gastric cancer. *Nanoscale Research Letters, 9*(1), 1–10. https://doi.org/10.1186/1556-276X-9-264

Wang, C., Chen, J., Talavage, T., Irudayaraj, J. (2009). Gold nanorod/Fe_3O_4 nanoparticle "nano-pearl-necklaces" for simultaneous targeting, dual-mode imaging, and photothermal ablation of cancer cells. *Angewandte Chemie, 121*(15), 2797–2801. https://doi.org/10.1002/ange.200805282

Wang, C., Fan, W., Zhang, Z., Wen, Y., Xiong, L., Chen, X. (2019). Advanced nanotechnology leading the way to multimodal imaging-guided precision surgical therapy. *Advanced Materials, 31*(49), 1904329. https://doi.org/10.1002/adma.201904329

Wang, C. H., Chang, C. W., Peng, C. A. (2011). Gold nanorod stabilized by thiolated chitosan as photothermal absorber for cancer cell treatment. *Journal of Nanoparticle Research, 13*(7), 2749–2758. https://doi.org/10.1007/s11051-010-0162-5

Wang, C., Irudayaraj, J. (2008). Gold nanorod probes for the detection of multiple pathogens. *Small, 4*(12), 2204–2208. https://doi.org/10.1002/smll.200800309

Wang, C., Xu, C., Xu, L., Sun, C., Yang, D., Xu, J., He, F., Gai, S., Yang, P. (2018). A novel core-shell structured upconversion nanorod as a multimodal bioimaging and photothermal ablation agent for cancer theranostics. *Journal of Materials Chemistry B, 6*(17), 2597–2607. https://doi.org/10.1039/c7tb02842c

Wang, D., Skinner, J. P., Ruan, Q., Tetin, S. Y., Collier, G. B. (2015). Affinity assisted selection of antibodies for Point of Care TSH immunoassay with limited wash. *Clinica Chimica Acta, 438*, 55–61. https://doi.org/10.1016/j.cca.2014.07.027

Wang, H., Ouyang, W., Liu, H. (2024). Tumor microenvironment responsive nanozymes for multimodal imaging of tumors. *Nano TransMed, 3*, 100032. https://doi.org/10.1016/j.ntm.2024.100032

Wang, H., Wu, X., Dong, P., Wang, C., Wang, J., Liu, Y., Chen, J. (2014). Electrochemical biosensor based on interdigitated electrodes for determination of thyroid stimulating hormone. *International Journal of Electrochemical Science*, *9*(1), 12-2. https://doi.org/10.1016/S1452-3981(23)07694-0

Wang, J., Zhang, H. Z., Li, R. S., Huang, C. Z. (2016). Localized surface plasmon resonance of gold nanorods and assemblies in the view of biomedical analysis. *TrAC - Trends in Analytical Chemistry, 80*, 429–443. https://doi.org/10.1016/j.trac.2016.03.015

Wang, J., Zhang, L., Huang, Y., Dandapat, A., Dai, L., Zhang, G., Lu, X., Zhang, J., Lai, W., Chen, T. (2017). Hollow Au-Ag nanoparticles labeled immunochromatography strip for highly sensitive detection of clenbuterol. *Scientific Reports, 7*(1), 41419. https://doi.org/10.1038/srep41419

Wang, L. L., Chen, J. T., Wang, L. F., Wu, S., Zhang, G. Z., Yu, H. Q., Ye, X. D., Shi, Q. S. (2017). Conformations and molecular interactions of poly-γ-glutamic acid as a

soluble microbial product in aqueous solutions. *Scientific Reports, 7*(1), 1-11. https://doi.org/10.1038/s41598-017-13152-2

Wang, X., Mei, Z., Wang, Y., Tang, L. (2017). Comparison of four methods for the biofunctionalization of gold nanorods by the introduction of sulfhydryl groups to antibodies. *Beilstein Journal of Nanotechnology, 8*(1), 372–380. https://doi.org/10.3762/bjnano.8.39

Wang, Y., Black, K. C. L., Luehmann, H., Li, W., Zhang, Y., Cai, X., Wan, D., Liu, S. Y., Li, M., Kim, P., Li, Z. Y., Wang, L. V., Liu, Y., Xia, Y. (2013). Comparison study of gold nanohexapods, nanorods, and nanocages for photothermal cancer treatment. *ACS Nano, 7*(3), 2068–2077. https://doi.org/10.1021/nn304332s

Wang, Y., Guo, S., Chen, H., Wang, E. (2008). Facile fabrication of large area of aggregated gold nanorods film for efficient surface-enhanced Raman scattering. *Journal of Colloid and Interface Science, 318*(1), 82–87. https://doi.org/10.1016/j.jcis.2007.09.057

Wang, Y., Pasternak, M., Sathiyamoorthy, K., Kolios, M. C. (2021). Anti-HER2 PLGA-PEG polymer nanoparticle containing gold nanorods and paclitaxel for laser-activated breast cancer detection and therapy. *Biomedical Optics Express, 12*(4), 2171-2185. https://doi.org/10.1364/boe.419252

Wani, T. A., Zargar, S., Wakil, S. M., Darwish, I. A. (2016). New analytical application of antibody-based biosensor in estimation of thyroid-stimulating hormone in serum. *Bioanalysis, 8*(7), 625–632. https://doi.org/10.4155/bio-2015-0034

Watt, J., Hance, B. G., Anderson, R. S., Huber, D. L. (2015). Effect of seed age on gold nanorod formation: A microfluidic, real-time investigation. *Chemistry of Materials, 27*(18), 6442–6449. https://doi.org/10.1021/acs.chemmater.5b02675

Wiesner, J., Wokaun, A. (1989). Anisometric gold colloids. Preparation, characterization, and optical properties. *Chemical Physics Letters, 157*(6), 569-575. https://doi.org/10.1016/S0009-2614(89)87413-5

Xia, F., Gao, X., Shen, X., Xu, H., Zhong, S. (2022). Preparation of a gold@europium-based coordination polymer nanocomposite with excellent photothermal

properties and its potential for four-mode imaging. *New Journal of Chemistry, 46*(34), 16461–16470. https://doi.org/10.1039/d2nj01021f

Xia, L., Zhang, C., Li, M., Wang, K., Wang, Y., Xu, P., Hu, Y. (2018). Nitroxide-radicals–modified gold nanorods for in vivo CT/MRI-guided photothermal cancer therapy. *International Journal of Nanomedicine, 13*, 7123–7134. https://doi.org/10.2147/IJN.S171804

Xie, L., Ying, X., Li, X., Tan, X., Zhang, T., Zhang, X., Cai, W., An, F., Liu, X., Han, S. (2023). Engineering of gold nanorods as multifunctional theranostic agent for photothermal-enhanced radiotherapy of cancer. *Materials and Design, 225*, 111456. https://doi.org/10.1016/j.matdes.2022.111456

Xie, X., Liao, J., Shao, X., Li, Q., Lin, Y. (2017). The effect of shape on cellular uptake of gold nanoparticles in the forms of stars, rods, and triangles. *Scientific Reports, 7*(1), 3827. https://doi.org/10.1038/s41598-017-04229-z

Xu, C., Chen, F., Valdovinos, H. F., Jiang, D., Goel, S., Yu, B., Sun, H., Barnhart, T. E., Moon, J. J., Cai, W. (2018). Bacteria-like mesoporous silica-coated gold nanorods for positron emission tomography and photoacoustic imaging-guided chemo-photothermal combined therapy. *Biomaterials, 165*, 56–65. https://doi.org/10.1016/j.biomaterials.2018.02.043

Xu, C., Feng, Q., Yang, H., Wang, G., Huang, L., Bai, Q., Zhang, C., Wang, Y., Chen, Y., Cheng, Q., Chen, M., Han, Y., Yu, Z., Lesniak, M. S., Cheng, Y. (2018). A light-triggered mesenchymal stem cell delivery system for photoacoustic imaging and chemo-photothermal therapy of triple negative breast cancer. *Advanced Science, 5*(10), 1800382. https://doi.org/10.1002/advs.201800382

Xu, C., Yang, D., Mei, L., Li, Q., Zhu, H., Wang, T. (2013). Targeting chemophotothermal therapy of hepatoma by gold nanorods/graphene oxide core/shell nanocomposites. *ACS Applied Materials and Interfaces, 5*(24), 12911–12920. https://doi.org/10.1021/am404714w

Xu, K., Shi, J., Pourmand, A., Udayakumar, T. S., Dogan, N., Zhao, W., Pollack, A., Yang, Y. (2018). Plasmonic optical imaging of gold nanorods localization in small animals. *Scientific Reports, 8*(1), 9342. https://doi.org/10.1038/s41598-018-27624-6

Xu, W., Qian, J., Hou, G., Suo, A., Wang, Y., Wang, J., Sun, T., Yang, M., Wan, X., Yao, Y. (2017). Hyaluronic acid-functionalized gold nanorods with pH/NIR dual-responsive drug release for synergetic targeted photothermal chemotherapy of breast cancer. *ACS Applied Materials and Interfaces, 9*(42), 36533–36547. https://doi.org/10.1021/acsami.7b08700

Xu, X., Zhao, Y., Xue, X., Huo, S., Chen, F., Zou, G., Liang, X. J. (2014). Seedless synthesis of high aspect ratio gold nanorods with high yield. *Journal of Materials Chemistry A, 2*(10), 3528–3535. https://doi.org/10.1039/c3ta13905k

Yan, E., Cao, M., Wang, Y., Hao, X., Pei, S., Gao, J., Wang, Y., Zhang, Z., Zhang, D. (2016). Gold nanorods contained polyvinyl alcohol/chitosan nanofiber matrix for cell imaging and drug delivery. *Materials Science and Engineering C, 58*, 1090–1097. https://doi.org/10.1016/j.msec.2015.09.080

Yang, H. W., Liu, H. L., Li, M. L., Hsi, I. W., Fan, C. T., Huang, C. Y., Lu, Y. J., Hua, M. Y., Chou, H. Y., Liaw, J. W., Ma, C. C. M., Wei, K. C. (2013). Magnetic gold-nanorod/ PNIPAAmMA nanoparticles for dual magnetic resonance and photoacoustic imaging and targeted photothermal therapy. *Biomaterials, 34*(22), 5651–5660. https://doi.org/10.1016/j.biomaterials.2013.03.085

Yao, D., Wang, Y., Zou, R., Bian, K., Yuan, S., Zhang, B., Wang, D. (2021). Wavelength-adjustable butterfly molecules in dynamic nanoassemblies for Extradomain-B fibronectin-modulating optical imaging and synchronous phototherapy of triple-negative breast cancer. *Chemical Engineering Journal, 420*, 127658. https://doi.org/10.1016/j.cej.2020.127658

Ye, X., Zheng, C., Chen, J., Gao, Y., Murray, C. B. (2013). Using binary surfactant mixtures to simultaneously improve the dimensional tunability and monodispersity in the seeded growth of gold nanorods. *Nano Letters, 13*(2), 765–771. https://doi.org/10.1021/nl304478h

Yin, F., Yang, C., Wang, Q., Zeng, S., Hu, R., Lin, G., Tian, J., Hu, S., Lan, R. F., Yoon, H. S., Lu, F., Wang, K., Yong, K. T. (2015). A light-driven therapy of pancreatic adenocarcinoma using gold nanorods-based nanocarriers for co-delivery of doxorubicin and siRNA. *Theranostics, 5*(8), 818–833. https://doi.org/10.7150/thno.11335

Yin, J., Chen, D., Wu, S., Li, C., Liu, L., Shao, Y. (2017). Tumor-targeted nanoprobes for enhanced multimodal imaging and synergistic photothermal therapy: Core-shell and dumbbell Gd-tailored gold nanorods. *Nanoscale, 9*(43), 16661–16673. https://doi.org/10.1039/c7nr03847j

You, D. J., Park, T. S., Yoon, J. Y. (2013). Cell-phone-based measurement of TSH using Mie scatter optimized lateral flow assays. *Biosensors and Bioelectronics, 40*(1), 180–185. https://doi.org/10.1016/j.bios.2012.07.014

Yuan, H., Liang, H., Hou, P., Li, J. (2021). Advanced nanomaterials for multimodal molecular imaging. *Chemical Research in Chinese Universities, 37*(4), 840–845. https://doi.org/10.1007/s40242-021-1196-1

Yüce, M., Kurt, H. (2017). How to make nanobiosensors: Surface modification and characterisation of nanomaterials for biosensing applications. *RSC Advances, 7*(78), 49386–49403. https://doi.org/10.1039/c7ra10479k

Yue, L., Sun, C., Cheng, Q., Ding, Y., Wei, J., Wang, R. (2019). Gold nanorods with a noncovalently tailorable surface for multi-modality image-guided chemo-photothermal cancer therapy. *Chemical Communications, 55*(90), 13506–13509. https://doi.org/10.1039/c9cc07131h

Zeng, Z., Gao, H., Chen, C. X., Xiao, L., Zhang, K. (2022). Bioresponsive nanomaterials: recent advances in cancer multimodal imaging and imaging-guided therapy. *Frontiers in Chemistry, 10*, 881812. https://doi.org/10.3389/fchem.2022.881812

Zhan, Q., Qian, J., Li, X., He, S. (2010). A study of mesoporous silica-encapsulated gold nanorods as enhanced light scattering probes for cancer cell imaging. *Nanotechnology, 21*(5), 055704. https://doi.org/10.1088/0957-4484/21/5/055704

Zhang, D., Wei, L., Zhong, M., Xiao, L., Li, H. W., Wang, J. (2018). The morphology and surface charge-dependent cellular uptake efficiency of upconversion nanostructures revealed by single-particle optical microscopy. *Chemical Science, 9*(23), 5260–5269. https://doi.org/10.1039/c8sc01828f

Zhang, H., She, Z., Su, H., Kerman, K., Kraatz, H. B. (2016). Effects of bipyramidal gold nanoparticles and gold nanorods on the detection of immunoglobulins. *Analyst, 141*(21), 6080–6086. https://doi.org/10.1039/c6an01111j

Zhang, H., Sun, Y., Wang, J., Zhang, J., Zhang, H., Zhou, H., Song, D. (2012). Preparation and application of novel nanocomposites of magnetic-Au nanorod in SPR biosensor. *Biosensors and Bioelectronics, 34*(1), 137–143. https://doi.org/10.1016/j.bios.2012.01.032

Zhang, L., Yang, X. Q., An, J., Zhao, S. D., Zhao, T. Y., Tan, F., Cao, Y. C., Zhao, Y. D. (2018). In vivo tumor active cancer targeting and CT-fluorescence dual-modal imaging with nanoprobe based on gold nanorods and InP/ZnS quantum dots. *Journal of Materials Chemistry B, 6*(17), 2574–2583. https://doi.org/10.1039/c7tb02643a

Zhang, L., Zhao, F., Li, Z., Fang, Y., Wang, P. (2016). Tailoring of localized surface plasmon resonances of core-shell Au@Ag nanorods by changing the thickness of Ag shell. *Plasmonics, 11*(6), 1511–1517. https://doi.org/10.1007/s11468-016-0204-7

Zhang, N., Li, J., Hou, R., Zhang, J., Wang, P., Liu, X., Zhang, Z. (2017). Bubble-generating nano-lipid carriers for ultrasound/CT imaging-guided efficient tumor therapy. *International Journal of Pharmaceutics, 534*(1–2), 251–262. https://doi.org/10.1016/j.ijpharm.2017.07.081

Zhang, W., Ji, Y., Meng, J., Wu, X., Xu, H. (2012). Probing the behaviors of gold nanorods in metastatic breast cancer cells based on UV-vis-NIR absorption spectroscopy. *PLoS ONE, 7*(2), e31957. https://doi.org/10.1371/journal.pone.0031957

Zhang, Y., Liu, X., Wang, L., Yang, H., Zhang, X., Zhu, C., Wang, W., Yan, L., Li, B. (2020). Improvement in detection limit for lateral flow assay of biomacromolecules by test-zone pre-enrichment. *Scientific Reports, 10*(1), 9604. https://doi.org/10.1038/s41598-020-66456-1

Zhang, Y., Song, N., Fu, J., Liu, Y., Zhan, X., Peng, S., Yang, Z., Zhu, X., Chen, Y., Wang, Z., Yu, Y., Shi, Q., Fu, Y., Yuan, K., Zhou, N., Ichim, T. E., Min, W. (2016). Synergic therapy of melanoma using GNRs-MUA-PEI/siIDO2-FA through targeted gene silencing and plasmonic photothermia. *RSC Advances, 6*(81), 77577-77589. https://doi.org/10.1039/C6RA13297A

Zhang, Z., Lin, M. (2014). Fast loading of PEG-SH on CTAB-protected gold nanorods. *RSC Advances, 4*(34), 17760–17767. https://doi.org/10.1039/c3ra48061e

Zhang, Z., Sang, W., Xie, L., Dai, Y. (2019). Metal-organic frameworks for multimodal bioimaging and synergistic cancer chemotherapy. *Coordination Chemistry Reviews, 399*, 213022. https://doi.org/10.1016/j.ccr.2019.213022

Zheng, P., Raj, P., Wu, L., Mizutani, T., Szabo, M., Hanson, W. A., Barman, I. (2024). Quantitative detection of thyroid-stimulating hormone in patient samples with a nanomechanical single-antibody spectro-immunoassay. *Small, 20*(6), 2305110. https://doi.org/10.1002/smll.202305110

Zhou, J., Cao, Z., Panwar, N., Hu, R., Wang, X., Qu, J., Tjin, S. C., Xu, G., Yong, K. T. (2017). Functionalized gold nanorods for nanomedicine: Past, present and future. *Coordination Chemistry Reviews, 352*, 15–66. https://doi.org/10.1016/j.ccr.2017.08.020

Zhou, T., Yu, M., Zhang, B., Wang, L., Wu, X., Zhou, H., Du, Y., Hao, J., Tu, Y., Chen, C., Wei, T. (2014). Inhibition of cancer cell migration by gold nanorods: Molecular mechanisms and implications for cancer therapy. *Advanced Functional Materials, 24*(44), 6922–6932. https://doi.org/10.1002/adfm.201401642

ABSTRACT

Name of the student: **Sanjana Varma** Registration No: **10BB19J26012**
Faculty of Study: **Biological Sciences** Year of Submission: **2025**
AcSIR academic centre/ CSIR Lab: **CSIR- National Chemical Laboratory, Pune**
Name of the Supervisor: **Dr. Bhushan P. Chaudhari**
Title of the thesis: **Functionalized gold nanorods for sensing thyroid stimulating hormone and bioimaging application**

Gold nanorods (GNRs) are ideal agents for probing diseases through imaging and sensing due to their favorable optical properties, ease of surface functionalization and biocompatibility. We synthesized GNRs and further modified them with 11-mercaptoundecanoic acid (11-MUA) (MUA-GNRs), which were functionalized with TSH antibodies and biosynthesized poly-γ-glutamic acid (γPGA) for biosensing the thyroid stimulating hormone (TSH) through lateral flow assay (LFA) and multimodal bioimaging of breast cancer using computed tomography (CT) and photoacoustic imaging (PAI), respectively, to combat them efficiently owing to their increasing incidences around the world.

To synthesize monodisperse and stable GNRs of aspect ratio around 3.8 by the seed-mediated growth method, 1 mM gold precursor concentration, 0.2 M cetyltrimethylammonium bromide (CTAB), 250 µl silver nitrate (4 mM), 75 µl ascorbic acid, and 12 µl seed aged for 30 min, pH 3 and 2 h synthesis time were optimized. Further, GNRs were surface modified with 11-MUA to decorate GNRs with the -COOH group as well as to replace CTAB. We optimized an alkaline aqueous solvent, 2 ml 11-MUA, to modify 5 ml GNRs, 800 rpm stirring speed and 8 h as the time required to surface modify GNRs. The MUA-GNRs were further functionalized with TSH antibody to prepare stable conjugate for the LFA. Furthermore, GNRs and MUA-GNRs were functionalized with biosynthesized γPGA for bioimaging studies. Characterization of these particles by using various high-end techniques confirmed the synthesis of highly stable rod-shaped particles with longitudinal SPR band in the NIR region and their successful surface modification.

Further, the optical density (OD) of the conjugate, the concentration of the capture antibody and the sample volume were optimized to enhance the sensitivity of the LFA. The limit of detection (LOD) of the LFA was found to be 0.3 µIU/ml, and it did not show any cross-reactivity with the other structurally similar hormones. The LFA could semi-quantitatively elucidate hypothyroidism and hypothyroidism based on the TSH without using any quantification method. Therefore, TSH antibody functionalized GNRs acted as an excellent sensing probe. Furthermore, the cell viability assay established the great biocompatibility of the γPGA-MUA-GNRs in both cancerous (MCF-7 & MDA-MB-231) and normal breast (MCF-10A) cell lines. The γPGA-MUA-GNRs were also hemocompatible with <3% hemolysis at its maximum concentration. The cellular uptake studies showed higher uptake of γPGA functionalized GNRs compared to other groups of GNRs in all three cell lines. A good linear relationship was recorded between the CT/Photoacoustic intensity and the concentrations of γPGA-MUA-GNRs based on gold content. Therefore, γPGA-MUA-GNRs offered enhanced dual-modal CT and PAI imaging contrast compared to conventional agents.

Details of Publications

Research Article Emanating from Thesis

1. **Varma, S.,** Burade, D. K., Chaudhari, B.P., (2024). Functionalized gold nanorods (GNRs) as a label for the detection of thyroid-stimulating hormone (TSH) through lateral flow assay (LFA). *Emergent Materials,* 1-17. https://doi.org/10.1007/s42247-024-00976-8

Other Articles

2. **Varma, S.,** Bamb, A. L., Tambe, S., Burade, D. K., Jagdale, S., Pande, B., Vamkudoth, K.R., Chaudhari, B. P. (2025). Understanding the antimicrobial and antioxidant potential of bioinspired platinum nanoparticles synthesized using Ocimum tenuiflorum. *BioNanoScience, 15* (1), 178. https://doi.org/ 10.1007/s12668-024-01788-0

3. Auti, A., Yadav, P., Bodkhe, R., Bhandari, Y., **Varma, S.**, Chaudhari, B., Rahi, S., Ghormade, V., Vamkudoth, K. (2024). Development of novel ssDNA aptamers for detection of receptor-binding domain of SARS-COV-.2. *ACS Omega* (Accepted).

4. Bhandari, Y., **Varma, S.**, Sawant, A., Beemagani, S., Jaiswal, N., Chaudhari. B.P., Vamkudoth, K.R. (2023). Biosynthesis of gold nanoparticles by Penicillium rubens and catalytic detoxification of ochratoxin A and organic dye pollutants. *International Microbiology, 26* (4), 765-80. https://doi.org/10.1007/s10123-023-00341-5

5. Moudgil, A., **Varma, S.**, Shinde, M.D., Vamkudoth, K.R., Sarkar, D.M., Shende, R.A., Amalnerkar, D., Chaudhari, B.P. (2022). One-pot concurrent biosynthesis of biphasic CuxO (cuprous and cupric oxide) nanoparticles using leaf extract of Eichhornia crassipes and investigation of their potent healthcare applications. *Emergent Materials, 5*(2), 323-33. https://doi.org/10.1007/s42247-022-00347-1

6. Nisar, A., Ajabia, D.K., Agrawal, S.B., **Varma, S.**, Chaudhari, B.P., Tupe, R.S. (2022). Mechanistic insight into differential interactions of iron oxide nanoparticles with native, glycated albumin and their effect on erythrocytes parameters. *International Journal of Biological Macromolecules, 212*, 232-247. https://doi.org/10.1016/j.ijbiomac.2022.05.106

7. Mane, P.C., Shinde, M.D., **Varma, S.**, Chaudhari, B.P., Fatehmulla, A., Shahabuddin, M., Amalnerkar, D.P., Aldhafiri, A.M., Chaudhari, R.D. (2020). Highly sensitive label-free bio-

interfacial colorimetric sensor based on silk fibroin-gold nanocomposite for facile detection of chlorpyrifos pesticide. *Scientific Reports, 10* (1), 4198. https://doi.org/10.1038/s41598-020-61130-y

Review Article

8. **Varma, S.,** Bamb, A. L., Haldar, N., Gajbhiye, V., Amalnerkar, D., Chaudhari, B. P. (2025). Gold nanorods (GNRs): A golden nano compass to navigate breast cancer by multimodal imaging approaches. *Journal of Biomedical Materials Research Part B: Applied Biomaterials, 113*(2), e35543. https://doi.org/10.1002/jbm.b.35543

Book Chapters

9. **Varma, S.**, Bagade, M.M., Amalnerkar, D., Shinde, M.D., Chaudhari, B.P. (2023). Nanoparticles for the delivery of antiviral phytotherapeutics. In *Advances in Phytonanotechnology for Treatment of Various Diseases*, pp. 307-341. CRC Press. https://doi.org/10.1201/9781003231721-13

10. **Varma, S.**, Jaiswal, N., Vyawahare, N., Pawar, A.T., Tupe, R.S., Wankhade, V., Vamkudoth, K.R., Chaudhari, B.P. (2022). Nanophytovirology approach to combat plant viral diseases. In *Nanotechnology in Agriculture and Environmental Science*, pp. 127-154. CRC Press. https://doi.org/10.1201/9781003323945-11

11. **Varma, S.**, Jaiswal, N., Shende, R.A., Chaudhari, B.P. (2022). Insight into fungi-mediated nano-synthesis for healthcare applications: An Indian perspective. In *Progress in Mycology: Biology and Biotechnological Applications,* pp. 205-243. Singapore: Springer Nature Singapore. https://doi.org/10.1007/978-981-16-3307-2_8

12. Gajbhiye, K.R., Dhapte, V., **Varma, S.**, Chaudhari, B.P., Gajbhiye, V. (2022). Redox-responsive nanomedicine for breast cancer therapy. In *Targeted Nanomedicine for Breast Cancer Therapy*, pp. 407-439. Academic Press. https://doi.org/10.1016/B978-0-12-824476-0.00005-X

List of Papers with abstract presented (oral/poster) at national/international conferences/seminars with complete details.

Poster Presentation

1. **Varma, S**., Chaudhari, B. P., Surface functionalization strategies for gold nanorods: A biomedical perspective. Best poster award in National Science Day celebration held during February, 2023 at CSIR-National Chemical Laboratory, Pune, India.

Emergent Materials
https://doi.org/10.1007/s42247-024-00976-8

ORIGINAL ARTICLE

Functionalized gold nanorods (GNRs) as a label for the detection of thyroid-stimulating hormone (TSH) through lateral flow assay (LFA)

Sanjana Varma[1,2] · Dimpal K. Burade[1,2] · Bhushan P. Chaudhari[1,2]

Received: 13 August 2024 / Accepted: 11 December 2024

Abstract
Thyroid-stimulating hormone (TSH) is an important biomarker of thyroid dysfunctions. Different types of nano biosensors have been developed to detect TSH. However, there is a lacuna in the development of sensitive paper-based nano biosensors due to less sensitivity and instability of the labels. Interestingly, the intense color and localized surface plasmon resonance (LSPR) property make gold nanorods (GNRs) an efficient lateral flow assay (LFA) label instead of spherical gold nanoparticles. The rapidity, simplicity and user-friendly functioning of LFAs make them a predominant technique compared to electrochemical techniques for point-of-care diagnosis. This proof-of-concept study underlines the role of stable GNRs as a novel label for LFAs. The TSH antibody functionalized GNRs can semi-quantitatively diagnose hyperthyroidism and hypothyroidism. The limit of detection (LOD) of the LFA is 0.3 µIU/mL, determined by visually analyzing the color development at the test line without employing any quantification method. Moreover, the study provides a comprehensive understanding of seed-mediated synthesis and functionalization of GNRs, which would benefit the researchers in suitably designing the GNRs-based labels for LFAs. Considering their exceptional characteristics, GNR-based LFAs are expected to surpass other labelling nanomaterials in detecting various biological markers. This enhanced sensitivity could significantly improve the clinical utility of diagnostic kits.

Keywords Gold nanorods · Labels · Lateral flow assay · Thyroid stimulating hormone

1 Introduction

Thyroid-stimulating hormone (TSH) is a controller of the hormonal output of the thyroid gland. It is secreted by the thyrotropic cells which are present in the anterior pituitary gland; due to this, it is also referred to as thyrotropin or thyrotropic hormone. The TSH is regulated by thyroid-releasing hormone (TRH) produced by the hypothalamus [1, 2, 3]. TSH is a glycoprotein hormone of approximately of 28 kDa. It comprises of two subunits, that are alpha and beta subunits [1, 3, 4]. The α-subunit is common in TSH, follicle-stimulating hormone (FSH), human chorionic gonadotropin (hCG) hormone and luteinizing hormone (LH) whereas the specific biological activity of each hormone is provided by the β-subunit of these hormones [4]. TSH activates the thyroid gland to generate its hormones thyroxine (T4) and, subsequently triiodothyronine (T3) [1–4]. TSH has crucial functions in the body like regulation of metabolism, regulation of temperature of the body, cholesterol, heart rate [2, 3] as well as it is also crucial for controlling the reproductive, nervous and skeleton-related functions [3].

TSH levels in the serum are determined to assess thyroid-related diseases. The normal TSH level in a healthy person ranges from 0.5 µIU/mL to 5 µIU/mL. Mainly, elevated TSH levels above 5 µIU/mL are considered as subclinical hypothyroidism or hypothyroidism; however, values below 0.5 µIU/mL indicate the condition of hyperthyroidism. TSH estimation is the first-line diagnosis for thyroid disorders, which covered the market of 1.68 billion USD in 2021 and is anticipated to reach 2.56 billion USD by 2028 due to the enhancing global prevalence of various thyroid-associated diseases [5]. Conventionally, several immunoassays are used to determine the TSH levels in the body. However, the lack of sensitivity and difficult operational conditions

✉ Bhushan P. Chaudhari
bp.chaudhari@ncl.res.in

1 Biochemical Sciences Division, CSIR-National Chemical Laboratory, Pashan, Pune 411008, India

2 Academy of Scientific and Innovative Research (AcSIR), Ghaziabad 201002, India

Published online: 19 December 2024

lead to the development of the point-of-care (POC) testing method for analyzing TSH [1, 2, 6]. There are many POC electrochemical biosensors for sensitive estimation of TSH. However, the electrochemical sensors have the limitations of passivation, and instability also it gets influenced by environmental factors [7]. The paper-based sensors could beat the limitations of electrochemical sensors but these are mainly qualitative and require the use of high-end techniques for the quantitative estimation. Also, the commercially available TSH testing kits are qualitative and only used for the detection of hypothyroidism; however, due to low TSH levels in hyperthyroidism, there are no LFAs for detection of hyperthyroidism based on TSH [3]. Therefore, there is an imperative need to develop ergonomic and sensitive paper-based devices for the estimation of both hypothyroidism and hyperthyroidism based on TSH levels, which can eventually modified to sense other biological markers, too.

POC paper-based nano biosensors, mainly lateral flow assay (LFA), are gaining more importance these days due to their rapidity, sensitivity, selectivity, cost-effective, robust and user-friendly nature [2, 8–11]. The LFA test strips can identify and quantify varieties of analytes in intricate mixtures [10], where the sample is added to a test device, and the outcomes are demonstrated in less than 30 min [11]. However, the principle on which LFAs work is competitive or sandwich assays [12]. Nanoparticles are majorly used as labels for LFAs like gold nanoparticles (AuNPs), latex beads, quantum dots, upconversion nanoparticles, liposomes, magnetic nanoparticles, etc., [8, 12–14]. However, these labels, apart from AuNPs, carry disadvantages: low sensitivity, photobleaching, instability, and batch-to-batch variations [13, 14], generating the need for more efficacious labels for LFA. Jeong et al. have prepared LFA for the assessment of TSH using fluorescent dye (Alexa Fluor 647) as a label. They have noted a LOD of 1μIU/mL [1]. However, this LOD is quite high, so it cannot determine hyperthyroidism. This might be due to the less sensitive nature of the label due to photobleaching [13]. Similarly, Znoyko et al. have designed LFA for TSH estimation using magnetic nanoparticles as a label [15]. However, the magnetic nanoparticles LFAs require prolonged detection time, and the problem of excessive magnetic enrichment is also associated with them [16]. Further, it involves the use of specific magnetic readers for quantification [12]. AuNPs are commonly explored labels for colorimetric detection of analytes [2, 10]. It was inferred that GNRs and gold nanoshells may enhance the sensitivity of LFAs compared to spherical gold nanoparticles when their optical and thermal contrast detection were compared [11]. Bikkarolla et al. prepared LFA for TSH sensing using 150 nm gold nanoshells as labels, which could detect both hypothyroidism and hyperthyroidism [2]. But, it is difficult to achieve the reproducibility and maintain the stability of gold nanoshells [17], which could affect their sensitivity.

Gold nanorods (GNRs) possess promising optical properties, their surface can be modulated with ease as well as they are biocompatible. These attributes make them superlative agents for disease imaging and sensing [18]. GNRs comprise of two SPR bands, corresponding to a transverse (short axis) and a longitudinal (long axis) band [19–21]. GNRs are well-versed in properties like strong scattering ability, less plasmon damping, and LSPR, which makes them a perfect sensing nanomaterial. The LSPR spectrum changes with the change in the aspect ratio (AR) and refractive index of the surroundings of GNRs [21, 22]. This is one of the major properties that enable GNRs to sense the specific target binding actions [19–21]. Moreover, GNRs show a diverse color range with various aspect ratios when in colloidal suspension [23], which makes them a suitable colorimetric label for LFA.

There are many methods for the synthesis of GNRs; however seed-facilitated growth method is the most preferred [20, 24]. Although, in other methods, precise control of different parameters is difficult, which may cause the quality of the gold nanorods to fluctuate, the operation is also very complex as well as the output is relatively low [25]. Besides this, the surface functionalization of GNRs is necessary to explore them for various applications [26]. Four major ways are currently adopted to functionalize GNRs with specific biomolecules for multiple applications. The ways are direct ligand exchange, layer-by-layer self-assembly, surface coating method, and biofunctional linkers [24, 27], which could be employed to design GNR-based labels for LFAs.

Considering the significant edge of GNRs over AuNPs, we have done a proof of concept study to demonstrate GNRs as a competent label for LFAs. The study also aimed to develop a user-friendly LFA, which could potentially determine both hypothyroidism and hypothyroidism without engaging any techniques for quantification. To the best of our knowledge, rod-shaped gold nanoparticles have not been exercised as labels for LFA to sense TSH, although many other types of sensors have employed GNRs for TSH estimation. We implemented a systematic study to design functionalized GNRs as a label for LFA. We investigated several factors that play a role in synthesising GNRs using the seed-mediated growth method. Subsequently, the surface alteration of GNRs was achieved by replacing hexadecyltrimethylammonium bromide (CTAB) with 11-mercaptoundecanoic acid (11-MUA), which also acted as a linker for attaching a TSH antibody with covalent peptide linkage. This robust and stable functionalized GNRs served as an effective label for sensitive and selective detection of TSH. Thus, the study introduced clinically practical and simplified

LFA for monitoring hypothyroidism and hyperthyroidism qualitatively and semi-quantitatively. Remarkably, with further refinement and thorough real-sample studies, the clinical adaptation of the device could be achieved.

2 Materials and methods

2.1 Materials

All chemicals or reagents were commercially available and used as received. Gold (III) chloride trihydrate ($HAuCl_4.3H_2O$), Hydrochloric acid (HCl), 11-Mercaptoundecanoic acid (11-MUA), Boric acid, L-Ascorbic acid (AA), N-(3-Dimethylaminopropyl)-N'-ethyl carbodiimide hydrochloride (EDC), Tween 20, CTAB, Carbonate-Bicarbonate Buffer, Sodium tetraborate decahydrate ($Na_2B_4O_7{\cdot}10H_2O$), Sodium azide (NaN_3), Silver nitrate ($AgNO_3$), Bovine Serum Albumin (BSA), Sodium dodecyl sulfate (SDS), TSH from human pituitary, Anti-Mouse IgG (whole molecule) antibody produced in goat, FSH from human pituitary, LH from human pituitary, hCG, Phosphate Buffered Saline pH 7.4 Sterile (PBS), Sucrose and N-hydroxysulfosuccinimide sodium salt (NHS) were purchased from Sigma-Aldrich Chemicals Private Limited (USA). Sodium borohydride ($NaBH_4$), Sodium hydroxide (NaOH) and Sodium chloride (NaCl) were bought from HiMedia Laboratories Private Limited (India). Mouse Monoclonal TSH antibody (10–2429) and Mouse Monoclonal TSH antibody (10–2427) were purchased from Fitzgerald Industries International (USA). The sample pad (Whatman MF1), test pad (Nitrocellulose membrane, Whatman FF120HP), absorbent pad (Whatman CF4) and conjugate pad (Whatman standard 14) were procured from Cytiva (USA). Ultrapure de-ionized (DI) water (18 MΩ) was utilized to make all solutions. Entire procedures were conducted at room temperature unless specified otherwise. All experiments are performed in triplicates. Graphs were plotted using Origin software and GraphPad Prism was used for statistical analysis.

2.2 Synthesis of GNRs

GNRs were synthesized by seed-mediated growth method [28]. It is a two-step protocol. In the first step, 3–5 nm gold nanoseeds were synthesized using $HAuCl_4.3H_2O$ (0.5 mM) and CTAB (0.2 M). These $HAuCl_4.3H_2O$ and CTAB were mixed in a 1:1 v/v ratio and kept under stirring at room temperature (RT) for some time. Following this, 600 µL freshly prepared and ice-cold $NaBH_4$ (10 mM) was added to the mixture while stirring dropwise. Further stirring was carried on for 2 min and after that, the prepared seeds were left at RT for some time. This is known as seed aging. However, in the second step, 5 mL $HAuCl_4.3H_2O$ (0.5 mM), 5 mL CTAB (0.2 M) and 200µL $AgNO_3$ (4 mM) were mixed. To this mixture, then 70 µL, 78.8 mM AA was added, which led to the transition of the orange-yellow color of the mixture to colorless. Further, 12 µL seed was added to the mixture and kept at 31 °C. The color change of the growth solution gradually changed in 10 to 20 min. To separate the GNRs, the mixture was centrifuged twice at 12,000 rpm for 15 min.

2.3 Effect of different factors on GNRs synthesis

The effect of $HAuCl_4.3H_2O$ concentration (0.25 mM, 0.5 mM, 1 mM, 2 mM, 4 mM and 8 mM), CTAB concentration (0.1 M and 0.2 M), $AgNO_3$ concentration (2 mM, 4 mM, 6 mM, 8 mM and 10 mM), $AgNO_3$ volume (100, 150, 200, 250 and 300 µL), AA volume (65, 70, 75, 80 and 85 µL), seed aging time (5 min, 15 min, 30 min, 45 min and 1 h), seed volume (6, 12, 18, 24 and 30 µL), pH (2, 3, 4, 5, 6, 7, 8, 9, 10 and 11) and time (30 min, 1, 2, 4, 6, 8, 10, 12, 14, 16, 18, 20, 22 and 24 h) in controlling the size and shape of GNRs were studied. It was assessed on the basis of their LSPR spectrum and zeta potential analysis. The experiments were done by varying one factor at a time by keeping other factors constant.

2.4 Surface modification of GNRs

The CTAB from the GNR surface was replaced by 11-MUA using the pH-mediated method reported by Cao et al. [21]. Briefly, 20 mM 11-MUA solution was prepared by dispersing MUA in water, then dropwise 0.2 M NaOH solution was added to it under stirring, followed by sonication. This was repeated until the MUA dissolved. Now, to 5 mL GNRs suspension, 2 mL 11-MUA was incorporated under vigorous stirring and the reaction was continued till 24 h. Lastly, the MUA-modified GNRs were purified by centrifugation 2 times at 8000 rpm for 20 min. The surface-modified GNRs were resuspended in pH 9 borate buffer (0.01 M). Also, certain conditions for the surface modification of GNRs were optimized. This includes the volume of 11-MUA, stirring speed and time.

2.5 Attachment of detection antibody on MUA-GNRs to form label for LFA

Mouse Monoclonal TSH antibody (10–2427) was covalently attached to the surface of MUA-GNRs by the EDC/NHS method [21]. Herein, 20 µL of EDC (0.05 M) and 20 µL of NHS (0.1 M) were added to 1 mL MUA-GNRs and vortexed for 25 min to stimulate the -COOH group of 11-MUA. Further to this mix, 50 µL of 2 mg/mL TSH antibody was added and vortexed gently. Subsequently, after 1 h

incubation, the antibody functionalized GNRs (Ab-GNRs) were separated by centrifugation at 8000 rpm for 20 min and it was cleaned twice with the washing buffer comprised of pH 9 borate buffer (0.01 M) with 1% BSA and also resuspended in the same and stored at 4 °C. The washing buffer also blocks the surface of GNRs so that nonspecific binding can be prevented. Further, the binding efficiency of the antibody on GNRs was determined by the Bradford assay [29].

2.6 Characterization

The LSPR spectrum was recorded by a UV-visible spectrophotometer (Lambda 750, PerkinElmer). The electrostatic stability and surface charge of GNRs were represented by zeta potential value, which was determined by particle size analyzer, Malvern Zetasizer Pro (Malvern Panalytical, UK) at 25°C. All the samples were evaluated in triplicate, and three independent measurements were noted for every sample. The morphology, elemental evaluation (Energy dispersive X-ray (EDX) spectrum), crystallinity (selected area electron diffraction (SAED) pattern) and d-spacing of GNRs were ascertained by High-resolution transmission electron microscopy (HRTEM) on JEOL-JEM-F200. The samples were prepared by drop-casting the GNRs suspension on a 200-mesh carbon-coated copper grid and air-dried. The scanning transmission electron microscopy (STEM) function of HRTEM was used to map the elements. Field-emission scanning electron microscopy (FESEM) (FEI NOVA NANOSEM 450) was also employed to characterize GNRs. FTIR spectra were recorded to determine the presence of functional groups on GNRs. The infrared spectral profiles were recorded on Tensor 27 (Bruker) in the wavenumber range of 4000–600 cm^{-1}. Further, elemental analysis was confirmed by X-ray photoelectron spectroscopy (XPS) (XPS - K ALPHA, Thermo Fisher Scientific Instruments) by preparing a thin film of samples on a silicon wafer. X-ray diffraction (XRD) analysis was undertaken to validate the crystallinity of GNR using an 'X' Pert Pro powder XRD (PANalytical) by using the freeze-dried powder of GNRs.

2.7 Sensitivity and selectivity of the label to detect TSH

The sensitivity of labels (Ab-GNRs) to detect TSH was determined by the red shift in the longitudinal SPR band of the GNRs [20]. More shift means more binding of TSH. Herein, 500 µL of Ab-GNRs was mixed with different concentrations of 50 µL TSH (0.01, 0.05, 0.1, 0.5, 1, 5, 10, 15 and 20 µIU/mL) and kept to react for 20 min. Further, the mixture was centrifuged at 8000 rpm for 15 min and the pellet was resuspended in 500 µL DI water to record the LSPR spectrum [30]. Additionally, the shift in longitudinal SPR was also tested by using FSH, LH and hCG hormones to determine the selectivity of conjugate towards TSH.

2.8 Preparation of LFA

The protocol reported by Parolo et al. was used to prepare LFAs [12]. The procedure involves the preparation of the test line and control line on the test pad by using the dispenser (SS Easy Printer, LPM-02) and drying them at 37 °C in a dehumidified environment. After that, the sample pad was soaked in a specific blocking buffer and dried for 2 h at 37 °C. Then, the conjugate pad was prepared by spraying the conjugate (Ab-GNRs) and subsequently drying it. Before spraying the conjugate, it was dispersed conjugate buffer which comprised of BSA and sucrose. Finally, these pads were mounted together, and 4 mm strips were cut using a cutter (SS Programmable Strip Cutter Model M-70) and mounted on a backing cassette. The LFA strips were stored in a moisture-free environment. Furthermore, various LFA working conditions were optimized. Firstly, the label's optical density (OD) to be sprayed on the conjugate pad was optimized by varying it from 5 to 20 OD. Following that, the concentration of the capture antibody, i.e., mouse monoclonal TSH antibody (10–2429), was optimized to prepare the test line. 1–3 mg/mL of capture antibody was used for this. Further, to optimize the sample volume, 30, 40 and 50 µL of a specific concentration of TSH was added and the intensity of color formation at the test line was observed through the naked eye. Finally, the LFA's performance was tested using TSH procured from Sigma-Aldrich. For this, different concentrations of TSH (0.01 µIU/mL to 20 µIU/mL) were prepared in the assay buffer and added to the sample loading area of LFA. After 10 min, the color intensity at the test line was assessed qualitatively.

2.9 Selectivity testing of LFA

The selectivity of the prepared LFA was tested by adding 50 µL of FSH (15 mIU/mL), LH (25 mIU/mL) and hCG (100 mIU/mL) hormones on the LFA and the color development at the test line was assessed.

3 Results and discussion

3.1 Synthesis and effect of various factors on synthesis of GNRs

The foremost purpose of the study was to prove that GNRs can be employed as a label in paper-based LFAs for colorimetric detection of the analyte. For this, we have comprehensively studied the factors that control the synthesis and

functionalization of GNRs, which subsequently aided in the preparation of stable GNR-based bioconjugates or labels for LFA. GNRs were synthesized by seed-mediated growth method, which was divided into 2 steps. First is the formation of seed (3–5 nm) [18] gold nanoparticles, followed by the incorporation of these seeds into the growth solution, which helps in the formation of rod-shaped gold nanoparticles [28].

On varying the $HAuCl_4.3H_2O$ concentration, it was found that at 8 mM $HAuCl_4.3H_2O$, the spherical gold nanoparticles were formed as only one SPR band appeared and at lower concentrations, 0.25 mM and 0.5 mM, the particles were not of proper rod shape, confirmed by the undifferentiated SPR bands. This result was in line with the findings of Boyne et al., where, as the concentration of $HAuCl_4.3H_2O$ increased, there was a plasmonic blue shift in the longitudinal SPR band of GNRs [31]. An equivalent trend was witnessed in this study from 1 mM $HAuCl_4.3H_2O$ concentration. At 1mM concentration, a well-defined LSPR spectrum of GNRs with longitudinal SPR at the highest wavelength was observed (Fig. 1a). Further, it was found that CTAB concentration also holds a vital role in the production of GNRs. At 0.1 M CTAB, the longitudinal SPR band was observed at a significantly lower wavelength compared to the 0.2 M concentration (Fig. 1b and Fig. S1a). Conclusively, at 0.1 M, shorter rods with more spherical particles formed. Although, the higher concentration of CTAB leads to the formation of more cylindrical particles [32]. The other major contribution in controlling the AR of GNRs was given by $AgNO_3$. Silver ions (Ag^+), after binding with bromine of CTAB form AgBr, these AgBr were deposited favorably on the lateral faces of GNRs, which averts the deposition of gold on the side faces, leading to the formation of rod shape. AgBr also controls the growth of GNRs and enhances their stability [18, 24, 27, 33]. After varying the $AgNO_3$ concentration, a longitudinal SPR band at the highest wavelength was found at 4 mM $AgNO_3$ concentration; however, based on the statistical unpaired t-test, there was no significant difference between the wavelength of longitudinal SPR bands of GNRs at 4 mM and 6 mM concentrations (Fig. 1c and Fig. S1b). Interestingly, as the concentration of Ag^+ rises, the size of GNRs increases but up to a specific limit; after that, the trend reverses [28], which was also seen in our findings. After 6 mM $AgNO_3$ concentration, there was a blue shift in the longitudinal SPR bands of GNRs (Fig. 1c). Similarly, on changing the volume of $AgNO_3$ at its 4 mM concentration, there was a significant shift in the longitudinal SPR band, mainly up to 250 µL $AgNO_3$ due to the increase in the aspect ratio of GNRs but after it, based on statistical unpaired t-test, the increase in wavelength of the longitudinal SPR band was non-significant (Fig. 1d and Fig. S1c).

Further, the role of AA was also studied. AA is a weak reducing agent that reduces Au^{3+} to Au^+. Subsequently, the complete reduction of Au^+ to Au^0 was undertaken by seeds [34, 35]. Herein, we have not found any specific trend of change of the longitudinal SPR band on increasing volume of AA, although the maximum longitudinal SPR was found at 75 µL of AA (Fig. 1e). However, based on an unpaired t-test, there was no significant difference in the longitudinal SPR band at 70 and 75 µL of AA (Fig. S1d). It was also observed that the absorbance, i.e. the yield of GNRs, increased on increasing the volume of AA (Fig. 1e). This was corroborated by the study by John et al. [35]. Increasing the volume of AA would significantly increase the reaction rate, resulting in more reduction of Au^{3+} to Au^+ [36]. Moreover, in the presence of sufficient AA only, the gold seed could reduce Au^+ to Au^0 [35]. Thus, as the volume of AA increased, the reduction of Au^{3+} augmented, leading to an increased yield of GNRs. Furthermore, the role of seed volume was studied. Multiple studies suggest that as the number of seeds increases, the AR of GNRs decreases, leading to shorter nanorods [34, 37]. Contrarily, we have found an increase in longitudinal SPR wavelength after 6 µL seed volume (Fig. 1f). Although, based on the statistical unpaired t-test, the change in longitudinal SPR wavelength was non-significant from 12 to 30 µL of seed (Fig. S1e). Also, it was noticed that as the seed volume increased, the absorbance of the longitudinal SPR band decreased, resulting in a reduction of the yield of GNRs (Fig. 1f).

Notably, pH holds a vital role in the synthesis of GNRs; under acidic pH, the reduction potential of AA is low and higher in the basic pH. The lower reduction potential of AA is essential for rod formation [33]. Also, at alkaline pH, CTAB molecules are desorbed from the gold surface [18]. So, the pH above 6.6 does not support rod formation [32]. It was found that with the decrease in pH, the aspect ratio of GNRs increases [18, 38]. Thus, a similar trend was detected in the study when the pH was varied from 2 to 11. Also, above 6 pH, the LSPR spectra of GNRs did not show appropriately differentiated transverse and longitudinal SPR bands (Fig. 1g). The unpaired t-test results on varying the pH were given in Fig. S1g. Furthermore, the effect of time on the generation of GNRs was evaluated. Based on a statistical unpaired t-test, it was found that till 8 h, there was no significant change in the wavelength of the longitudinal SPR band, but after that, substantial change was observed in the longitudinal SPR wavelength (Fig. 1h and Fig. S1h). However, the synthesis of well-defined gold nanorods was observed at 2 h. Based on one-way ANOVA, it was also found that seed aging time does not significantly affect the aspect ratio of GNRs (Fig. 1i and Fig. S1f), although all the other parameters had a significant effect (Fig. S1a-h).

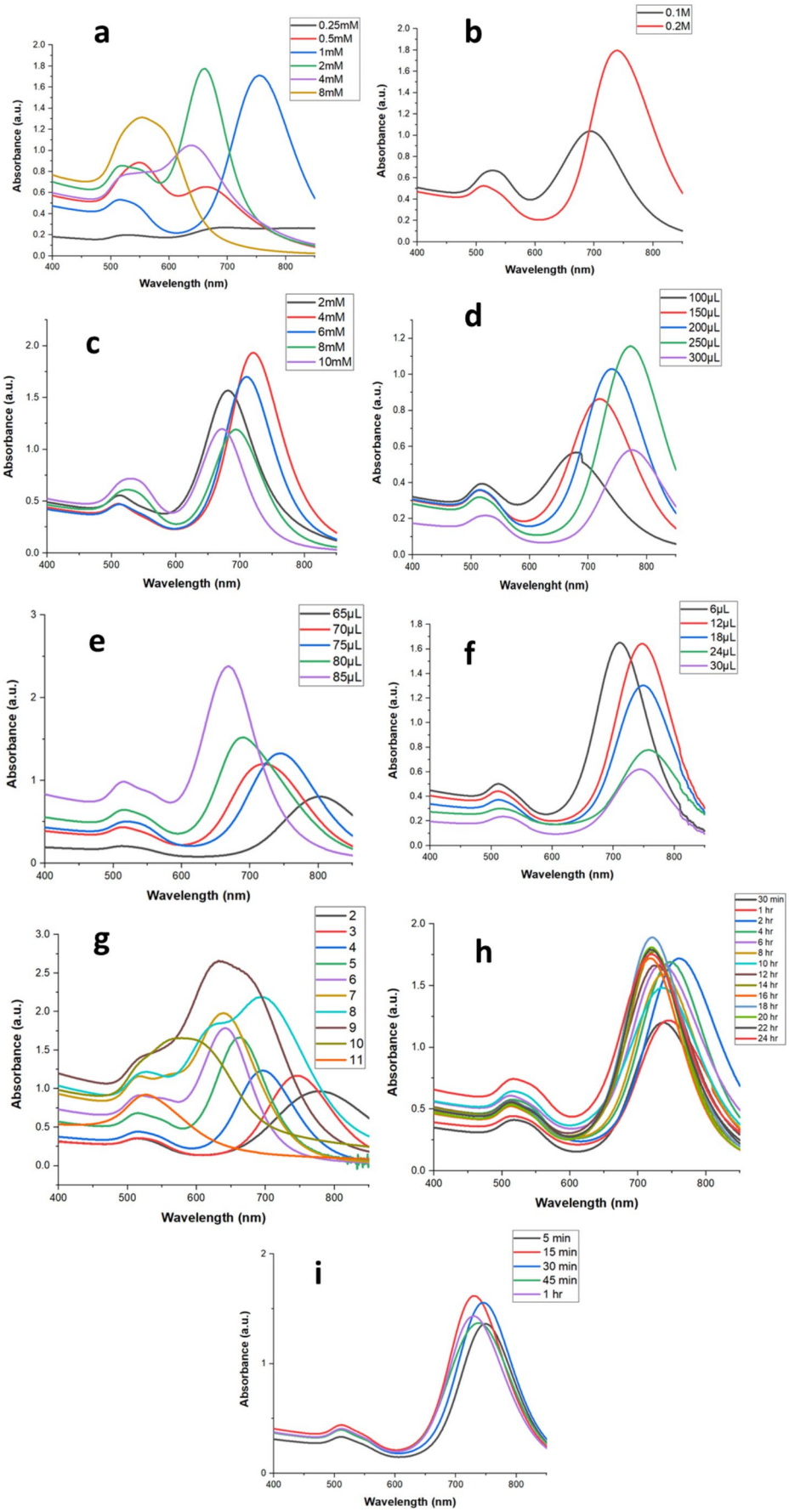

Fig. 1 Effect of various factors on longitudinal SPR band of GNRs. **a** $HAuCl_4.3H_2O$ concentration, **b** CTAB concentration, **c** $AgNO_3$ concentration, **d** 4 mM $AgNO_3$ volume, **e** AA volume, **f** Seed volume, **g** pH, **h** Time and **i** Seed aging time

Simultaneously, the zeta potential was found to be very stable (above +40mV) while studying the effect of all the factors. Therefore, based on one-way ANOVA, any of these factors, except $HAuCl_4.3H_2O$ concentration, do not affect the zeta potential of GNRs significantly (Fig. S2a-i). Finally, based on the effect of each factor on morphology, size and aspect ratio on GNRs, 1 mM $HAuCl_4.3H_2O$, 0.2 M CTAB, 250 µL $AgNO_3$ (4 mM), 75µL AA and 12µL seed aged for 30 min was used to synthesize GNRs of aspect ratio around 3.8 in 2 h (pH 3). These GNRs were further employed to prepare bioconjugate for LFA-based detection of TSH.

3.2 Surface modification and optimization of various factors for modification of GNRs

The CTAB bilayer on the surface of earlier synthesized GNRs needed to be replaced by 11-MUA for further functionalization of GNRs. CTAB is toxic in nature as well as it blocks the binding of biomolecules on GNRs which affects the performance of GNRs for sensing applications. Herein, the ligand exchange strategy was used to swap CTAB from the boundaries of nanorods. 11-MUA binds with gold with its sulfur (S) group and the carboxyl (-COOH) group at the other end can be used to form a covalent linkage with other biomolecules such as antibodies, peptides, etc. [23, 39]. After the modification of GNRs with 11-MUA, the transverse SPR band remains unaffected; however, the red shift in the wavelength of the longitudinal SPR band was detected. It was due to the variation in the refractive index of the surroundings after surface modification [23]. The zeta potential of MUA-modified GNRs (MUA-GNRs) was changed from positive to negative due to the -COOH group of 11-MUA. This change in charge of zeta potential was one of the confirmations of ligand exchange, which was in agreement with the findings of other studies [40, 41].

3.2.1 Optimization of surface modification conditions

The various surface modification conditions were optimized. Initially, the volume of 11-MUA used to modify 5 mL of GNRs was optimized based on its effect on the longitudinal SPR band shift and zeta potential. At 2 mL 11-MUA, the maximum red shift was observed in the longitudinal plasmon wavelength (LPW) of GNRs (Fig. 2a). Also, based on the unpaired t-test, there was a significant difference in the red shift of LPW between 2 mL and 3 mL 11-MUA. Contrarily, the red shift was insignificant between 1 mL and 2 mL, but the absorbance was very low at 1 mL 11-MUA; hence, 2 mL 11-MUA was optimized for surface modification of GNRs (Fig. S3a). Notably, the amount of 11-MUA was found to be an essential factor in controlling the modification of GNRs. Further, on varying the stirring speed for MUA-GNRs preparation, a significant maximum red shift was observed in the LPW of GNRs at 800 rpm, so the stirring speed was optimized at 800 rpm (Fig. 2b and Fig. S3b). Interestingly, the red shift decreased at 900 rpm. Therefore, stirring speed plays a significant role in the surface alteration of GNRs with 11-MUA. Lastly, the time was optimized at 8 h; however, this factor significantly affected the LPW red shift of GNRs (Fig. 2c and Fig. S3c). The maximum shift was attained at 12 h, but as there was no significant difference between 12 h and 8 h, to keep it economical, 8 h was fixed as a time for surface modification of GNRs. At optimized parameters, the final red shift in LPW of GNRs after MUA modification was found to be around 20 nm ± 4 nm (Fig. 3a), which was congruent with the concept that the component of greater refractive index was attaching on the surface of GNRs by replacing CTAB [41].

Fascinatingly, the zeta potential at every point in the optimization of various surface modification conditions of GNRs was above − 30 mV, suggesting the tremendous electrostatic stability of MUA-GNRs along with the confirmation of the surface modification (Fig. S4a-c).

3.3 Attachment of TSH-antibody on MUA-GNRs to form Ab-GNRs

The TSH-antibody was covalently attached to the MUA-GNR by forming a covalent peptide bond between the terminal -COOH group of 11-MUA and the amine ($-NH_2$) group of antibody [20, 21]. Moreover, the covalent conjugation of antibodies not only encourages proper orientation of antibodies as well as enhances the sensitivity of antigen and antibody binding, thus leading to more sensitive detection of any antigen [42]. Here, the -COOH group of 11-MUA was stimulated by carbodiimide chemistry (EDC/NHS), which subsequently generated NHS ester. This activated-NHS ester crosslinker reacts with the $-NH_2$ group of antibodies, resulting in the covalent functionalization of GNRs with TSH antibodies by forming peptide bonds [21, 43]. The antibody conjugation promotes a red shift of the longitudinal SPR band of the MUA-GNRs. The red shift of 41 nm ± 3 nm was detected after the attachment of the TSH antibody on MUA-GNRs (Ab-GNRs) (Fig. 3a). This shift was an outcome of the alteration in dielectric properties around the surface of GNRs [19]. Although, the transverse SPR band of Ab-GNRs remained unchanged. This finding was corroborated by the findings of some studies [21, 44]. BSA blocked the unoccupied sites by the antibodies on the surface of Ab-GNRs to avoid nonspecific binding, resulting in the formation of a functionalized label or bioconjugate (Ab-GNRs) to prepare LFA for TSH detection.

Furthermore, the zeta potential of Ab-GNRs was decreased compared to the zeta potential of MUA-GNRs,

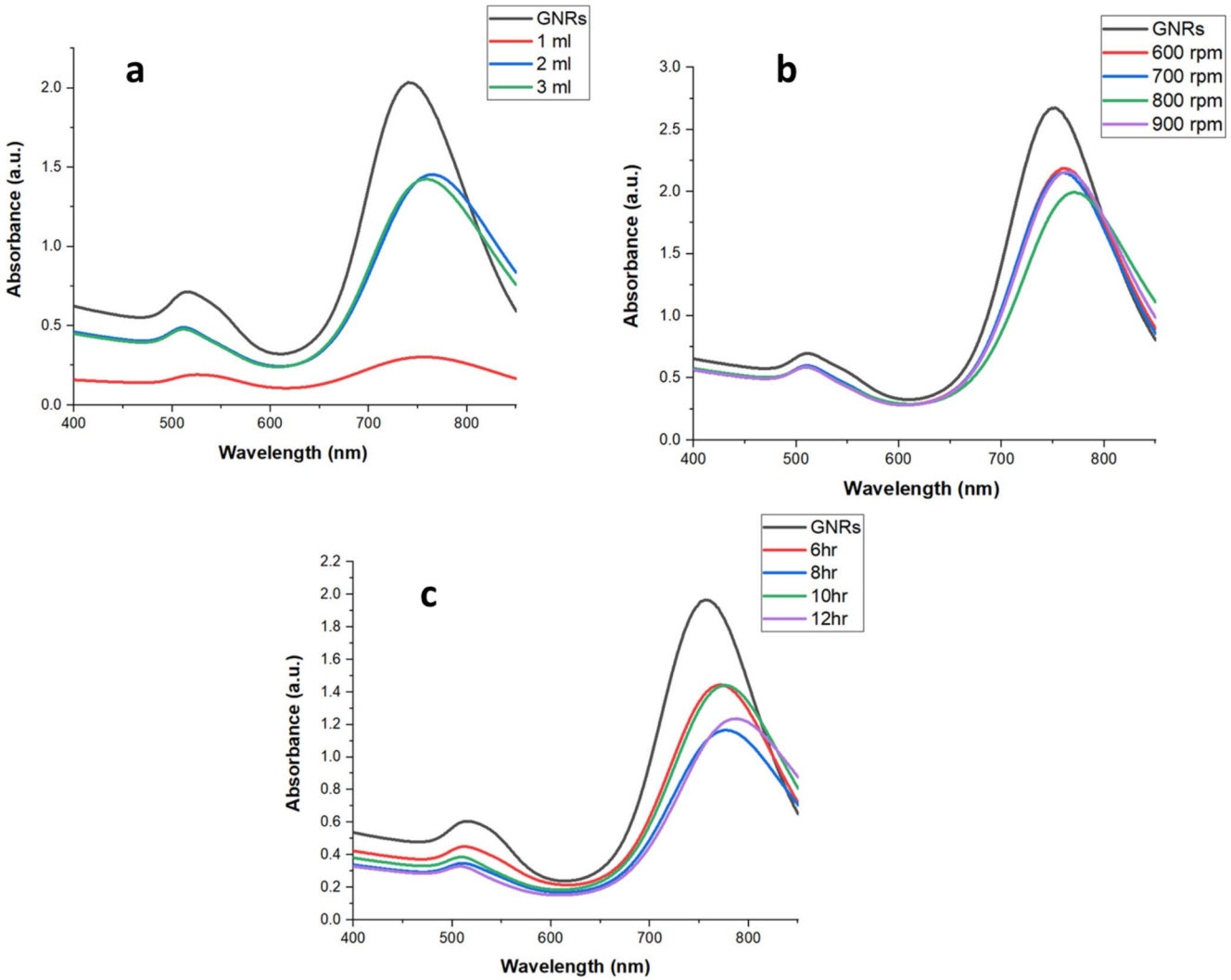

Fig. 2 Effect of various factors on red shift of LPW of GNRs after surface modification with 11-MUA. **a** 11-MUA volume, **b** Stirring speed and **c** Time

which also confirms the conjugation of antibodies (Fig. 3b). However, it was less than −30 mV but still, the bioconjugate was stable because functionalization biomolecules provide steric stability to the GNRs [45]. Further, the insignificant change in the LPW (Fig. 3c) and zeta potential of Ab-GNRs till 15 days (Fig. 3d) confirmed the stability of Ab-GNRs for 15 days at 4 °C in washing buffer, which also contains 5%w/v sucrose [46], which was more than enough for preparing LFA. The binding efficiency of TSH antibody on MUA-GNRs was determined by Bradford assay [47], where BSA was used to plot the standard curve. The binding efficiency of TSH-antibody was found to be 83.38 ± 0.34%.

3.4 Characterization

3.4.1 UV-visible-NIR (near infrared) spectroscopy and zeta potential analysis

The synthesized GNRs had shown longitudinal SPR at 751 nm. This longitudinal SPR was red-shifted to 773 nm after 11-MUA modification; further, after conjugation of the TSH antibody, the band again shifted to 814 nm, confirming the successful functionalization of GNRs to form a bioconjugate for LFA. However, there was no significant shift in the transverse SPR band. It was observed around 512 nm (Fig. 3a). The zeta potential study reveals information about the surface charge of the nanoparticles. The GNRs have zeta potential + 49.98 ± 6.29 mV, and the positive charge was due to CTAB. Further, after 11-MUA modification, MUA-GNRs showed zeta potential − 36.53 ± 2.96 mV. This

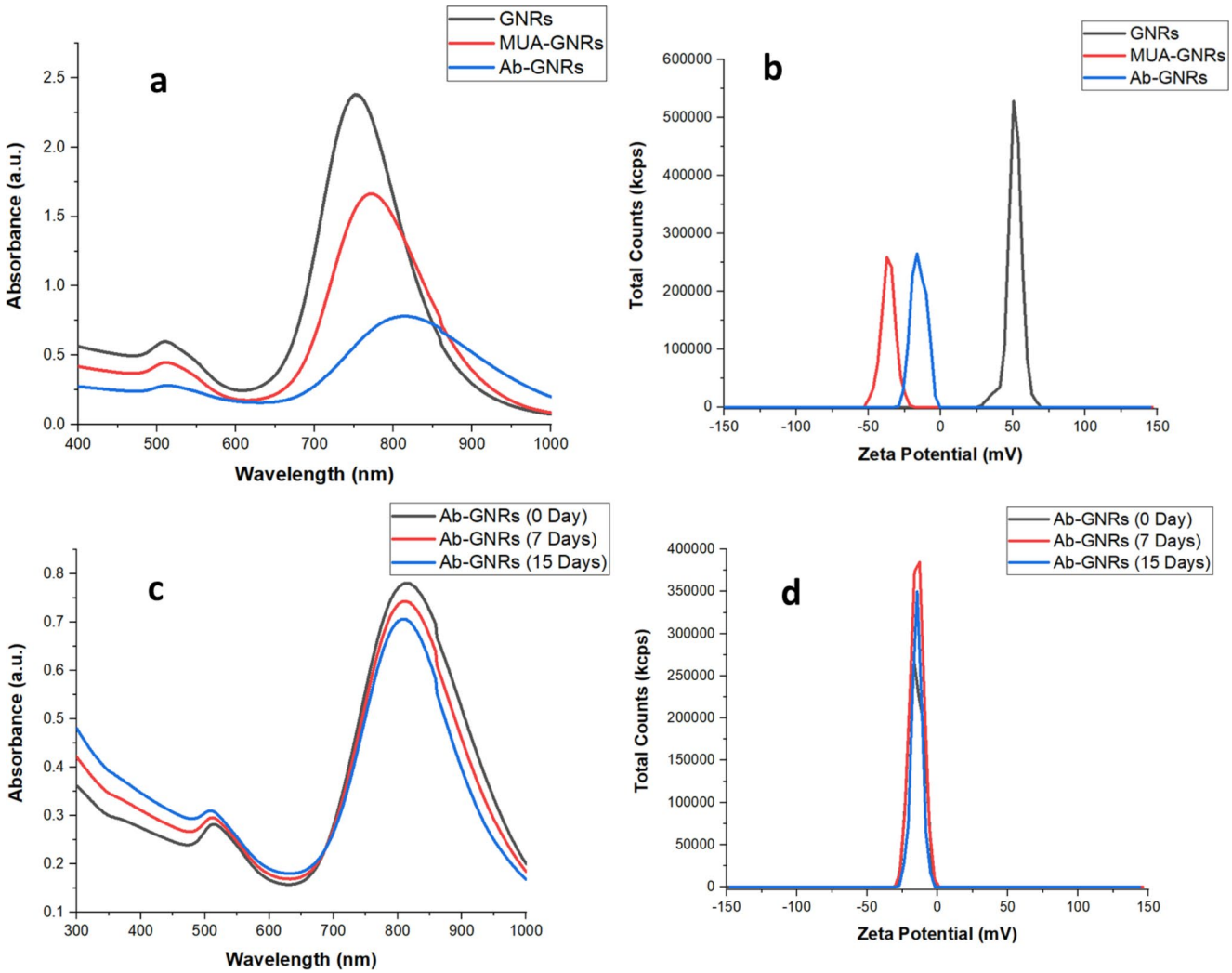

Fig. 3 (**a**) UV-visible-NIR spectra of GNRs, MUA-GNRs and Ab-GNRs at optimal conditions (**b**) Zeta potential of GNRs, MUA-GNRs and Ab-GNRs. Stability studies of Ab-GNRs, (**c**) UV-visible-NIR spectra of Ab-GNRs at various time points and (**d**) Zeta potential of Ab-GNRs at various time points

change of zeta potential from positive to negative also confirms the surface alteration of GNRs with 11-MUA. Finally, the Ab-GNRs showed a zeta potential -15.14 ± 0.78 mV (Fig. 3b). Our findings of zeta potential were consistent with the reported values [41, 47, 48]. The decrease in zeta potential after antibody conjugation also confirms the functionalization with antibodies.

3.4.2 Electron microscopy analysis

Based on HRTEM analysis, the size of GNRs, MUA-GNRs and Ab-GNRs was found to be 41.72 ± 5 nm x 11 ± 2 nm, 42.97 ± 3.23 nm x 11.9 ± 1.76 nm and 43.56 ± 5.16 nm x 11.59 ± 1.93 nm, respectively (Fig. 4a-c). These findings were in agreement with the FESEM analysis (Fig. S5a-c). Further, the SAED patterns were also obtained by using HRTEM, confirming the crystalline nature of GNRs, MUA-GNRs and Ab-GNRs (Fig. 4d-f) [49, 50]. The fringes of GNRs, MUA-GNRs and Ab-GNRs were captured by HRTEM (Fig. S6a-c). The spacing between the fringes was found to be in agreement with the other studies [51, 52]. The XRD pattern of GNRs is given in Fig. S6d. The peaks at 2Θ values 38.24°, 44.46°, 64.69° and 77.66° correspond to planes (111), (200), (220) and (311), respectively (Fig. S6d). This result was also similar to the earlier reported values [53, 54].

3.4.3 Elemental analysis

EDX spectra of GNRs, MUA-GNRs, and Ab-GNRs were obtained using HRTEM. The GNRs spectrum showed the presence of gold (Au), carbon (C) and bromine (Br) (Fig. S7a). The Br was due to the CTAB [54, 55]. However, the EDX analysis also confirms the modification of GNRs with

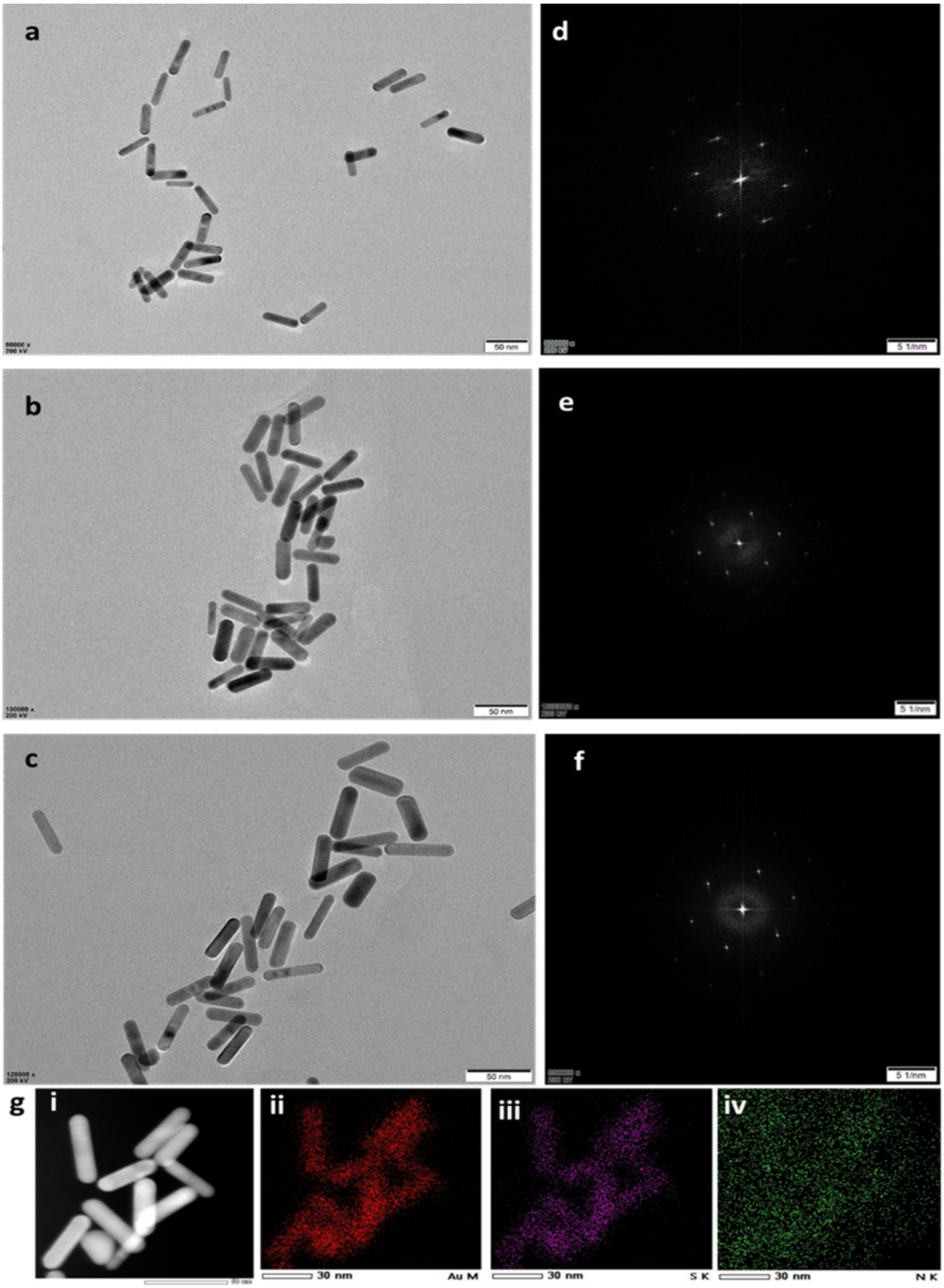
a
50 nm
d
5 1/nm
b
50 nm
e
5 1/nm
c
50 nm
f
5 1/nm
g
i
ii
30 nm
Au M
iii
30 nm
S K
iv
30 nm
N K

Fig. 4 (**a**) HRTEM image of GNRs, (**b**) HRTEM image of MUA-GNRs, (**c**) HRTEM image of Ab-GNRs, (**d**) SAED pattern of GNRs, (**e**) SAED pattern of MUA-GNRs, (**f**) SAED pattern of Ab-GNRs and (**g**) (i) STEM image and mapping of Ab-GNRs showing (ii-iv) gold (Au), sulfur (S) and nitrogen (N)

11-MUA, because, in unmodified GNRs, there was the presence of bromine (Br) due to CTAB, but in MUA-GNRs, there was the presence of sulfur (S) instead of Br (Fig. S7b). Further, the EDX analysis of Ab-GNRs showed the presence of sulfur (S), nitrogen (N), carbon (C), oxygen (O) and gold (Au) (Fig. S7c). The presence of nitrogen in the spectrum of Ab-GNRs confirms the presence of antibodies on GNRs. The copper (Cu) was present in the spectrum due to the copper grid used for the analysis. Further, the elements were also determined by the STEM mapping of Ab-GNRs, which showed the presence of Au, S and N (Fig. 4g). The XPS studies further supported the findings of EDX and STEM mapping analysis.

XPS spectra of all the types of GNRs showed the dual peak located around 83.98 eV and 87.68 eV corresponding to transitions Au $4f_{7/2}$ and Au $4f_{5/2}$ of Au^0 oxidation state, respectively (Fig. 5a-d) [56]. The spectrum of GNRs showed the signal for Br 3d, Br 3p and Br 3s (Fig. 5a and b), C 1s and N 1s (Fig. 5a) due to the presence of CTAB on their surface. However, the peaks of Br were not detected in the spectrum of MUA-GNRs; instead, due to the Au-S bond, the peak of S 2p (Fig. 5c) was found, confirming the replacement of CTAB by 11-MUA [41, 56–58]. Further, the antibody attachment on the surface of MUA-GNRs was confirmed due to the occurrence of S 2p and N 1s signals in the spectrum of Ab-GNRs (Fig. 5a and d). The S 2p signal was due to the 11-MUA, whereas the N 1s signal may be due to the amine group of antibodies because the N 1s signal was absent in the MUA-GNRs spectrum. This XPS study confirmed the successful functionalization of TSH antibodies on the surface of MUA-GNRs.

3.4.4 FTIR analysis

FTIR analysis helps to find the functional groups on the surface of GNRs. The CTAB-coated GNRs exhibited solid symmetric and asymmetric C-H stretching at 2916 and 2853 cm^{-1}; along with this, a C-H scissoring was also observed between 1430 and 1470 cm^{-1}, which corresponds to the hydrocarbon portion of CTAB [41, 59–61]. The band at 1729 cm^{-1} in GNRs could be due to the carboxyl groups [61]. The bending of more than 4 adjacent CH_2 groups was observed at 726 cm^{-1} (Fig. 6) [41, 59, 60]. In the FTIR spectrum of MUA-GNRs, the broad and sturdy O-H absorptions were detected due to the 11-MUA between 3200 and 3600 cm^{-1}. Additionally, C-H stretching was seen around 2900 cm^{-1}. Also, the sturdy C=O and C-O stretching approaches were detected at 1714 cm^{-1} and 1055 cm^{-1}, respectively, corresponding to 11-MUA [41, 62]. Remarkably, the peak at 702 cm^{-1} was due to the C-S stretching (Fig. 6) [56]. Furthermore, the spectrum of Ab-GNRs consists of peaks at 1644, 1150, and 858 cm^{-1}, which are the characteristic peaks of IgG antibody and the TSH antibody belongs to the IgG class [62]. The amide I and II regions of the IgG antibody were signified by peaks at 1644 and 1533 cm^{-1} [63, 64]. Although, the peak at 1644 cm^{-1} may also correspond to -CO-NH- (peptide bond) between GNRs and antibodies, confirming the functionalization (Fig. 6) [65, 66].

3.5 Sensitivity and selectivity of the label (Ab-GNRs) to detect TSH

Before preparing LFA, the efficiency of label or bioconjugate (Ab-GNRs) to detect the TSH was evaluated by measuring the red shift in LPW of Ab-GNRs after adding different concentrations of TSH in the bioconjugate. This shift in LPW was due to the change in the refractive index of the medium owing to the antigen-antibody binding interaction taking place at the surface of Ab-GNRs. Thus, monitoring LSPR is the surface-sensitive optical technique to determine biomolecular interaction at the surface of nanoparticles [30]. Particularly, it was found that on increasing the concentration of TSH, the red shift was also increased significantly till 10 µIU/mL TSH concentration. While, after it, the shift was not significant, this might be because of the saturation of binding sites on the detecting probe (Ab-GNRs) (Fig. 7a and b). From this, it can be interpreted that the curve shows a linear relationship till 10 µIU/mL TSH. However, due to the saturation of binding sites, the curve fails to show the linear relation after 10 µIU/mL TSH concentration. Thus, based on the shift in the wavelength of the longitudinal SPR band, the bioconjugate was able to detect a minimum 0.05 µIU/mL of TSH. The average red shift of 1.15 nm was observed at this concentration of TSH (Fig. 7b). The red shift at 0.01 µIU/mL was insignificant. So, based on UV-visible-NIR spectroscopy, the limit of detection (LOD) of the bioconjugate was 0.05 µIU/mL. Similarly, Salahvarzi et al. used the AuNPs for LSPR sensing of TSH; they recorded an LOD of 1.71 mIU/L [30], which was much higher than the LOD of our Ab-GNRs. Therefore, the optical sensing study supported the sensitivity of GNRs for estimating TSH over spherical gold nanoparticles.

Further, as the α subunit of TSH, hCG, LH and FSH are identical, whereas the difference in the β-subunit provides the specificity to the hormones [4, 67]. Therefore, the selectivity of the bioconjugate for TSH was also checked by separately adding 50 µL of FSH (15 mIU/mL), LH (25 mIU/mL) and hCG (100 mIU/mL) in the bioconjugate. However,

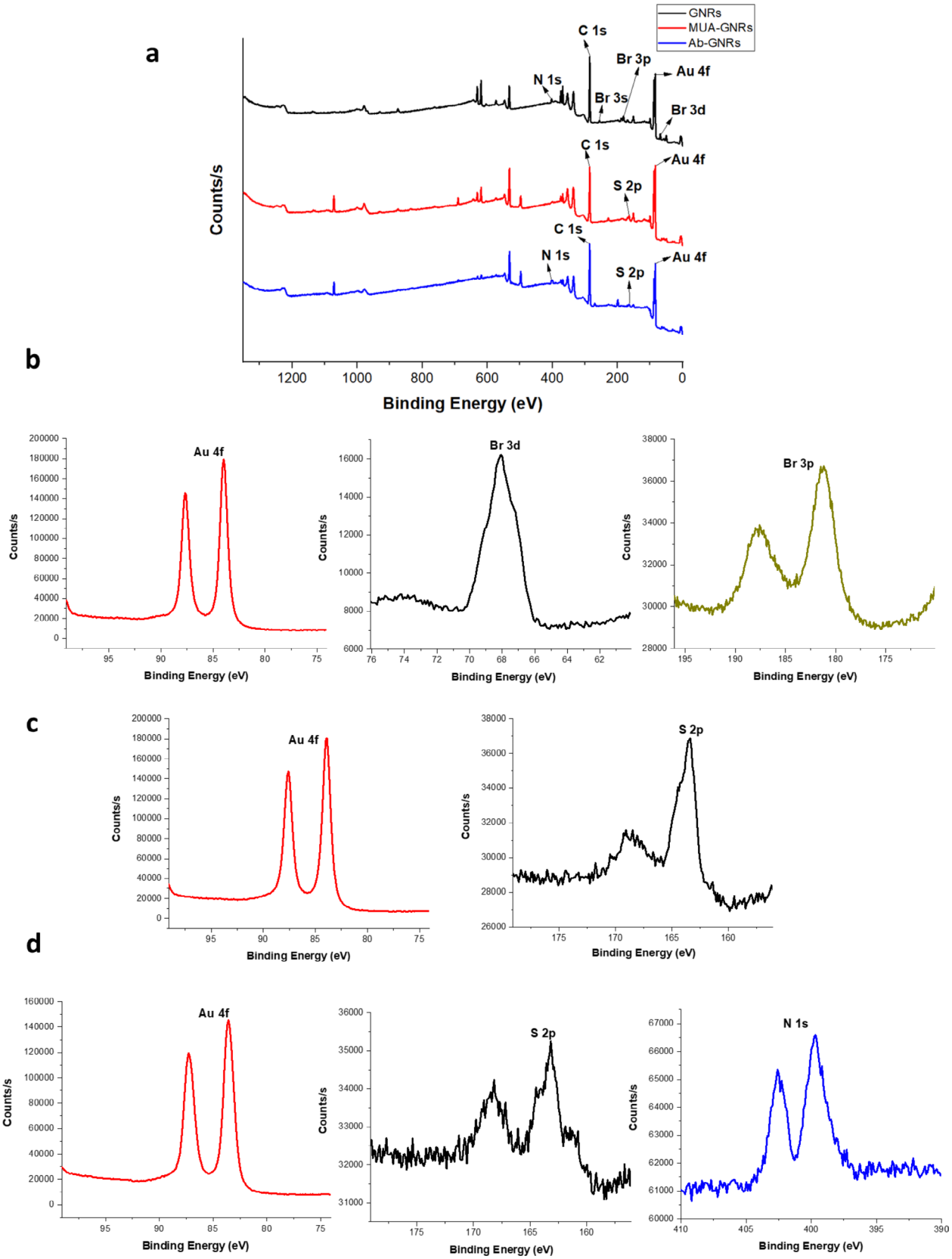

Fig. 5 XPS spectra. (**a**) XPS spectra of GNRs, MUA-GNRs and Ab-GNRs (**b**) Detailed XPS spectra of GNRs (**c**) Detailed XPS spectra of MUA-GNRs and (**d**) Detailed XPS spectra of Ab-GNRs

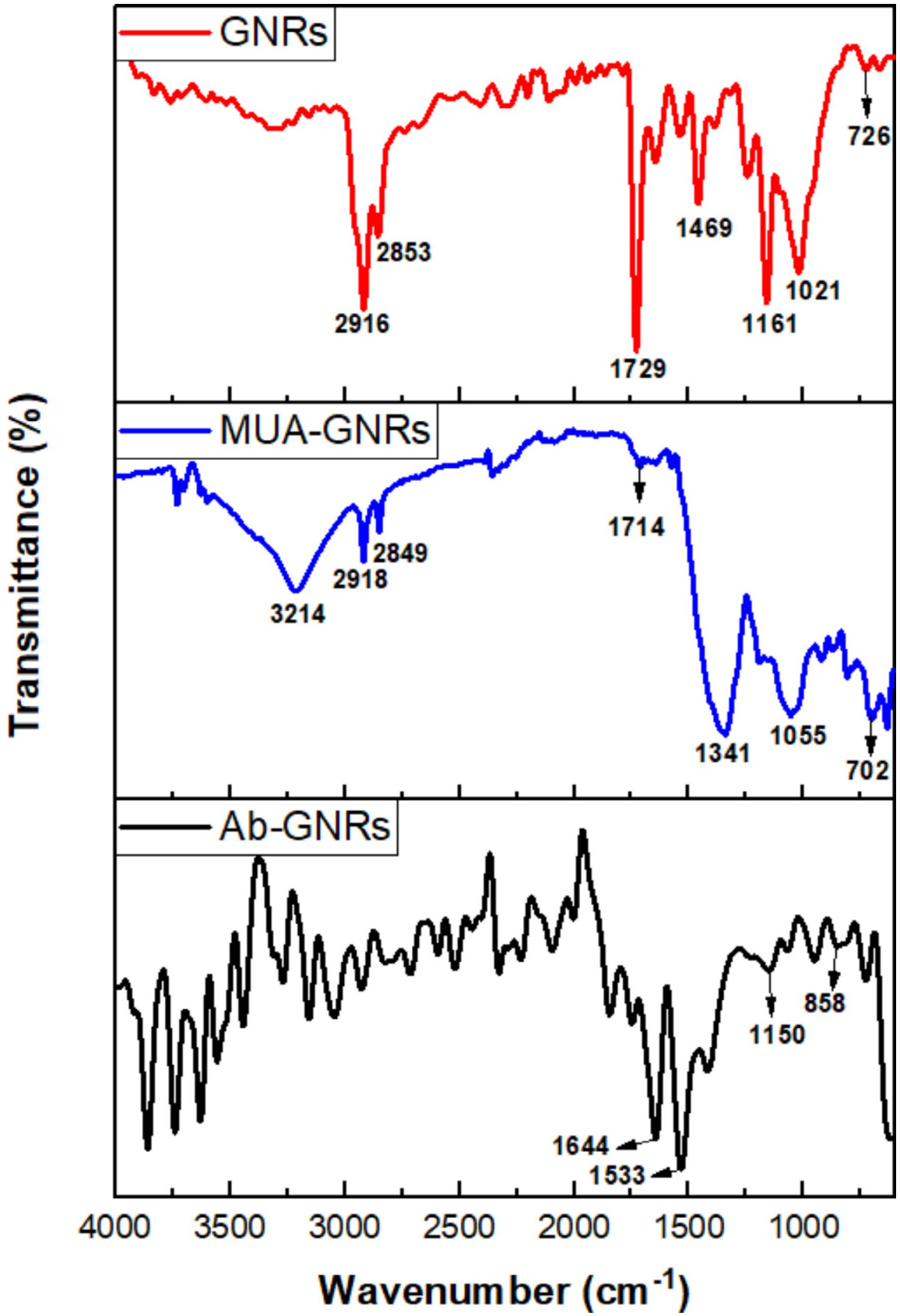

Fig. 6 FTIR spectra of GNRs, MUA-GNRs and Ab-GNRs

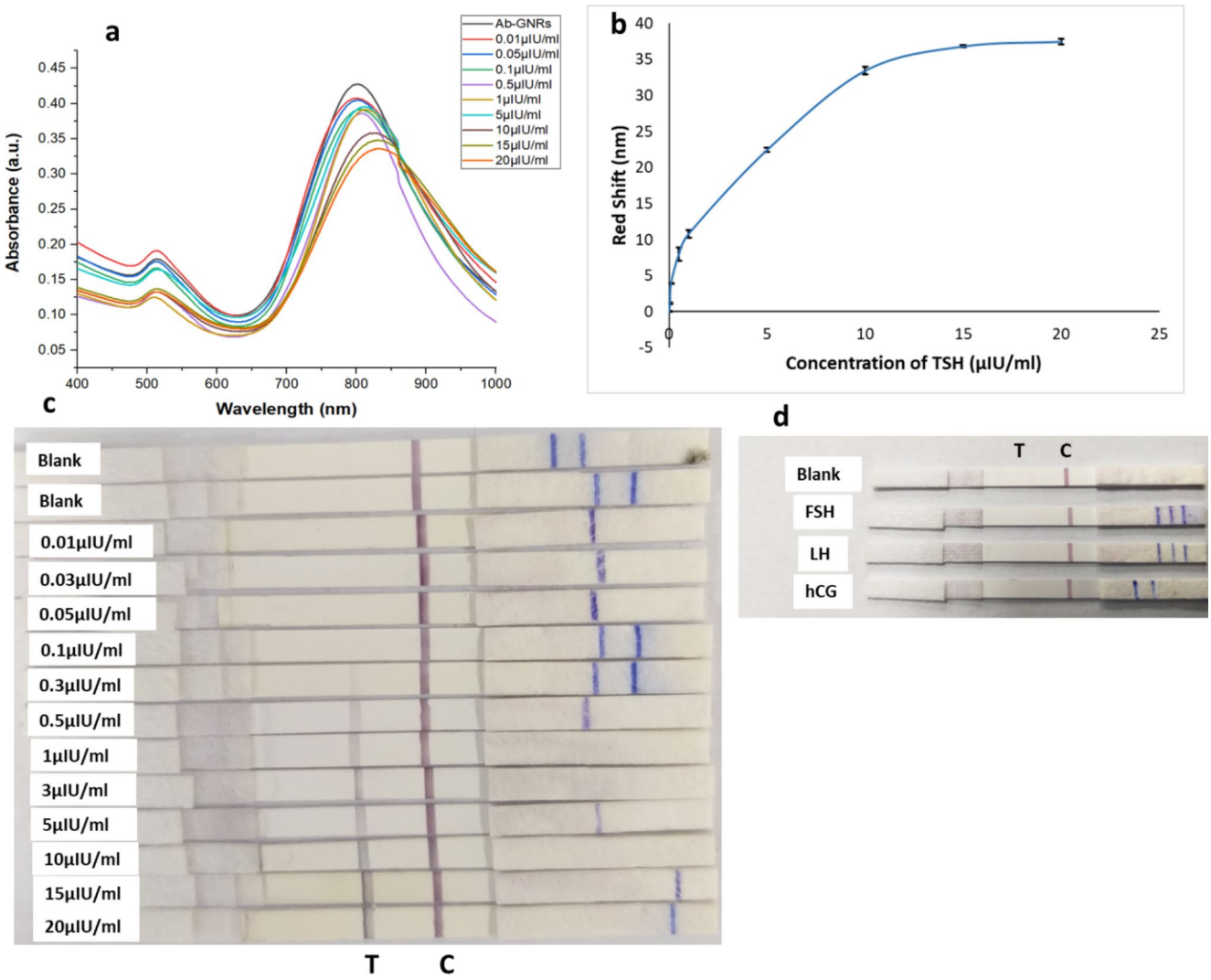

Fig. 7 (**a**) Sensitivity testing of Ab-GNRs to detect TSH based on UV-visible spectroscopy analysis, (**b**) Red shift in the wavelength of the longitudinal SPR band of Ab-GNRs at different concentrations of TSH, (**c**) Performance and sensitivity testing of the LFA to detect TSH and (**d**) Selectivity testing of LFA towards TSH

after adding these hormones, no red shift was observed in the LPW of Ab-GNRs (Fig. S8a-c). Therefore, the bioconjugate or label was found to be selective for TSH.

3.6 Performance of the LFA

The sample pad, conjugate pad, test pad and the adsorbent pad were amassed after being prepared separately. Subsequently, it was cut into 4 mm width strips and tested for its performance. The basic principle of LFA involves that when the TSH is present in the sample, it binds with the TSH antibody conjugated GNRs to form TSH-Ab-GNRs and these TSH-Ab-GNRs were further captured by the capture antibody on the test line, which has specificity for another epitope of TSH. Thus, the accumulation of TSH-Ab-GNRs on the test line leads to color development at the test line. Although, the color will always develop on the control line whether TSH is present or absent in the sample because, at the control line, the secondary antibody to the primary TSH antibody, which was conjugated on GNRs, was immobilized. So, the unreacted Ab-GNRs bind at the control line, subsequently leading to color development there. The generation of color at the control line also confirms the effective functioning of the LFA [12, 13].

Further, the OD of the conjugate (Ab-GNRs) to be sprayed on the conjugate pad was optimized to 20, as the intense color was observed at 20 OD (Fig. S9a). To optimize the OD of the bioconjugate, we did not prepare the test line on the test pad; it was optimized based only on the color development at the control line. Next, the concentration of antibodies to be dispensed on the test line was finalized to 3 mg/mL based on color intensity determined by the naked

Table 1 Comparison of different shaped gold nanoparticles based LFAs for TSH detection

Nanoparticle	Readout system used	LOD	Time of detection	Reference
Spherical gold nanoparticles	Cell phone camera	0.31 µIU/mL	12 min	[68]
Spherical gold nanoparticles	Without readout system SERS	1.5 µIU/mL 0.025 µIU/mL	10 min	[3]
Gold nanoshells	Without readout system	0.16 µIU/mL	30 min	[2]
GNRs	Without readout system	0.3 µIU/mL	10 min	Present study

eye at the test line after adding the TSH (Fig. S9b). Similarly, the sample volume for LFA was optimized to 50 µL (Fig. S9c). For this, different volumes of 5 µIU/mL TSH were used and color intensity at the test line was evaluated.

Subsequently, the performance of LFA was assessed by using different concentrations of TSH from 0.01 to 20 µIU/mL, which was prepared in the assay buffer. 50 µL of these TSH at various concentrations was added to the strips and after 10 min, the intensity of the test line was checked by the naked eye. Based on this, the LOD of the LFA was found to be 0.3 µIU/mL (Fig. 7c). Similarly, You et al. achieved the same LOD for the estimation of TSH using AuNPs as the label for LFA, but their study involved the use of cell phone to quantify the signal [68]. In contrast, our study attained the same LOD with GNRs as a label without employing any quantification method. Also, Choi et al. developed LFA for TSH sensing using AuNPs as labels. By traditional LFA, they noticed the LOD of 1.5 µIU/mL; however, on employing Surface Enhanced Raman Spectroscopy (SERS) with LFA, the LOD decreased [3]. From this, it can be concluded that GNRs are more sensitive labels than AuNPs. Moreover, due to the LOD of 0.3 µIU/mL, our LFA device was able to diagnose both hyperthyroidism and hypothyroidism without using any quantitative technique. For the hyperthyroidism condition, a very faint line or no test line will appear on the device, as the LOD of the device was closer to a normal minimal limit of TSH. However, a darker test line will appear for the hypothyroidism condition because the TSH concentration increases above 5 µIU/mL in hypothyroidism. Thus, the LFA was sensitive in assessing thyroid conditions qualitatively and semi-quantitatively. Table 1 summarizes the analytical performance of different studies that have used various shapes of gold nanoparticles as labels in LFA to detect TSH (Table 1).

Further selectivity of the LFA towards TSH was determined. For selectivity testing, 50 µL FSH (15 mIU/mL), LH (25 mIU/mL) and hCG (100 mIU/mL) were added to the sample pad of LFA and observed for color development at the test line after 10 min. After adding FSH, LH and hCG, no color was developed at the test line, confirming the LFA's selectivity towards TSH (Fig. 7d). It also shows that this device will reduce the chances of false positive results.

4 Conclusions

This innovative research utilized rod-shaped gold nanoparticles as a unique label in paper-based biosensors (LFA), enabling the detection of hypothyroidism and hyperthyroidism without involving high-end quantification techniques. To our knowledge, the study represents the pioneering application of GNRs as a label for sensing TSH through LFA. The ergonomic, rapid and robust LFA was competent to detect TSH selectively and sensitively till 0.3 µIU/mL. Besides this, the study comprehensively encompasses the major and minor aspects that regulate the synthesis and functionalization of GNRs. The GNRs were synthesized using a seed-based growth process, and the factors involved in this method were meticulously scrutinized to control the aspect ratio of GNRs. The surface modification facilitated the covalent attachment of TSH antibody on the surface of GNRs, which boosted the label's (Ab-GNRs) performance for sensing TSH. Conclusively, the study established GNRs as a sensitive label for LFA compared to the spherical gold nanoparticles, which were also substantiated by the optical study. Moreover, this GNR could potentially serve as a versatile label for detecting diverse biological and environmental indicators. Furthermore, the performance of the LFA can also be improved further by diligently exploring the factors involved in its fabrication. This could lead to its successful implementation in clinical diagnostics. Correspondingly, this LFA could be extended to form a multiplex device to assess all the thyroid hormones together in a single device.

Supplementary Information The online version contains supplementary material available at https://doi.org/10.1007/s42247-024-00976-8.

Acknowledgements Sanjana Varma is grateful to the Academy of Scientific and Innovative Research (AcSIR), Ghaziabad-201002 (India) for her PhD registration and the Council of Scientific and Industrial Research (CSIR), India, for her fellowship (Award Letter No.: 31/011(1077)/2019-EMR-I).

Author contributions Sanjana Varma contributed to data curation, formal analysis, methodology, and writing – original draft. Dimpal K. Burade contributed to data curation, formal analysis, and methodology. Bhushan P. Chaudhari contributed to conceptualization, funding acquisition, resources, supervision, validation, and writing – review & editing.

Data availability The authors confirm that the data supporting the findings of this study are available within the article. Raw data are available from the corresponding author on reasonable request.

Declarations

Competing interests The authors have no relevant financial or non-financial interests to disclose.

References

1. J.H. Jeong, T.K. Kim, S.W. Oh, E.Y. Choi, Biochip J. **7**, 408 (2013). https://doi.org/10.1007/s13206-013-7413-3
2. S.K. Bikkarolla, S.E. McNamee, P. Vance, J. McLaughlin, Biosens. (Basel). **12**, 182 (2022). https://doi.org/10.3390/bios12030182
3. S. Choi, J. Hwang, S. Lee, D.W. Lim, H. Joo, J. Choo, Sens. Actuators B Chem. **240**, 358 (2017). https://doi.org/10.1016/j.snb.2016.08.178
4. T.A. Wani, S. Zargar, S.M. Wakil, I.A. Darwish, Bioanalysis. **8**, 625 (2016). https://doi.org/10.4155/bio-2015-0034
5. P. Zheng, P. Raj, L. Wu, T. Mizutani, M. Szabo, W.A. Hanson, I. Barman, Small. **20**, 6 (2024). https://doi.org/10.1002/smll.202305110
6. H. Wang, X. Wu, P. Dong, C. Wang, J. Wang, Y. Liu, J. Chen, Int. J. Electrochem. Sci. **9**, 12 (2014). https://doi.org/10.1016/S1452-3981(23)07694-0
7. F. Rossi, T. Trakoolwilaiwan, V. Gigli, C. Tortolini, A. Lenzi, A.M. Isidori, N.T.K. Thanh, R. Antiochia, Nanoscale **16**, 18134 (2024). https://doi.org/10.1039/d4nr02075h
8. G.A. Posthuma-trumpie, J. Korf, Anal. Bioanal Chem. **393**, 569 (2009). https://doi.org/10.1007/s00216-008-2287-2
9. H.V. Hsieh, J.L. Dantzler, B.H. Weigl, Diagnostics. **7**, 29 (2017). https://doi.org/10.3390/diagnostics7020029
10. C. Parolo, A. Merkoçi, Chem. Soc. Rev. **42**, 450 (2013). https://doi.org/10.1039/c2cs35255a
11. J.D. Bishop, H.V. Hsieh, D.J. Gasperino, B.H. Weigl, Lab. Chip. **19**, 2486 (2019). https://doi.org/10.1039/c9lc00104b
12. C. Parolo, A. Sena-Torralba, J.F. Bergua, E. Calucho, C. Fuentes-Chust, L. Hu, L. Rivas, R. Álvarez-Diduk, E.P. Nguyen, S. Cinti, D. Quesada-González, A. Merkoçi, Nat. Protoc. **15**, 3788 (2020). https://doi.org/10.1038/s41596-020-0357-x
13. M. Sajid, A.N. Kawde, M. Daud, J. Saudi Chem. Soc. **19**, 6 (2015). https://doi.org/10.1016/j.jscs.2014.09.001
14. B.E. Bahadır, M.K. Sezgintürk, TrAC - Trends Anal. Chem. **82** (2016). https://doi.org/10.1016/j.trac.2016.06.006
15. S.L. Znoyko, A.V. Orlov, V.A. Bragina, M.P. Nikitin, M.P.P.I. Nikitin, Talanta. **216** (2020). https://doi.org/10.1016/j.talanta.2020.120961
16. A. Ghosh, A. Banerjee, R. Srivastava, in *Surface engineering and functional nanomaterials for point-of-care analytical devices*, ed. by B. Purohit, P. Chandra (Springer Nature Singapore, 2023), p. 323. https://doi.org/10.1007/978-981-99-3025-8_14
17. Y.C. Wang, É. Rhéaume, F. Lesage, A. Kakkar, Molecules. **23**, 11 (2018). https://doi.org/10.3390/molecules23112851
18. J. Cheng, L. Ge, B. Xiong, Y. He, J. Chin. Chem. Soc. **58**, 822 (2011). https://doi.org/10.1002/jccs.201190128
19. H. Zhang, Z. She, H. Su, K. Kerman, H.B. Kraatz, Analyst. **141**, 6080 (2016). https://doi.org/10.1039/c6an01111j
20. H. Huang, F. Liu, S. Huang, S. Yuan, B. Liao, S. Yi, Y. Zeng, P.K. Chu, Anal. Chim. Acta. **755**, 108 (2012). https://doi.org/10.1016/j.aca.2012.10.020
21. J. Cao, E.K. Galbraith, T. Sun, K.T.V. Grattan, Sens. Actuators B Chem. **169**, 360 (2012). https://doi.org/10.1016/j.snb.2012.05.019
22. P.L. Truong, B.W. Kim, S.J. Sim, Lab. Chip. **12**, 1102 (2012). https://doi.org/10.1039/c2lc20588b
23. J. Cao, T. Sun, K.T.V. Grattan, Sens. Actuators B Chem. **195**, 332 (2012). https://doi.org/10.1016/j.snb.2014.01.056
24. J. Zhou, Z. Cao, N. Panwar, R. Hu, X. Wang, J. Qu, S.C. Tjin, G. Xu, K.T. Yong, Coord. Chem. Rev. **352**, 15 (2017). https://doi.org/10.1016/j.ccr.2017.08.020
25. Q. Li, Y. Cao, in *Nanorods*, ed. by O. Yalçın (IntechOpen, Shanghai, China, 2012), p. 159
26. C. Gui, D.X. Cui, Cancer Biol. Med. **9**, 221 (2012). https://doi.org/10.7497/j.issn.2095-3941.2012.04.002
27. X. Huang, S. Neretina, M.A. El-Sayed, Adv. Mater. **21**, 4880 (2009). https://doi.org/10.1002/adma.200802789
28. B. Nikoobakht, M.A. El-Sayed, Chem. Mater. **15**, 1957 (2003). https://doi.org/10.1021/cm0207321
29. M.M. Bradford, Anal. Biochem. **72**, 248 (1976). https://doi.org/10.1016/0003-2697(76)90527-3
30. A. Salahvarzi, M. Mahani, M. Torkzadeh-Mahani, R. Alizadeh, Anal. Biochem. **516**, 1 (2017). https://doi.org/10.1016/j.ab.2016.10.003
31. D.A. Boyne, A.C. Chipara, M.H. Griep, RSC Adv. **6**, 63634 (2016). https://doi.org/10.1039/c6ra12058j
32. S. Koeppl, C. Solenthaler, W. Caseri, R. Spolenak, J. Nanomater. **2011**, 515049 (2011). https://doi.org/10.1155/2011/515049
33. L. Scarabelli, A. Sánchez-Iglesias, J. Pérez-Juste, L.M. Liz-Marzán, J. Phys. Chem. Lett. **6**, 4270 (2015). https://doi.org/10.1021/acs.jpclett.5b02123
34. S.L. Smitha, K.G. Gopchandran, N. Smijesh, R. Philip, Prog Nat. Sci.: Mater. Int. **23**, 36 (2013). https://doi.org/10.1016/j.pnsc.2013.01.005
35. C.L. John, S.L. Strating, K.A. Shephard, J.X. Zhao, RSC Adv. **3**, 10909 (2013). https://doi.org/10.1039/c3ra41521j
36. L. Roach, P.L. Coletta, K. Critchley, S.D. Evans, J. Phys. Chem. C **126**, 6 (2022). https://doi.org/10.1021/acs.jpcc.1c10447
37. T.K. Sau, C.J. Murphy, Langmuir. **20**, 6414 (2004). https://doi.org/10.1021/la049463z
38. X. Ye, C. Zheng, J. Chen, Y. Gao, C.B. Murray, Nano Lett. **13**, 765 (2013). https://doi.org/10.1021/nl304478h
39. L. Vigderman, B.P. Khanal, E.R. Zubarev, Adv. Mater. **24**, 4811 (2012). https://doi.org/10.1002/adma.201201690
40. J. Wang, L. Zhang, Y. Huang, A. Dandapat, L. Dai, G. Zhang, X. Lu, J. Zhang, W. Lai, T. Chen, Sci. Rep. **7**, 41419 (2017). https://doi.org/10.1038/srep41419
41. J. He, S. Unser, I. Bruzas, R.J. Cary, Z. Shi, R. Mehra, K. Aron, L. Sagle, Colloids Surf. B Biointerfaces. **163**, 140 (2018). https://doi.org/10.1016/j.colsurfb.2017.12.019
42. J.P. Oliveira, A.R. Prado, W.J. Keijok, P.W.P. Antunes, E.R. Yapuchura, M.C.C. Guimarães, Sci. Rep. **9**, 13859 (2019). https://doi.org/10.1038/s41598-019-50424-5
43. K.M. Mayer, S. Lee, H. Liao, B.C. Rostro, A. Fuentes, P.T. Scully, C.L. Nehl, J.H. Hafner, ACS Nano. **2**, 687 (2008). https://doi.org/10.1021/nn7003734
44. F. Cao, Q. Yao, X. Wang in *Photonic Therapeutics and Diagnostics XII*, ed. by H.W. By, G.J. Kang, K.W. Tearney, L. Gregory, M.C. Marcu, P.J. Skala, B. Campagnola, N. Choi, H. Kollias, A. Zeng, B.J.F. Mandelis, J.F. Wong, Ilgner (SPIE, San Francisco, California, United States, 2016), p 96894A. https://doi.org/10.1117/12.2212140
45. S.M. Ansar, S. Chakraborty, C.L. Kitchens, Nanomaterials. **8**, 5 (2018). https://doi.org/10.3390/nano8050339
46. W. Jung, J. Han, J. Kai, J.Y. Lim, D. Sul, C.H. Ahn, Lab. Chip. **13**, 4653 (2013). https://doi.org/10.1039/c3lc50403d
47. F. Cao, Q. Yao, T. Yang, Z. Zhang, Y. Han, J. Feng, X.H. Wang, RSC Adv. **6**, 46594 (2016). https://doi.org/10.1039/c6ra01557c

48. A.P. Leonov, J. Zheng, J.D. Clogston, S.T. Stern, A.K. Patri, A. Wei, ACS Nano. **2**, 2481 (2008). https://doi.org/10.1021/nn800466c
49. G. Kedawat, I. Sharma, K. Nagpal, M. Kumar, G. Gupta, B.K. Gupta, ACS Omega. **4**, 7 (2019). https://doi.org/10.1021/acsomega.9b01157
50. S. Anandhakumar, R. Rajaram, J. Mathiyarasu, Analyst. **139**, 14 (2013). https://doi.org/10.1039/C4AN00480A
51. L. Zhang, F. Zhao, Z. Li, Y. Fang, P. Wang, Plasmonics. **11**, 1511 (2016). https://doi.org/10.1007/s11468-016-0204-7
52. S. Si, C. Leduc, M.H. Delville, B. Lounis, ChemPhysChem. **13**, 193 (2012). https://doi.org/10.1002/cphc.201100710
53. A.R. Marlinda, A. Pandikumar, S. Jayabal, N. Yusoff, A.B. Suriani, N.M. Huang, Microchim Acta. **183**, 3077 (2016). https://doi.org/10.1007/s00604-016-1922-4
54. A. Abareshi, M.A. Pirlar, M. Houshiar, New. J. Chem. **45**, 1 (2021). https://doi.org/10.1039/D0NJ04580B
55. E. Yan, M. Cao, Y. Wang, X. Hao, S. Pei, J. Gao, Y. Wang, Z. Zhang, D. Zhang, Mater. Sci. Eng., C **58** (2016). https://doi.org/10.1016/j.msec.2015.09.080
56. L. Su, S. Hu, L. Zhang, Z. Wang, W. Gao, J. Yuan, M. Liu, Small. **13**, 1602809 (2017). https://doi.org/10.1002/smll.201602809
57. Y. Tao, J. Yang, L. Chen, Y. Huang, B. Qiu, L. Guo, Z. Lin, Microchim Acta. **185**, 1–9 (2018). https://doi.org/10.1007/s00604-018-2897-0
58. Y.R. Toh, P. Yu, X. Wen, J. Tang, T. Hsieh, Nanoscale Res. Lett. **8**, 1 (2013). https://doi.org/10.1186/1556-276X-8-103
59. M. Almada, B.H. Leal-Martínez, N. Hassan, M.J. Kogan, M.G. Burboa, A. Topete, M.A. Valdez, J. Juárez, Mater. Sci. Eng., C **77** (2017). https://doi.org/10.1016/j.msec.2017.03.218
60. J.G. Mehtala, D.Y. Zemlyanov, J.P. Max, N. Kadasala, S. Zhao, A. Wei, Langmuir. **30**, 46 (2014). https://doi.org/10.1021/la5029542
61. G. Su, C. Yang, J.J. Zhu, Langmuir. **31**, 2 (2015). https://doi.org/10.1021/la504041f
62. H. Huang, S. Huang, S. Yuan, C. Qu, Y. Chen, Z. Xu, B. Liao, Y. Zeng, P.K. Chu, Anal. Chim. Acta. **683**, 242 (2011). https://doi.org/10.1016/j.aca.2010.10.033
63. A.L. Daniel-Da-Silva, S. Fateixa, A.J. Guiomar, B.F.O. Costa, N.J.O. Silva, T. Trindade, B.J. Goodfellow, A.M. Gil, Nanotechnology. **20**, 355602 (2009). https://doi.org/10.1088/0957-4484/20/35/355602
64. G. Baird, C. Farrell, J. Cheung, A. Semple, J. Blue, P.L. Ahl, Protein J. **39**, 318 (2020). https://doi.org/10.1007/s10930-020-09907-y
65. Y. Zhang, N. Song, J. Fu, Y. Liu, X. Zhan, S. Peng, Z. Yang, X. Zhu, Y. Chen, Z. Wang, Y. Yu, Q. Shi, Y. Fu, K. Yuan, N. Zhou, T.E. Ichim, W. Min, RSC Adv. **6**, 77577 (2016). https://doi.org/10.1039/C6RA13297A
66. H. Mirshekari, B. Dabirmanesh, S. Daneshjou, K. Khajeh, Colloid Interface Sci. Commun. **61**, 100795 (2024). https://doi.org/10.1016/j.colcom.2024.100795
67. D. Wang, J.P. Skinner, Q. Ruan, S.Y. Tetin, G.B. Collier, Clin. Chim. Acta. **438**, 55 (2015). https://doi.org/10.1016/j.cca.2014.07.027
68. D.J. You, T.S. Park, J.Y. Yoon, Biosens. Bioelectron. **40**, 1 (2013). https://doi.org/10.1016/j.bios.2012.07.014